Search for Dark Matter with the LUX–ZEPLIN Detector – acoustic sensor performance and detector response



Cees Carels

Wolfson College
University of Oxford

A thesis submitted for the degree of
Doctor of Philosophy

Trinity 2018

Abstract

The LUX-ZEPLIN experiment needs acoustic sensors to monitor the liquid xenon contained in its time projection chamber (TPC) for irregularities that could spoil a stable liquid xenon environment that is required for a dark matter search. I have developed and implemented algorithms that distinguish the occurrence of bubbling and other sounds, and I have carried out tests using a PVDF sensor and a readout system developed at Oxford; demonstrating that the hardware and analysis meet the requirements for their purpose in LUX-ZEPLIN. Acoustic sensors can be used as a veto to strengthen the fidelity of detector data.

The primary event data in LUX-ZEPLIN will come from arrays of photomultiplier tubes, which detect light emitted from recoil events in the TPC. Waveform data from TPC events will be collected through a bespoke data acquisition system. A simulation of the detector response is needed in order to ensure that reliable event analysis will be possible when the experiment starts taking data. I have constructed an analytical model of the full signal chain from the photomultiplier tubes to the digitisers, including all analogue front-end electronics and interconnecting cabling, and I created a Monte Carlo simulation software package in which I have embedded this model. I have used the model and the software to carry out simulations to evaluate the design of the LUX-ZEPLIN electronics readout system. The model and the simulation I have created play a central role in performing event analysis on simulated data in preparation for real data taking with the LUX-ZEPLIN experiment.

Acknowledgements

First and foremost, my appreciation and thanks go to Professor Hans Kraus for his guidance as a supervisor. His experience and wisdom have been an invaluable source of learning and personal academic growth over the course of the last years.

I also thank the LUX-ZEPLIN collaboration for providing the opportunities to contribute to what I am confident will become one of the most significant dark matter searches. In particular, a thank-you to my colleagues in Oxford, and the teamwork in the cleanroom during the final assembly of the sensors.

I would also like to thank my family and friends for their immeasurable support. Their continuous encouragement has been instrumental.

To the memory of my Dad and my Grandmother.

Contents

List of Tables **7**

List of Figures **8**

Glossary **13**

Introduction **17**

1 Dark Matter **19**

1.1 Cosmology 20

1.2 Astrophysics 23

1.3 Particle Physics 28

1.4 Dark Matter Searches 33

2 Dark Matter Detectors **44**

2.1 Liquid Noble Elements in Direct Searches: Liquid Xenon 45

2.2 Two-Phase Time Projection Chambers 56

2.3 Direct Search Experiments 61

3 LUX-ZEPLIN **67**

3.1 The Science Case for LUX-ZEPLIN (LZ) 69

3.2 Overview of the LZ Experiment 71

3.3 Detector Hardware 76

4 Acoustic Sensors **79**

4.1 Low-Pass Filters and High-Pass Filters 80

4.2 Purpose of the Acoustic Sensors 82

4.3 Acoustic Signal Chain: Sensing Method and Electronics 85

4.4 Classifying Acoustic Event Topologies 94

4.5 Detecting Pump Noise 104

4.6 SLAC System Test 109

5 Detector Electronics Response Model **119**

5.1 Overview of the LUX-ZEPLIN Detector Electronics Response Simulation Framework . . . 120
5.2 Physics Modules . . . 122
5.3 PMT Response . . . 124
5.4 Cable Model . . . 130
5.5 Amplifier Model . . . 136
5.6 Digitisation and Triggering . . . 154
5.7 ^{83m}Kr Calibration Source Simulation . . . 158
5.8 Energy Reconstruction . . . 160
5.9 Expected Event Data Processing . . . 163

6 Summary and Outlook **165**

7 References **166**

A Acoustic Sensors Quality Control, and Installation **187**

B Minnaert Resonance Frequency **188**

C Software Packages **189**
C.1 DER . . . 189

D Cable Derivation **191**

E Amplifier Derivation **193**
E.1 Low-Gain . . . 193
E.2 High-Gain . . . 197
E.3 Laplace Transform for Sallen-Key Element . . . 205

F Digitiser Anti-Aliasing Filter Derivation **207**

G Event Builder Specifications **208**

List of Tables

1.1 Overview of several key parameters derived from Wilkinson Microwave Anisotropy Probe (WMAP) data. 21
2.1 Key properties of several noble elements used for dark matter searches. 45
3.1 Overview of several key parameters of the LZ detector. 73
4.1 Acoustic sensors cleanliness protocol. 85
4.2 Piezoelectric charge constants. 86
4.3 Reduced quantities for each sub-band. 102
4.4 Classification ratios for each feature. 103
4.5 Sub-band truth information for acoustic classification algorithm. 103
4.6 Characteristic frequencies of key acoustic event topologies. . . . 117
5.1 Overview of mathematical forms of various filter types. 137
5.2 Time constants for each stage of the low-gain and high-gain channels of the amplifier. 148
5.3 Data processing rates and compression ratios for simulated events that were processed by the LZ Event Builder. 164

List of Figures

1.1 Galaxy rotation curves. 25
1.2 Gravitational lensing in the Bullet Cluster. 27
1.3 Limits from axion searches. 32
1.4 Diagram for a generic Dark Matter (DM)-Standard Model (SM) interaction. 33
1.5 DAMA/LIBRA annual modulation signal. 36
1.6 Spin-independent limits of several direct detection experiments. 37
1.7 Maxwell-Boltzmann velocity distribution. 38
1.8 Nuclear form factor for xenon (Xe). 39
1.9 Differential scattering rate for dark matter recoil in liquid xenon. 41
1.10 Large Underground Xenon (LUX) cross-section at 90 % C.L. . . 43
2.1 Weakly Interacting Massive Particle (WIMP) integral spectrum for various liquid noble elements. 47
2.2 Overview of scintillation and ionisation processes in xenon. . . . 50
2.3 Increase in yield of electron and nuclear recoils at low energies. . 53
2.4 Anti-correlation of yields. 54
2.5 Total quanta versus energy in the LUX experiment. 55
2.6 Operating principle of a dual-phase Time Projection Chamber (TPC). 57
2.7 Example calibration in the LUX experiment (Run-3). 63
2.8 Combined limit plot from several direct searches. 65
3.1 Cross-sectional view of the LZ detector. 68
3.2 Projected LZ spin-independent WIMP-nucleon interaction cross-section limit. 70
3.3 Change in light yield as a function of change in the liquid level relative to the anode. 75
3.4 Photomultiplier tube signal processing chain of the LZ TPC. . . 77
4.1 Circuit diagram and Bode plot for a first-order low-pass filter. . 81
4.2 Circuit diagram and Bode plot for a first-order high-pass filter. . 81

4.3 Monitoring targets for acoustic sensors that will be on the exterior surface of the inner cryostat vessel of the LZ experiment. . 82
4.4 Differential acoustic sensor unit. 83
4.5 Acoustic sensor front-end electronics readout chain, shown for a single readout channel. 86
4.6 Front-end readout electronics. 88
4.7 Circuit diagram for the acoustic sensor and the readout board. . 89
4.8 Transfer function of the amplifier block on the acoustic sensor readout board. 90
4.9 Acoustic sensor software trigger rate. 93
4.10 A harmonically oscillating bubble that expands and contracts. . 95
4.11 The characteristic damped oscillator shape of a bubble acoustic signal. 96
4.12 Detecting a droplet acoustic signal. 97
4.13 Minnaert bubble resonance frequency with distance from the liquid level. 98
4.14 Detecting tapping on the cryostat vessel acoustically. 98
4.15 Overview of setup for producing and detecting resistor-induced bubbling at cold temperatures. 99
4.16 Acoustically detecting bubbling caused by heating using a resistor in liquid nitrogen. 100
4.17 Distinguishing between bubbles and droplets. 102
4.18 Apparatus setup showing the BC.2511/12 pump. 104
4.19 Measured and analysed acoustic signal from bubble production in a water-filled metal vessel under influence of vibrational pump noise. 105
4.20 Closeup of pump noise analysed signal. 106
4.21 Closeup of the analysed signal in the presence of pump noise. . . 107
4.22 Fast Fourier Transform (FFT) of measured acoustic baseline signal from a vacuum pump while it is switched off. 108

4.23 FFT of measured acoustic baseline signal from a vacuum pump while it is switched on. 108
4.24 System Test TPC at SLAC. 110
4.25 Acoustic sensors epoxied with Master Bond® EP29LPSP epoxy at the SLAC System Test. 111
4.26 Spectrogram view of time-series data collected at the LZ System Test at SLAC. 112
4.27 Algorithmic bubble detection at the SLAC LZ System Test. . . 114
4.28 Hypothesis test for bubble identification. 115
4.29 Time domain representation of a single tap event on the exterior of the main vessel at the SLAC System Test setup. 116
4.30 FFT representation of average intensity of tapping at the SLAC System Test. 117
5.1 Flow-diagram showing an overview of the key software packages used for LZ Monte Carlo simulations. 121
5.2 Organisation of Detector Electronics Response (DER) physics modules. 123
5.3 Schematic of photomultiplier tube (PMT) base cable termination from the PMT into the amplifier. 125
5.4 Equivalent circuit for the PMT + PMT base system. 125
5.5 Example simulated PMT pulse produced by DER. 126
5.6 PMT pulse area distribution. 128
5.7 Measurements of Hamamatsu R11410 dark rate. 129
5.8 Equivalent circuit for a cable. 130
5.9 Model prediction of attenuation of 45 feet of Axon A21482C cable. 133
5.10 Simulated and measured attenuation of 45 feet of Axon A21482C cable. 134
5.11 Signal flow diagram for the implementation of the cable. 135
5.12 Block diagram of the amplifier. 136
5.13 Circuit diagram for the first stage (Block 1) of the low-gain channel of the amplifier board. 139

5.14 Transfer function of the first stage of the low-gain channel of the amplifier board. 139
5.15 Circuit diagram for the second stage (Block 2) of the low-gain amplifier board. 140
5.16 Transfer function of the second stage of the low-gain channel of the amplifier board. 141
5.17 Circuit diagram for the first stage (Block 1) of the high-gain channel of the amplifier board. 142
5.18 Transfer function of the first stage of the high-gain channel of the amplifier board. 142
5.19 Circuit diagram for the second stage (Block 2) of high-gain channel of the amplifier board. 143
5.20 Transfer function of the second stage of the high-gain channel of the amplifier board. 143
5.21 Circuit diagram for the third stage (Block 3) of the high-gain channel of the amplifier board. 144
5.22 Transfer function of the third stage of the high-gain channel of the amplifier board. 145
5.23 Pole plot of the final stage of the high-gain amplifier channel. . . 146
5.24 Comparison of the transfer function at high frequencies including the effect of the open-loop gain. 147
5.25 Transfer function of the amplifier board. 149
5.26 Transient response of the low-gain and high-gain amplifier channels. 150
5.27 Circuit diagram of the digitiser. 151
5.28 Transfer function of the digitiser. 151
5.29 Series-parallel termination of the output of the amplifier and the input of the digitiser board. 152
5.30 Transient response of the analogue signal chain. 153
5.31 Identification of PODs from waveforms. 155
5.32 Simulated digitised sample waveforms. 157

5.33 Decay scheme of ^{83m}Kr. 158
5.34 High-gain summed top PMT array S2 for a ^{83m}Kr decay event. . 159
5.35 High-gain summed bottom and top PMT array S1 for a ^{83m}Kr decay event. 159
5.36 Reconstructed recoil energy distribution for simulated electron recoil events. 161
5.37 Scatter plot of the reconstructed recoil energy versus the Monte Carlo truth. 162

Glossary

ADC Analogue-to-Digital Converter.

ADMX Axion Dark Matter eXperiment.

ATLAS A Toroidal LHC ApparatuS.

BACCARAT Basically A Component-Centric Analog Response to AnyThing.

BBN Big Bang Nucleosynthesis.

BIBO Bounded-Input, Bounded-Output.

BSM Beyond the Standard Model.

CAST CERN Axion Solar Telescope.

CDMS Cryogenic Dark Matter Search.

CJPL China Jinping Underground Laboratory.

CMB Cosmic Microwave Background.

CP Charge Parity.

CRESST Cryogenic Rare Event Search with Superconducting Thermometers.

DAMA/LIBRA DArk MAtter / Large sodium Iodide Bulk for RAre processes.

DAQ Data Acquisition.

DC Direct Current.

DEAP Dark matter Experiment using Argon Pulse-shape.

DER Detector Electronics Response.

DFSZ Dine-Fischler-Srednicki-Zhitnitsky.

DM Dark Matter.

EB Event Builder.

EDELWEISS Expérience pour DEtecter Les WIMPs En Site Souterrain.

ER Electron Recoil.

FFT Fast Fourier Transform.

FWHM Full Width Half Maximum.

FWTM Full Width Tenth Maximum.

GEANT4 GEometry ANd Tracking.

ICP-MS Inductively Coupled Plasma Mass Spectrometry.

ICV Inner Cryostat Vessel.

KSVZ Kim-Shifman-Vainshtein-Zakharov.

LAr Liquid Argon.

LBNL Lawrence Berkeley National Laboratory.

LCE Light Collection Efficiency.

LHC Large Hadron Collider.

LIGO Laser Interferometer Gravitational-Wave Observatory.

LN liquid nitrogen.

LNGS Laboratori Nazionali del Gran Sasso.

LSP Lightest Supersymmetric Particle.

LSW Light Shining through Walls.

LUX Large Underground Xenon.

LXe liquid xenon.

LZ LUX-ZEPLIN.

LZap LZ analysis program.

MACHO Massive Astrophysical Compact Halo Object.

MOND Modified Newtonian Dynamics.

MSSM Minimal Supersymmetric Standard Model.

NAA Neutron Activation Analysis.

NERSC National Energy Research Scientific Computing Center.

NR Nuclear Recoil.

OSQAR Optical Search for QED Vacuum Birefringence.

PDE Photon Detection Efficiency.

PEEK Polyether ether ketone.

PMT photomultiplier tube.

POD Pulse Only Digitisation.

PTFE Polytetrafluoroethylene.

PVDF Polyvinylidene fluoride.

PZT lead zirconate titanate.

QCD Quantum Chromodynamics.

QE quantum efficiency.

RMS Root Mean Square.

SM Standard Model.

SNOLAB Sudbury Neutrino Observatory Laboratory.

SPICE Simulation Program with Integrated Circuit Emphasis.

SURF Sanford Underground Research Facility.

SUSY Supersymmetry.

TDR Technical Design Report.

TeVeS Tensor Vector Scalar.

TPB Tetraphenyl butadiene.

TPC Time Projection Chamber.

UKDC UK Data Centre.

USDC US Data Centre.

VUV Vacuum Ultraviolet.

WIMP Weakly Interacting Massive Particle.

WMAP Wilkinson Microwave Anisotropy Probe.

Xe xenon.

XENON1T XENON1T.

XENONnT XENONnT.

ZEPLIN-III ZonEd Proportional scintillation in LIquid Noble gases.

Introduction

LZ is being designed for construction at the Sanford Underground Research Facility (SURF) in the former Homestake Mine in Lead, South Dakota, USA. The primary goal of LZ is to make a discovery by detecting the interaction of dark matter in the experiment, and LZ must be able to constrain the spin-independent WIMP-nucleon interaction cross-section to at least $3 \times 10^{-48}\,\mathrm{cm}^2$ at a WIMP mass of 40 GeV [1]. It is thought that a dark matter interaction (recoil event) with a liquid xenon (LXe) atom can produce detectable scintillation light and ionisation signals. LXe is particularly suited to this task: it has a high scintillation yield owing to its atomic structure. By having a high interaction cross-section, it can efficiently shield against external backgrounds which cause scattering of neutrons and high-energy photons. The position of such events can be localised using the detector instrumentation which allows background events to be vetoed [2].

Chapter 1 is an exposition of the historical and present-day evidence in favour of the existence of dark matter. It will start from the large scale structural evolution of the universe, motivating the need for an explanation of cosmological observations, down to astrophysical measurements of galaxies, focussing on the most widely accepted model of the universe and the way in which dark matter fits into it. The discussion then shifts to dark matter particle search experiments, including collider and indirect searches, and a number of direct search experiments.

Chapter 2 provides a concise overview of two-phase TPCs in direct search experiments, explaining why liquid xenon is a highly desirable detector medium for dark matter searches using this technology. The nuclear and electronic response of liquid xenon to particle recoils are discussed in detail. Practical considerations of detector design, such as material selection, the size of the detector, and event reconstruction, are also covered. Several two-phase xenon

TPC direct searches are highlighted, in particular LUX and ZEPLIN-III[1], of which LZ is a direct descendent.

Chapter 3 will introduce and motivate the science case for LZ, providing a broad overview of the detector. The technical aspects of the design of the detector are described as a function of achieving the physics goals of the experiment.

Chapter 4 covers the contribution of the thesis to LZ sensor hardware, characterising the performance and diagnostic utility of acoustic sensors which complement the event veto systems at LZ. The sensor performance is shown with real data taken in a liquid xenon environment that closely resembles LZ: the System Test at SLAC. Analysis algorithms are developed which enable automatic detection of acoustic events, such as bubbling and droplets in liquid.

Chapter 5 covers the contribution of the thesis to the detector response of the PMT readout system of the LZ detector. An analytical model is developed which predicts the expected response of the analogue electronics in LZ, including the photomultiplier tubes, the amplifier, the digitiser, and the interconnecting cabling. The model is implemented into a Monte Carlo simulation in software, and applied to the production of simulated physics events that are used to quantify the Data Acquisition (DAQ) performance, and the resource requirements for event processing at LZ.

[1] ZonEd Proportional scintillation in LIquid Noble gases (ZEPLIN-III).

1 Dark Matter

The dark matter content of the universe continues to be one of the large unknowns in our understanding of physics. The universe is thought to be composed of a significant fraction of dark matter, and so it is a necessary topic of study.

The question of the nature of dark matter is very broad, and it is tackled from several branches of physics, including cosmology, astrophysics, and particle physics. There are no clear answers about dark matter yet; a myriad of theoretical and experimental pathways have provided well-motivated assumptions, theories, and searches.

Cosmological measurements of the Cosmic Microwave Background (CMB) radiation made with the Wilkinson Microwave Anisotropy Probe (WMAP), and astrophysical measurements of galaxy rotation curves and gravitational lensing, characterise dark matter. In particular, they are consistent with the idea that a large fraction of the matter density of the universe is due to non-baryonic (beyond the Standard Model) particles. Many constraints place the estimates of the dark matter mass consistent with the electroweak scale [3], and strongly disfavour dark matter interactions through the electromagnetic and strong force.

Still other theories exist, which do away with dark matter particles entirely. For example, there are theories which modify Newton's laws of motion, such as Modified Newtonian Dynamics (MOND) [4], later embedded in a framework consistent with general relativity in Tensor Vector Scalar (TeVeS) theory [5]. The bottom line of these theories is the introduction of a dependence of the acceleration on a characteristic acceleration scale a_0 and a function $\mu(a/a_0)$ which is determined from data [6]. These theories address the issue of large amounts of missing matter in the outer regions of galaxies, without necessitating a dark matter particle.

1.1 Cosmology

1.1.1 Evolution of the Universe

The expansion of the universe is governed by its density of matter and energy. The Friedmann Equation is a dynamical description that decomposes the total density of the universe into its matter and energy content

$$\left[\left(\frac{1}{a(t)}\frac{\mathrm{d}a(t)}{\mathrm{d}t}\right)^2 - \frac{8}{3}\pi G\rho(t) - \frac{1}{3}\Lambda c^2\right] a(t)^2 = -kc^2, \tag{1}$$

where t is time, $a(t)$ is the scale factor, G is the gravitational constant, k is the curvature constant, ρ is the density function, Λ is the cosmological constant, and c is the speed of light [7].

The Hubble parameter H is identified and the critical density ρ_c are calculated

$$H = \frac{1}{a\,(t)}\frac{\mathrm{d}a\,(t)}{\mathrm{d}t},\ \rho_c = \frac{3H_0^2}{8\pi G}, \tag{2}$$

where H_0 is the Hubble constant (the present-day value of $H\,(t)$).

The density parameter is defined as $\Omega = \rho/\rho_c$, where ρ is the measured value of the density. The parameter Ω is split into matter-, radiation-, and dark energy-components $\Omega = \Omega_m + \Omega_r + \Omega_\Lambda$. The size of each of the density terms determines the curvature parameter k which distinguishes the curvature of the universe as open (eternal expansion), closed (expansion and eventual collapse), or flat (expansion tends to 0), as shown in Eq. (3).

$$k = \begin{cases} < 0 & \text{if } (\rho < \rho_c) \text{ Open universe} \\ > 0 & \text{if } (\rho > \rho_c) \text{ Closed universe} \\ = 0 & \text{if } (\rho = \rho_c) \text{ Flat universe} \end{cases} \tag{3}$$

Dark matter impacts the evolution and currently observed structure of the universe. On cosmological scales, the abundance of dark matter can be inferred by studying the CMB.

1.1.2 Wilkinson Microwave Anisotropy Probe (WMAP)

The CMB is the radiation emitted from the surface of last scattering when photons decoupled from matter. In the early universe, photons were scattered between ionised matter. As the universe expanded, the ionisation and hence scattering rate decreased. Eventually, the rate became low enough that photons were no longer trapped. The scattering rate provides information about the matter density.

The CMB is a source of data about the state of the early universe, providing evidence of the Big Bang Theory and the proportions of the (dark) matter and radiation content of the universe. One observes that there is an anisotropy in the CMB (due to baryon acoustic oscillations). From the anisotropy, one can infer the curvature of the universe and the relative densities of different types of matter and radiation [8]. WMAP provide very precise measurements of the CMB over the course of nine years. Several key parameters inferred from analysing WMAP (and other) data are shown in Table 1.1.

Since the baryonic matter in the early universe is only a small proportion of the total ($\sim 4.6\,\%$), non-baryonic dark matter ($\sim 23\,\%$) is postulated to explain the CMB [9]. Close agreement of WMAP data with similar measurements made with the Planck Surveyor [10] indicate that it is likely that $k = 0$.

Table 1.1: Overview of several parameters derived from a fit to WMAP (and other experimental) data from nine years of WMAP data (see [11] and references therein). Shown are the Hubble constant, the baryonic density, the dark matter density, and the dark energy density respectively [11].

Parameter	**Value**
H_0	$(70.0 \pm 2.2)\,\mathrm{km\,s^{-1}\,Mpc^{-1}}$
Ω_b	0.0462 ± 0.0024
Ω_c	0.233 ± 0.023
Ω_Λ	0.721 ± 0.025

1.1.3 Galactic Structure

Table 1.1 suggests that dark matter constitutes a large fraction of the matter of the universe. Since the mass distribution dynamically affects the clustering of matter, it is inferred that dark matter plays a major role in the evolution of galaxies.

The dark matter mass is unknown, generally three regimes are considered: cold (CDM), warm (WDM), and hot (HDM). The naming relates to the Lorentz factor $\beta = v/c$ since the average velocity of a dark matter particle depends on its mass. This in turn affects the current abundance of dark matter.

The leading cosmological theory is ΛCDM. Galaxy formation is bottom-up, as substructures cluster together over time and form larger structures as the universe expands [12] - the Λ refers to the cosmological constant in Eq. (1).

HDM implies a top-down approach. Galactic evolution starts with large structures and substructures appear over time. HDM is significantly lighter ($\beta \sim 1$), with typical mass constraints on the order of up to 10^2 eV [13], making neutrinos a plausible particle candidate. WDM is an intermediate with an expected mass of approximately 0.5 keV [14].

Simulations of galactic structure formation that incorporate dark matter models can be tested against the observed structure of galaxies today. Whilst CDM produces accurate simulations of overall galaxy structure, WDM and HDM seem to better realise substructure. The CDM simulations also predict a higher number of satellite galaxies, and halo cusps in Dwarf Spheroidal galaxies (dSphs) with which real data do not necessarily agree [3].

Nonetheless, large scale simulations of the formation of galaxies such as [15] have bolstered the view that dark matter is CDM [16]. The CMB, and Lyman-α forest measurements, are consistent with ΛCDM [17], supporting ΛCDM as the leading theory.

1.2 Astrophysics

The number of astrophysical observations that can be used to infer properties about dark matter are numerous, such as the satellites which make observations of the radio-emissions of galaxies and galaxy clusters. Also, sophisticated simulations of galactic structure formation have facilitated detailed studies on increasingly smaller substructures of galaxies, which in turn constrain the dark matter mass.

The Chandra-X telescope makes measurements of X-rays in haloes, measuring mass abundance ratios, comparing to cosmological measurements in order to study if there is an abundance of dark matter; as well as observing whether the emissions from gas from larger scale galactic structures and halos are consistent with ΛCDM [18]. Chandra-X has measured that the ordinary matter temperature in galaxies clusters is 10 MK to 100 MK, from which it is inferred that the dark matter in this region must be approximately five times more dense [18]. This is consistent with ΛCDM.

Measurements of the Lyman-α forest (which is the observation of varying intensities and redshifted wavelengths of the 1216 Å hydrogen Lyman-α absorption line) provide a way to determine the spatial distribution of hydrogen in regions of space. Such data enable making inferences about the matter density [17,19]. The inferred density suggests the presence of dark matter.

Astrophysics data establish evidence in favour of the existence of dark matter. Importantly, it provides indirect measurements that provide information about its exact nature. Thus, it is necessary to discuss a number of astrophysical results to understand the constraints that have been placed on dark matter.

1.2.1 Galaxy Rotation Curves

Galaxy rotation curves provide some of the earliest known evidence for the existence of an unknown missing amount of matter, which came to be known as dark matter. Advances in sensitive measurement equipment have enabled measurements of, for example, gravitational lensing, to provide evidence for dark matter.

In 1933, Zwicky first noted that the observations of Hubble and van Maanen of the rotational velocity of N.G. 4051, and the rotational velocity of Messier 33 of van Maanen and Pease could not be reconciled by existing theories or observational error. The discrepancy in rotational velocity was an order of magnitude or greater [20].

Zwicky concluded that the density predictions made by Hubble of the overall matter density of the universe of $\rho \sim 10^{-28}\,\mathrm{g\,cm^{-3}}$ could be consistent with Einstein and de Sitter's prediction based on the measured rate of expansion of the universe, if one introduces what he called "dark (cold) matter". Then, the overall density of visible matter is consistent with observations, provided one accepts that the overall density of the universe is higher than had been accounted for until then [20]. Einstein revisited the general theory of relativity, introducing a cosmological parameter Λ (an idea which he later mistakenly revoked), producing a non-static inflationary universe [21] in light of measurements by Hubble [22].

To first order, Zwicky analysed the Coma cluster by applying the Virial theorem [20, 23]

$$\langle K\rangle = -\frac{1}{2}\langle U\rangle,\ U = -\frac{3}{5}\frac{GM^2}{R} \tag{4}$$

where $\langle K\rangle, \langle U\rangle$ are the time-averaged kinetic and potential energy, and $M = 1.6\times10^{45}\,\mathrm{g}, R = 10^6\,\mathrm{ly}$ are the mass (based on the visible matter) and radius that Zwicky used to calculate a rotational velocity of $\sqrt{\langle v^2\rangle} \approx 80\,\mathrm{km\,s^{-1}}$. The large discrepancy between this result and the data led him to conclude that the cluster's mass density must be higher by a factor of 400 or more [20].

The Coma cluster is one of the earliest examples cited as evidence for a new phenomenon [20, 24] consisting of excess invisible matter. In the 1970s, the work of Vera Rubin and others provided strong experimental evidence for the existence of dark matter by measuring emission spectra [25, 26] to determine the rotational velocity curves of galaxies - a few examples are shown in Fig. 1.1.

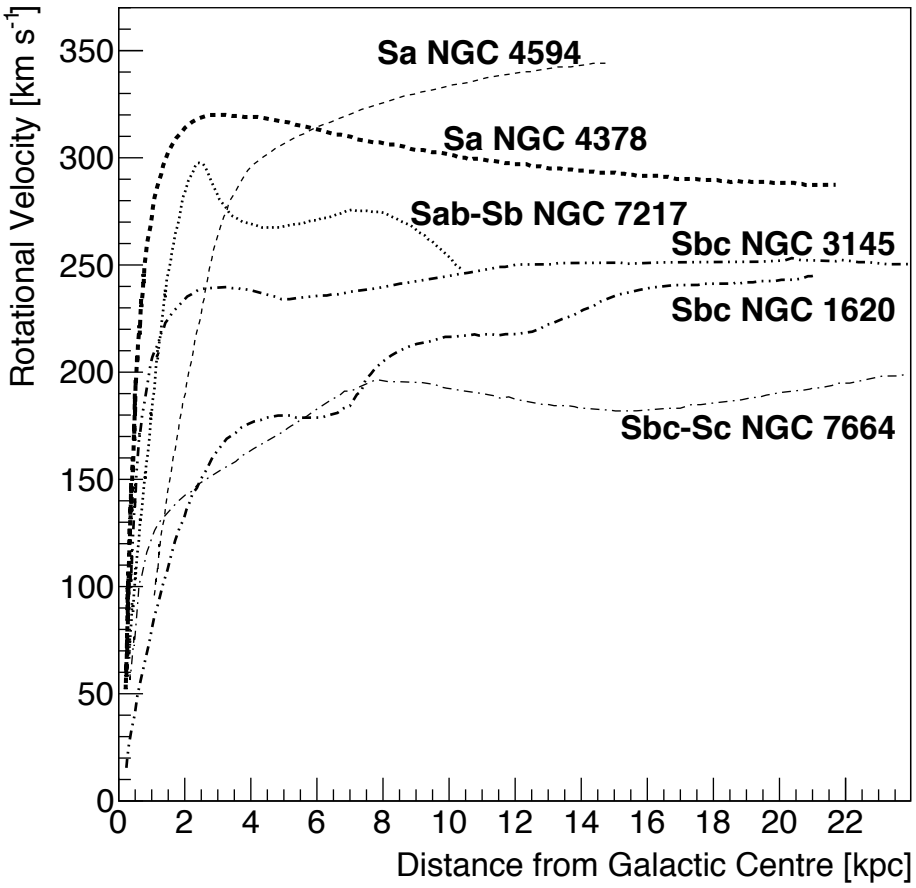


Figure 1.1: Measurements (data from [26]) of the rotational velocities of galaxies show the absence of an exponential decay in the rotational velocity with increasing radius from the galactic centre, which would otherwise be expected based purely on the visible component of the disk. Instead, the rotational velocity stays roughly constant [26], suggesting the presence of dark matter.

1.2.2 Gravitational Lensing

Gravitational lensing measurements also provide evidence for the existence of dark matter. Einstein's Theory of General Relativity assumes that light always travels along a geodesic. In practice, a massive object curves the spacetime around it, causing light that passes by it to appear curved.

There are broadly three regimes of lensing: strong (e.g. Abell 370), weak lensing, and micro-lensing (small fluctuations of moving objects at very large distances). Each focusses on different masses and different distance scales.

It is known that dark matter exists because the amount of lensing is more than could be explained by only visible matter, and the light from matter behind the dark matter is curved by its presence. From this it can be inferred that dark matter interacts with the gravitational force but *not* electromagnetically.

Shown in Fig. 1.2 is an image of the Bullet Cluster, considered one of the best examples of evidence in favour of the existence of dark matter. Excesses far away from the galactic centre could not be seen through direct analysis of only the visible light observed from the cluster [27, 28]. The baryonic matter and X-ray components decouple during the merger, facilitating a measurement of the spatial distribution of the gravitational potential, from which the presence of weakly interacting dark matter can be inferred [27]. It is difficult to account for the inferred excesses of non-luminous matter in galaxies and galaxy clusters using purely the known baryonic matter.

1.2.3 Massive Astrophysical Component Halo Objects

A Massive Astrophysical Compact Halo Object (MACHO) is generically any very massive entity in space in the halo of a galaxy. The density profile that is used to model the halo affects the overall predicted dark matter mass. A particularly challenging aspect of studying MACHOs is that it relies on accurate measurements of subtle lensing effects, which can skew results towards false detection of ordinary matter [29]. For a long time, MACHOs were proposed



Figure 1.2: Taken from [27], gravitational lensing in the Bullet Cluster. Two galaxies are in a collision path. The contours, superimposed on the image, are reconstructed from gravitational lensing, from which the presence of excess invisible matter can be inferred.

as the dark matter candidate.

In particular, black holes, due to their large mass, were thought to be plausible dark matter candidates. Results such as those from WMAP would preclude primordial black holes that were formed after the early universe expansion (big bang nucleosynthesis) as dark matter candidates because those black holes would be largely baryonic. Primordial black holes are generally disfavoured as the dominant dark matter candidate at this time, since a large portion of the mass parameter space has been ruled out.[2]

[2]On the other hand, recent results from the Laser Interferometer Gravitational-Wave Observatory (LIGO), an experiment that has detected gravitational waves, may provide evidence in favour of dark matter primordial black holes, or that there is dark matter clustering around black holes. This is covered in greater detail in [30–33] and [34–37].

1.3 Particle Physics

1.3.1 Dark Matter Candidates

The evidence in favour of the existence of dark matter from a cosmological and astrophysical point of view is well-established. However, it is difficult to reconcile these features on a large scale and still be precise about the nature of dark matter. Particle candidate theories such as WIMPs and axions have been proposed to explain the dark matter.

Many beyond the standard model quantum field theories predict a candidate dark matter particle. Based on the cosmological and astrophysical observations that the dark matter is predominantly non-baryonic, and that it can be observed not to have disappeared over high redshifts, the dark matter must have existed since at least Big Bang Nucleosynthesis (BBN). Therefore, the particle is usually assumed to be stable over at least the lifetime of the age of the universe.

Estimates on the dark matter mass and interactions are constrained by a myriad of cosmological/astrophysical data such as WMAP, Planck [38], rotation curves [39], gravitational lensing measurements [29], and simulations of galaxy formation [3]. Based on these observations, many (but not all) theories specify that the dark matter does not interact directly via the electromagnetic force [40], and that the particle is charge neutral.

Supersymmetry (SUSY) models are examples of a class of particles from a beyond the standard model theory. SUSY partners standard model particles with supersymmetry particles (sparticles). Stability is achieved by imposing R-parity, a combined symmetry of particle spin S, lepton number L, and baryon number B [41, 42][3]

$$R = (-1)^{2S+L+3B}. \tag{5}$$

SUSY models usually have a Lightest Supersymmetric Particle (LSP), and

[3] All SM particles have $R = 1$ and all supersymmetric particles have $R = -1$.

when the LSP is stable, it can be prescribed to play the role of the dark matter [3]. A promising dark matter candidate is a spin-1/2 neutralino, having a mass consistent with cosmological observations on the electroweak scale in the range 100 GeV to 1000 GeV [3, 43]. Under the Minimal Supersymmetric Standard Model (MSSM), the LSP is disfavoured by direct detection experiments (where, increasingly, low-mass WIMP searches are gaining traction), in which case it could likely only be detected on Earth by producing it in collider searches. No experimental evidence for SUSY has been found yet; though many models are still to be tested.

A spin-3/2 gravitino in a minimal supergravity model (mSUGRA) would allow for multiple LSPs, but the Higgs mass restricts the neutralino density to a region where it is difficult to reconcile with the observed relic density [3].

Alternatively, the dark matter particle could be a graviton, a heavy neutrino, a Kaluza-Klein particle [3], a sterile neutrino, a spin-0 photon, or belong to a so-called Little-Higgs scenario [44][4].

Neutrinos belong to another class of particle that has been proposed as the dark matter. However, owing to their small mass, neutrinos are a hot dark matter candidate, and do not fit well into structure formation schemes. A fourth flavour of neutrino as the dominant dark matter contributor has been generally disfavoured and is somewhat contrived [3].

Effective field theories and simplified models have also come into play. They bridge the gap between high-energy collider searches, and the low-energy threshold nuclear physics usually encountered in direct detection experiments. These theories drop some of the symmetry considerations of full quantum field theories, and do not directly predict the existence of new particles. However, they can help to understand the parameter space and response across different types of detectors [46–48].

[4]Many other non-WIMP possibilities have been proposed, but these are not covered here for brevity. A more detailed treatment can be found in [45].

1.3.2 Weakly Interacting Massive Particles (WIMPs)

WIMPs are a leading class of dark matter particle candidates. They are well-supported by cosmological observations such as the expected current relic abundance and galactic structure formation, being charge neutral and interacting at least via the gravitational force. As the early universe expanded and cooled, their annihilation rate tends to zero

$$P(annihilation) \propto e^{-(m_{DM}/(k_B T))}, \tag{6}$$

where m_{DM} is the dark matter mass, k_B is the Boltzmann constant, and T is the temperature. The rate depends on the number density n which decreases as the universe expands

$$\Gamma = \langle \sigma_{\text{ann}} v \rangle n. \tag{7}$$

As $P(annihilation) \to 0$, so $\Gamma \to 0$, and the abundance of dark matter tends to a constant value (this is known as freeze-out). The current abundance is given by

$$\Omega h^2 \approx \frac{3 \times 10^{-27}\,\text{cm}^3\,\text{s}^{-1}}{\langle \sigma_{\text{ann}} v \rangle}, \tag{8}$$

where $h = H_0/100\,\text{km}\,\text{s}^{-1}\,\text{Mpc}^{-1}$ is the reduced Hubble constant, and $\sigma_{\text{ann}} v$ is the product of the interaction/annihilation cross-section and the velocity of the particle [3, 49]. The WIMP (mass) is expected to correspond to a cross-section consistent with the electroweak scale of a few hundred GeV [50]. It is the "WIMP miracle" that a particle candidate is predicted that naturally fits into cosmological observations [45].

A WIMP fits into ΛCDM, which makes it a particularly well-motivated candidate. As such, they are widely sought for in all manner of particle physics experiments around the world.

1.3.3 Axions

The $U(1)$ problem is an issue arising in the standard model about why axial $U(1)$ symmetry is not conserved by Quantum Chromodynamics (QCD). A solution to the problem, through adding the following term to the Lagrangian

$$L = \theta \frac{g^2}{32\pi^2} F_a^{\mu\nu}, \tag{9}$$

breaks Charge Parity (CP) symmetry, and leads to the question why QCD does not conserve CP [51]. θ is parametrised as $\bar{\theta} = \theta - \arg(m_1, m_2, ..., m_n)$, and if CP symmetry is violated, $\bar{\theta}$ is non-zero. An experimental limit comes from the neutron electric dipole moment $|d_n| < 2.9 \times 10^{-26}\, e\,\mathrm{cm}$ [52], which suggests $\bar{\theta} < 10^{-9}$; but there is no solid motivation why $\bar{\theta}$ should have this value [3].

The theory behind the axion particle was realised by the work of Peccei-Quinn, who proposed a mechanism to resolve the strong CP problem [53]. By introducing a new quantum field with which could be associated a mass term [3, 54]

$$m \sim 6\,\mu\mathrm{eV} \times \frac{10^{12}\,\mathrm{GeV}}{f_a}, \tag{10}$$

where f_a is the decay constant for axions, the issue can be judiciously avoided by minimising the potential function in the modified QCD Lagrangian. The specifics of the mass depend on the choice of potential that determines how the $U_{\mathrm{PQ}}(1)$ symmetry is broken [3]. The axion is a quasi-Nambu-Goldstone boson, because it results from *dynamic* minimisation of the vacuum potential, causing $\bar{\theta}$ to vanish [3, 54].

Experimental searches driven by Sikivie and others [55] are motivated by axions as a potentially observable particle. The range of predicted axion masses is quite large, from a few keV down to 10^{-24} eV. On the other end of the spectrum, heavy QCD axion-like particles have been suggested with masses as high as 750 GeV. This makes for a large parameter space for experiments to search for axion dark matter [54].

Axions are able to fit into ΛCDM [54,56–58], a boon for axion searches. Many experiments, such as the CAST[5] telescope [59,60], or the OSQAR[6] experiment, look for evidence of (solar) axions coupling to (X-ray energy) photons [54]. OSQAR is a Light Shining through Walls (LSW) experiment that casts a polarised laser light at an optical barrier in a magnetic field. The axion-photon-coupling would create a photon on the other side of the barrier, providing an experimental signature [61]. Another example is ADMX[7] [62], which uses an adjustable microwave cavity and a magnetic field to produce photons [63,64]. Limits on the coupling of the axion to two-gamma ($A \rightarrow \gamma\gamma$), along with models due to KSVZ[8] and DFSZ[9], are shown in Fig. 1.3. The fact that the axion can be motivated independently from the need to explain dark matter, coupled with the fact that there are experimental pathways for their detection, make axions an attractive alternative to the WIMP hypothesis.

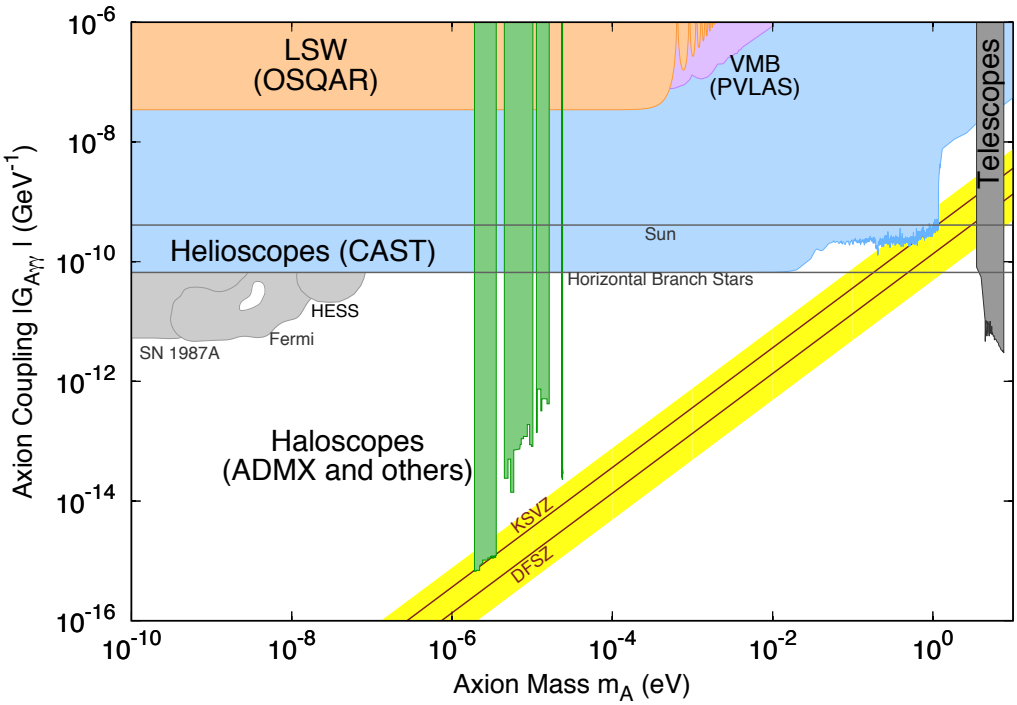


Figure 1.3: Limits from axion searches (taken from [65]).

[5]CERN Axion Solar Telescope (CAST).
[6]Optical Search for QED Vacuum Birefringence (OSQAR).
[7]Axion Dark Matter eXperiment (ADMX).
[8]Kim-Shifman-Vainshtein-Zakharov (KSVZ).
[9]Dine-Fischler-Srednicki-Zhitnitsky (DFSZ).

1.4 Dark Matter Searches

The experimental searches for dark matter are typically organised into three categories: **collider**, **indirect**, and **direct** searches. The assumption is that at some level, the dark matter interacts with a standard model particle, as shown in Fig. 1.4.

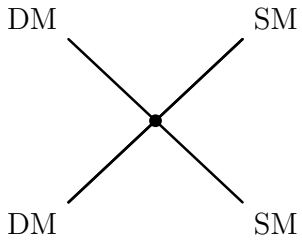


Figure 1.4: Diagram for a generic DM-SM interaction. Left-to-right: indirect detection, right-to-left: production, bottom-to-top: direct detection [66].

Collider searches include production/decay experiments such as those at the Large Hadron Collider (LHC), which collides protons at a high centre of mass energy of several TeV. It is thought that it may be possible to produce Beyond the Standard Model (BSM) particles at the LHC that might be consistent with dark matter. For example, if a LSP is produced due to a supersymmetric particle decay, then it may indirectly produce a signature of a WIMP.

Primarily, this involves looking at QCD jets, where the number and energy of the jets can be used to make event selections and inferences about the energy deposited in the collision [67]. Since the WIMP is likely to pass through the detector without interacting, one must reconstruct the energy depositions of all particles produced. A key signature of a WIMP would be to infer that there is missing transverse momentum from an interaction in which the dark matter travels out of the detector.

Although quoting experimental results depends highly on the underlying field theory model and the event cuts, the ATLAS[10] collaboration have excluded

[10] A Toroidal LHC ApparatuS (ATLAS).

heavy (750 GeV to 1200 GeV) mediators for dark matter in the range 230 GeV to 480 GeV for $\sqrt{s} = 13\,\text{TeV}$ at an integrated luminosity of $36.1\,\text{fb}^{-1}$ [68], where $\sqrt{s}$ is the total centre of mass energy.

Indirect searches look for signals of excesses of, for example, the neutrino and gamma-ray flux in galaxies, which provide indications of the presence of dark matter. For instance, the Fermi Large Array Telescope looks for excesses of gamma-rays in dark matter rich galaxies which would be created by annihilation into $b\bar{b}/\tau\bar{\tau}$ [69]. It has a sensitivity range of 20 MeV to 300 GeV [69, 70].

The IceCube [71] detector looks for neutrinos with energies $\geq$ 10 GeV that come from a presumed dark matter excess in the Sun. The idea is that dark matter is gravitationally captured after it loses sufficient energy through scattering [3, 71, 72]. IceCube has detected some of the highest energy neutrinos, but no excess signals that point to concrete evidence of a dark matter detection.

Another particularly promising and unambiguous signal would be DM $\rightarrow 2\gamma$. Kinematically, the energy of the photons should sum to the dark matter four-momentum. With no other obvious backgrounds, such a signal would be compelling evidence of the detection of dark matter [3].

Direct searches rely on the assumption that there is a sufficient flux of dark matter (estimated at $10^5(100\,\text{GeV}/m_{\text{DM}})\text{cm}^{-2}\,\text{s}^{-1}$) particles passing through the Earth, and that it might be possible to detect dark matter through its direct interaction with ordinary matter [3]. Therefore, the anticipated event rate, and the ability of the experiment to detect dark matter, depend on the underlying astrophysical models. The detector technology is a critical aspect of these experiments, because it depends on an a priori assumption about how the dark matter will interact with the proposed target material.

Among the direct searches, a variety of detector technologies are employed. For example, cryogenic experiments generally operate at temperatures below

77 K [3]. These detectors achieve ≤ 1 keV resolution, and have set strong limits on low mass WIMPs (< 10 GeV).

Cryogenic searches operate by measuring a combination of phonon, ionisation, and scintillation energy deposited due to a WIMP recoil in crystals. In these detectors, whether or not a signal is a WIMP as opposed to a standard model particle is known by analysing the proportion of the phonon, ionisation, and scintillation energies. The characteristic response depends on the crystal and how the signal is extracted from it [3, 73].

For example, the EDELWEISS experiment[11] measures phonon and ionisation signals [74]. The CRESST[12] experiment measured phonon and scintillation and ionisation yield. CRESST uses $CaWO_4$ crystals, and pushed the threshold energy for nuclear recoils from 300 eV for CRESST-II to 100 eV for CRESST-III [75–77]. CDMS[13] used an array of 19 germanium detectors, achieving 612 kg d of exposure, improving upper limits on the WIMP mass at around 10 GeV [78]. Scaling the experiment to a larger size increases the exposure to WIMPs passing through the Earth, but it also complicates the design of the experiment considerably.

Some direct searches focus on the predicted **annual modulation** [3] of the WIMP flux, due to the Earth orbiting the Sun. The Earth-Sun velocity relative to the galaxy adds for half of the year, and subtracts for the other half of the year - being maximal (minimal) on approximately 2 June (December) [3]. If the WIMPs are assumed to have a roughly constant density over the distance covered in a year, then it is expected that the flux of dark matter particles crossing the Earth is increased when the relative motion adds, and decreased when it subtracts [3].

The amplitude of the modulation signal depends on the detector mass and its

[11] Expérience pour DEtecter Les WIMPs En Site Souterrain (EDELWEISS). In English: Experiment for detecting WIMPs underground.

[12] Cryogenic Rare Event Search with Superconducting Thermometers (CRESST).

[13] Cryogenic Dark Matter Search (CDMS).

exposure time, and on the dark matter particle recoil rate[14] in the range of energies to which the detector is sensitive [79]. Systematics such as coincident events can be rejected by having multiple detectors in the experiment operating at the same time. Thus, an experimental signal should be well-characterised by the rate of change of the modulation, and the times of year when that rate of change is expected to be maximised [3].

From experimental results from a combined 2.17 ton yr exposure, the DAMA/LIBRA[15] experiment report a 11.9σ confidence level result that shows a modulation signal. DAMA/LIBRA report that their results are consistent with dark matter theories [3, 80–82]. The modulation that has been measured is shown in Fig. 1.5. Discussion is ongoing whether the result is due to systematics, and other results that appear to negate DAMA/LIBRA [83].

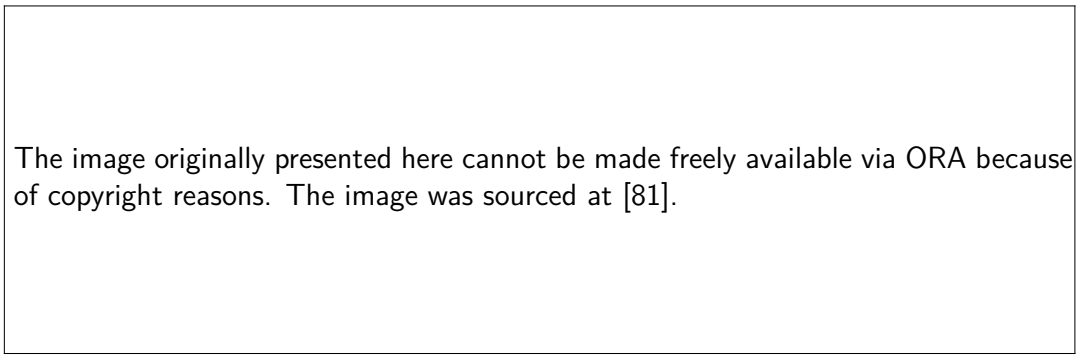


Figure 1.5: Annual modulation signal measured by DAMA/LIBRA taken from [81], showing a 1.13 ton yr exposure taken during phase-2, in addition to the 1.04 ton yr exposure of phase-1. Six-monthly lines are indicated by alternating dashed and dotted vertical lines. A model fit of the expected modulation is shown as the cosine solid line. The measured modulation is shown by the round data points. The horizontal and vertical error bars indicate the binning and the residual uncertainty, respectively. The residual represents the measured rate for events that occurred only in one detector at a time (rejecting multiple coincidences), accounting for the measured rate in the other detectors [80].

[14] The rate also depends on astrophysical models and the dark matter density.
[15] DArk MAtter / Large sodium Iodide Bulk for RAre processes (DAMA/LIBRA).

Experimental limits produced by several direct detection experiments are shown in Fig. 1.6.

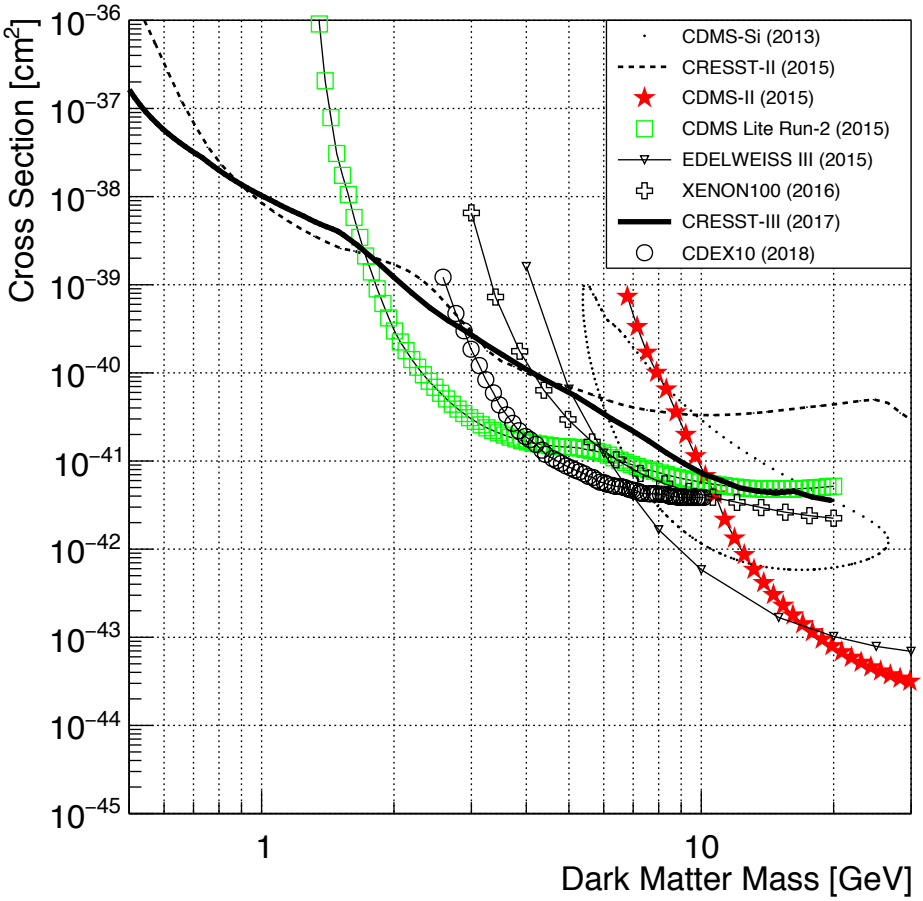


Figure 1.6: Spin-independent limits of several direct detection experiments (data from [84–91]).

Direct searches have provided some of the strongest limits on the WIMP-nucleon interaction cross-section [92]. If a collider experiment sees evidence of a new particle that could be consistent with dark matter, and/or if indirect searches find evidence of excesses that point to dark matter, direct searches are still critical to verify the signal against the expected flux of dark matter passing through the Earth. Direct searches play perhaps the most necessary role in definitively providing evidence in favour of or against a firm detection of dark matter.

1.4.1 Maxwell-Boltzmann velocity distribution integral

The dark matter flux influences how dark matter may be detected on Earth through direct searches. The Maxwell-Boltzmann velocity distribution $f(v)$ for the flux of dark matter particles in the galaxy is integrated over velocities $v > v_{min}$ to evaluate the flux in the frame of the detector [72]

$$\int_{v>v_{min}} \frac{f(v)}{v}\,\mathrm{d}v. \tag{11}$$

The definite integral result for the various cases of the velocity distribution are outlined in [72]. The overall velocity integral for a 50 GeV WIMP is shown in Fig. 1.7 [72, 93–95].

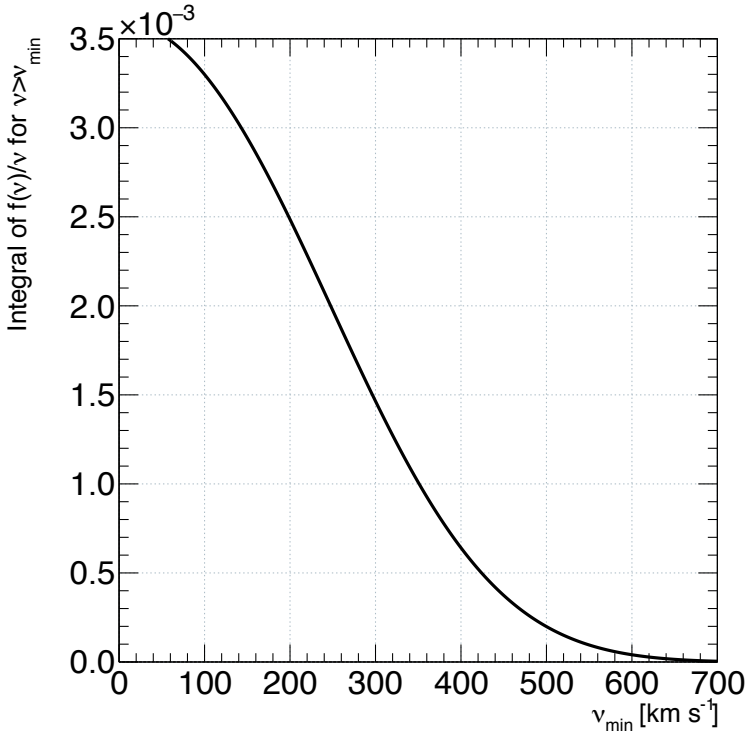


Figure 1.7: Integrated Maxwell-Boltzmann velocity distribution. The integral was evaluated for recoil energies E_r from 0 keV to 100 keV. $v > v_{min}$ where $v_{\mathrm{min}} = \sqrt{(m_{\mathrm{Xe}}E_r/(2\mu_N^2)}$ (μ_N is the DM-nuclear reduced mass system), $v_{esc} = 544\,\mathrm{km\,s^{-1}}$, $v_0 = 220\,\mathrm{km\,s^{-1}}$, and $\langle\vec{v}_{\text{Earth-halo}}\rangle = 245\,\mathrm{km\,s^{-1}}$ is the time averaged relative velocity v in the Earth-halo reference frame.

1.4.2 Nuclear Form Factor

The probability of a nuclear interaction with a target material (e.g. liquid xenon) in a direct detector scales with energy, and for the spin-independent case it is given by the nuclear form factor

$$F^2(q, A) = \left(\frac{3j_1(qr_n)}{qr_n} \right)^2 \exp\left(-q^2 s^2\right), \tag{12}$$

where $q = \sqrt{2m_{\mathrm{Xe}}E_r}$, $r_n = \sqrt{R^2 - 5s^2}$, $R = 1.2A^{1/3}\mathrm{fm}$, $s = 1\,\mathrm{fm}$ is the surface thickness [96], and

$$j_1(qr_n) = \frac{\sin(qr_n)}{(qr_n)^2} - \frac{\cos(qr_n)}{qr_n} \tag{13}$$

is the Bessel function of the first kind. Fig. 1.8 shows the calculated nuclear form factor for the range $E_r \in (0, 100)$ keVnr (where the unit keVnr is the nuclear recoil energy) [72, 93–95].

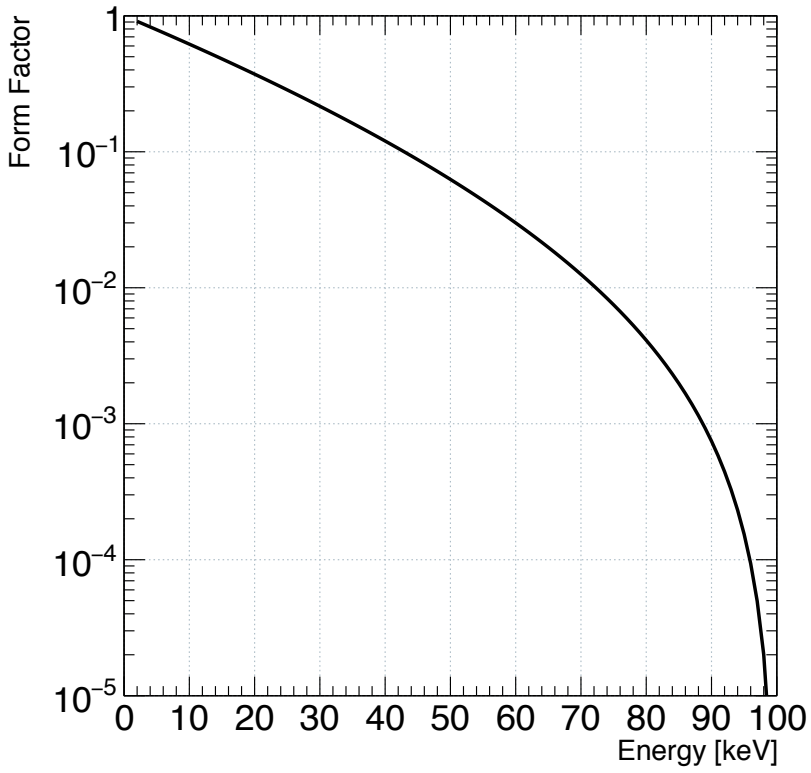


Figure 1.8: Nuclear form factor plotted for Xe with $A = 131.29$ over the range 0 keVnr–100 keVnr.

1.4.3 Differential Rate

The differential rate is the detector-specific number of nuclear recoil events due to dark matter

$$\frac{dR}{dE} = \frac{\rho_0 \sigma_A}{2 m_{\mathrm{DM}} \mu_N^2} F^2(q, A) \int_{v_{min}}^{v_{max}} \frac{f(v)}{v} \, \mathrm{d}v, \tag{14}$$

where $\rho_0 = 0.3\,\mathrm{GeV\,cm^{-3}}$ is the dark matter density [97, 98], and $F^2(q, A)$ is the nuclear form factor as a function of the momentum transfer q [72, 93–95]. The function $f(v)$ is the Maxwell-Boltzmann velocity distribution function for dark matter as a function of the velocity v.

The zero-momentum transfer cross-section is

$$\sigma_A = A^2 \sigma_0 \frac{\mu_N^2}{\mu_n^2}, \tag{15}$$

where $A = 131.29$ is the atomic mass number of xenon, and $\sigma_0 = 10^{-36}\,\mathrm{cm}^2$ is the effective cross-section. μ_N and μ_n are respectively the reduced mass of the dark matter-nuclear and dark matter-nucleon systems, defined by

$$\mu_N = \frac{m_{\mathrm{DM}} m_{\mathrm{Xe}}}{m_{\mathrm{DM}} + m_{\mathrm{Xe}}}, \; \mu_n = \frac{m_{\mathrm{DM}} m_p}{m_{\mathrm{DM}} + m_p} \tag{16}$$

where m_p is the mass of the proton. The differential rate, shown in Fig. 1.9, is integrated over the WIMP region of interest (6 keV to 30 keV) to obtain the expected number of events in the detector [72, 93–95].

1.4.4 Setting a Limit

Setting a limit involves prescribing a relative probability that dark matter has not been detected at a particular value of the dark matter mass. A variety of approaches exist to do this. In practice, the Profile Likelihood Method is often used because it allows incorporating many experimental parameters into a single model. A first order pedagogical approach to explain the concept of exclusion limit setting is the frequentist cut-and-count method due to Feldman

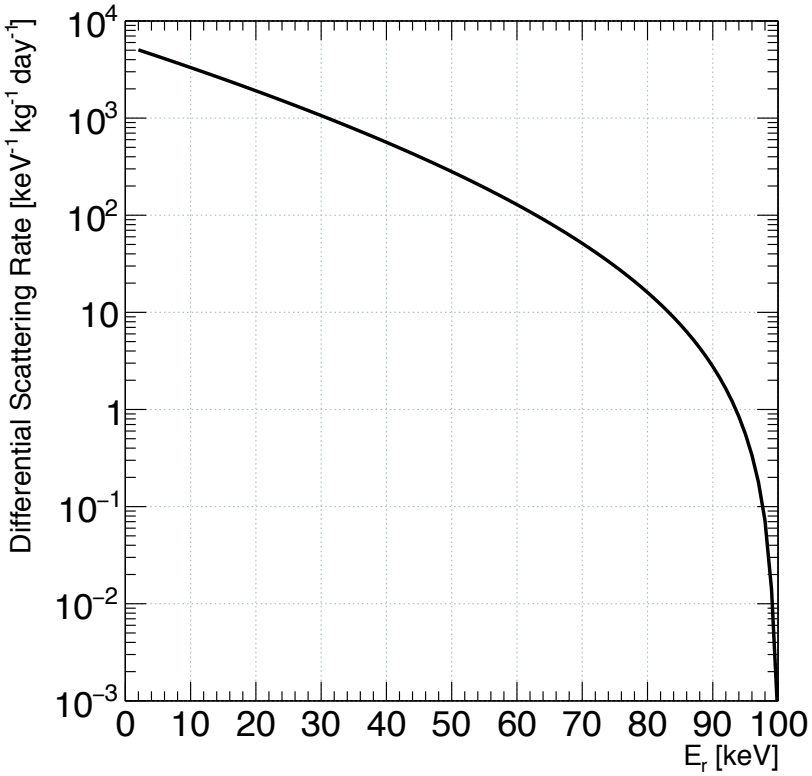


Figure 1.9: Graphical representation of the functional form of the differential rate of Eq. (14) in liquid xenon. The integral over the target mass and the number of live exposure days gives the total number of events.

and Cousins. By using the Feldman-Cousins approach, one can construct confidence belts so as to achieve the desired coverage α. The coverage represents a limiting value for which one finds the true value of a parameter of interest μ in a proportion α of the total number of measurements [94]

$$P(x \in [x_1, x_2]\,|\mu) = \alpha, \tag{17}$$

where x_1, x_2 represent the interval constructed from the parameter of interest μ. The upper limit is given by

$$P(x < x_1|\mu) = 1 - \alpha. \tag{18}$$

For a low-background search, an acceptance region of zero events is selected, for which a 90 % C.L. implies an upper limit of 2.4 events.

Hypothesis tests are constructed, specifying the confidence level (set by α)

- $\boldsymbol{H}_0$: there are no statistically significant observed events in the rejection region at 90 % C.L.
- $\boldsymbol{H}_1$: there are statistically significant observed events in the rejection region at 90 % C.L.

Failure to reject $\boldsymbol{H}_1$ constitutes a discovery.

To define acceptance and rejection regions for the hypothesis test, a discriminating parameter is used as the test-statistic. The parameter that is often used in dark matter limit setting for experiments such as LUX is $\log_{10}(\mathrm{S2/S1})$, where S1, S2 denote the primary and secondary source of photons produced in a recoil. This parameter distinguishes between electronic and nuclear recoils, the physics of which will be explained more thoroughly in Chapter 2[16].

The spin-independent WIMP-nucleon interaction cross-section σ is calculated for the example case of the LUX experiment

$$\sigma = \frac{2.4\sigma_0}{M \times D \times R}, \tag{19}$$

where R is the integral of Eq. (14), $M = 118.3\,\mathrm{kg}$ is the active detector mass of LUX, and $D = 85.3\,\mathrm{d}$ is the number of days for which the experiment acquired data [72, 93–95]. To obtain a limit curve, the cross-section is calculated for various WIMP masses. A first order application of the Feldman-Cousins method to LUX data yields a minimum cross-section of $\sigma \sim 7 \times 10^{-46}\,\mathrm{cm}^2$ and is shown in Fig. 1.10 - a close approximation of the published LUX result [95] which used the Profile Likelihood Ratio method.

The value of the differential cross-section is sensitive to the velocity distribution and the form factor [72, 93–95]. The value of the cross-section depends on the underlying parameters in the differential rate calculation, such as astrophysical

[16]For now it is sufficient to know that these are two types of events that the experiment distinguishes.

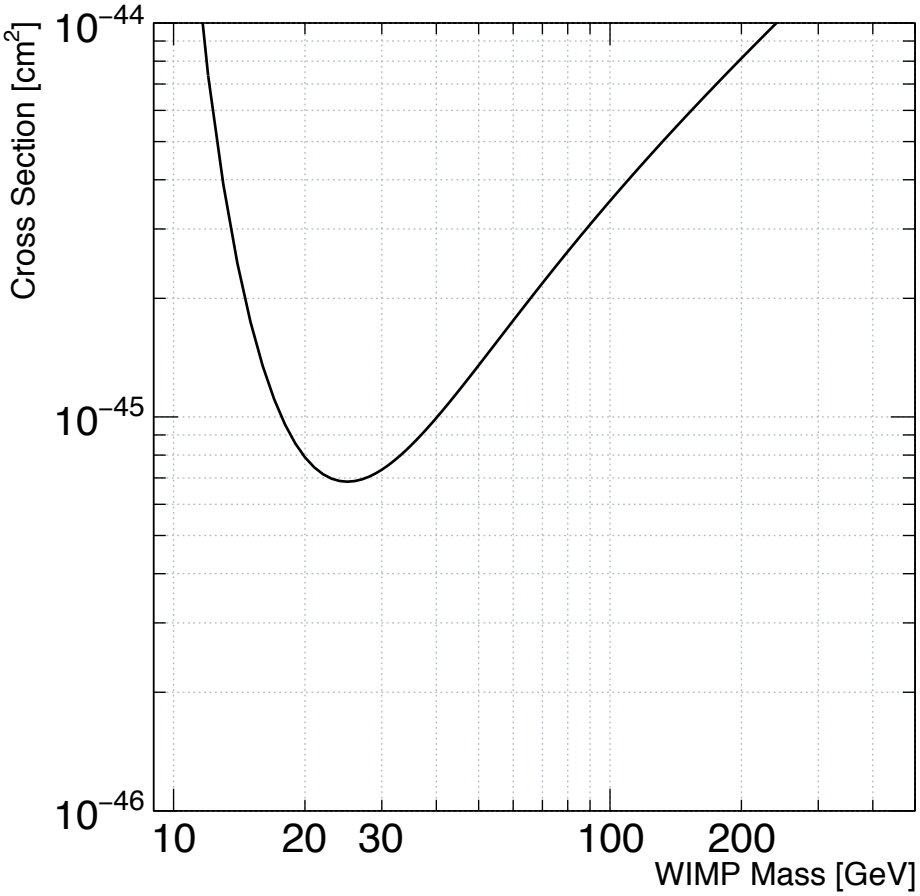


Figure 1.10: LUX cross-section at 90 % C.L. for an exposure of 10 090 kg d.

models of the dark matter flux, which depend on coupling constants under particular quantum field theories, as well as detector sensitivities [99].

Dark matter constitutes a large fraction of the total matter content of the universe. The WIMP hypothesis is well-motivated from cosmological and astrophysical data, and a variety of experimental pathways for the detection of dark matter as a particle have and continue to be explored in the field of particle physics. Both direct, indirect, and collider experiments provide stringent limits on dark matter. The limit-setting process for a low-background direct search experiment has been discussed.

2 Dark Matter Detectors

The dark matter is thought not to interact electromagnetically. Many direct searches quantify the energy depositions of nuclear recoil events, expecting that a dark matter particle interacts with the nucleus of a target material. This chapter focuses on direct detection liquid noble element low-background experiments, in particular two-phase TPC experiments using LXe as the target material. A brief exposition is given of the ZEPLIN-III and LUX experiments (whose corresponding collaborations have shaped LZ) as well as of XENON1T and PandaX-II. Other types of dark matter detectors, such as DarkSide and DEAP[17] which use liquid argon, are also discussed.

Understanding the physics of the detector and characterising its response in terms of the detector medium and background events is critical to obtain event data that can be understood in the context of the expected background contributions to the experiment. Extensive efforts are made to reduce the impact of backgrounds by shielding the detector from external sources, selecting low-background components to avoid radioactive decays that produce nuclear recoils that can mimic WIMP-nucleon scattering, and reducing surface contaminants by cleaning its components.

To these experiments, there are many unwanted background sources of radiation at the surface of the Earth such as cosmic rays (particle showers that can have energies as high as 10^{20} eV [100] that can decay to produce e^-, μ, γ). For comparison, 3.5 km underground, the overall muon flux is reduced by approximately a factor of 100 (dependent on the composition of the Earth's crust and geospatial latitude and muon energy) [100]. Therefore, low-background experiments are increasingly located deep underground.

Direct detection searches do not focus exclusively on nucleon scattering. For instance, there are leptophilic models where the dark matter does *not* interact with quarks, but with leptons [101].

[17] Dark matter Experiment using Argon Pulse-shape (DEAP).

2.1 Liquid Noble Elements in Direct Searches: Liquid Xenon

Liquid noble elements have been found to be useful in dark matter searches. This is due to both their nuclear and chemical properties and the way in which they complement the requirements of low-background searches. A noble element is less likely to interact chemically with other parts of the detector, which is advantageous to controlling experimental parameters and keeping the detector medium pure. It is necessary to understand the dynamics of liquid noble elements as a detector medium with respect to particle interactions before discussing their application in direct detection experiments. An overview of how liquid noble gases may be used for the direct detection of particle dark matter is given.

The main options in dark matter searches are xenon, argon, and neon [3]. It is desirable to have a dense, chemically inert, and radio-pure target material. Several key properties of noble elements relevant to dark matter searches are shown in Table 2.1.

Table 2.1: Key properties of several noble elements used for dark matter searches. The density is quoted at the boiling point. The W-value corresponds to the scintillation energy, that is related to the measured mean energy for liberating an electron thereby leaving the nucleus ionised [3, 102–104]. It can be seen that xenon has the highest boiling point, and the lowest energy required to be ionised. It is also by far the densest target material of the three.

Property	**Unit**	**Xe**	**Ar**	**Ne**
Atomic number	-	54	18	10
Density	$\mathrm{kg\,m^{-3}}$	2940	1400	1210
Boiling point	K	165.0	87.3	27.1
W-value	eV	13.8 ± 0.9	19.5 ± 1.0	~ 35
Scintillation wavelength	nm	178	128	78

Noble elements with a high proton number Z are particularly useful because the interaction cross-section goes as A^2, as shown in Eq. (15). The high density of the element means unwanted external backgrounds are more likely to be stopped at the outer regions of the detector. The outer region of the liquid is used sacrificially, leaving a central fiducial volume that has fewer background events. This, combined with the fact that scintillation from liquid xenon cannot induce further scintillation, implies that detectors using liquid xenon benefit from self-shielding as they become larger without suffering from a decrease in signal due to their own light yield.

Radio-purity is critical to reduce background events. A detector must be free from as many contaminants as possible throughout its lifetime, and active forms of purification are now common on the larger experiments. For example, in the case of LXe, it is important to remove ^{85}Kr and ^{222}Rn, and to a lesser extent, the isotope ^{136}Xe [1][18]. Argon typically has a $1\,\mathrm{Bq\,kg^{-1}}$ contribution from ^{39}Ar [97]. Although xenon is expensive because of its low abundance, argon is expensive to purify [105].

An overview of WIMP integrated event rates for various atomic elements is shown in Fig. 2.1, based on an idealised detector and a calculated threshold energy capability of the detector. Nominal values are shown as the circles on each of the respective integral rates. The integrated rate expected from liquid xenon decreases quite steeply, but it is still competitive with argon until the threshold nuclear recoil energy of approximately 60 keV. The nuclear form factor is the reason for the decrease in the rate, as shown in Fig. 1.8.

2.1.1 Xenon Physics

When a particle recoils from a xenon atom, the xenon atom responds in a variety of ways. Higher energy interactions will probe the nucleus at a closer distance and result in more energy deposited in the recoil. As a result of ionising

[18] ^{136}Xe has a double beta decay with a long half-life ($\sim 10^{21}$ yr), but experiments are still dominated by other backgrounds at this time.

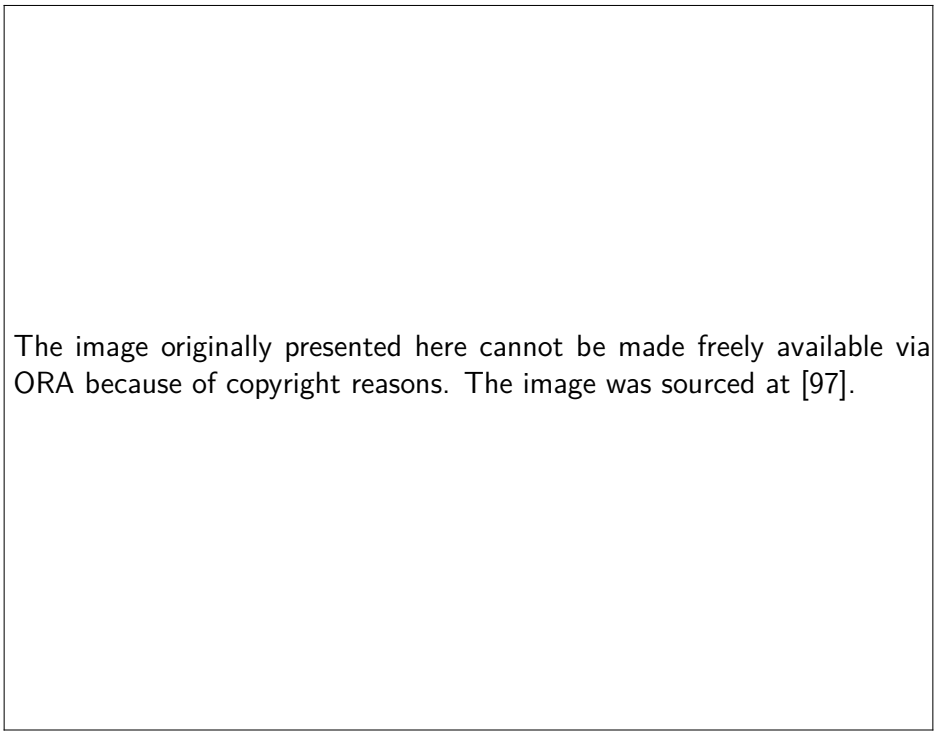


Figure 2.1: Taken from [97], a comparison of the expected WIMP integral event rate for dark matter detection in various elements as a function of the threshold nuclear recoil energy resolvable in the detector. The response of xenon outperforms argon up until about 60 keV [97].

radiation, excited states, sub-excitation states, and ions are produced.

Part of the recoil energy goes into exciting the xenon atom. The process of excitation and subsequent de-excitation of the xenon induces scintillation, which is the process by which photons are emitted from the xenon. The pathways for producing Vacuum Ultraviolet (VUV) light via scintillation (due to atomic excitation and de-excitation) are shown in Eq. (20). Ionisation, recombination, and VUV emission are shown in Eq. (21) [3, 97].

$$\begin{aligned} \mathrm{e}^- + \mathrm{Xe} &\longrightarrow \mathrm{Xe}^* + \mathrm{e}^- \\ \mathrm{Xe}^* + \mathrm{Xe} &\longrightarrow \mathrm{Xe}_2^* \\ \mathrm{Xe}_2^* + \mathrm{Xe} &\longrightarrow \mathrm{Xe}_2^* + \mathrm{Xe} \\ \mathrm{Xe}_2^* &\longrightarrow \mathrm{Xe} + \mathrm{Xe} + h\nu. \end{aligned} \tag{20}$$

$$
\begin{aligned}
&\mathrm{e}^- + \mathrm{Xe} \longrightarrow \mathrm{Xe}^+ + 2\,\mathrm{e}^- \\
&\mathrm{Xe}^+ + \mathrm{Xe} + \mathrm{Xe} \longrightarrow \mathrm{Xe}_2^+ + \mathrm{Xe} \\
&\mathrm{e}^- + \mathrm{Xe}_2^+ \longrightarrow \mathrm{Xe}^{**} + \mathrm{Xe} \\
&\mathrm{Xe}^{**} + \mathrm{Xe} \longrightarrow \mathrm{Xe}^* + \mathrm{Xe} + \mathrm{heat} \\
&\mathrm{Xe}^* + \mathrm{Xe} + \mathrm{Xe} \longrightarrow \mathrm{Xe}_2^* + \mathrm{Xe} + \mathrm{heat} \\
&\mathrm{Xe}_2^* \longrightarrow \mathrm{Xe} + \mathrm{Xe} + h\nu,
\end{aligned}
\tag{21}
$$

where the subscript refers to a dimer, and the star refers to an excited state. The LXe dimer exists in a metastable excited molecular singlet (lifetime $\sim 3\,\mathrm{ns}$) or triplet state (lifetime $\sim 27\,\mathrm{ns}$) - where the decay to the ground state of the latter is permitted due to spin-orbital coupling. The decay of either of the excimer states to the (repulsive) ground state results in VUV emission and molecular dissociation [97, 106]. The de-excitation processes cascade into light and heat. The amount of light and heat provides information about the energy involved in the reaction. In large two-phase TPCs, only the photon component is generally measured - though in smaller experiments the heat deposition can also be measured.

If one assumes that radiation is the *only* way in which the energy difference in excitation and de-excitation is carried away, and an approximately one-to-one correspondence of dimer-to-photons, then one obtains the scintillation light yield of xenon [107, 108]

$$
n_\gamma = \left(N_q - n_e\right) \frac{1}{1 + \alpha\epsilon^\beta}. \tag{22}
$$

Nominally, in LZ, at $10\,\mathrm{keVer}$ (where the unit keVer denotes an electronic recoil), the yield will be 445 photons [1].

In Eq. (22):

$$
\begin{aligned}
N_q &= \frac{E}{W} \qquad (23)\\
n_e &= (1-r)\, N_i \\
r = 1 - \frac{\ln(1+N_i\zeta)}{N_i\zeta} \; or \; r &= \frac{A\frac{\mathrm{d}E}{\mathrm{d}x}}{1+B\frac{\mathrm{d}E}{\mathrm{d}x}} + (1-A/B) \\
\zeta &= \frac{\alpha'}{4a^2\langle\nu\rangle} \\
N_i &= \frac{N_q}{1+N_{ex}/N_i} \\
N_{ex} &= N_q - N_i \\
\text{which satisfy } N_i + N_{ex} &= N_q \\
\alpha_{\mathrm{LXe}} = N_{ex}/N_i &\approx 0.06,
\end{aligned}
$$

where E is the recoil energy, α' is a constant which is a function of the ion-hole mobility and dielectric, ν is the electron velocity, and a is a volumetric ionisation density parameter. N_i, N_{ex}, N_q are the number of ionisation, excitation, and electrons involved in the recoil. The expressions for r are the recombination probability, the first (Thomas-Imel model) and second (Doke-Birks) relation are used for short and long particle tracks respectively (A, B are experimentally deduced). Which one to use depends on the interaction(s) and the number of particles involved.[19] The factors ϵ, β account for quenching due to Penning ionisation [109]. Photons are produced with a characteristic energy $h\nu$, where h is the Planck constant, corresponding to VUV photons that have a wavelength centred at $\lambda = 178\,\mathrm{nm}$.

The electron that is liberated in the process of the recoil now has two possibilities: recombination or escaping recombination. Recombination means that the electron is re-captured by a xenon ion, and hence produces more scintillation. The production channels of ionisation and scintillation are shown in Fig. 2.2. The combination of prompt scintillation and recombination light is collectively called S1, since these photons are created immediately following the recoil. The

[19] A detailed treatment of this aspect is left to [108] and references therein.

secondary emission generated due to the electrons in the ionisation channel is called S2. The proportion of S2 to S1 depends on the energy of the recoil since the ionisation and scintillation channels are governed by the amount of recombination. Similarly, the proportion of S2 to S1 depends on the way in which the S2 signal is extracted [3, 102, 106, 108], since electrons are more likely to recombine when they are closer to the ionised nucleus than if they are quickly drifted away from it. Typically, an electric field applied to the liquid drifts electrons escaping recombination to the liquid surface. Next the charge is extracted into a gas region through a grid; resulting in electroluminescence ($\lambda = 171\,\text{nm}$ [110]) which is measured as the S2 signal.

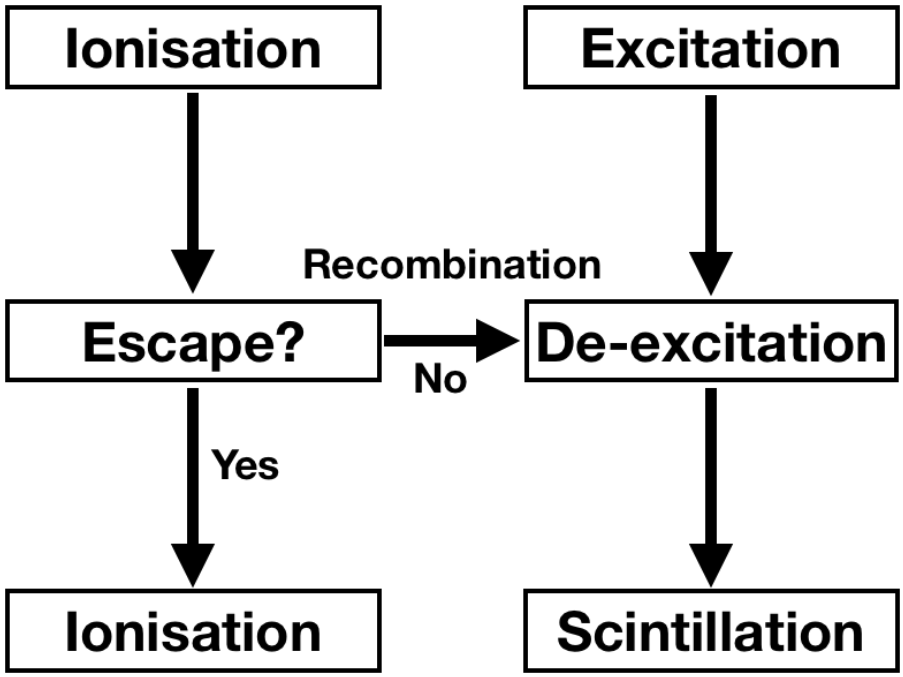


Figure 2.2: Overview of scintillation and ionisation processes in xenon. The initial recoil produces ionisation or excitation. The excitation pathway into an excited dimer state proceeds straight to de-excitation of the dimer, producing scintillation light (S1). The scintillation light that is produced cannot re-excite the ground state - this fact is what enables xenon detectors to scale to large volumes. The ionisation pathway has a probability to recombine and produce further scintillation light (S1), or it can escape recombination producing what is called the ionisation signal (S2) [109].

A variety of mathematical models for recombination exist [105]. The recombination probability is the probability that an electron that was emitted from the xenon atom recombines. The free electron thermalises on a timescale proportional to its energy loss as it interacts inelastically with the detector medium [105].

This probability depends on $\mathrm{d}E/\,\mathrm{d}x$, which is a measure of the rate at which the electron energy is lost to the liquid, i.e. the ionisation density of the particle track. In general, recombination also depends on the applied electric field that may be used to extract ionisation electrons. Recombination is generally guaranteed to occur when there is no applied field. The denser the medium, the higher the probability of recombination, and the higher the field strength required to extract electrons (preventing recombination) [105]. However, these are not the only factors that determine recombination.

Jaffe's model incorporates the electric field strength into a prediction of the measurable charge [105]

$$Q = \frac{Q_0}{1 + K/E}, \tag{24}$$

where Q, Q_0 denote the free charge and total produced charge respectively. E is the electric field strength, and K is the so-called recombination coefficient. It can be seen that this relation is none other than a scaling of the total charge resulting from the recoil. Measurements have established that K is an accurate predictor of ionisation density and recombination [105]. In form, Jaffe's model is similar to Birks' Law [111], predicting the amount of scintillation as a function of $\mathrm{d}E/\,\mathrm{d}x$.

The Onsager model[20] [112], like Jaffe's model, does not account for the significant momentum transfer due to electrons emitted from the second stage of ionisation (also known as δ-electrons [105]), and the connection to detector energy resolution [105]. To this effect, an extended model was introduced, which took

[20] Onsager models the free electron as thermalising under the influence of the electrostatic field of the atom, accounting for the possibility that an applied electric field may be present to extract charge. Recombination depends on when and if the electron loses sufficient energy to be captured by an ion [105].

these δ-electrons into account [113]. The Thomas-Imel model [114] is a recombination model used to understand recoils as short particle tracks [108].

The distinction between short and long particle tracks is useful to understand the difference between what constitutes an Electron Recoil (ER) and a Nuclear Recoil (NR). An ER predominantly concerns the electron shell of the nucleus, whereas an NR causes the entire nucleus to recoil.[21] Measurements [115] therefore show that $\mathrm{d}E/\,\mathrm{d}x$ *does* affect recombination but it is not the only factor that affects it.

$\mathrm{d}E/\,\mathrm{d}x$ is *not* the defining discriminant between ER and NR, since the yields vary non-linearly, are energy- and field-dependent, and recombination increases at different rates at low energies ($\sim 10\,\mathrm{keV}$) for ERs and NRs. Using particle tracks to inform recombination models which are used to explain these observations has been instrumental in improving the understanding needed to better exploit this detector technology to lower energy thresholds.

As shown in Fig. 2.3, the increase in yield at low energies is the observation that implies the energy resolution of xenon detectors can reach at least to 10 keV - seminal towards scaling xenon detectors to larger sizes [115]. With the promise of larger detectors comes a greater need to control and understand the energy thresholds for low energy NR. Equally, at higher recoil energies ($\sim 100\,\mathrm{keV}$), there is a drop in sensitivity due to the nuclear form factor, as shown in Fig. 1.8.

The Fano-Factor $0 \leq F \leq 1$ denotes the deviation away from the expected Poisson-distributed number of quanta due to ionisation. Since $F \propto W_i/I$, where W_i/I is the ratio of electron-ion pair energy to atomic ionisation potential[22], F is a measure of the ionisation resolution of the detector medium [105].

[21] Since scintillation and ionisation depend on the recoil, results for yields and energies are sometimes quoted in keVee (keVer), keVnr, to denote the equivalent energy that would produce the signal had it been due to an electron- or a nuclear- recoil, respectively.

[22] This is similar, but *not* identical to the W-value in Table 2.1, which represents the average energy required to produce scintillation light.



Figure 2.3: Taken from [115], the increase in yield of electron and nuclear recoils at low energies ($< 20\,\mathrm{keV}$). This observation enabled pushing the limits of the detector threshold sensitivity [115].

The fact that the ionisation pathway leads either to ionisation electrons emitted in the liquid, or to recombination which leads to further scintillation, implies that the ionisation and scintillation signals are *anti-correlated*, as shown in Fig. 2.4. The anti-correlation is evident due to varying the applied electric field, which also demonstrates that recombination is a function of the applied field.

The anti-correlation can be succinctly expressed in the following relation between the recoil energy and the ionisation and scintillation response [117]

$$E_{\mathrm{ER}}^{rec} = \left(\frac{\mathrm{S1}}{g_1} + \frac{\mathrm{S2}}{g_2}\right) W. \tag{25}$$

g_1, g_2 are detector specific parameters[23], obtained through measuring the S1 and the S2 signals with calibration sources. By construction, g_1 has units of photons per keV (or phd/ph), while g_2 has units of electrons per keV (com-

[23]They can be thought of as a type of gain.



Figure 2.4: Taken from [116], anti-correlation of yields obtained using ^{137}Cs as a calibration source [116].

monly expressed as phd/e) - the latter being the product of the electron emission probability, the light yield, and the Photon Detection Efficiency (PDE). The W-value is taken from Table 2.1, and Eq. (25) is generally quoted in units of keV. The relation to the total number of quanta can be further visualised by accounting for all the types of signals, as shown in Fig. 2.5.

For the case of nuclear recoils, the Lindhard factor[24] $\mathcal{L}^{-1}$ is multiplied through Eq. (25). The Lindhard factor is an energy-dependent factor that describes the lower yields [119] in the case of nuclear recoils due to energy lost to the electrons involved in the recoil. Eq. (25) thus becomes [117]

$$E_{\mathrm{NR}}^{rec} = \mathcal{L}^{-1}\left(\frac{\mathrm{S1}}{g_1} + \frac{\mathrm{S2}}{g_2}\right) W. \tag{26}$$

[24]Which is *not* the same as L_{eff}, which is the ratio of NR to ER scintillation yield, typically measured with reference to a calibration source. Although closely related to $\mathcal{L}$, it is also not to be confused with the more general description of the quenching factor [105,108,117], which is the ratio of "ionization or light produced by a recoil nucleus to the amount of ionization or light produced by an electron (or a gamma ray) for the same deposited energy" [105]. A detailed treatment of each of these concepts is left to [105] and references therein. The value of $\mathcal{L}^{-1}$ is substituted and explained as and when needed.

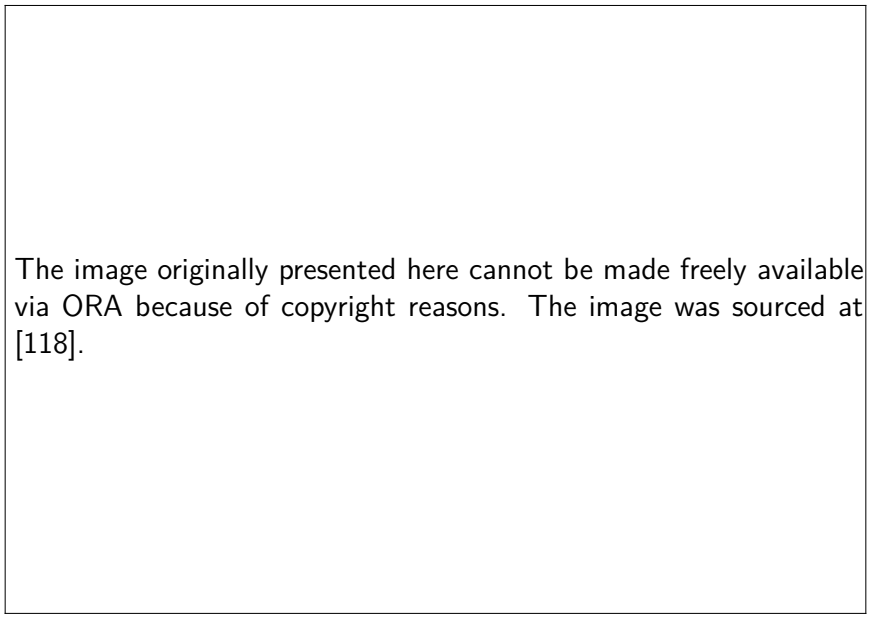


Figure 2.5: Taken from [118], total quanta versus energy in the LUX experiment. The totals for each type of signal are shown [118].

The Lindhard factor $\mathcal{L}$ can be deduced empirically from the absolute scintillation light yield, L_y, and estimated in terms of the atomic properties Z, A and the recoil energy E_{NR} as [117]

$$\mathcal{L} = \frac{kg\left(\epsilon\right)}{1 + kg\left(\epsilon\right)}, \tag{27}$$

where $\epsilon = 11.5\left(E_{\mathrm{NR}}/\mathrm{keV}\right) Z^{\left(-7/3\right)}$, $k = 0.133 Z^{\left(2/3\right)} A^{\left(-1/2\right)}$, and $g\left(\epsilon\right) = 3\epsilon^{0.15} + 0.7\epsilon^{0.6} + \epsilon$.

Quantifying the recoil energy of electron- and nuclear- recoil events factors into the sensitivity reach of the experiment. The detector design determines the proportion of S1 and S2 signals, as well as the ability to reconstruct the recoil type, energy, and position.

2.2 Two-Phase Time Projection Chambers

A TPC is a type of detector that is used to resolve temporal and positional detail about particle interactions occurring on short time and distance scales. In the case of direct searches, the TPC is sensitive to electronic and nuclear recoils, which occur when a particle interacts with the atoms that make up the detector medium. The two-phase TPC designation refers to the fact that one extracts both the prompt scintillation and the ionisation signals. This is achieved by passing from a liquid phase into a gas phase, where secondary emission that is delayed needs time to drift through the detector before being amplified and then detected as the S2 [1].

Extracting both the S1 and the S2 signal is central to the way in which a TPC works. The top and bottom of the TPC are instrumented with PMTs, which together measure the S1 and S2 signals. The charge escaping recombination is drifted through the liquid into the gas phase by applying an electric field inside a field cage. In the gas phase, the electrons emit photons via electroluminescence, forming the S2. The majority of the S2 photons reach the top PMTs (a small fraction is emitted or reflected towards the bottom PMTs) [1].

The operating principle of a two-phase TPC is illustrated in Fig. 2.6 in the context of a direct detection dark matter search. An incoming dark matter particle causes a nuclear recoil in the detector medium, producing prompt scintillation light and ionisation. The scintillation light reaches the top and bottom PMT arrays and this constitutes the S1 signal. The ionisation charge is drifted through the liquid into the gas phase by an electric field, producing S2 scintillation photons via electroluminescence. The resulting colour intensity shows the hit map of the recoil as detected by the top and bottom PMT arrays. The recoiled dark matter particle continues on and eventually leaves the TPC.

The VUV scintillation wavelength of liquid xenon requires that PMTs must be sensitive to a wavelength of 178 nm, or wavelength shifters would be needed

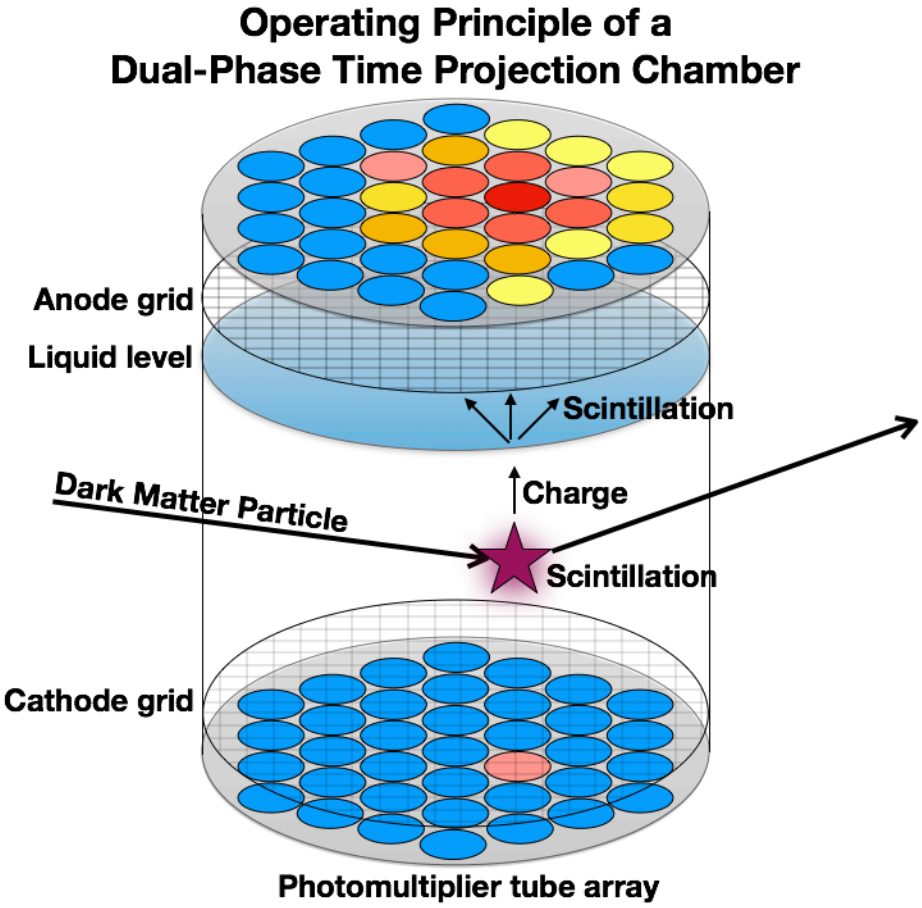


Figure 2.6: Operating principle of a dual-phase TPC. Dimensions are exaggerated for illustration purposes.

which would detriment the signal. Fortunately, there is a good refractive index compatibility between xenon and SiO_2 (fused silica) PMT windows (1.67 and 1.57 respectively [1]), minimising reflection of the signal at the PMT window. The complementarity of these physics properties increases the overall sensitivity of liquid xenon TPCs.

The use of reflective surfaces in the TPC increases the total Light Collection Efficiency (LCE), a term that denotes the relative amount of detectable scintillation light that depends on the detector geometry, material selection, and the quality of the instrumentation. Manufacturing a TPC from Polytetrafluoroethylene (PTFE) greatly improves the LCE, and it is a preferred choice due to its LXe friendliness. The fact that PTFE has a high reflectivity

(97 % [120]) at the LXe scintillation wavelength [97] makes it particularly fit for purpose. It is also relatively easy to obtain pure PTFE. It has a relatively low rate of chemical outgassing into the detector, and is a minor concern from a backgrounds perspective if active purification is used to remove outgassed particulates.

Quickly extracting the ionisation charge (S2) signal from the bulk liquid and into the gas phase reduces the lateral drift in the TPC and facilitates accurate position reconstruction of the recoil event. Therefore, one has to consider the electron mobility μ, approximately $0.2 \times 10^{-4}\,\mathrm{m^2\,V^{-1}\,s^{-1}}$ for liquid xenon, which informs the magnitude and the level of control over the applied electric field E to drift an electron of charge e and mass m_e at a drift speed $v_d = e\tau_e E/m_e$, where τ_e is the electron lifetime [23, 121]. Extraction therefore depends on the electric field, on the temperature of the liquid, and the number of impurities in the liquid, all of which are position dependent.

An electron that has escaped recombination initially can still be captured by xenon ions or by electronegative impurities. The electron affinity is the energy released through the process of attachment (detachment) of electrons to (from) electronegative impurities. The drift length is $r_d = v_d\tau_e$ (τ_e is nominally on the order of 1 ms in current TPCs [97]) which depends on each of the impurities and defines the characteristic distance scale an electron may travel before attachment. In particular, the impurities that are risky to LXe searches are H_2O and O_2 since they have a very high attachment probability - even in spite of a high applied field they can detriment the extraction process. Attachment is practically unavoidable due to the presence of impurities which are naturally present in detector components and in the liquid. For example, PTFE of the TPC walls slowly leaches into the liquid xenon. Thus, the goal is to keep the equivalent drift length significantly larger compared to the dimensions of the TPC. This is accomplished by minimising impurities, suitable component selection, and active purification of the liquid. A nominal 1.5 m drift length requires fewer than 0.015 ppt of Kr in liquid xenon [1, 105, 107].

For the same reasons, the applied electric field must also be sufficient that electrons that reach the LXe surface can be extracted into the gas phase. After charge extraction from the liquid phase into the gas phase, electroluminescence in the gas phase leads to the conversion of the charge into photons. This proceeds through the usual ionisation and scintillation channels shown in Fig. 2.2. A crude measurement of electrons-to-photons can be made using Jaffe's model (see Eq. (24) on page 51).

There are some subtleties in the terminology when it comes to quantifying the scintillation and ionisation yields. The difference is in whether it concerns the light produced at the interaction site, versus the light that is incident on the PMT, versus what is eventually stored to disk. Various units exist to express these differences: phe, or photons emitted, refers to the photons emitted at the interaction site.[25] By contrast, phd refers to the photons actually detected and that made it to disk.[26]

2.2.1 Backgrounds

Unwanted backgrounds due to radioactive sources affect the sensitivity of the experiment. Quantifying background sources is not the subject of this thesis; a very brief summary with a few illustrative examples are given here. The reader is directed to [1, 122–125] for more detail.

Backgrounds are sources of contamination which cause recoil events in the detector, and they hinder a dark matter search. Of particular interest are (α, n) reactions due to Uranium (^{238}U, ^{235}U) and Thorium (^{232}Th). For example, due to the decays of daughter particles produced further down in their decay chains (such as ^{210}Pb, and Rn), α particles can traverse the detector, interact, and lead

[25] The term phe sometimes refers to the number of photoelectrons, and depending on the way the reconstruction of photoelectron yield to photon yield is done, the value of these physically distinct units may appear equivalent. The distinction is generally evident from the context.

[26] When it refers to photoelectrons, the methods of analysis that are used to extract these quantities from the data that is stored on disk can also give either quantities in units of phe (which does not account for the double photoelectron response due to the PMT response), or in phd, which is the true number of photons at the interaction site *and* which were stored to an event file on a computer.

to the emission of a neutron which can induce a nuclear recoil [1, 122, 123]. If in the keV recoil energy range, a background event would be indistinguishable from a WIMP nuclear recoil, thus spoiling the discovery potential[27]. Trace quantities of these elements and the subchains of their daughter products are unavoidable as they exist in virtually all materials [1, 122–125].

The effects of background pathologies can be severe. For example, if ^{210}Pb or ^{218}Po are present on the cathode or near a PMT, then it would affect position reconstruction, energy reconstruction, and event discrimination power. Furthermore, ^{40}K exists in trace amounts in the fused silica SiO_4 windows in the PMTs, and can produce Cherenkov radiation when a β is emitted in the window. ^{222}Rn outgassing implies that it could traverse the liquid before decaying. Similarly, ^{226}Ra is undesirable because it is chemically interactive. Dust is a carrier of backgrounds; owing to its high surface area, it is a source of emanation from ^{220}Rn, ^{222}Rn, as well as ^{210}Pb [1, 122–125].

Screening with Germanium detectors, ICP-MS[28], and Neutron Activation Analysis (NAA); sourcing of detector components; and following cleanliness procedures keep the backgrounds of the detector as low as possible [1].

[27]Emission of high energy β particles can cause electron recoils which can detriment discrimination by creating more events in the electron recoil band.

[28]Inductively Coupled Plasma Mass Spectrometry (ICP-MS).

2.3 Direct Search Experiments

2.3.1 ZEPLIN-III

The ZEPLIN-III experiment was operated at the Boulby Underground Laboratory in England, UK. It had a total mass of 12 kg (5.1 kg to 6 kg fiducial mass across the two science runs) [126]. It consisted of 31 PMTs, and used an electric field to drift charge, enabling the detection of both primary scintillation light and electroluminescence light [126]. In addition to using the pulse area and pulse counting on single photoelectron signals, ZEPLIN-III sampled waveforms sufficiently fast to observe the pulse shape due to the singlet and triplet decay time constants of LXe - improving the discrimination between electronic and nuclear recoil events [127][29]. A veto made of plastic scintillator was placed around the polypropylene gadolinium shield surrounding the detector. This reduced the impact of nuclear recoils and gamma-rays due to background neutrons from the experiment [126, 128].

2.3.2 LUX

The LUX experiment was built at the Sanford Underground Research Facility in Lead, South Dakota, USA, in the Davis cavern at a depth of 1478 m (4850 feet) underground [129]. It had an active mass of 250 kg (118 kg fiducial mass)[30], and featured 61 top and bottom PMTs each, for a total of 122 PMTs. Pulse counting was employed by LUX for 20 keV primary scintillation signals [92, 129]. Tritium calibrations enabled the minimum threshold nuclear recoil energy to be pushed down to 1.1 keV [118, 131].

The muon flux in the cavern is estimated at $4.4 \times 10^{-9}\,\mathrm{cm}^{-2}\,\mathrm{s}^{-1}$ [129]. LUX used a large water shield to reduce the number of muons entering the TPC [129]. The total background rate was $(3.6 \pm 0.4) \times 10^{-3}\,\mathrm{evt\,keVee}^{-1}\,\mathrm{kg}^{-1}\,\mathrm{d}^{-1}$ [132][31].

[29] Pulse counting and pulse shape discrimination can be applied to both S1 and S2 signals although it is harder to resolve individual photoelectron peaks in larger S2 signals.

[30] 370 kg total [130].

[31] In the fiducial volume [132].

The 2017 publication on the total LUX data put strong limits on the spin-independent WIMP-nucleon interaction cross-section: $1.1 \times 10^{-46}\,\mathrm{cm}^2$ at 90 % C.L. for a 50 GeV WIMP mass for an exposure of $3.35 \times 10^4\,\mathrm{kg\,d}$ [131]. A comparison of cross-section limits set by various dark matter detection experiments is shown in Fig. 2.8.

The energy deposited through the decays of calibration sources can be related to the S1, S2 signals, thereby obtaining g_1, g_2. An example for the LUX Run-3 data is shown in Fig. 2.7. A detailed account of event analysis techniques can be found in [92, 97, 129].

Position reconstruction on detected events is achieved through measuring the light response function of each PMT. An algorithm called Mercury has been employed in ZEPLIN-III and then in LUX to achieve a centimetre level resolution on reconstructed events by mapping measured PMT signals into their most likely position [134]. S1 and S2 signals are corrected by accounting for the detector response such as position dependence of the event, accounting for the electric field in the TPC. Having obtained the corrected S1 and S2 quantities, energy reconstruction is achieved by employing Eq. (25) (see page 53) and Eq. (26) (see page 54).



Figure 2.7: LUX Run-3 calibration data, taken from [133]. The top and bottom plots are equivalent representations of the same data, with the corresponding recoil energy of the sources shown in the Doke plot (bottom). The Doke plot (named after Tadayoshi Doke) is a representation of recombination and N_{ex}/N_i. From a linear fit to the Doke plot (solid red line), the values $g_1 = (0.117 \pm 0.003)$ phd/ph, $g_2 = (12.1 \pm 0.8)$ phd/e are obtained [133].

2.3.3 XENON1T

XENON1T is located 1400 m underground at the Laboratori Nazionali del Gran Sasso (LNGS) and has a fiducial volume of 1 t (2 t active, 3.2 t total). Notable about the design of the outer vessel and the cryostat is that the intention is that XENON1T can be upgraded to the XENONnT experiment, whereby a larger TPC and active volume would increase sensitivity by an expected factor of 10. XENONnT would see the experiment's total volume of LXe increase to 8 t, or about 6 t active volume [135, 136]. The number of PMTs would also increase from a total of 248 (127 top and 121 bottom), to 476 (223 top and 253 bottom) [136]. In 2017, XENON1T reported a maximum sensitivity at a spin-independent WIMP-nucleon interaction cross-section of $7.7 \times 10^{-47}\,\mathrm{cm}^2$ for an exposure of approximately $3.56 \times 10^4\,\mathrm{kg\,d}$ [137]. In 2018, XENON1T reported results of the first 1 t yr of exposure (at 1.3 t fiducial volume): a sensitivity limit of $4.1 \times 10^{-47}\,\mathrm{cm}^2$ at 30 GeV (90 % C.L.) [138].

2.3.4 PandaX-II

PandaX-II is a dark matter search experiment in the China Jinping Underground Laboratory (CJPL) in Sichuan, China, located 2400 m (7874 feet) under the JinPing Mountain [139]. It contains 580 kg of LXe, up from 120 kg from its first stage [139], and a total of 110 (55 top and bottom) PMTs in the TPC. The total exposure for Run 9 and Run 10 combined is $5.4 \times 10^4\,\mathrm{kg\,d}$, and constrained the WIMP-nucleon (spin-independent) interaction cross section to an upper limit close to XENON1T (2017) for masses up to about 100 GeV. Results published in 2017 show PandaX-II set competitive limits for masses above 100 GeV. The highest sensitivity of PandaX-II Run 9 + Run 10 combined is reached at a WIMP mass of 40 GeV and is $8.6 \times 10^{-47}\,\mathrm{cm}^2$ (90 % C.L.). Experimental limits are shown in Fig. 2.8.

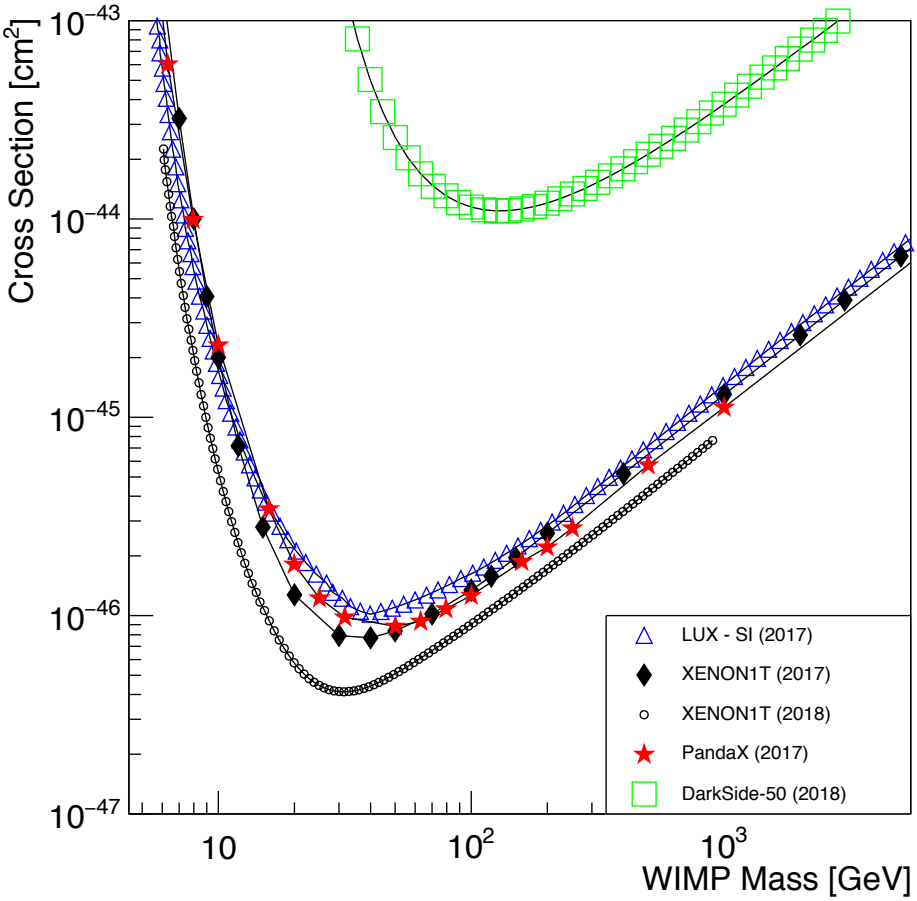


Figure 2.8: Published exclusion limits for several leading dark matter direct detection search experiments: LUX [131], PandaX [140], XENON1T (2017) [137] and XENON1T (2018) [138] (all using LXe), and DarkSide-50 which uses Liquid Argon (LAr) [141].

2.3.5 DarkSide and DEAP

DarkSide-50 is a dual-phase TPC LAr experiment of 50 kg total, 46.4 kg active volume, and 36.9 kg fiducial volume, operated at LNGS. The reported upper limit for spin-independent WIMP-nucleon sensitivity for 1422 kg d of data is 1.1×10^{-44} cm^2 at 90 % C.L. at a 100 GeV WIMP mass [141, 142]. DarkSide-50 reduced the effect of the intrinsic ^{39}Ar background to 0.1 evt for the search data, demonstrating the ability to scale LAr TPCs to larger sizes [142].

DEAP, specifically DEAP-3600, is a *single-phase* dark matter search experiment. Operated 2 km underground at Sudbury Neutrino Observatory Labora-

tory (SNOLAB) in Sudbury, Canada, holding 3600 kg of LAr ($\approx$ 2223 kg fiducial), the detector active volume is contained in an acrylic sphere instrumented externally with 255 concentric PMTs [143]. Active purification and removal of radon keep the number of background events below 0.6 evt in 3 yr. DEAP-3600 reported a spin-independent cross-section upper limit of $1.2 \times 10^{-44}\,\mathrm{cm}^2$ at 90 % C.L. at a WIMP mass of 100 GeV over 9.87 t d; with a threshold energy of 11 keVee [144].

LAr searches are different to LXe searches in a number of ways. The significantly longer time difference between the singlet ($<$ 6.2 ns) and triplet (1300 ns) [145] decay time constants for LAr facilitates pulse shape discrimination and ER versus NR discrimination [106]. While self-shielding is beneficial in dual-phase TPCs as well as in single-phase experiments, for LXe the smaller difference in the decay times of the singlet (3 ns) and triplet (27 ns) states implies LXe searches rely on self-shielding even more [106]. LXe is well-suited to dual-phase detectors, and its high light yield assists in achieving ER versus NR discrimination through the difference in timing between S1 and S2 signals and the reconstructed event position [106]. The wavelength of the LAr VUV scintillation light, shown in Table 2.1, necessitates the use of a chemical such as Tetraphenyl butadiene (TPB) which shifts the scintillation wavelength through fluorescence [146] before being detected on the PMTs.

The operation of two-phase LXe TPCs relies on understanding the electron and nuclear recoil response of liquid xenon at low recoil energies. The success of these experiments rests in having ultra-low background levels, and precise calibration of the detector response by measuring the S1 and S2 response for known background sources. The success and promise of this detector technology to scale to larger sizes has been shown by the world-leading limits on the spin-independent WIMP-nucleon interaction cross-section. LXe searches currently lead the sensitivity reach, although LAr searches have been shown to be scalable to larger sizes.

3 LUX-ZEPLIN

ZEPLIN-III and LUX set competitive and world-leading limits on the WIMP-nucleon interaction cross-section using two-phase LXe TPCs at the respective times that they were operated. LZ has nearly 240 members spread across 35 institutions in the United States, the United Kingdom, Portugal, Russia, and South Korea.

The LZ experiment design is a two-phase LXe TPC, as covered in Chapter 2, and it will be the largest experiment of its kind. The larger size of LZ as compared to ZEPLIN-III and LUX implies that analysing the event data that it will produce will be more involved. The development of suitable analysis software for the experiment is supported by detailed simulations of LZ event data, as detailed in Chapter 5.

LZ will be built in the Sanford Underground Research Facility in Lead, South Dakota, USA, in the Davis Cavern (4850 feet underground). This is the same site which the LUX experiment occupied until 2016 [1,122]. The active volume of LZ will be 7 t of LXe (5.6 t fiducial volume), this is more than an order of magnitude larger than previous generation direct search experiments such as ZEPLIN-III or LUX, and significantly more than XENON1T. An overview of the LZ detector is shown in Fig. 3.1.

This chapter summarises the physics case for LZ[32], focussing on the design parameters that drive the implementation of the event data acquisition systems of the experiment. In particular, this chapter is concerned with explaining the TPC, the PMT front-end electronics, and the DAQ system in order to provide the context for Chapter 4 and Chapter 5.

[32]Further information about all aspects of the experiment are covered in great detail in the LZ Technical Design Report (TDR) [1].

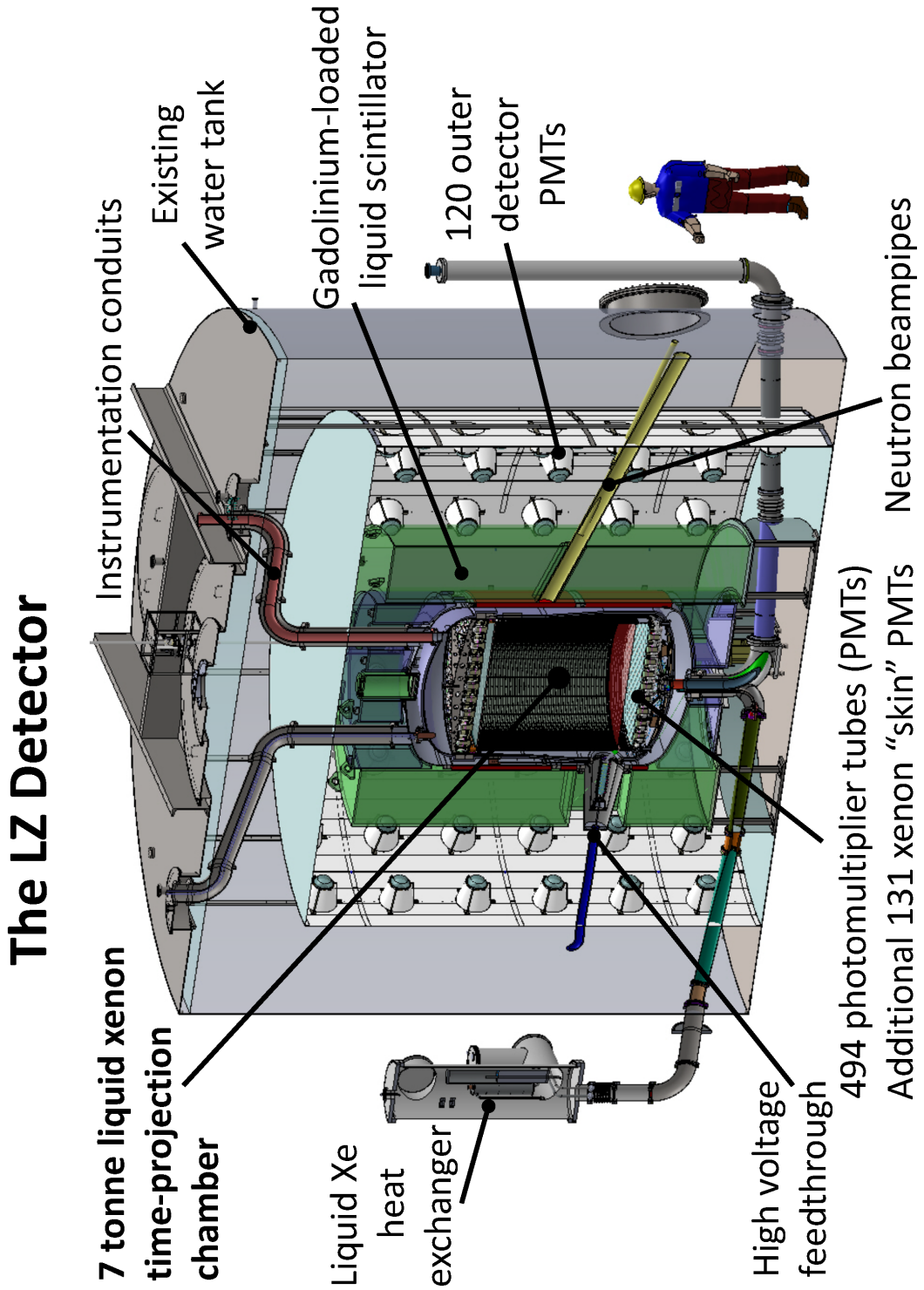


Figure 3.1: Cross-sectional view of the LZ detector taken from [147], showing key features of the detector, in particular the TPC and top and bottom PMT arrays, totalling 494 PMTs that monitor the TPC.

3.1 The Science Case for LZ

The aim of LZ is to detect dark matter. It is a requirement that the LZ sensitivity for the spin-independent WIMP-nucleon interaction cross-section is at least $3 \times 10^{-48}\,\mathrm{cm}^2$ at a WIMP mass of 40 GeV. In order to achieve the required sensitivity, at least 5600 t d of total exposure (1000 d at 5.6 t fiducial volume) must be achieved. The background rate due to radon, krypton, and argon must be no more than four times the electron recoil rates seen from solar neutrinos. The number of background counts due to components in the detector must be < 25 and < 0.7 for electron- and nuclear-recoils respectively. The projected sensitivity of the LZ experiment is shown in Fig. 3.2 [1].

Beyond dark matter, LZ can be sensitive to solar neutrinos[33], (neutrinoless) double beta decay (through ^{136}Xe), axions, and a variety of other types of rare events. LZ can provide lower energy thresholds on solar proton-proton neutrinos than Borexino, probing down to $O(10)$ keV [1].

Along with ^{8}B and supernovae sources, atmospheric sources of coherent neutrino-nucleus scattering possess an energy spectrum which are a background concern for LZ, since these NR events can look identical to that expected from a WIMP NR event at the upper end of the LZ sensitive mass-range. While supernovae are practically a random uncontrolled background, coincidences with other experiments which observe them can be used to remove these from a WIMP search analysis. To counter these issues, LZ must also quantify the flux of atmospheric neutrinos in detail with respect to its exact geospatial position. The LZ technical design report published estimate is that 0.5 such events will occur in 5600 t d of operation [1].

If the WIMP couples to charged particles, then leptonic interactions would produce ER recoils for which LZ will have an equivalent sensitivity on the order of $10^{-50}\,\mathrm{cm}^2$ (for electron coupling), $5 \times 10^{-50}\,\mathrm{cm}^2$ (for μ), up to $4 \times 10^{-49}\,\mathrm{cm}^2$

[33] Whether or not solar neutrino events are observable depends on whether the backgrounds are reduced beyond the minimal aim for the WIMP search of 20 mBq over the entire 10 t of LXe [1].

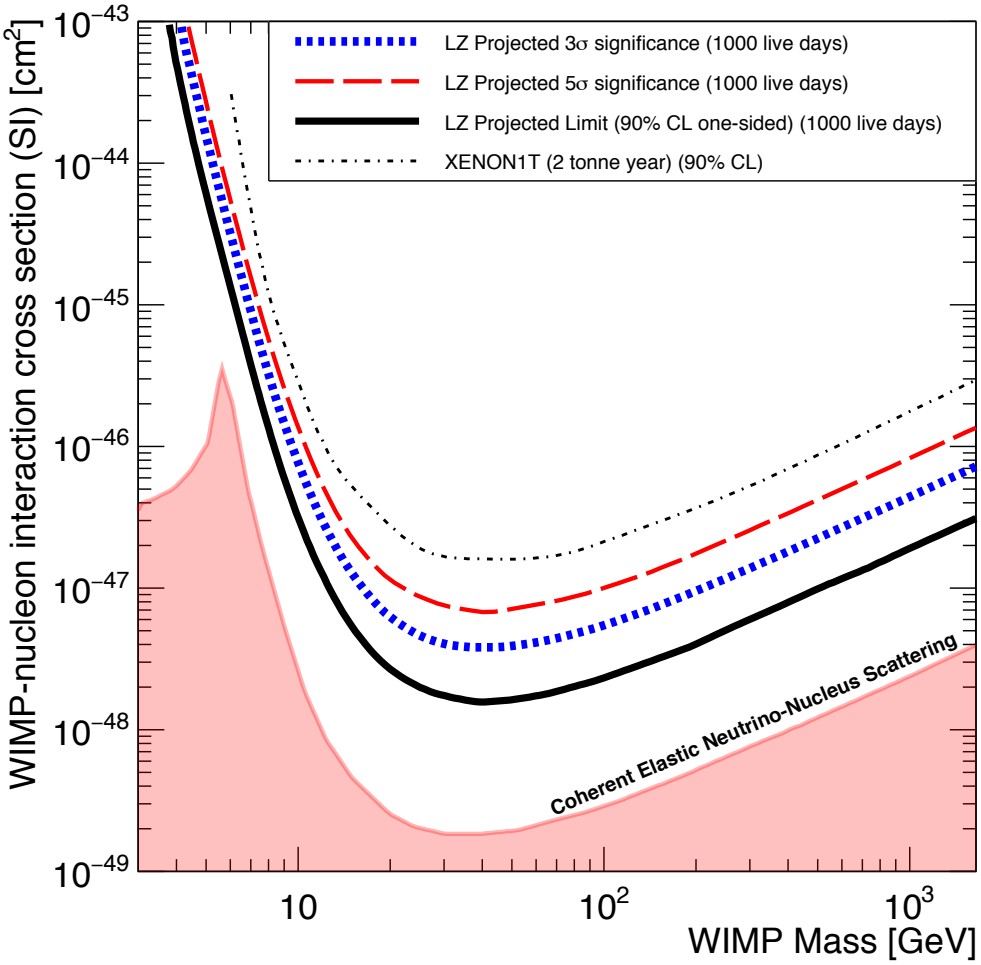


Figure 3.2: Projected LZ spin-independent WIMP-nucleon interaction cross-section limit, and a projection for XENON1T for 2 t yr of exposure (data from [148]). The requirement for LZ is $3 \times 10^{-48}\,\mathrm{cm}^2$ [1].

(for the τ), if the coupling is unique to one of e, μ, τ. For axial-vector mediated WIMP interactions to the electron, LZ will outcompete the DAMA result of $2 \times 10^{-32}\,\mathrm{cm}^2$ by roughly 6 orders of magnitude, placing it in the regime of Super-Kamiokande, at $6 \times 10^{-38}\,\mathrm{cm}^2$ [1].

3.2 Overview of the LZ Experiment

The active volume of LXe is 7 t (9.6 t total) [1]. A suitably large TPC comes with greater technical challenges such as radioactivity restrictions, and the high-voltage required to produce the electric field that will drift S2 charge. The LZ TPC will have a diameter of 1.456 m. The TPC will be housed inside a Ti cryostat. Low-radioactivity Ti has been sourced, only approximately 0.160 ± 0.001 counts will be seen due to this detector component over a 1000 day period [149]. The diameter of the cryostat varies with its height of 2.59 m, from 1.56 m to 1.66 m, and its thickness varies from 8 mm to 11 mm [1].

The electric drift field of LZ is foreseen at $0.3\,\mathrm{kV\,cm^{-1}}$, with a cathode voltage of not more than 50 kV. This follows from the requirements on the light yields for prompt scintillation light and electroluminescence in the gas phase (800 ph/e). The overall anticipated S2 PDE is 8.8 % (70 phd/e) for central events, and 6.9 % (55 phd/e) for edge events [1].[34]

The field in the gas phase is approximately $10\,\mathrm{kV\,cm^{-1}}$ for a gas gap of 8 mm - the field strength and the gas gap set the anticipated S2 pulse width because it translates directly to a 1.2 µs to 2.0 µs temporal spread. Furthermore, this ensures at least $5\,\mathrm{kV\,cm^{-1}}$ between the gate grid and the anode so that electrons at the liquid-gas interface have at least the required 0.61 eV to exceed the electron affinity of the LXe [1]. There is a reverse field region between the cathode and the bottom PMT array, having a baseline goal electric drift field of $2.9\,\mathrm{kV\,cm^{-1}}$. It exists due to the desire to maximise the field cage size; since it means there is a larger volume out of which S2 electrons can be extracted. The longest possible drift time is across the length of the TPC which corresponds to 880 µs [1].

The size of the detector and purity affect the electron attenuation and drift length, i.e. the ability to recover electrons from the liquid. Several calibration sources will be used to calibrate the response. For instance, $^{131\mathrm{m}}$Xe (164 keV),

[34] The S1 PDE is 8.5 % [1].

^{83m}Kr (41.5 keV), tritiated methane, and a dedicated external DD[35] neutron source (2.45 MeV) [1].[36]

Photons emitted in the TPC are detected by R11410-22 Hamamatsu photomultiplier tubes (diameter 3″) that are positioned at the top of the TPC in a xenon gas phase above the anode grid, and at the bottom of the TPC where they are located in the liquid just below the cathode grid. The bottom and top array may both detect S1 signals; but it is the top array of PMTs that is used for detecting the S2. The published design foresees 494 total PMTs: 253 in the top array, and 241 in the bottom array. PTFE walls surround the TPC to optimise the reflectivity and maximise the light-yield of the detector [1, 122].

Furthermore, LZ uses two additional veto detectors that will help to tag events that may have coincidences in the TPC. A first layer, known as the skin, exists below the PMTs in the bottom of the TPC, and between the exterior of the PTFE surface (15 mm thick for the wall plus an additional 1 mm for the panels) around the field cage of the TPC and the interior surface of the inner cryostat vessel. High energy photons that can propagate through these materials are read-out through Hamamatsu R8520 and R8778 PMTs that make up the skin PMTs in the skin detector. The volume immediately outside the inner cryostat vessel is a vacuum space, followed by a gadolinium-loaded linear alkyl benzene layer, which together with the TPC are in turn contained inside a water tank [122]. The water tank shields against gamma-particles, and the muon flux of $6.2 \times 10^{-5}\,\mathrm{m^{-2}\,s^{-1}}$ into the experimental hall, that come principally from the rock and extraterrestrial sources respectively. The Gd layer is instrumented with a further $\sim$ 100 PMTs. This is an important feature, because it means scattered neutrons due to (α, n) reactions occurring inside the TPC (such as may be emitted by the detector components) in the energy range from 0.5 MeV to 5 MeV can be tracked into the outer detector and rejected rather

[35] Deuterium-deuterium.
[36] A more complete summary of LZ calibration sources is provided in [1].

than be misidentified as a WIMP interaction [1, 122]. The additional detector subsystems surrounding the TPC enable LZ to measure its own backgrounds due to radioactivity of components [1].

The total contamination of the LZ experiment will also be pushed to unprecedentedly low levels so that there are fewer background events. This will reduce the impact of impurities that could affect charge recombination, and hence improve the S2 signal. In order to achieve the LZ electron lifetime goal, electronegative impurities such as O_2 (required to be no more than 0.4 ppb [1]), and H_2O, principally due to detector components (especially synthetic polymers such as PTFE) are maintained at the 0.1 ppb level through active recirculation and purification. The anticipated total contribution for 1000 live days will be about 6 events [1]. Several high-level parameters relating to cleanliness are shown in Table 3.1.

Table 3.1: Overview of several key parameters of the LZ detector (data from [1]). These goals pertain specifically to the response of liquid xenon and the effect of impurities on extracting useful waveform data from recoil events in the LZ detector.

Parameter	**Value**
Abundance: Kr	< 0.015 ppt
Abundance: ^{222}Rn	$< 2\,\mu\text{Bq}\,\text{kg}^{-1}$
Electron lifetime τ_e	> 0.8 ms
Charge drift length r_d	> 1.5 m

Combined with a millimetre level position resolution, the low contamination and additional veto systems will greatly benefit ER/NR discrimination power. Up to 99.5 % for electron recoils (for a drift field of $310\,\text{V}\,\text{cm}^{-1}$, PDE 7.5 %) discrimination is anticipated, with low-energy ER events of approximately 1.5 keV and NR events of lower than 4 keV anticipated to be resolvable [1].

It is the combination of knowledge of liquid xenon physics, the development of

radio-pure components (in particular PMTs), and xenon cleaning technology for the removal of Kr, that have made the prospect of scaling this detector technology to the size of LZ a realistic endeavour. These developments were the result of the preceding generations of searches such as LUX and ZEPLIN-III.

Existing experiments could not reach the level of background discrimination that will be seen at LZ due to the fact that these experiments are smaller and did not benefit from the self-shielding properties of xenon as much due to their smaller active volume. The large size of LZ, coupled with the skin and outer veto detector systems, will help tag neutron scatter events and gammas that may coincide with TPC events.

The WIMP search falls within the recoil energy range from 6 keVnr to 30 keVnr (1.5 keVee to 6.5 keVee) and the requirements are:

- ≥ 3 PMTs observe an S1 signal
- $0 < \mathrm{S1\,[phd]} < 20$
- $\mathrm{S2\,[phd]} > 350$

A suite of monitoring sensors are provided by the Oxford LZ group. Among these, acoustic sensors, the subject of Chapter 4, will be attached to the outside of the inner cryostat vessel which houses the TPC. The acoustic sensors will monitor for signs of disturbance to the liquid xenon volume, such as through vibrations or spurious bubble emission. This is important, since the light yield due to the S2 signal depends on the stability of the liquid, and on maintaining a parallel spacing between the grid wires with respect to the liquid level surface in the gas gap. The ER and NR S2 yields vary non-linearly as a function of distance from the liquid to the surface anode, as shown in Fig. 3.3 [1].

It is preferred that LZ science runs are long uninterrupted periods of stable operating conditions. During operations, the cryostat itself is inaccessible for inspection due to layers of shielding, and acoustic sensors provide a way to

monitor whether or not a liquid disturbance may be affecting the S2 extraction. The acoustic sensors will monitor the continued stability of the experiment and are therefore complementary to the physics requirements on the S1, S2 signals.

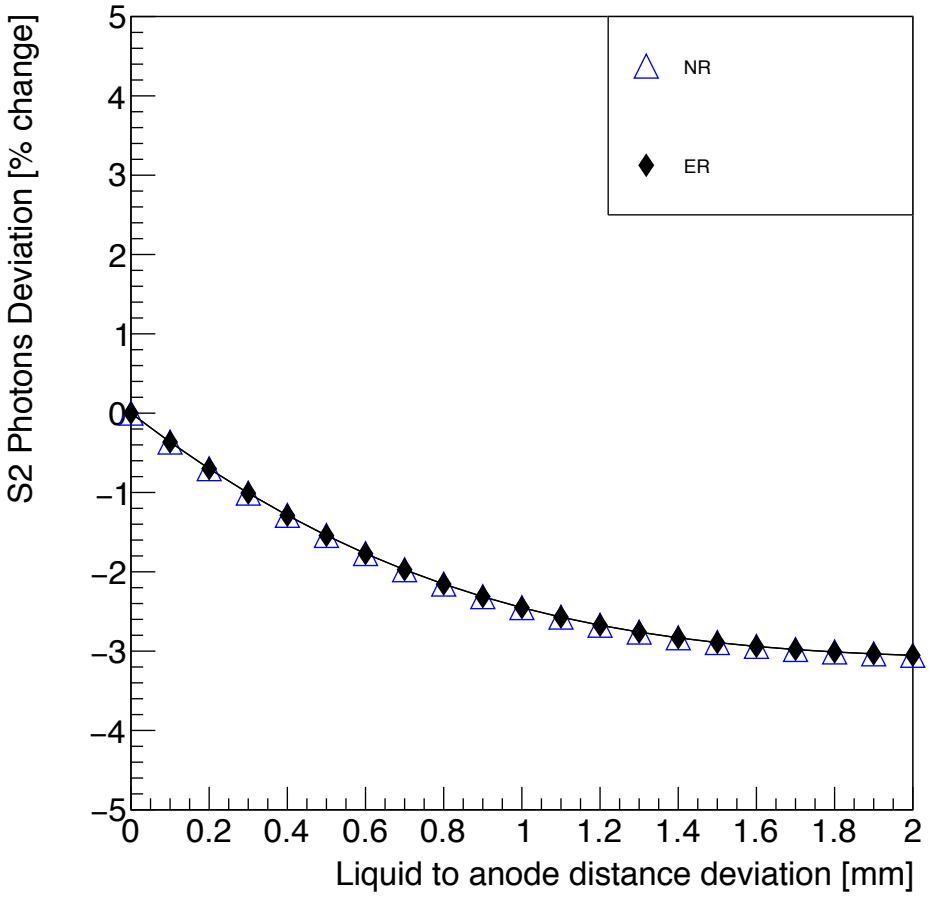


Figure 3.3: Change in electron and nuclear recoil yields as a function of the change in the liquid level relative to the anode, calculated for the LZ TPC.

Many factors determine the balance between the scintillation and ionisation light yields and the values of g_1, g_2 of Eq. (25) and Eq. (26). The detector and the data acquisition system response are complementary. In a non-optimal case, a mismatch between the yields and the data acquisition system can be detrimental to the ability to analyse event data. It is the subject of Chapter 5 to demonstrate a simulated environment of the detector readout system within which this can be assessed.

3.3 Detector Hardware

Shown in Fig. 3.4 is a diagrammatic overview of the PMT readout system for the TPC. A key feature of the LZ experiment is its dual-gain front-end electronics readout system. PMT signals are amplified in a low-gain and high-gain channel in parallel, with different gain and shaping parameters for incoming waveforms. The purpose of this system is to enhance the overall sensitivity of event data: the low-gain (high-gain) is optimised for high-energy (low-energy) events. Therefore, high-energy events may cause saturation and clipping of the amplified signals on the high-gain channel, but the low-gain channel would still provide useful information.

After amplification on the analogue front-end, the channel signals are digitised by separate digitiser boards. An active trigger is responsible for deciding which signal data are extracted and collected through the Data Extractor and Data Collector, respectively. Groups of 32 channels exist on a single DDC-32 digitiser board. There are 46 digitiser boards in total, accommodating all the PMTs and their low-gain and high-gain channels. The timestamp of when a board's data acquisition is triggered for a particular event is recorded.

Groups of DDC-32 digitiser boards are connected to groups of Data Extractor boards, which in turn are connected to Data Collector boards. Their purpose is to collect amplified and digitised waveform data, and to store the raw binary DAQ data to a computer hard drive. Raw DAQ data stored on disk are processed in real time by the LZ Event Builder system; which is responsible for converting the raw data into a ROOT file that is sent to LZ data centres for analysis. Once data have been stored on a computer hard drive on site at SURF, it is transferred from SURF to data centres in the US and the UK.

The sampling rate of the DDC-32 boards is 100 MHz (a timebase of 10 ns). The duration of single photoelectron PMT signals is on a similar order to the sampling rate, and therefore the shaping properties of the amplifier are required to prolong the duration of the waveforms so they can be effectively sampled.

The requirement is a detection efficiency of $\geq 90\,\%$ for single photoelectrons, and for the threshold trigger level it is at least 0.25 phe. It is expected that the DAQ will reach 93 % at a threshold of 1 phe (that is assuming that a single photoelectron was produced, i.e. after accounting for the collection efficiency of the PMT) [1].

The response of the front-end electronics determines the dynamic range of the TPC PMTs and this is the subject of Chapter 5. The PMTs for the TPC

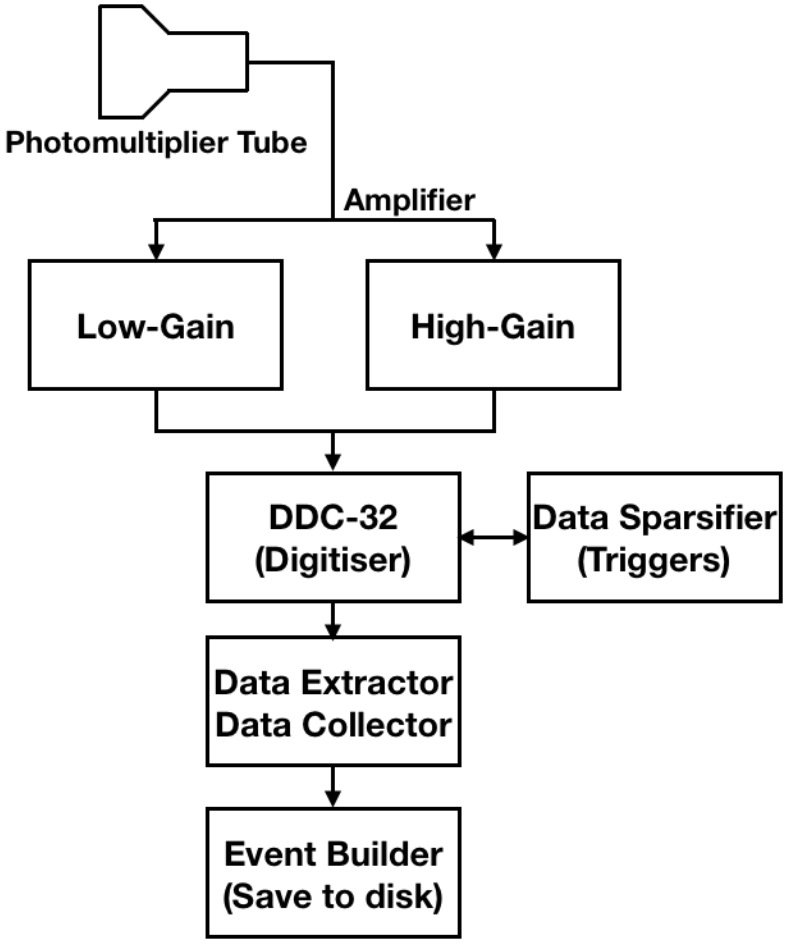


Figure 3.4: A system diagram showing the signal processing chain of the LZ TPC PMT readout system. PMT signals are amplified and shaped through separate channels (low-gain and high-gain) on the front-end electronics amplifier board.

(Hamamatsu model R11410-22) will operate at a nominal maximum gain of not more than 5×10^6 (high-voltage at no more than 1750 V), with the nominal

gain to be 3.5×10^6. The event rate that the DAQ will see, combined with the front-end electronics, determine the overall storage needs. Estimates have been made based on LUX data, and scaled by the estimated 40 Hz background event rate for LZ, to give 1.9 PB in 1000 d. The average expected size per event (including compression) is approximately 0.5 MB per event [1]. Chapter 5 puts these estimates to the test using simulated data to quantify more robustly the expected requirements on the processing rate and required disk space.

The DAQ will run a data reduction ("sparsification") system that collects only the significant deviations from the baseline after the signal is digitised. The aim is to store only those digitised samples which represent the actual waveform of the PMT signal. Additional samples before and after the waveform are added to capture the baseline around the waveform. The result is called the POD, and it is the basis of accounting for waveforms in the DAQ trigger systems after digitisation.

There are two main types of triggers foreseen for the DAQ, one for S1 signals and another for S2 signals. Both of these trigger on the numerical output of time-domain filters that integrate pulse areas with time constants of 60 ns to 100 ns for S1, and up to several µs for S2 pulses - similar to what was used for LUX [150]. The choice of timing has to do with the expected duration and amplitude of the response to the 236 keV gammas of activated LXe, which are a function of the design of the TPC and drift field [1]. The combination of S1 and S2 triggers enables detection of either S1 or S2 or S1+S2 events within a specified separation in time.

In short, LZ is one of the largest dark matter search experiments to be attempted. It will place stringent limits on the spin-independent WIMP-nucleon interaction cross-section. The technical aspects of LZ with regard to the response of liquid xenon as a detector medium have been discussed in relation to the requirements on cleanliness and radio-purity of detector components. The instrumentation and DAQ systems of LZ have been discussed in detail in the context of the PMT single photoelectron response for a WIMP search.

4 Acoustic Sensors

Acoustic sensors provide a way of monitoring for departures from the normal operating conditions in the TPC. The scale of the LZ TPC calls for a means of monitoring the stability of the liquid, the detector, and the detector environment. LZ, unlike comparable experiments such as XENON1T or PandaX, will use acoustic sensors to complement the process of monitoring the TPC.

In the top array region of the TPC there is a gaseous xenon phase. Electroluminescence (S2) signals produced in the liquid are extracted by an electric field into the gas phase, allowing their conversion into photons for detection on the top PMT array. The size of the gas gap, its uniformity with respect to the liquid surface, and the purity of the gas are important factors in achieving a good charge extraction [122].

Liquid stability is paramount because it affects reliable event detection and event position reconstruction. With the desire to purify the liquid comes the need to include cryogenic pumps that circulate the liquid and gaseous xenon. These pumps are large and produce a lot of noise, and efforts will be made to acoustically isolate them from the rest of the experiment. Although active steps have been taken by the collaboration to isolate the pump noise from the detector, they are still indirectly in contact with the TPC and the liquid, and can be a source of acoustic background that should be monitored by acoustic sensors.

Similarly, if a flange or feedthrough accidentally comes into direct mechanical contact (e.g. metal-to-metal contact), then this can be detected as an increase in vibrations and liquid instability. Knowledge of this means the issue can be addressed promptly as or before the experiment is acquiring event data. Likewise, acoustic sensors can provide information about the state of the TPC during and after filling the detector, such as through the sound of liquid and gas being pushed through the cryostat.

Moreover, sounds external to the detector and the TPC may be relevant, since, if acoustic signals are subsequently detected in the TPC, it would be useful to know about this in order to plan activities accordingly to minimise the impact during data taking.

Acoustic sensors provide LZ with the capability to diagnose the detector continuously while it is running; and this is an important aspect to ensuring controlled conditions in the experiment. In short, the data that acoustic sensors provide can be used as an additional event veto system, and this increases the level of confidence in the quality of the science output of the experiment.

4.1 Low-Pass Filters and High-Pass Filters

The analysis of the acoustic sensor data in this chapter will make use of band-pass filters; which isolate the frequency components that are used to identify acoustic features such as bubbling and droplets, while rejecting background noise. A band-pass filter consists of a low-pass filter and a high-pass filter: it passes frequencies within a lower and upper cutoff frequency and attenuates frequencies outside the pass-band.

A low-pass (conversely, a high-pass) filter attenuates signals with a frequency component above (below) a cutoff frequency f_c but not below (above) f_c. The implementation and properties of these filters can be understood by analysing electronic circuit diagrams, as shown in Fig. 4.1 and Fig. 4.2. The numerical values of the components R_F, R_G, C determine the gain $G = R_F/R_G$ and cutoff frequency $f_c = 1/(2\pi RC)$ (where $\tau = RC$ is called the time constant) of the filter. Fig. 4.1 shows the implementation of an active first-order low-pass filter, and a Bode plot highlighting the gain G in the pass-band, and the cutoff frequency (also called the corner frequency) f_c. The transfer function of the low-pass filter is given by

$$\frac{V_{out}}{V_{in}} = -\frac{R_F}{R_G}\frac{1}{1+i\omega R_F C},\ f_c = 1/(2\pi R_F C)\,. \tag{28}$$

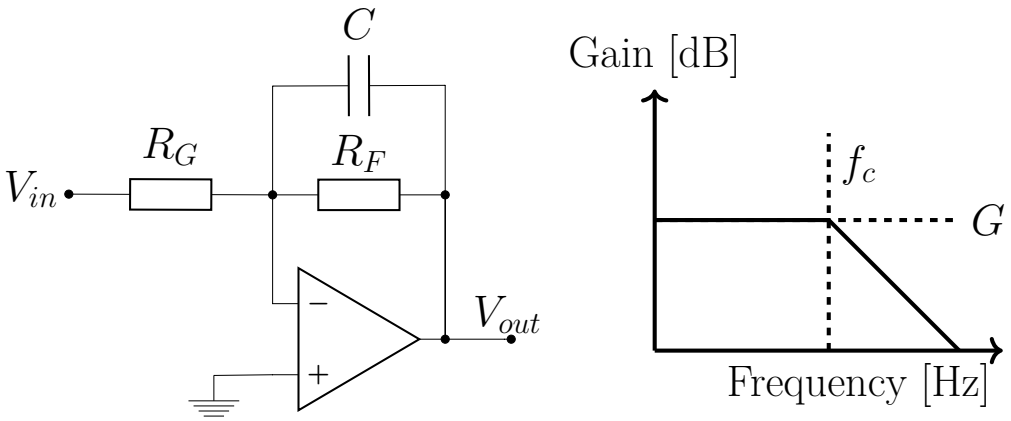


Figure 4.1: Circuit diagram and an idealised Bode plot for a first-order low-pass filter. For frequencies $f < f_c$ the signal is in the pass-band and has gain G, while for $f > f_c$ the signal is increasingly attenuated.

Fig. 4.2 shows the circuit diagram and a Bode plot for a high-pass filter.

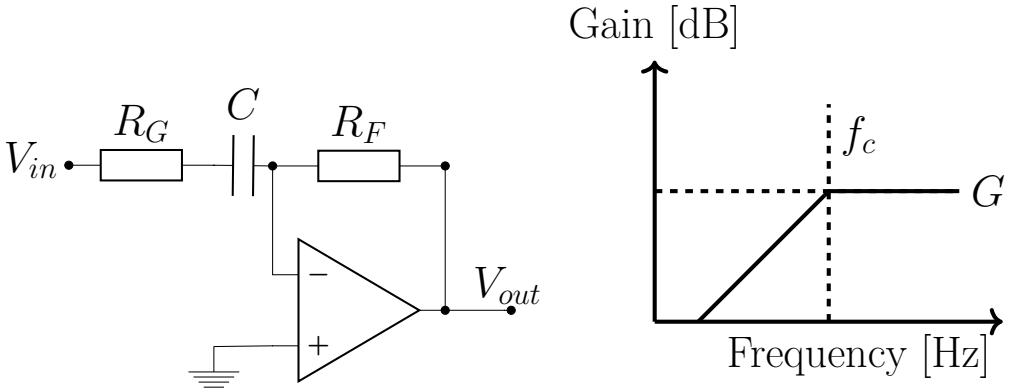


Figure 4.2: Circuit diagram and an idealised Bode plot for a first-order high-pass filter. For frequencies $f > f_c$, the signal is in the pass-band and has gain G, while for $f < f_c$ the signal is increasingly attenuated.

The transfer function of the high-pass filter is given by

$$\frac{V_{out}}{V_{in}} = -\frac{R_F}{R_G}\frac{i\omega R_G C}{1 + i\omega R_G C},\ f_c = 1/\left(2\pi R_G C\right). \tag{29}$$

Furthermore, since

$$\frac{i\omega\tau}{1 + i\omega\tau} = 1 - \frac{1}{1 + i\omega\tau}, \tag{30}$$

the expression for a high-pass filter can be derived from a low-pass filter.

4.2 Purpose of the Acoustic Sensors

The purpose of the acoustic sensors is to monitor the TPC and LXe. Therefore, the acoustic sensors are in the vacuum-space and monitor the LXe-space from the exterior surface of the Inner Cryostat Vessel (ICV). The locations follow from the need to monitor the liquid stability at the liquid level for the gas phase at the top array, and the cathode level at the bottom PMT array in the liquid. These locations are indicated in Fig. 4.3. A total of eight sensors

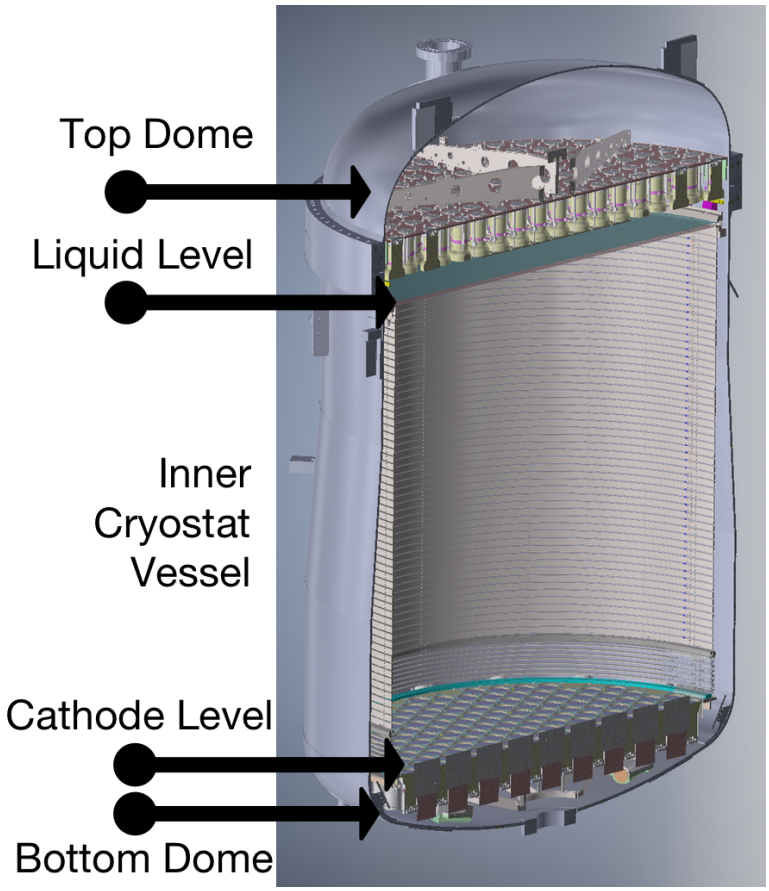


Figure 4.3: Monitoring targets for acoustic sensors that will be on the exterior surface of the inner cryostat vessel of the LZ experiment. Cryostat image from [151].

will be installed on the exterior surface of the ICV: one array of three sensors at the cathode level, one array of three sensors at the liquid level, and one sensor each on the top and bottom domes of the ICV. The liquid level and the cathode level sensor arrays provide equidistant radial coverage of the TPC

liquid and the ICV. Fig. 4.4 shows a finished acoustic sensor assembly.

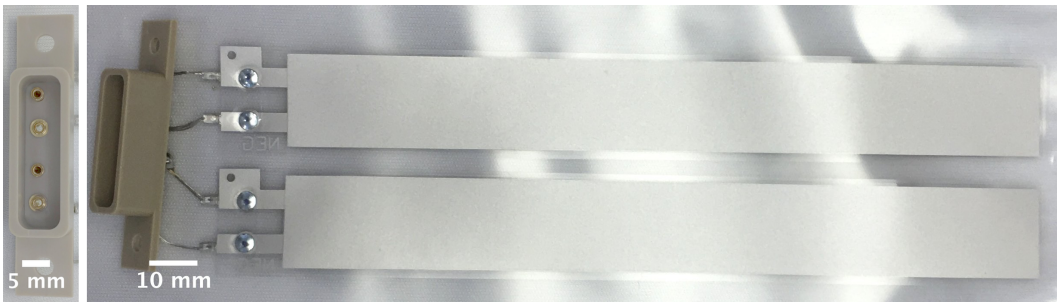


Figure 4.4: A single differential acoustic sensor unit, shown before final cleaning and packaging at Imperial College, London. Two individual films make up one differential sensor. A Polyether ether ketone (PEEK) connector shell, shown on the left, holds two pairs of Harwin signal and ground receptacles (H8504-05 and H3185-05) that accommodate the standard cabling solution for PMT cables in LZ.

Although highly unlikely given the extensive effort made by the collaboration to minimise the risk of undesired heating or cooling, detecting the presence of a bubble in the liquid could indicate a localised excess heating. Localised heating (and cooling) occurs due to the circulation system that convects LXe in order to maintain the temperature throughout the skin and TPC - thereby assisting the circulation and purification of the active volume of LXe. This is achieved by heaters below the bottom array of PMTs, which heat the wall and skin region, and thermosyphons at the liquid level which are used for cooling. The heated (cooled) fluid enters directly into the TPC from the bottom, and overheated liquid evaporates and is extracted from the top of the TPC. The heating power used will be no more than 30 W [1]. A balance must be maintained between heating the TPC liquid and the evaporation at the liquid level: heating too quickly results in liquid boil-off and hence in bubbling that perturbs the liquid. Conversely, if there is overcooling in the gas phase, LXe may condense to form droplets that would hit the liquid surface. Other sources of heating include the PMT bases in the cathode region, that may become warm and heat the liquid.

The experiment is intended to be acoustically isolated from vibrational effects such as from large coolers that will be in the experimental hall. However, some mechanical contact between the ICV and the rest of the experiment and its environment is unavoidable. If unintentional vibrational noise *is* detected by the acoustic sensors, it is an indication that the liquid is being perturbed by external factors, which can then be corrected. The ability to detect acoustic events coincident with recoil events inside the TPC therefore helps to assess departures from what is supposed to be an acoustically quiet experiment. Events should be vetoed if there is doubt as to the experimental conditions at the time a TPC event was detected. The feasibility of having acoustic sensors in the experiment is demonstrated by having achieved suitable data analysis algorithms and procedures for the detection and identification of relevant acoustic events.

The low-mass material composition of the sensor, PVDF[37], was selected to minimise the effect on background counts in the detector. The cleaning procedures most relevant to the acoustic sensors are for the removal of radon due to dust. Developing a suitable cleanliness protocol is non-trivial due to the constraints on chemically compatible cleaning agents and methods given the material composition of the sensors. A non-abrasive cleaning process was developed, and is shown in Table 4.1. The process is part of the cleanliness protocol for the acoustic sensors in LZ. The sensor films have few surfaces, which facilitates the removal of dust and inspection for removal of contaminating surface particulates. A microscopic examination was performed to confirm the process does not damage the sensors.

Cleanliness requirements and the low temperature conditions in LZ informed the type of epoxy (Master Bond®, EP29LPSP[38]) used to adhere the sensors to the cryostat. The acoustic impedance of Master Bond® epoxy EP29LPSP is not known, but it is expected to be in the range 0.88 MRayl to 6.25 MRayl[39]

[37]Polyvinylidene fluoride (PVDF).
[38]This epoxy is suitable for use in low temperature cryogenic environments.
[39]Specific acoustic impedance: $1\,\mathrm{Rayl} = 1\,\mathrm{kg\,s^{-1}\,m^{-2}}$.

Table 4.1: Acoustic sensors cleanliness protocol.

Method	Solution	Period	Purpose
1. Hand clean	Flux clean	N/A	Remove flux residue
2. Hand clean	Isopropyl alcohol	N/A	Rub off dust
3. Ultrasonic bath	De-ionised water	20 min	Remove dust
4. Air gun	Nitrogen	N/A	Quick drying
5. Bagging	N/A	N/A	Triple bagging

[152]. The acoustic impedance of titanium is 27.32 MRayl [153]. Thus, between 39.4 % to 88.0 % of the acoustic pressure is reflected from the epoxy-titanium interface.

PVDF has an acoustic impedance of 3.81 MRayl [154] and is better matched to the epoxy than common alternative materials such as lead zirconate titanate (PZT) (35 MRayl [155]). To first order, a PVDF-epoxy sensor interface reflects between 5.9 % to 39 % of the signal whereas a PZT-epoxy interface reflects between 49 % to 90 % of the signal.

The sensors were tested in Oxford and have been installed and have acquired acoustic data at the System Test at the SLAC National Accelerator Laboratory in Stanford, USA, which is a downsized version of the LZ experiment. In the following sections, the sensors and their readout system are discussed.

4.3 Acoustic Signal Chain: Sensing Method and Electronics

The design of the LZ experiment and cleanliness controls drive the decisions on how the sensors are adhered, operated, and read out. The front-end electronics readout signal chain is shown in Fig. 4.5. Each sensor is adhered to the exterior of the ICV. The front-end readout electronics interface to the LZ slow-control system, to which reduced quantities from the raw data stream can be offered. Full waveform data pass to a software-based trigger, after which raw waveforms can be stored to disk for further offline analysis. The trigger

is flexible, it operates on a per-channel basis, and can be adjusted without having to disengage the front-end electronics.

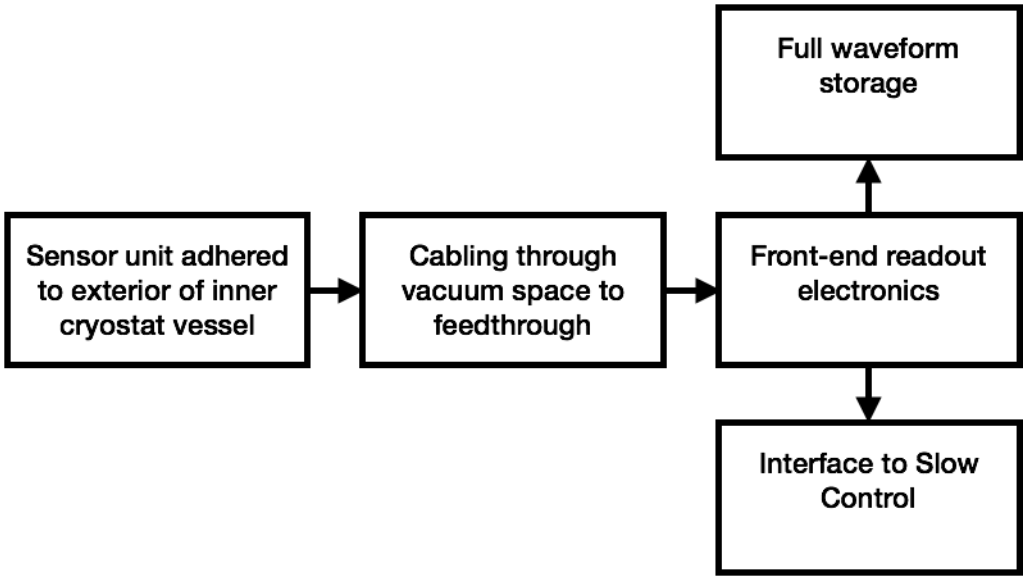


Figure 4.5: Acoustic sensor front-end electronics readout chain, shown for a single readout channel.

The charge constants of Table 4.2 suggest PZT outperforms PVDF. A selection of commercial PZT sensors of a similar size as the PVDF films were tested. However, in practice these were found to produce very little signal for comparable stresses, which contributed to preferring PVDF.

Table 4.2: Piezoelectric charge constants, comparison between PVDF and PZT. The first index denotes the axis of the polarisation that is induced due to the deformation applied along the axis that is denoted by the second index. Axis 3 is the polarisation axis parallel to the direction of deformation, and axis 1 is in the plane of the sensor along its length.

Constant	**PVDF**	**PZT**	**Reference**
$d_{33}\left[\mathrm{pC\,N^{-1}}\right]$	30	410	[156]
$d_{31}\left[\mathrm{pC\,N^{-1}}\right]$	23	110	[157]

The acoustic sensors are made of a piezoelectric film with silver electrodes acting as a capacitor - they are manufactured by a company called TE Connec-

tivity. Acoustic signals propagate as pressure waves which temporarily deform the sensor film, imparting mechanical energy, which is then converted into an electrical signal via the piezoelectric effect. The commercial availability of the sensor films offers a low-cost readily available sensor.

The total charge generated by the sensor depends linearly on the area A and the piezoelectric constant

$$Q = Ad_{3i}\sigma_i, \tag{31}$$

where $i \in \{1, 2, 3\}$ denotes the direction of the axis of the stress σ [158].

Furthermore, a sensitive bandwidth of 1 Hz to 10^9 Hz [157] is typical of PVDF sensors. In real LZ, where characteristic frequencies such as from bubble production vary with depth and are not necessarily known, having a wide sensitivity is advantageous. Another advantage of PVDF sensors is that they have a low mass, reducing the material contribution to radioactive contamination; making them easy to integrate into the experiment without impacting on the design of the cryostat.

4.3.1 Front-End Electronics

The acoustic sensors are adhered to the outer surface of the inner cryostat vessel inside the vacuum space. Several meters of coaxial cable will connect the sensors to a feedthrough, to which the readout electronics are connected from the outside. A charge amplifier was selected for the readout electronics, since it greatly suppresses the effect of the input cable capacitance. Electronic noise therefore depends mostly on the readout electronics [159]. To further reduce the effect of electronic noise, and to integrate easily into the LZ grounding scheme, the sensor readout mode is differential. Ground signals do not enter the signal path, thereby greatly suppressing the effect of common-mode noise. Two individual sensor films comprise a single acoustic sensor unit, whereby an acoustic signal is sensed on both sensors and converted into electrical signals of opposite polarity. The front-end electronics board is shown in Fig. 4.6.

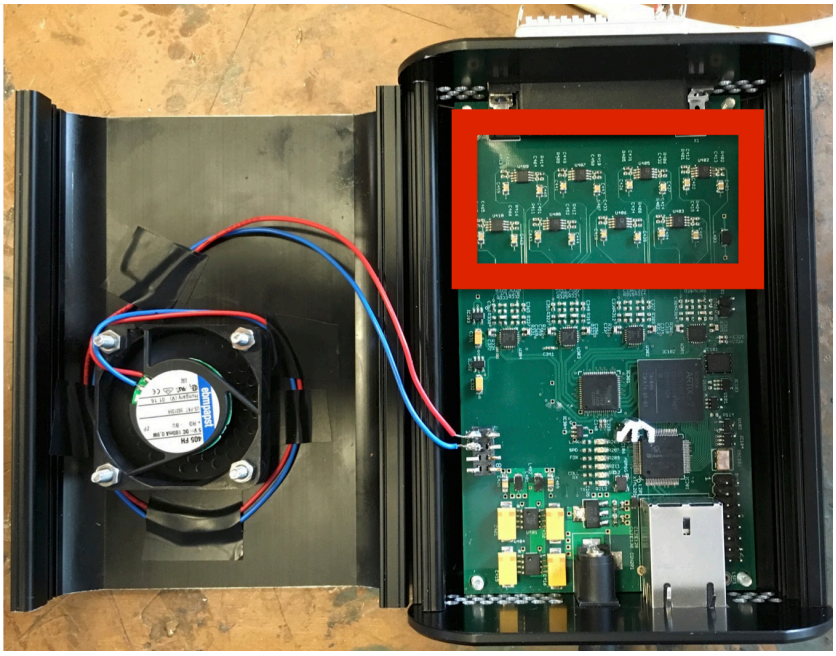


Figure 4.6: Front-end readout electronics, developed by the LZ group in Oxford. This figure provides a visual representation of a portion of the signal chain. The red square box superimposed on the electronics board highlights the amplifier blocks, eight in total, each of which provides an analogue band-pass filter for each of the eight channels.

The readout board features eight channels to accommodate all sensors needed for LZ. The front-end electronics amplifies input signals from the acoustic sensors[40]. Each differential amplifier channel has a band-pass filter on it. The gain and filter properties on the readout board were chosen based on the measured range of frequency bands of acoustic signals of interest. The circuit diagram is shown in Fig. 4.7.

The sensor is modelled as a charge source, possessing a capacitance and an internal resistance. The sensor signal is a high input impedance current source at the input to the inverting input terminal at V_{in}. The op-amp is a charge amplifier with a low input impedance, so the terminal at V_+ acts as a virtual ground, and the blocking capacitor appears in parallel with capacitors C_S, C_G in the lower diagram of Fig. 4.7.

[40]The board can be read out over an Ethernet connection using dedicated software for collecting full waveforms for processing.

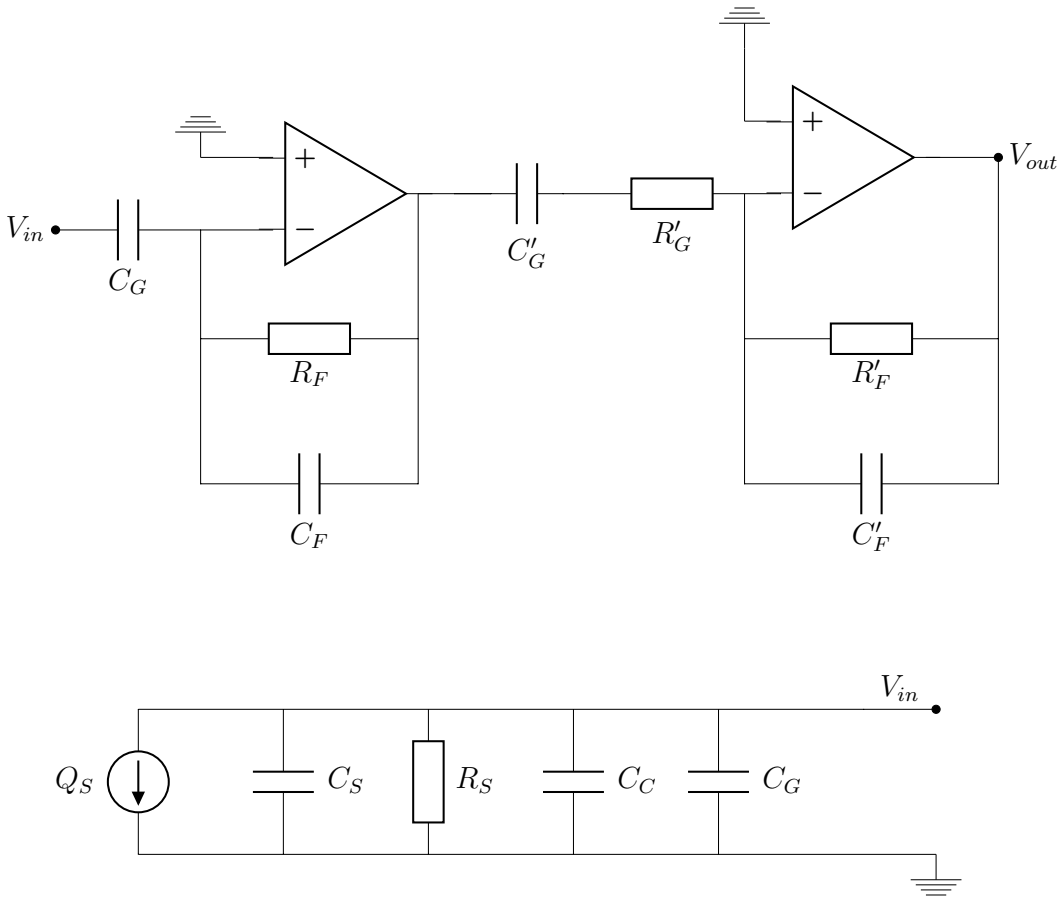


Figure 4.7: Circuit diagram for the acoustic sensor and the readout board. The sensor input is a current source with an internal capacitance C_S and an internal resistance R_S. C_C is the cable capacitance.

The total charge at the input V_{in} is [160, 161]

$$Q = V \times (C_S + C_C + C_G)\,. \tag{32}$$

The transfer function of the first stage is [158]

$$V(t) = \frac{R_F}{R_G} \frac{i\omega R_G C_G}{(1 + i\omega R_F C_F)(1 + i\omega R_G C_G)} \frac{i(t)}{i\omega (C_S + C_G + C_C)}. \tag{33}$$

The total series resistance R_G cancels, and $C_G \gg C_C, C_S$ so that

$$V(t) = R_F \frac{1}{(1 + i\omega R_F C_F)} i(t) \tag{34}$$

which has a low-pass corner frequency of 1.6 Hz ($R_F = 100\,\mathrm{M\Omega}$, $C_F = 1\,\mathrm{nF}$). Although the transfer function appears as a low-pass filter, for an ideal op-amp, C_F balances the current through R_F, and the circuit integrates the current [160, 162–164]. Therefore, for $i\omega R_F C_F \gg 1$, the transfer function reduces to

$$V(t) = \frac{Q}{C_F}. \tag{35}$$

The output of the first op-amp is a low output impedance voltage source. The second stage is a voltage mode amplifier configured as a band-pass filter

$$\frac{V_{out}}{V'_{in}} = \frac{R'_F}{R'_G}\frac{1}{(1+i\omega R'_F C'_F)}\frac{i\omega R'_G C'_G}{(1+i\omega R'_G C'_G)}, \tag{36}$$

where V'_{in} is the output of the first op-amp. The corner frequencies are $f_L \approx 1881\,\mathrm{Hz}$ and $f_H \approx 17\,\mathrm{MHz}$ ($R'_G = 180\,\Omega, C'_G = 470\,\mathrm{nF}, R'_F = 2000\,\Omega, C'_F = 4.7\,\mathrm{pF}$.) Fig. 4.8 shows that in the pass-band, the gain of the low-pass and the high-pass filter is approximately 1, and the overall gain is $R'_F/R'_G \approx 11$.

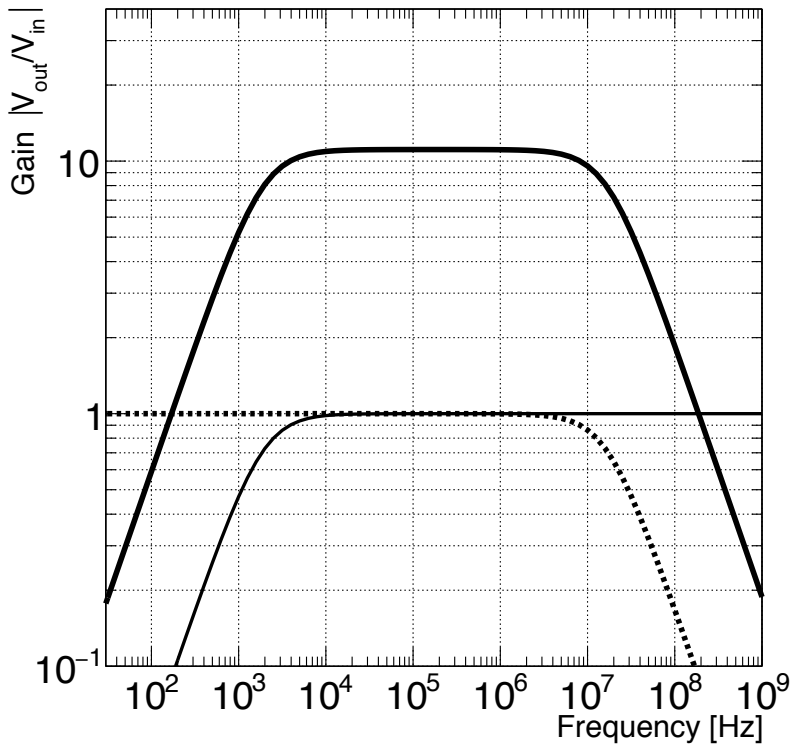


Figure 4.8: Transfer function of the amplifier block on the readout board.

4.3.2 Trigger

An adaptive trigger has been implemented in software which enables collecting waveform data when it represents a departure from the general acoustic environment. The algorithm for the trigger consists of a filter implemented in the time-domain. The filter output is used to calculate the long-running baseline average for each channel, which is compared to the raw signal. The number of standard deviations that the waveform data represent (as compared to the long-running baseline average) is the threshold condition for the trigger.

The raw voltage signal is averaged within a time window, and passes through a first-order low-pass filter with time constant τ and timebase T

$$accu_i = \exp\left(-T/\tau\right) \times accu_{i-1} + \Big(1 - \exp\left(-T/\tau\right)\Big) \times \bar{x}_i, \tag{37}$$

where i denotes the i-th time window and $accu_i$ is the filter output which depends on the preceding values of $accu$.

The average Root Mean Square (RMS) value of the filter output is calculated as a non-linear regression from the sum of the square difference of the raw voltage output within the time window of size N and the filter output of that event (which is $accu_i$)

$$\bar{RMS}_i^k = \sqrt{\frac{1}{N}\sum_{j=1}^{j=N} RMS_j^k + \Big(x_j - accu_i\Big)^2}, \tag{38}$$

with j the index of the raw data within the event window i at iteration k.

The average RMS is passed through a first-order low-pass filter to calculate the long running RMS denoted $LRMS$

$$LRMS_i = \exp\left(-T/\tau\right) \times LRMS_{i-1} + \Big(1 - \exp\left(-T/\tau\right)\Big) \times \bar{RMS}_i. \tag{39}$$

The trigger condition is set by comparing the $LRMS$ to the difference between

the input and filtered signal

$$|x_j - accu_i| > n \times LRMS_i, \tag{40}$$

where n is the number of standard deviations used as the trigger condition.

The trigger is insensitive to the absolute baseline or changes to the baseline level of noise that happen on timescales comparable to or longer than τ. This is desirable in LZ, where the acoustic environment is different during filling than during normal operation, for example. The absolute value of the baseline of recorded waveforms is used to monitor for longer term changes in the acoustic environment. The trigger remains active for as long as the waveform remains above threshold. Each channel triggers separately, and only waveforms on those channels which activate the trigger are stored.

To test the performance of the trigger before it is used in LZ, a test experiment was performed whereby acoustic signals were supplied to the sensors through a speaker connected to a signal generator. The response of the trigger is shown in Fig. 4.9.

First, a regular background sound of around 2 Hz is introduced; which persists for the duration of the time window shown in the figure. Because the acquisition rate is slightly out of phase with the 2 Hz signal, the trigger rate fluctuates up and down a bit.

The signal generator is then used to produce a continuous background noise through the speaker. The speaker signal floods the acoustic sensors with a continuous background noise that is louder than the 2 Hz signal. The causes a sharp rise in the rate at around $t = 70$ s.

The threshold of the adaptive trigger responds, and the rate drops to reflect that the new signal dominates over the one originally added. From the fit one recovers a filter time constant of (5.02 ± 0.08) s, which is in close agreement with the actual time constant of 5 s. The trigger rate decreases to nearly 0 Hz,

since there is no longer a discernible departure from the continuous source of noise. When the continuous source of noise is disabled at around $t = 145\,\mathrm{s}$ (leaving only the 2 Hz signal), the threshold condition adjusts again to the previous level, and the trigger rate level returns to about 2 Hz.

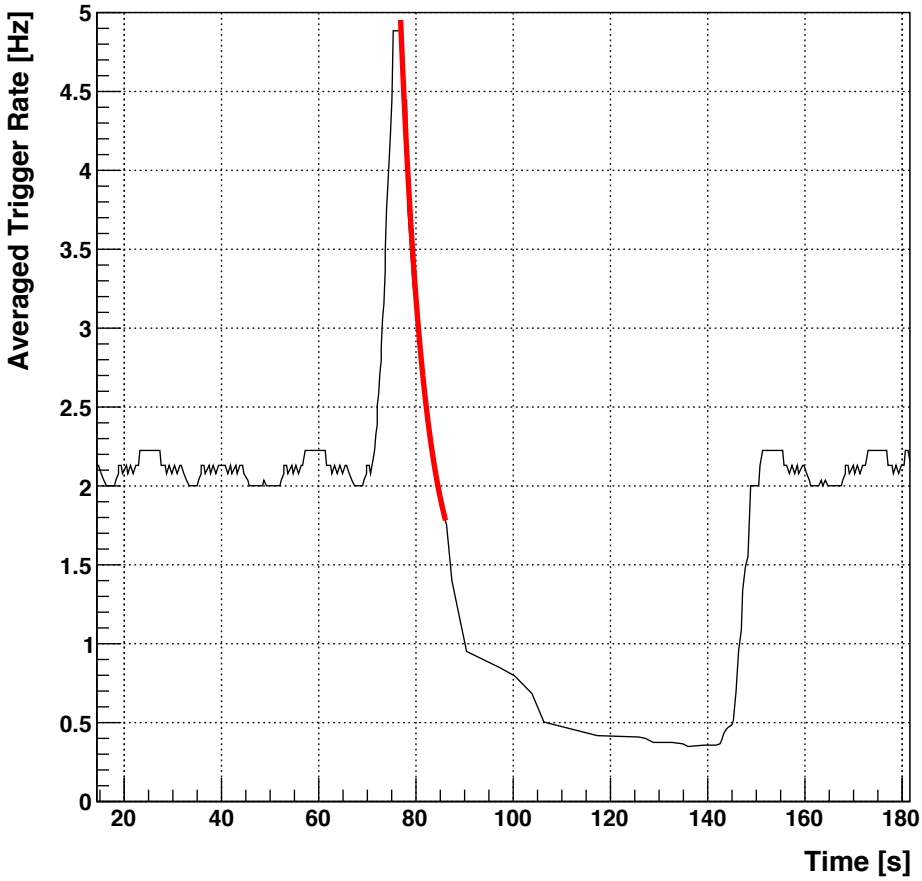


Figure 4.9: Acoustic sensor software trigger rate. A persistent 2 Hz signal is emitted through a speaker. At about $t = 70\,\mathrm{s}$, a continuous noise is added through the speaker; the rate increases before adjusting to the new level of noise. At about $t = 145\,\mathrm{s}$, the continuous noise is switched off, and the trigger threshold re-adjusts. The trigger rate returns to the persistent 2 Hz signal. The data are superimposed with a fit (shown as the red line) to recover the time constant of the filter.

4.4 Classifying Acoustic Event Topologies

Classifying acoustic event topologies starts with making a distinction between event-like signals (such as bubbles, droplets, and tapping on the cryostat vessel), and background-like sources of sound (such as pump noise) that are part of the general acoustic environment. The ability to distinguish event-like and background-like sources of sounds quantifies the state of the acoustic environment at LZ.

4.4.1 Detecting Bubbling

Bubbles occur in all manner of situations: from boiling water in a kettle, to rain drops falling into a pond whose sound is caused by the bubbles created below the liquid surface [165]. Knowing what sound a bubble makes depends on the dynamic behaviour of the bubble after it is created in a liquid. Modelling the behaviour of the liquid (and the resulting bubble) in detail involves knowing at least the pressure and density of the liquid, and with more sophistication the initial conditions and boundary conditions of the liquid, the dissipation of energy, and surface tension.

To first order, a bubble can be modelled as a damped harmonically oscillating sphere of gas (Fig. 4.10) inside a liquid. The pressure of the surrounding liquid acts as a restoring force - compressing the bubble as it expands and contracts.

The equation of motion for a damped harmonic oscillator is given by the second order linear homogeneous differential equation

$$m\frac{\mathrm{d}^2 x}{\mathrm{d}t^2} + b\frac{\mathrm{d}x}{\mathrm{d}t} + kx = 0, \tag{41}$$

where x is the displacement at time t; m, k are the mass and spring constant; and b is a constant in units of angular frequency.

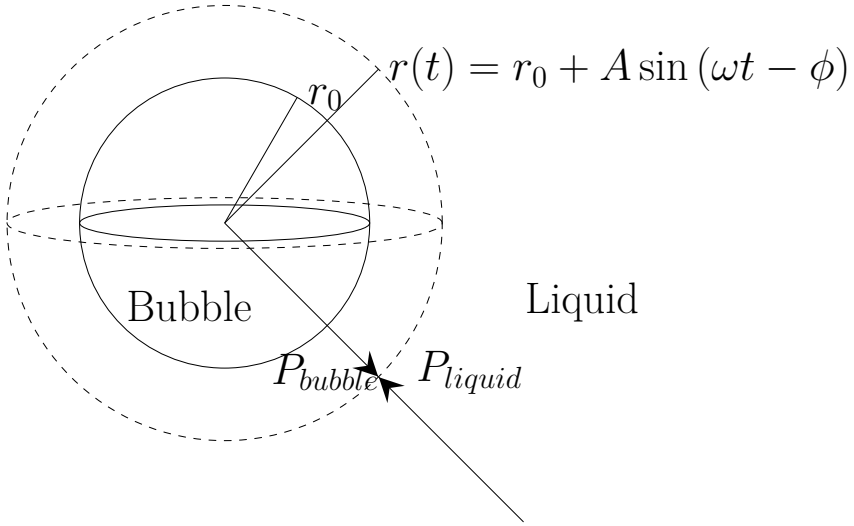


Figure 4.10: A harmonically oscillating bubble that expands and contracts due to the pressure of the surrounding liquid. The initial radius is r_0, the amplitude of the oscillation is A, the angular frequency is ω and the phase is ϕ.

Using the ansatz solution $x = Ae^{st}$ for the equation of motion yields a quadratic equation. The quadratic has complex solutions of the form $s = \alpha + i\beta$ which define the conditions of the oscillation fixed by the discriminant $\Delta = b^2 - 4mk$

$$\Delta = \begin{cases} > 0 & \text{if } b^2 > 4mk \text{ Overdamped} \\ = 0 & \text{if } b^2 = 4mk \text{ Critical damping} \\ < 0 & \text{if } b^2 < 4mk \text{ Lightly damped.} \end{cases} \tag{42}$$

The case of lightly damped oscillations has the general solution

$$x = A_1 \left(\sin(\omega t) + \cos(\omega t)\right) \exp(-b/2m). \tag{43}$$

In lieu of LXe, bubble production was initially studied in a tank of water, since its acoustic impedance ($1.509 \times 10^5\,\mathrm{g\,cm^{-2}\,s^{-1}}$ at 303.15 K) is relatively close to that of LXe ($1.8 \times 10^5\,\mathrm{g\,cm^{-2}\,s^{-1}}$ at 166 K) [166]. Bubbles exhibit the behaviour predicted by Eq. (43) in Fig. 4.11. The signal in the time domain which arises from bubble formation behaves as a damped harmonic

oscillator, exhibiting exponential decay of the amplitude over roughly 100 ms. A secondary excitation comes in the form of a beat frequency which is of lower frequency, and is attributed to the reverberations of the tank.

Droplets appear more impulse-like, but also show oscillatory behaviour; Fig. 4.12 shows the time-domain response recorded for a droplet of water dropped into a body of water. The amplitude of the signal of a water droplet impacting the water surface is smaller than for the bubble generated in water, and this is attributed to the surface tension of the water.

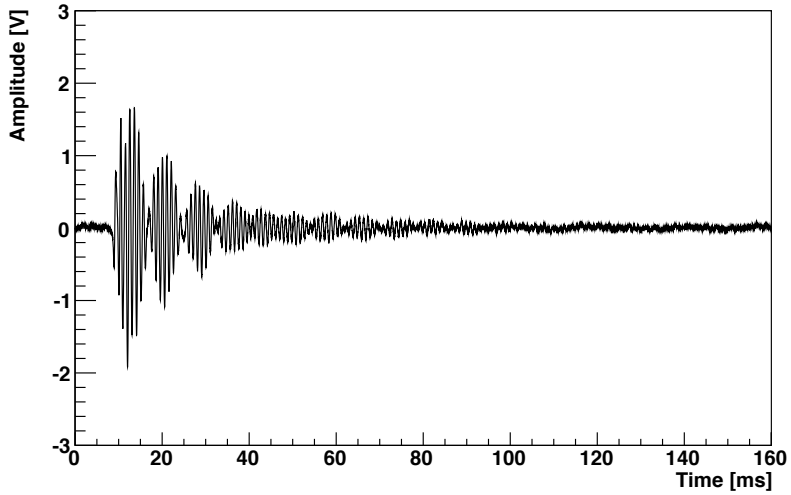


Figure 4.11: The characteristic damped oscillator shape of a bubble acoustic signal, and a secondary beat frequency.

A well-established equation is due to Minnaert [167, 168] (derivation in Appendix B), which predicts the resonance frequency f of a bubble oscillating as shown in Fig. 4.10

$$f = \frac{1}{2\pi r}\sqrt{\frac{3\gamma p}{\rho}}, \tag{44}$$

where r is the radius of the bubble, $p = P_0$ is the pressure in the medium, ρ is the density of the medium, and γ is the polytropic coefficient. For example, a bubble of radius 5 mm (for $P_0 \sim 101\,\mathrm{kPa}$, $\gamma = 1.33$, and $\rho = 3100\,\mathrm{kg\,m^{-3}}$ in LXe) has a Minnaert resonance frequency of 363 Hz. This was confirmed at the SLAC System Test: bubbles in LXe exhibit bubbling at around 350 Hz, as

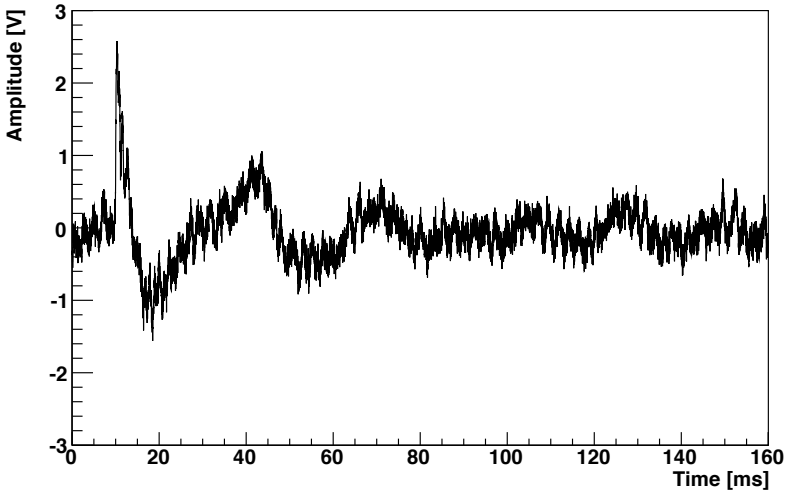


Figure 4.12: Acoustic signal for a droplet of radius $\approx$ 1 mm released from a height of 16 cm (data taken with a gain of 10). Compared to the bubble signal, the droplet signal is sharper and more impulse-like.

shown in a spectrographic view later in this chapter in Fig. 4.26[41].

To bring into this the dependence on depth, Fig. 4.13 shows the frequency for various sized bubbles as a function of the distance relative to the xenon liquid level in the LZ TPC, accounting for the density of xenon in both the liquid- and gas-phase. The maximum depth shown is 1.5 m which corresponds to the cathode level.

At the cathode level, the separation in frequency is roughly 100 Hz mm^{-1} above 200 Hz. This degree of separation is largely constant as a function of depth until about 30 cm below the liquid level. There are multiple combinations of depths and radii of bubbles that produce the same resonance frequency, Fig. 4.13 is indicative of what is to be expected at LZ.

Fig. 4.14 shows the time-domain response recorded for a tap on a metal vessel containing a body of water. The result is a very short sharp sound, which is distinct from both bubbles and droplets. The baseline takes some time to restore after the impulse.

[41] The data were verified by listening to the audio sequence.

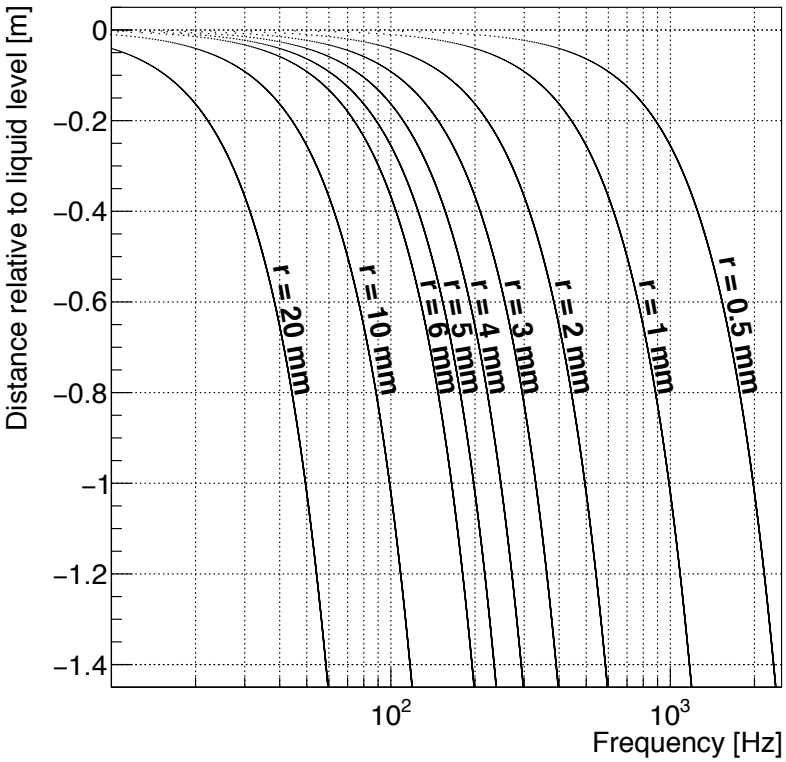


Figure 4.13: Minnaert bubble resonance frequency with distance from the liquid level for bubbles of various radii.

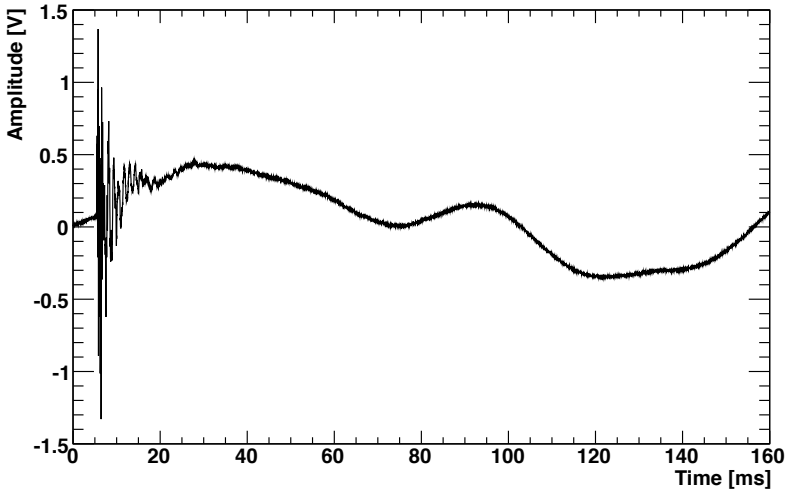


Figure 4.14: Tapping on the cryostat vessel.

Since LZ will operate with liquid xenon, the capability to detect bubbling at low temperatures was also demonstrated using liquid nitrogen, greatly surpassing the temperature conditions that will be encountered at LZ in liquid xenon. A simple experimental setup was created for acoustic experiments in liquid nitrogen (LN), as shown in Fig. 4.15. In this setup, bubbles were produced using a resistor that was pulsed using a signal generator. 10 V square pulses (duration: 130 ms) were used to heat the liquid. First order band-pass filters were used to isolate parts of the signal in various frequency bands. The time-domain representation of the raw and analysed acoustic signal are shown in Fig. 4.16. Bubble onset occurs within $\approx$ 30 ms (0.1 J) of the start of the pulse.

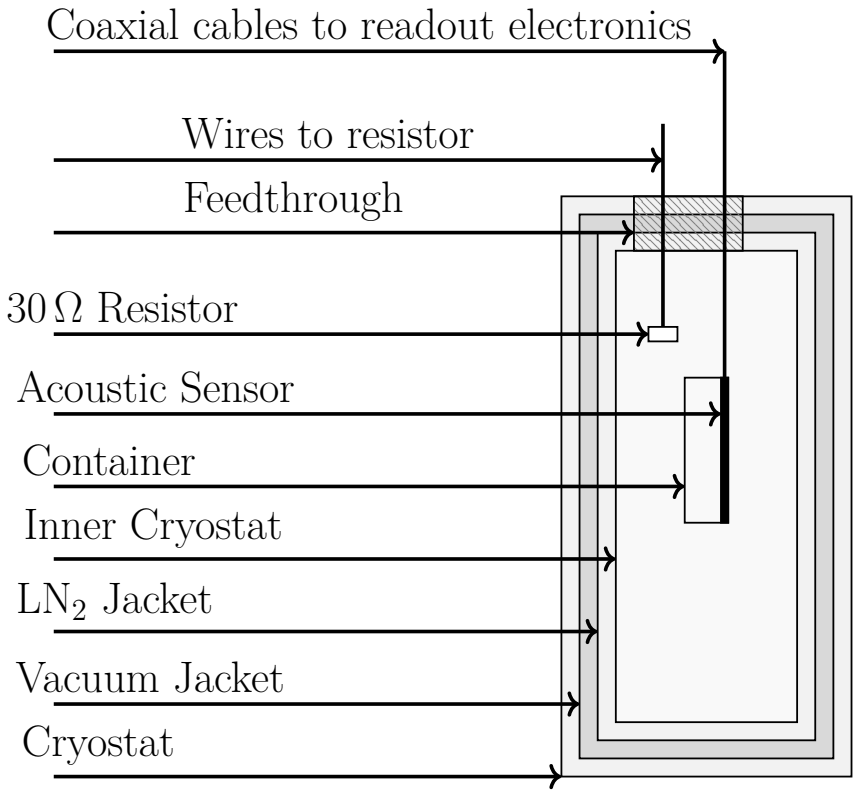


Figure 4.15: Overview of setup for producing and detecting resistor-induced bubbling at low temperatures. A repurposed ^{4}He cryostat was fitted with the full acoustic sensor readout chain. The helium reservoir was filled with LN for acoustic experiments. The liquid nitrogen jacket provides a thermal shield which reduces the boil-off of LN in the inner cryostat.

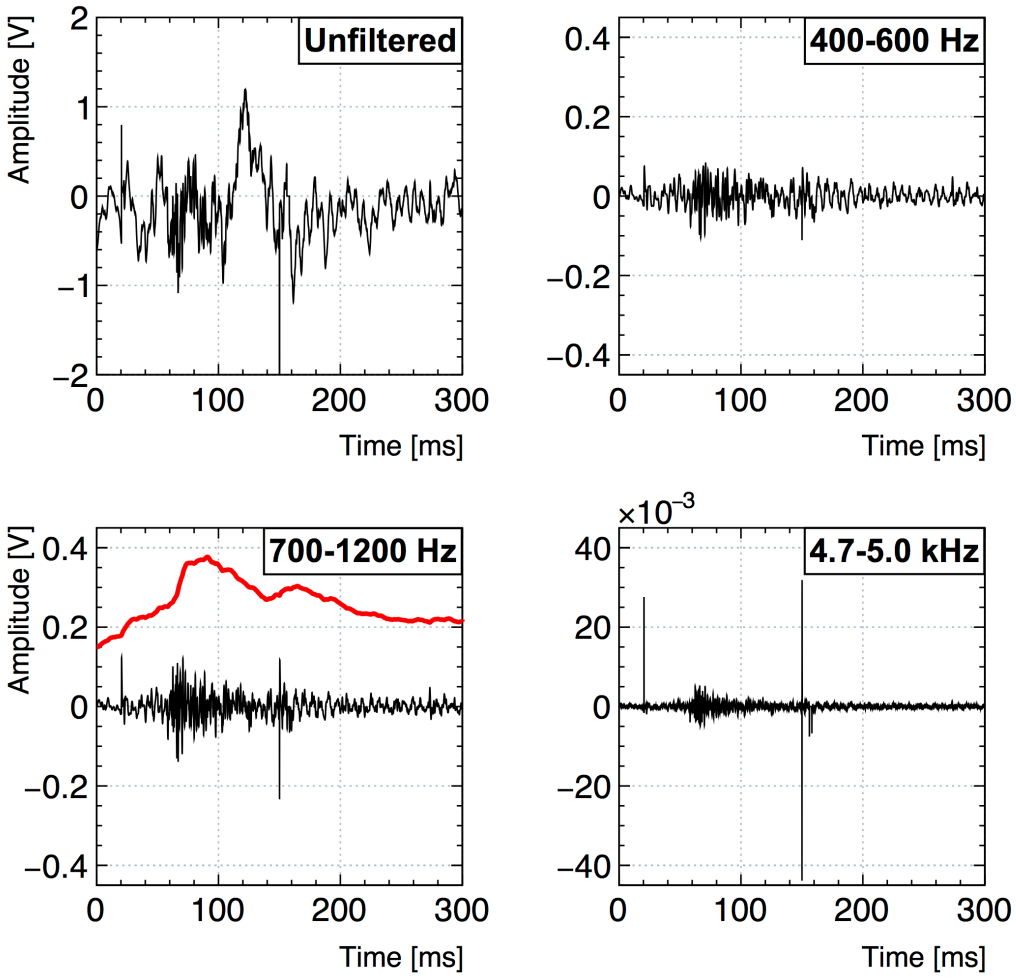


Figure 4.16: Bubbling caused by heating using a 30 Ω resistor in liquid nitrogen. Top left: Unfiltered signal, top right: application of a band-pass filter of 400 Hz–600 Hz, bottom left: a band-pass filter of 700 Hz–1200 Hz, bottom right: a band-pass filter of 4700 Hz–5000 Hz. The identification of the presence of a bubble is seen in the bottom left plot. As indicated by the red line (a smoothed RMS version of the filtered signal), the 700 Hz–1200 Hz band was selected for its discrimination ability. The red line rises above the filtered signal, demonstrating the ability to isolate the presence of a bubble using band-pass filters, and to trigger on the bubble in the time domain. The solid black vertical lines extending from the signal are remnants of crosstalk from when the resistor was pulsed.

4.4.2 Distinguishing between bubbles and droplets

Towards distinguishing the type of sound, a classification algorithm is constructed. For each recorded acoustic event, the mean values of the ratios of the normalised RMS are calculated across three frequency sub-bands (constructed from second order Butterworth band-pass filters). Then, when a new event arrives, the ratio in each sub-band is calculated and matched to the feature of the ratio it most closely agrees with.

The classification algorithm is trained by collecting data in-situ, tagging each feature by recording separate data files. Bubbles were produced with a syringe that pushes air through a tube placed at the bottom of a metal dewar of water. Droplets were released from a syringe at a fixed height of 20 cm above the liquid level[42]. A separate run of background-only data (no bubbles and no droplets) was recorded for comparison.

Fig. 4.17 suggests that bubbles can be distinguished from droplets by the ratio of the normalised[43] mean RMS across sub-band 2 (700 Hz to 1200 Hz) and sub-band 1 (400 Hz to 600 Hz), with bubbles having a relatively higher ratio as compared to the ratio for droplets (which is closer to unity). Lastly, for illustration, the third sub-band is shown at a higher interval (4700 Hz to 5000 Hz) where no strongly distinguishable characteristic frequency signal amplitude is expected to appear.

The mean μ and standard deviation σ of the distributions $\mathcal{N} \sim \left(\mu_i^j, \sigma_i^j\right)$ of each feature in each sub-band are calculated, where $i \in \{1, 2, 3\}$ denotes the frequency sub-bands, and index $j \in \{1, 2, 3\}$ denotes background, bubbles, and droplets respectively. Table 4.3 shows the distributions for each type of event for each sub-band.

[42]The radii of the bubbles and droplets were on the order of millimetres.
[43]The normalisation is for the same type of event across the three sub-bands.

Table 4.3: Reduced quantities for each sub-band (64 events for each event type, 192 events in total).

Event Type	**Band 1** (μ, σ) [400 Hz–600 Hz]	**Band 2** (μ, σ) [700 Hz–1200 Hz]	**Band 3** (μ, σ) [4700 Hz–5000 Hz]
Background	$(0.013065, 0.000538)$	$(0.011376, 0.000384)$	$(0.011661, 0.000392)$
Bubble	$(0.072619, 0.030513)$	$(0.164587, 0.071878)$	$(0.105126, 0.044708)$
Droplet	$(0.114634, 0.041421)$	$(0.112869, 0.022962)$	$(0.109282, 0.032999)$

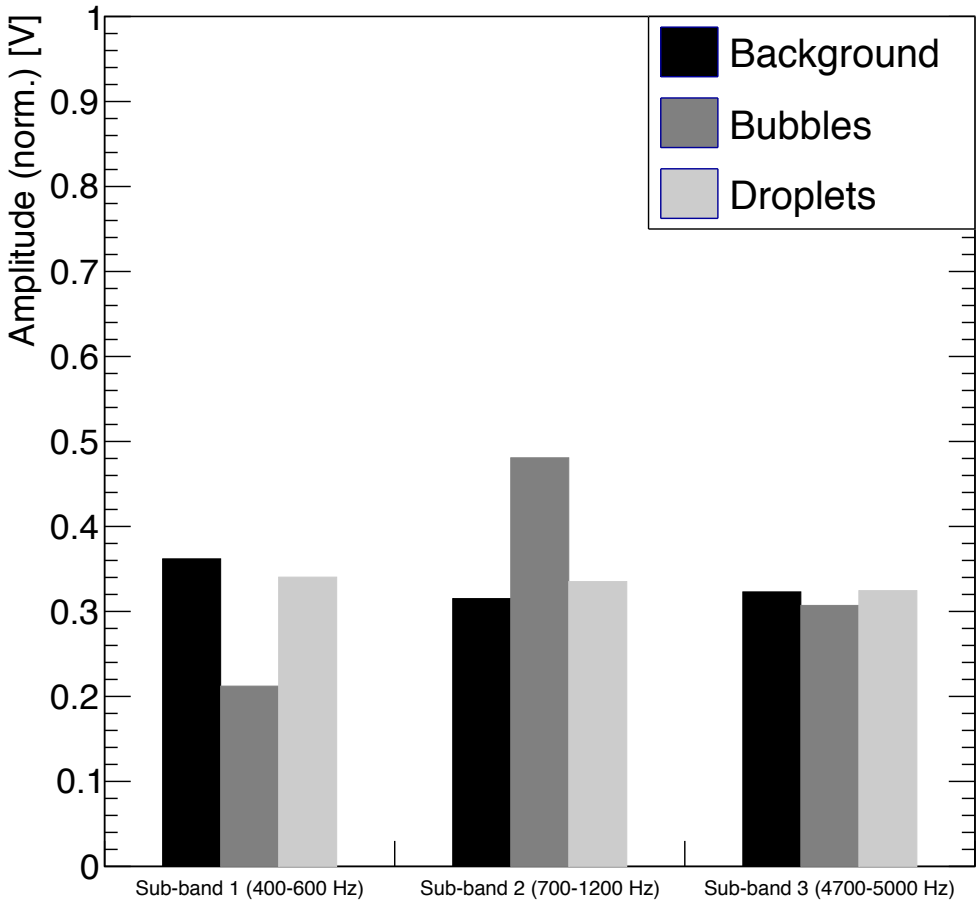


Figure 4.17: Normalised mean RMS by frequency sub-band for three sub-bands selected to reflect the presence of bubbles or droplets, versus the absence of an interesting acoustic event.

The ratio across the sub-bands distinguishes between bubbles and droplets. The parameters of interest are the ratios $F^j_{i,i'}$ of the mean values which are shown in Table 4.4.

Table 4.4: Classification ratios for each feature.

Event Type	**Parameter**	**Value** (± 1 S.E.)
Background	$F^1_{2,1} = \mu^1_2/\mu^1_1$	0.8708 ± 0.0063
Bubble	$F^2_{2,1} = \mu^2_2/\mu^2_1$	2.266 ± 0.1344
Droplet	$F^3_{2,1} = \mu^3_2/\mu^3_1$	0.985 ± 0.0516

Table 4.5 shows the success rate of the classification due to the algorithm, where each event is classified and then compared to what type of sound it actually is. Bubbles are reliably distinguished. Droplet signals have a short

Table 4.5: Sub-band truth information for acoustic classification algorithm.

Event Type	**Correctly Identified**	**Misidentified as Background, Bubble, Droplet**
Background	93.8 %	0.0 %, 0.0 %, 6.2 %
Bubble	100 %	0.0 %, 0.0 %, 0.0 %
Droplet	90.6 %	9.4 %, 0.0 %, 0.0 %

duration, and there is an overlap between $F^1_{2,1}$ and $F^3_{2,1}$, which implies that droplets are misidentified as background when fluctuations which are different across frequency sub-bands skew the event into a different classification. That some droplet events are classified as background is obviated by using an adaptive trigger, as in Fig. 4.9 (see page 93), to detect signals which are departures from the background noise.

4.5 Detecting Pump Noise

A number of (cryogenic) pumps will operate at LZ for xenon circulation, maintaining vacuum, and circulating air in the experimental hall in the mine. They cannot be switched off, and there is a risk that vibrational noise will interfere with the acoustic environment at LZ, forming an irreducible source of acoustic background for the acoustic sensors. In the worst-case scenario, pump noise can cause the TPC to vibrate and disturb the liquid surface. It is important that the acoustic sensors can still fulfil the purpose of bubble detection in the presence of such a background. This was tested and confirmed using a mock setup, as shown in Fig. 4.18, with a motor in mechanical contact with a vessel filled with water.

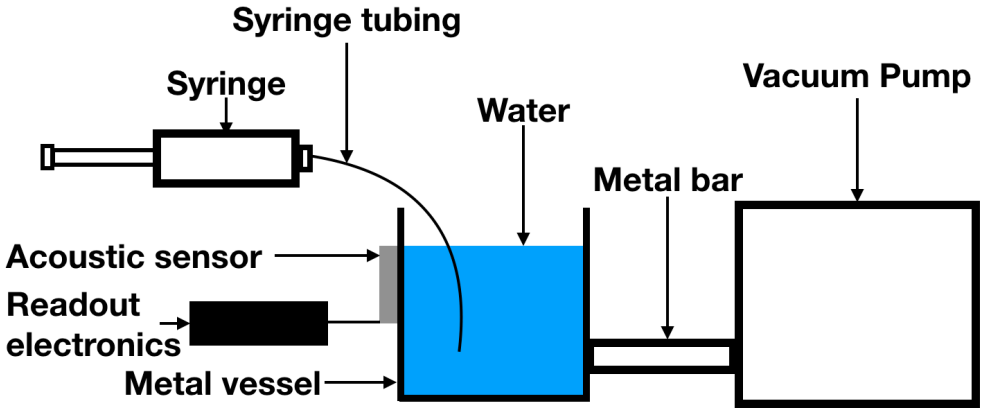


Figure 4.18: Apparatus setup showing the BC.2511/12 pump, syringe, metal bar, and sensor setup. The pump can be switched on and off, and the vibrations that it produces while it is on are transferred to the metal vessel via a metal bar.

In lieu of an actual cryocooler, the acoustic noise of a vacuum pump BC.2511/12 in a test setup at room temperature has been monitored. A single acoustic sensor unit was attached opposite to the side where the metal bar was in contact with the vessel. The vessel was then filled with water to match the level of the sensor.

Bubbles were produced inside the liquid by using a syringe attached to a plastic tube submerged in the liquid. It was observed that the amplitude of the

acoustic baseline signal due to the effect of pump noise was somewhat reduced after the vessel was filled, in contrast to when it was empty; indicating the liquid attenuates vibrations in the vessel. Fig. 4.19 shows the raw and analysed data after application of various band-pass filters, each with a bandwidth of 700 Hz.

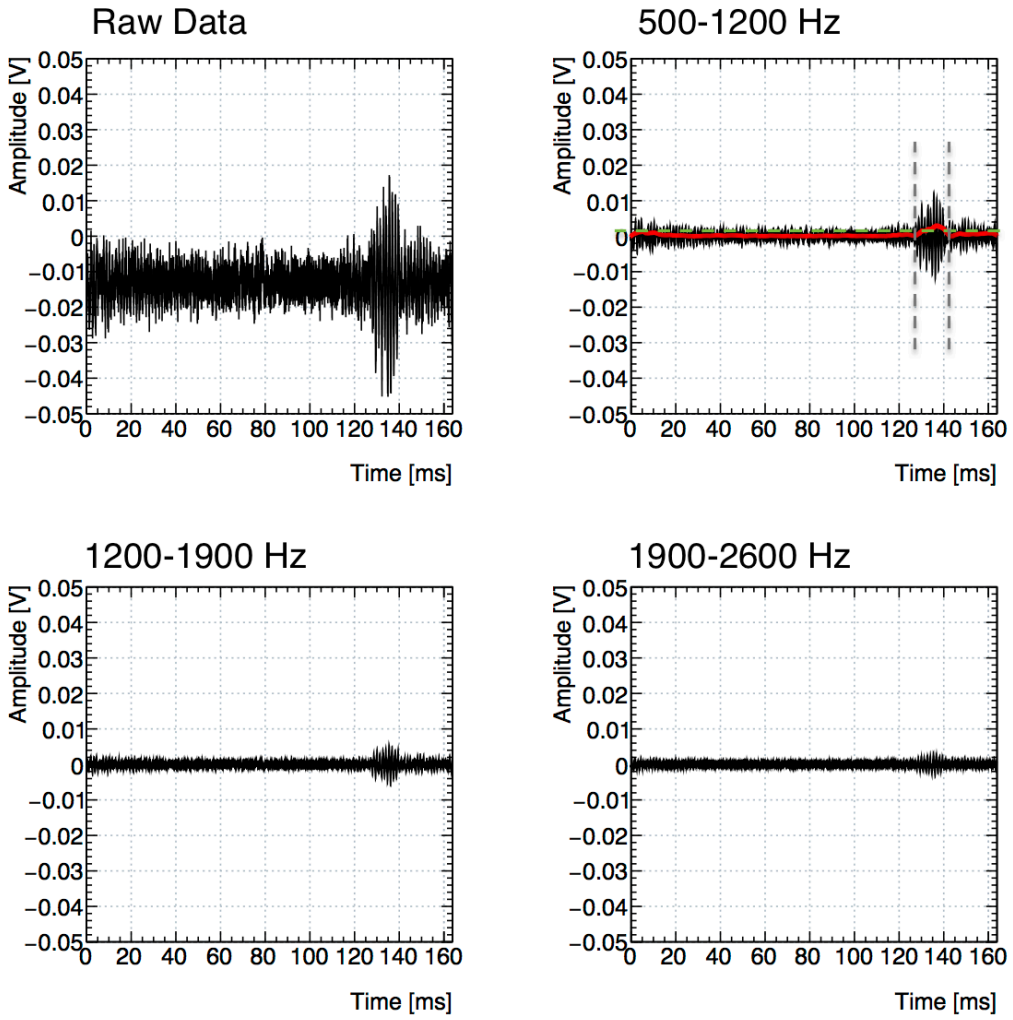


Figure 4.19: Measured and analysed acoustic signal from bubble production in a water-filled metal vessel under the influence of vibrational pump noise. The plot in the top right shows vertical dashed lines to indicate the main component of the onset and decay of the bubble signal.

By inspecting the difference in amplitude of the induced bubble acoustic signal and the baseline acoustic signal for various bandwidths, the 500 Hz to 1200 Hz band (top-right) was found to correspond to a suitable range for the detection of bubble production. The signal-to-noise ratio decreases in higher frequency bands, as is indicated by the drop in overall amplitude in the plots on the bottom left and right (drawn on the same scale), respectively.

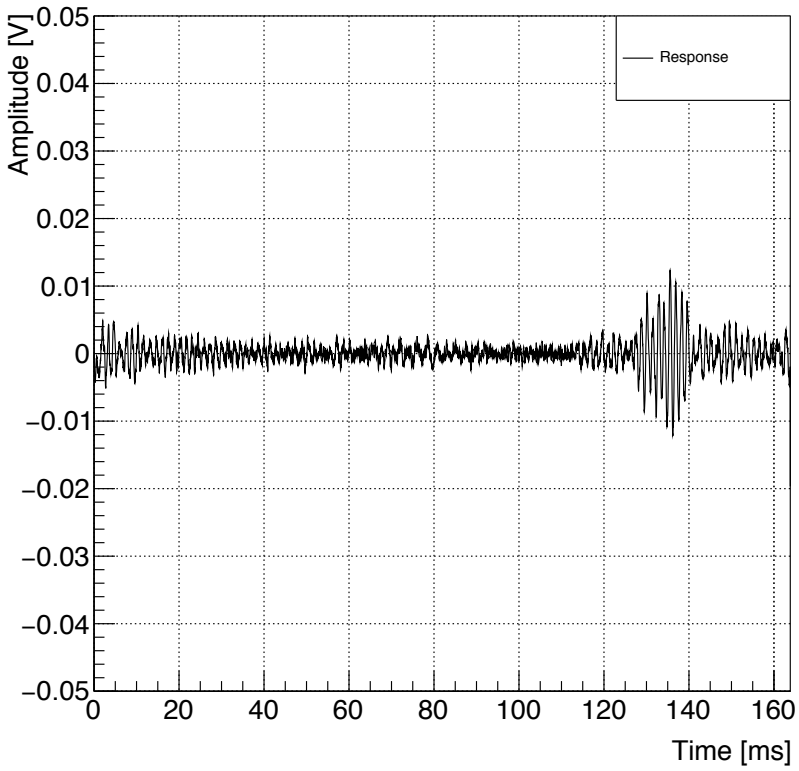


Figure 4.20: Closeup of the same 500 Hz to 1200 Hz filtered signal as was shown in Fig. 4.19.

Further application of a modulus, simple moving average, and smoothing with a 10 Hz to 50 Hz band-pass filter, followed by another application of the modulus, was found to improve the resolution of the onset and decay of the bubble acoustic signal. This method was effective at distinguishing between signal and background in the aforementioned 500 Hz to 1200 Hz band, where the analysis is shown as a solid red line, superimposed above the aforementioned filtered signal. Closeups of this filtered signal and subsequent analysed signal are shown in Fig. 4.20 and Fig. 4.21, respectively.

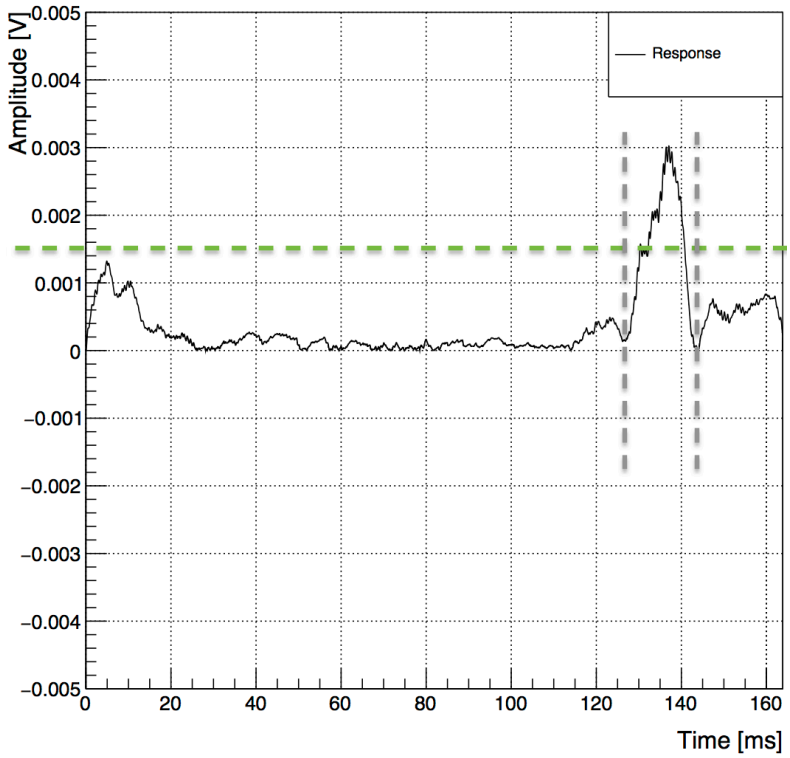


Figure 4.21: Closeup of the analysed waveform of the same 500 Hz to 1200 Hz band-pass filtered signal as shown in Fig. 4.20.

This algorithmic discrimination allows one to set a threshold value for amplitude triggering, as is indicated by the dashed horizontal green line which sits above the quieter baseline analysed signal and triggers on the rise. The dashed grey vertical lines indicate, to first order, the main component of the bubble oscillation, which is followed by a smaller tail.

The FFT plots of the measured acoustic baseline signal in the absence of bubble production are shown for the case of the pump being off/on in Fig. 4.22 and Fig. 4.23, respectively. Since there is a degree of overlap in bandwidth at lower frequencies, the presence of pump noise due to metal contact can be distinguished by the presence of 1 kHz to 10 kHz excesses. Despite the presence of the pump noise which becomes more noticeable in the 1 kHz to 10 kHz band, the amplitude of the bubble is noticeable predominantly in the 500 Hz to 1200 Hz frequency band (top right plot in Fig. 4.19), diminishing considerably at higher frequency bands (bottom left and bottom right plot).

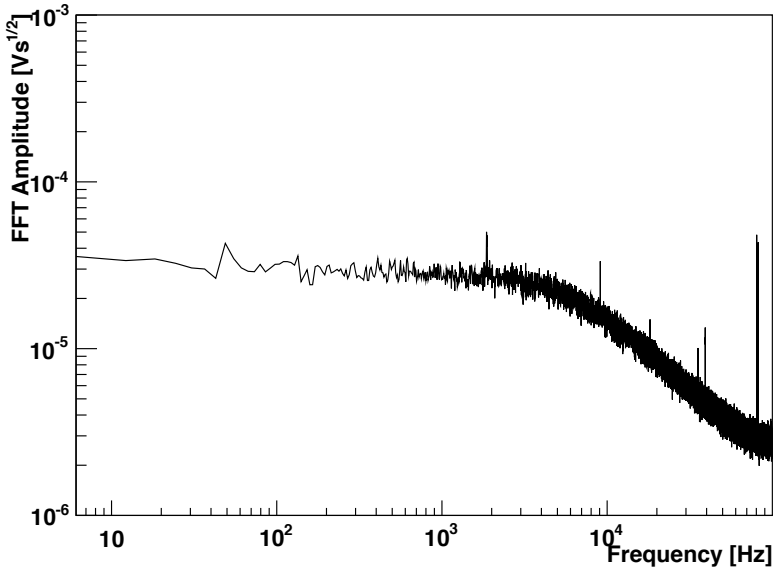


Figure 4.22: FFT of measured acoustic baseline signal with the pump off.

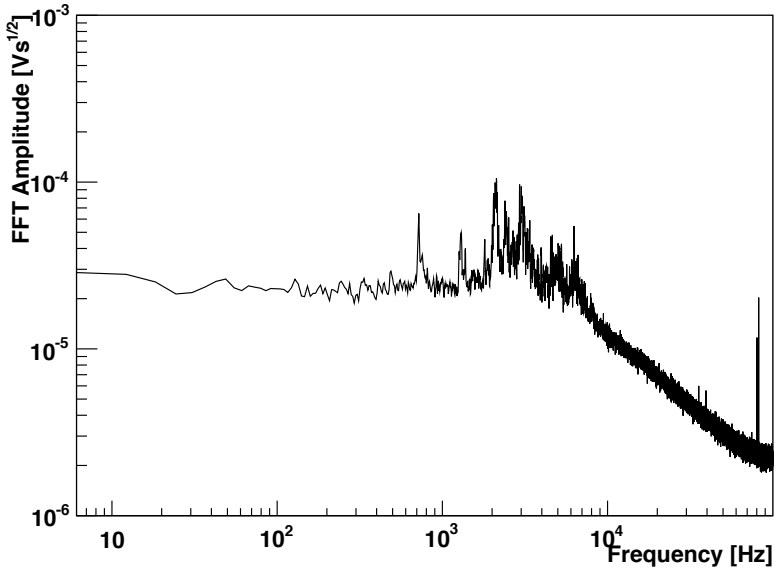


Figure 4.23: FFT of measured acoustic baseline signal with the pump on.

Thus, for lower amplitude signals, bubbles must be identified through their lower frequency components. Having the ability to acoustically measure the presence of a bubble with pump noise in the background, however, does not reduce the importance of mitigating against this source of sound.

4.6 SLAC System Test

The SLAC System Test is a smaller version of the full-scale LZ experiment. It provides a convenient way to test and prototype how the LZ detector will operate and be monitored. Its purpose is to test the various subsystems that will operate at full-scale real LZ.

All systems operate in a very similar manner to LZ. For instance, the experiment runs with LXe and performs active circulation of the liquid through the TPC. The amount of xenon circulating in the System Test is comparable, though less than, the former LUX experiment (145 kg). The TPC is a scaled-down version of the LZ TPC. The purification system closely resembles the one that will be used in LZ.

Testing acoustic sensors in the System Test is an important part of the readiness of the sensors and the LZ analysis software. To that end, the actual acoustic sensors for LZ are fitted and operated in a xenon environment at the System Test. Acoustic sensors fit into the System Test very similarly to how they will be installed in real LZ. Shown in Fig. 4.24 is the System Test TPC with the inner cryostat vessel removed so that the TPC is visible.

The sensors are epoxied onto the exterior surface of the inner cryostat vessel of the System Test (Fig. 4.25), commensurate with the liquid level (anode level) and at the cathode level at the top and bottom of the TPC respectively. The setup depicted provides the closest equivalent to LZ, and the sensors are in the same positions as where they will be installed in LZ.



Figure 4.24: The System Test TPC, exposed without the inner cryostat vessel. The white cylinder is the TPC (made out of PTFE), and a number of xenon-space monitoring sensors. The distance from the floor to the top of the TPC is approximately 2 m. Image credit to the LZ Collaboration, with modifications for illustration purposes.

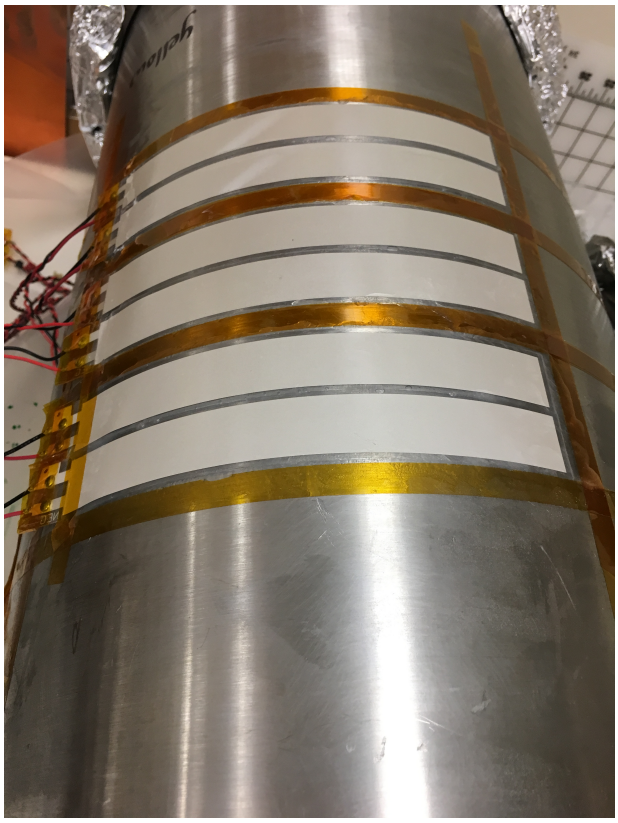


Figure 4.25: Acoustic sensors epoxied to the inner cryostat vessel with Master Bond® EP29LPSP epoxy at the SLAC System Test. Three sensors were instrumented on the side of the vessel that is shown in this figure. Further sensors were epoxied on the other side of the vessel to provide radial coverage of the TPC. Kapton tape is used as a guideline during epoxying, mostly to reduce the flow of epoxy owing to the smaller circumference of the System Test vessel.

The System Test enables testing analysis routines in a more realistic setting, such as identifying bubbles in LXe amid the noise of pumps that cool and circulate LXe. A first order identification of features was facilitated by a spectrographic view of acoustic data, shown in Fig. 4.26. These data were taken while the main vessel was partially filled with LXe. During filling, liquid is pushing the remaining gas out of the system. This can be confirmed by examining an audio sample of the raw waveform, or equivalently by examining the spectrogram.

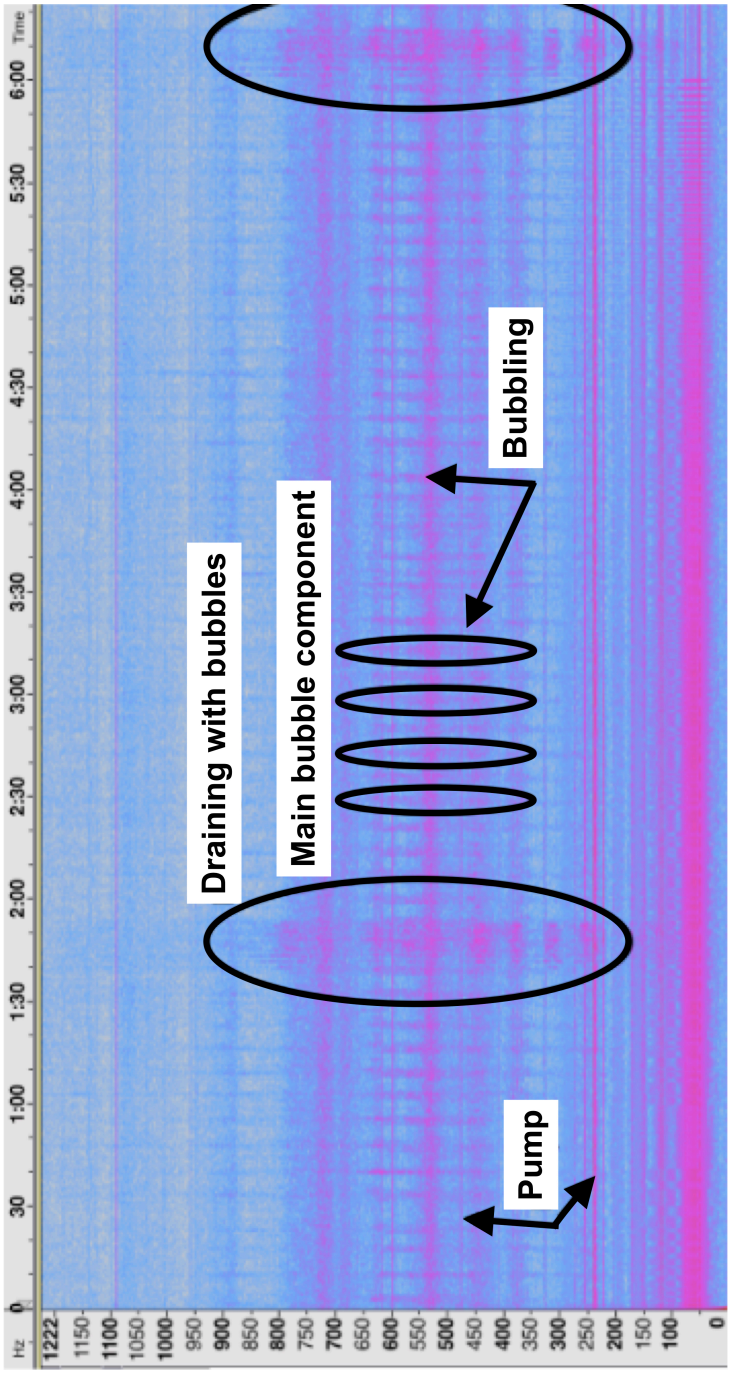


Figure 4.26: Spectrogram view of time-series data collected at the LZ System Test at SLAC. The abscissa shows the time in minutes, the ordinate shows frequency in hertz, and the colour shows the relative intensity. Numerous additional sources of noise appear in the data at lower and higher frequencies. These are attributed to pumps in the vicinity of the cryostat, which cause the platform from which the cryostat is suspended to vibrate.

An algorithmic method of bubble detection was developed to mitigate against additional noise in the acoustic data due to the environment at the System Test. It has been tested at the System Test and shown to work robustly. Isolation of the bubble feature was achieved by applying band-pass filters to each event, followed by calculating the logarithm of the ratio of the RMS of each event to the moving average of the previous 100 events

$$p_i = \log\left(\left(\sqrt{\frac{1}{N}\sum_{i=1}^{i=N} x_i}\right)/MVAV_i\right) \tag{45}$$

The identified acoustic events are then expressed as a z-score

$$z_i = \frac{p_i - \mu}{\sigma}. \tag{46}$$

The result of the application of this method to data taken at the System Test is demonstrated in Fig. 4.27, where the correct identification of exactly 4 bubble events from 11 489 background events is shown. The horizontal axis is the time of day, over a period of acoustic data acquisition of about 20 min. The vertical axis is the number of standard deviations σ away from the mean μ. The small data points are background-like events (which did not pass the cut). For presentation purposes, the bubble events are shown as large data points. A trigger can be set at 3.5 standard deviations above the mean.

In order to gain statistical insight into what a higher rate of bubbling looks like, data taken during a high rate of bubbling are compared to a quiet period using Eq. (46), and are shown in Fig. 4.28. To quantify the probability of the successful identification of a bubble, an hypothesis test is constructed

$$\boldsymbol{H} = \begin{cases} \boldsymbol{H}_0 & \text{There is no bubble.} \\ \boldsymbol{H}_1 & \text{There is a bubble.} \end{cases} \tag{47}$$

The significance level of the hypothesis test is set to $\alpha = 0.01$ so that the

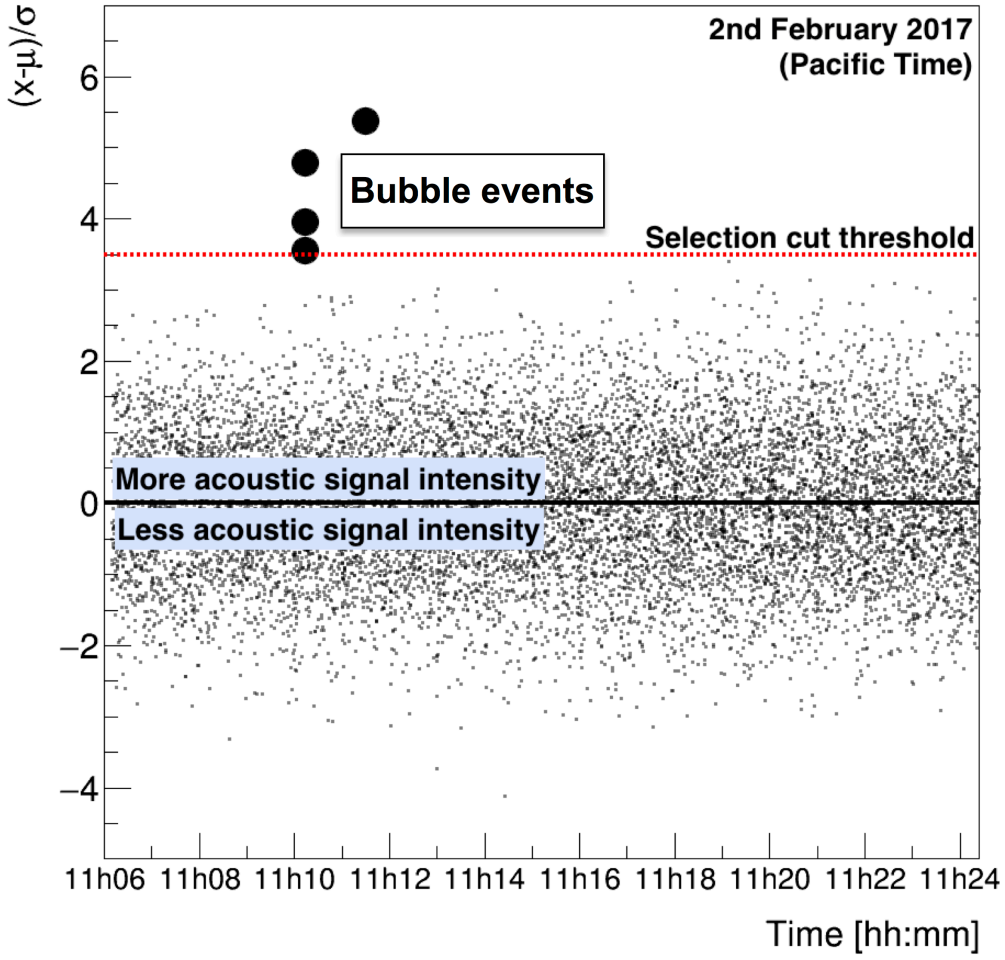


Figure 4.27: Algorithmic bubble detection at the SLAC LZ System Test.

confidence level is 99 % and the probability of making a Type I error (which is α) - that is identifying a bubble when there is no bubble - is 1 %.
The probability of a Type II error, that is failing to identify a bubble when there is a bubble, is β. The power of the test is the probability of correctly identifying a bubble when there is a bubble: $P = 1 - \beta$.

Eq. (45) is applied to 27 878 events taken at the System Test, corresponding to the background events and the bubble events which are identified by the green (left) and red (right) distributions. The area of the region belonging to the background distribution that is to the right of the critical value is the probability of a Type I error, and is calculated from the samples which represent background events. The area of the region belonging to the bubble distribution that is to the left of the critical value z_{crit} is the probability of

a Type II error, and is calculated from the samples which represent bubble events. The result of the test is that $\alpha = 1\,\%, \beta = 1\,\%, P = 99\,\%$. By construction, the null hypothesis will be correctly accepted 99 % of the time. The alternative hypothesis will be correctly accepted 99 % of the time.

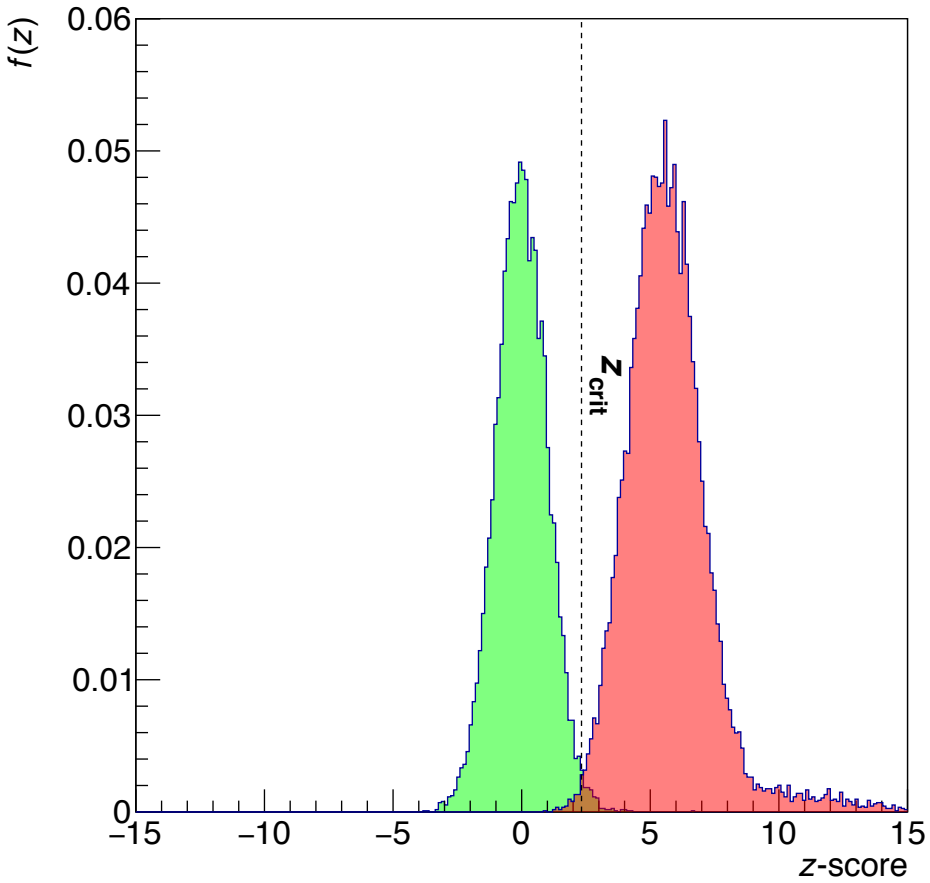


Figure 4.28: Hypothesis test for bubble identification with the background population (distribution on the left) and bubble population (distribution on the right) shown. The critical value z_{crit} corresponds to a significance level of $\alpha = 0.01$. The region belonging to the background distribution that is to the right of z_{crit} corresponds to the probability of a Type I error, while the region belonging to the bubble distribution that is to the left of z_{crit} corresponds to the probability of a Type II error.

Tap detection at the System Test is demonstrated in Fig. 4.29, and the FFT averaging over many taps is shown in Fig. 4.30. There is a vacuum between the inner cryostat vessel (on the outside surface of which are the acoustic sensors) and the exterior cryostat vessel. Therefore, although the event is still impulse-like, the detection of this sound is indirect, since it propagates through several contact points of vessels before causing the inner cryostat vessel to resonate, thereby prolonging its duration. The frequency spectrum is used to identify the features of a tap. There is a marked increase in the frequency range of 500 Hz to 1000 Hz, which enable taps to be identified by selecting higher frequency bands such as 800 Hz to 1000 Hz, as compared to bubbling in the 500 Hz to 550 Hz band. In the time domain, the increase at 150 ms corresponds to the tap, followed by a quick return to the baseline as can be compared before and after the event.

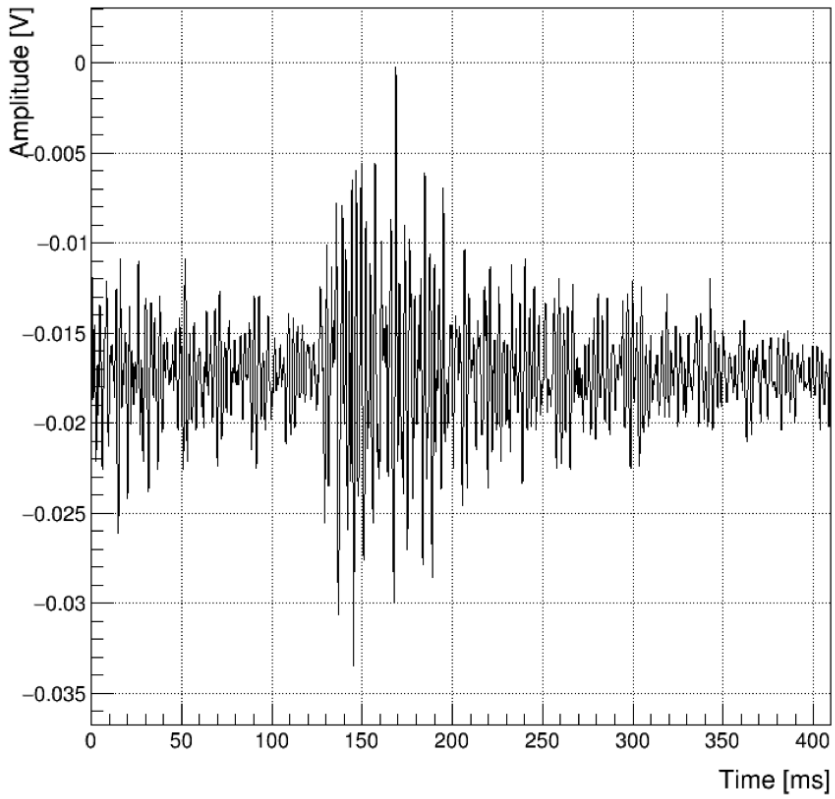


Figure 4.29: Time domain representation of a single tap event on the exterior of the main vessel at the SLAC System Test.

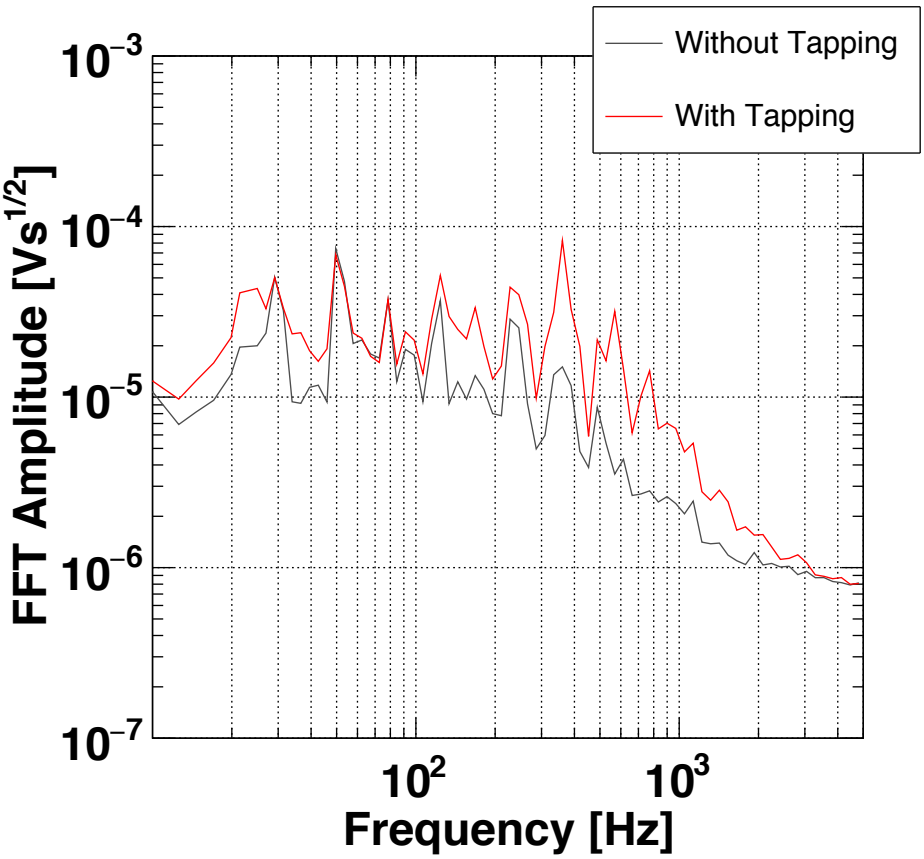


Figure 4.30: After averaging over several taps, the FFT representation shows a wide frequency range over which the intensity is higher than when there are no taps.

Table 4.6: Characteristic frequencies of key acoustic event topologies. The observed frequency bands are based on tests carried out in Oxford and at the SLAC System Test which closely mimics the environment of LZ.

Event Type	**Typical Frequency Band** [Hz]
Tap on outer vessel	1000
Bubbling	500-550
Draining + Bubbling	300-330, 400-460, 550-600
Pump at System Test	Resonance at 240 + harmonics

The acoustic sensor performance has been quantified using data taken in a liquid xenon experiment that closely resembles LZ. A selection of different types of acoustic events has been measured, characterised, and analysed. Several key sources of sounds that were identified in the System Test are summarised in Table 4.6. The acoustic sensors form part of the LZ slow-control system, which will continuously provide diagnostic information about the state of the detector. The analysis algorithms developed in this chapter demonstrate reliable detection of bubbling, and 90 % correct identification of bubbles in a noisy environment; enabling the experiment to identify acoustic features automatically as part of the diagnostic data during LZ operations.

5 Detector Electronics Response Model

Towards achieving event reconstruction fidelity at LZ, and in preparation for real data taking, the detector design should be verified with simulations of the detector response and the development of analysis algorithms based on simulated data. To support this effort, the data acquisition electronics must be implemented in a software simulation. My contribution was to develop from scratch the Detector Electronics Response (DER) model[44], a newly developed simulation package specifically designed to create simulated data that would be produced by the LZ readout electronics when it acquires event data. It simulates the complete front-end electronics, from photon hits on PMTs through to amplifiers and digitisation, accounting for the interconnecting cabling, and provides simulated DAQ output in the same format as the real LZ DAQ and the Event Builder system (which produces event files from the DAQ).

For an experiment the scale of LZ, and given the high cost of the DAQ, it is worth understanding the front-end electronics analytically, both to verify the design and to understand the single photoelectron response of the detector. While generic simulations of electronics and single waveforms are achievable through existing means, such as SPICE[45], this is generally inadequate for Monte Carlo simulations of full event data, where high data throughput and processing speeds are required. Generating single waveform pulses in SPICE takes a considerable amount of time (on the order of 30 s per waveform), whereas for the purposes of LZ hundreds of millions of waveforms must be simulated. Also, SPICE and its ilk do not offer the same level of customisability within a wider software framework that is needed for LZ simulations. For example, it cannot trivially be made compatible with LZ detector simulations of recoil events, nor embedded into a wider simulation framework.

[44] The Usage Guide can be found online (`http://teacher.pas.rochester.edu:8080/wiki/pub/Lz/DetectorElectronicsResponse/UsageGuide.pdf`).

[45] Simulation Program with Integrated Circuit Emphasis (SPICE) is a program used to simulate electronics in great detail and offers flexibility as an engineering tool in designing circuits.

The input to the DER is simulated photon arrival times on PMTs, that come from BACCARAT[46] (a software package built on GEANT4[47]), which simulates particle physics processes in and around the LZ detector by tracking energy depositions of particles in matter through detector volumes. The DER is geared towards BACCARAT simulation data[48], and supports the same output data structures and file formats as the LZ DAQ and Event Builder (EB) format. The DER is integrated into the collaboration's larger software framework, and it is used for large scale production of simulated datasets, on the order of several hundred terabytes, that represent many months worth of data in real LZ. The DER constitutes a major part of simulating the full chain of detector physics.

It is a requirement that LZ develops analysis tools in advance of real data-taking. The DER makes it possible to produce simulated physics events that are anticipated at LZ. This enables quantifying detector parameters, to ensure the data acquisition systems are optimal, and to test event data processing rates. Furthermore, the DER facilitates developing analysis tools and algorithms that will be used on real data, in advance of commissioning and the start of data taking. DER data can be passed to the LZ event display that will be used to inspect realtime data from the DAQ; enabling the collaboration to meaningfully use the event display tools in analyses with simulated data.

5.1 Overview of the LUX-ZEPLIN Detector Electronics Response Simulation Framework

BACCARAT produces simulated physics events by calculating particle interactions and particle propagation in and around the LZ experiment in detail. In particular, the simulation includes the TPC and LXe physics, the skin and the outer detector system, all PMTs, and many of the supporting structures

[46] Basically A Component-Centric Analog Response to AnyThing (BACCARAT).
[47] GEometry ANd Tracking (GEANT4).
[48] The DER can be readily adapted to provide interfaces to other photon simulation packages apart from BACCARAT or GEANT4.

such as the cryostat of the detector. BACCARAT data are passed to the DER, and the DER uses this to simulate the detector event data.

Shown in Fig. 5.1 is an overview of key software. BACCARAT is responsible for propagating particles through the detector. DER uses the photon hits on PMT photocathodes to process the PMT signal, followed by the analogue electronics, and DAQ response. Along with Monte Carlo truth information produced by BACCARAT, DER provides the detector response output to the LZ analysis program (LZap). LZap is the software analysis package that processes simulated and real detector data. DER is a pivot point in the simulation chain between BACCARAT and LZap.

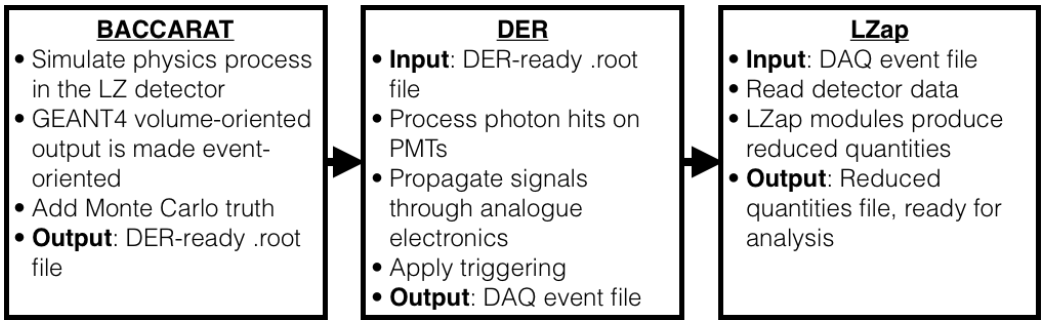


Figure 5.1: Flow-diagram showing an overview of the key software packages used for LZ Monte Carlo simulations and data analysis.

The DER matches the real data format, so that LZap processes the input it receives from simulations and real data in the same way. The utility of the software toolchain of BACCARAT, DER, and LZap, is to study the different event types that are anticipated to be seen at LZ, ensuring that the detector response and analysis are optimal and ready. Accurate simulations of the detector electronics response are necessary for the development of the analysis algorithms in LZap. Many hundreds of terabytes of simulated data have been produced by the DER and analysed through LZap, during collaboration-wide large scale mock data challenges that prepare the collaboration for data analysis when LZ starts taking real data.

5.1.1 Compatibility

LZ uses massively parallel systems at production centres such as PDSF[49] for the US Data Centre (USDC) and GridPP for the UK Data Centre (UKDC), which run many jobs simultaneously. The DER simulation runs interactively or on batch systems, the default settings require no user intervention, and settings can be customised in a terminal before submitting jobs. All DER simulations are self-described, with detailed information on how and where each simulation was run.[50]

The DER simulated detector data output files comply with two key LZ interface control documents.[51] These interfaces concern the event format (raw DAQ binary format and EB root format), and the numbering of the PMT channels. A single LZap module based on these interfaces is used to retrieve data from the DER output ROOT files in the same way as expected from real data[52]. Strictly enforcing that the DER conforms with the specification for the actual DAQ data achieves simulated data sets that can be interacted with in exactly the same way as real data.

5.2 Physics Modules

The DER physics modules are provisioned through C++ classes that enable selecting and modifying the simulation parameters and output format[53] of the simulation without requiring a recompilation of computer code. A class diagram of the devices implemented in the DER is shown in Fig. 5.2.

The modules contain implementations for all of the PMT types that will be

[49] PDSF is a computer cluster operated at the National Energy Research Scientific Computing Center (NERSC) at Lawrence Berkeley National Laboratory (LBNL).

[50] At the time of writing, the DER can also be run on non-production environments such as OS X and macOS operating system software, and numerous flavours of Linux®. OS X is a trademark of Apple Inc., registered in the U.S. and other countries. macOS is a trademark of Apple Inc., registered in the U.S. and other countries. The DER is an independent software and has not been authorized, sponsored, or otherwise approved by Apple Inc. Linux® is the registered trademark of Linus Torvalds in the U.S. and other countries.

[51] LZ-ICD-08-0007 and LZ-ICD-08-0008.

[52] It is located in the internal LZ Git repository in a raw data module.

[53] The detector output data classes represent either the raw DAQ (binary) format, or the Event Builder (ROOT) format, as well as Monte Carlo truth.

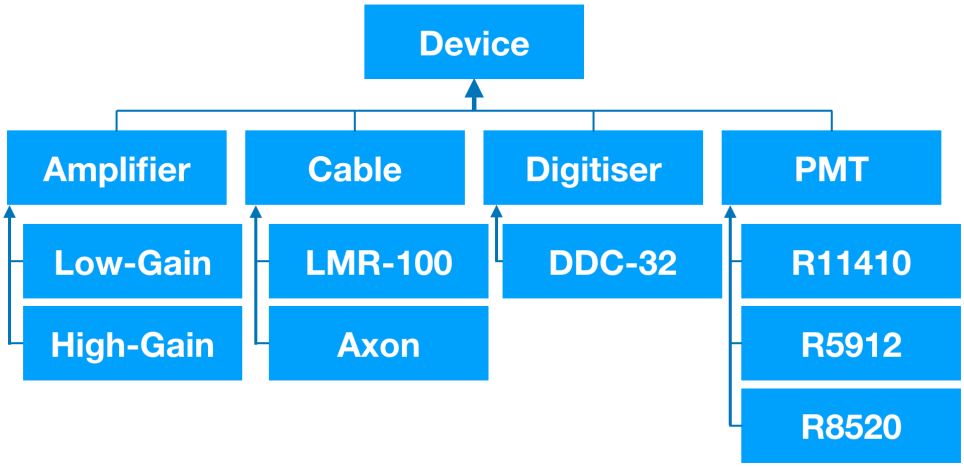


Figure 5.2: Class hierarchy diagram showing the organisation of the physics modules. The photons are processed by the appropriate PMT module, R11410 for the TPC PMTs, and the others for the Skin and Outer detector. The Axon cable passes the PMT signal to the amplifier board. The LMR-100 cable passes the signal from the amplifier to the DDC-32 digitiser board.

used in LZ; the PMT properties such as the gain, quantum efficiency, and single versus double photoelectron fraction can be individually adjusted through configuration files that incorporate measured data. Similarly, implementations exist for numerous iterations of the design of the amplifier boards and interconnecting cabling. The device modules are incorporated and connected through signal chain modules; which propagate signals through the device modules and the trigger before being packaged as detector output data which are written to disk.

Starting from photons incident on PMTs, the PMT response propagates through the PMT cabling into the amplifier and then the digitiser. In the following sections, the focus is on the components of the analogue signal chain of the TPC readout system[54].

[54]The reader may find it convenient to refer back to the section on low-pass filters and high-pass filters on page 80 in Chapter 4.

5.3 PMT Response

Internally, a PMT consists of a series of dynodes, with a potential difference between each stage. When a single photon is incident on the PMT photocathode, there is a probability that it will liberate at least one photoelectron from the photocathode. This probability is generally referred to as the PDE of the PMT, which for LZ PMTs is typically in the region of 25 % to 30 %. The photoelectron that is liberated produces a cascade of electrons through the dynode chain inside the PMT, resulting in a total approximate number of electrons at the end of the dynode chain that is proportional to the nominal quoted gain of the PMT.

The total charge Q that is developed by the dynodes is the integrated current at the PMT stage

$$Q = Ne = (3.5 \times 10^6) \times (1.602 \times 10^{-19}\,\mathrm{A\,s}) \approx 0.56\,\mathrm{pA\,s}, \tag{48}$$

where N is the number of electrons produced in the PMT dynode chain, assuming a nominal gain of 3.5×10^6 (the nominal gain for the Hamamatsu R11410 PMTs that will be operated at LZ) and e is the electron charge. Therefore

$$1\,\mathrm{phe} \approx 0.56\,\mathrm{pA\,s}. \tag{49}$$

The PMT base and cable termination are both 50 Ω, shown in Fig. 5.3. At 50 Ω termination at both ends, the total resistance adds in parallel to give 25 Ω total impedance. Therefore, there is approximately 14 pV s output from the PMT at 3.5×10^6 nominal PMT gain. The equivalent circuit for the lumped PMT + base system with cable is shown in Fig. 5.4. From Fig. 5.4, the transfer function is [170]

$$v(t) = \frac{NeG \cdot R}{\tau - \tau'} \left(\exp\left(-t/\tau'\right) - \exp\left(-t/\tau\right) \right), \tag{50}$$

where τ, τ' are the time constants that determine the rise- and fall-time re-

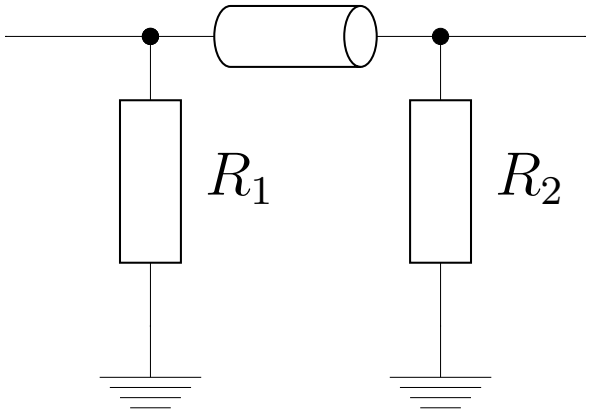


Figure 5.3: Schematic of PMT base cable (represented as a cylinder) termination from the PMT into the amplifier. $R_1, R_2 = 50\,\Omega$, $R_{\text{total}} = 25\,\Omega$.

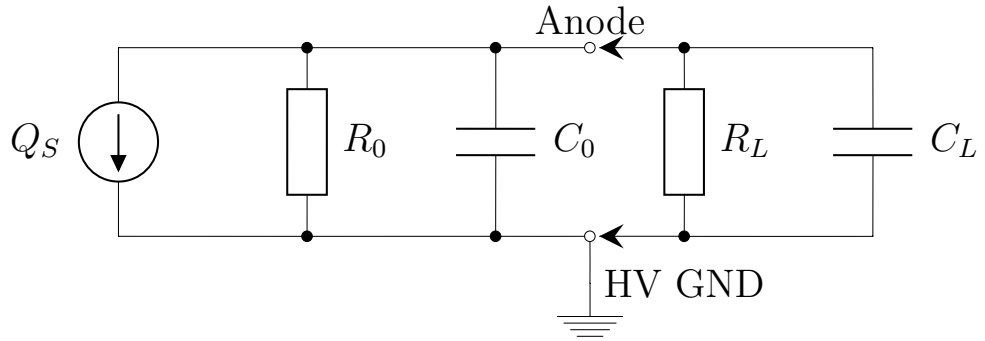


Figure 5.4: Equivalent circuit for the PMT + PMT base system where R_0, R_L (C_0, C_L) are the output and load resistance (capacitance), respectively (image redrawn from [169]).

spectively, the PMT gain is G, and where

$$R = \frac{R_0 R_L}{R_0 + R_L}, C = C_0 + C_L, \tag{51}$$

which define $\tau = RC$ as indicated in Fig. 5.4, where R_0, C_0 and R_L, C_L are the output and load resistances and capacitances, respectively.

As an example, for $N = 1, e \sim 1.602 \times 10^{-19}\,\text{C}$, $G = 3.5 \times 10^6$, $\tau = 3.81\,\text{ns}, \tau' = 4.76\,\text{ns}$, and $R \sim 50\,\Omega$, a voltage of 1 mV [169] is nominal. The rise- and fall-time produced with these parameters are 2.46 ns and 14.44 ns respectively, compared to the literature values of 2.6 ns and 9.7 ns [171]. This is a first-order approximation PMT response but does not affect the total area gain of

the signal due to the shaping of the signal at the amplifier stage. Fig. 5.5 shows a sampled PMT pulse, illustrating the functional form of Eq. (50) for the case of 1 phe.

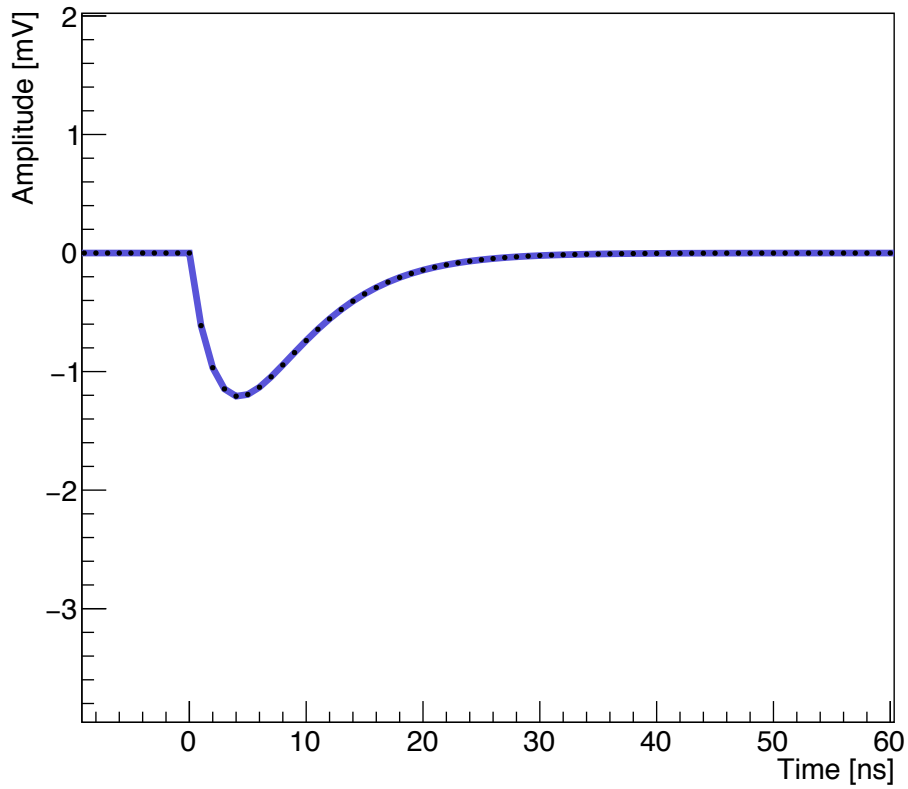


Figure 5.5: Example simulated PMT pulse with $(10-90\%)$ rise and fall times of 2.46 ns and 14.44 ns respectively. As predicted by the equivalent circuit of the PMT+PMT base system, the signal amplitude is on the order of 1 mV.

The digitisation sampling interval is 10 ns. Thus, due to the short rise time of the PMT single photoelectron response, the PMT signal must undergo active shaping and amplification in the front-end analogue electronics, which increases the duration of the signal (this will be shown in subsequent sections). Therefore, after amplification, the resulting waveform will be much longer than the sampling interval, and there is no concern that the short rise time of the PMT leads to missing a PMT signal.

The PMT response module is based on the photon arrival times on the PMT photocathode, to within a resolution of 1 ns. The model produces PMT response waveforms for each PMT. The PMT PDE determines the probability that a photon produces a signal

$$PDE = CE \times QE, \tag{52}$$

where CE is the Collection Efficiency and QE is the quantum efficiency (QE). Nominal values for LZ Hamamatsu R11410 PMTs are $CE = 0.90, QE = 0.30$ giving $PDE \sim 0.27$. The implementation draws from a Bernoulli distribution biased at the PDE (nominally 25 % to 30 %). This value is a bit lower than what Hamamatsu quote for the QE ($\sim 30\,\%$) because Hamamatsu measure the total QE which is the combined single *and* double photoelectron response.

The double photoelectron response (emission of a secondary photoelectron after a single photon is incident on the PMT) is accounted for by a $\sim 22\,\%$ probability to enhance the single photoelectron response. The pulse area (measured in phe) of the PMT response sees an enhancement although the true number of photons (in phd) is unchanged. Thus, summing the overall PDE for single and double photoelectron emission gives approximately 32 %, which is consistent with Hamamatsu's quoted nominal performance of the R11410 PMT (values in [172, 173]).

The single and double photoelectron pulse area distributions of a PMT are shown in Fig. 5.6. The distributions in this figure were produced by separate Monte Carlo runs[55], to illustrate the effect of double photoelectron emission on the pulse areas produced by the PMT. $\mu_{1\text{phe}}, \mu_{2\text{phe}}$ are the means of the single and double photoelectron pulse area distributions, respectively. The mean shifts from $\mu_{1\text{phe}} \approx 13.9747\,\text{pV s}$ to $\mu_{\text{total}} \approx 17.0557\,\text{pV s}$ due to double photoelectron emission, from which one recovers the double photoelectron emission

[55] 927 887 entries for the single photoelectron distribution, and 928 057 entries for the distribution including the double photoelectron effect, with a bin width of 0.5 pV s.

probability $\left(\mu_{\text{total}} - \mu_{\text{1phe}}\right)/\mu_{\text{1phe}} \approx 22\,\%$. The standard deviation of the gain anticipated in LZ PMTs is 30 %. The distributions are sampled from the same underlying Gaussian distribution, the double photoelectron pulse area distribution is sampled from the same single photoelectron distribution twice. The increase in the width of the distribution is visible on the right side of the double photoelectron portion of the distribution.

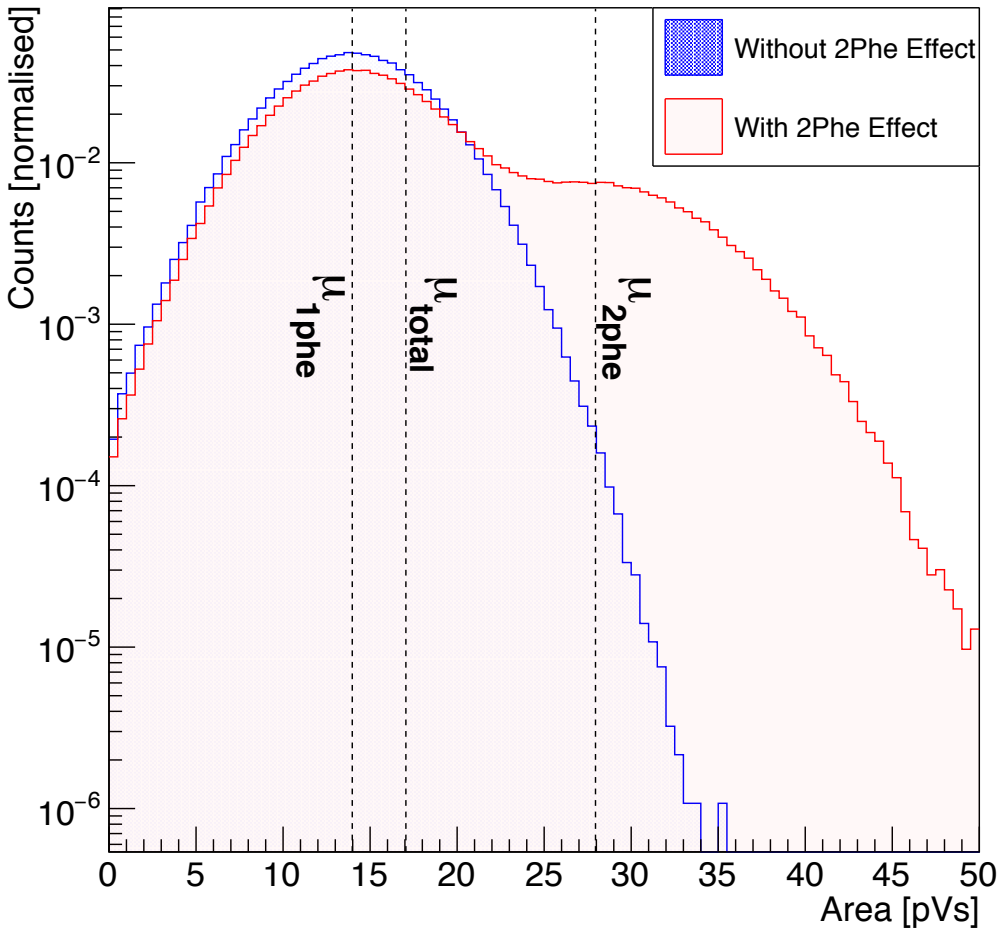


Figure 5.6: Pulse area distribution for single photoelectron emission with superimposed pulse area distribution that includes a 22 % probability of double photoelectron emission. The pulse areas are calculated from the output of the DER PMT model.

Dark counts (spontaneous emission of charge from the photocathode and the dynode chain [174]) are accounted for by producing a number of counts from a Poisson distribution, which gives the number of dark count single photoelectrons. The dark count single photoelectrons are uniformly distributed in time in the simulation. The number of dark counts, nominally 40 Hz based on measured data from [171], is determined from the inverse of the dark rate, shown in Fig. 5.7.

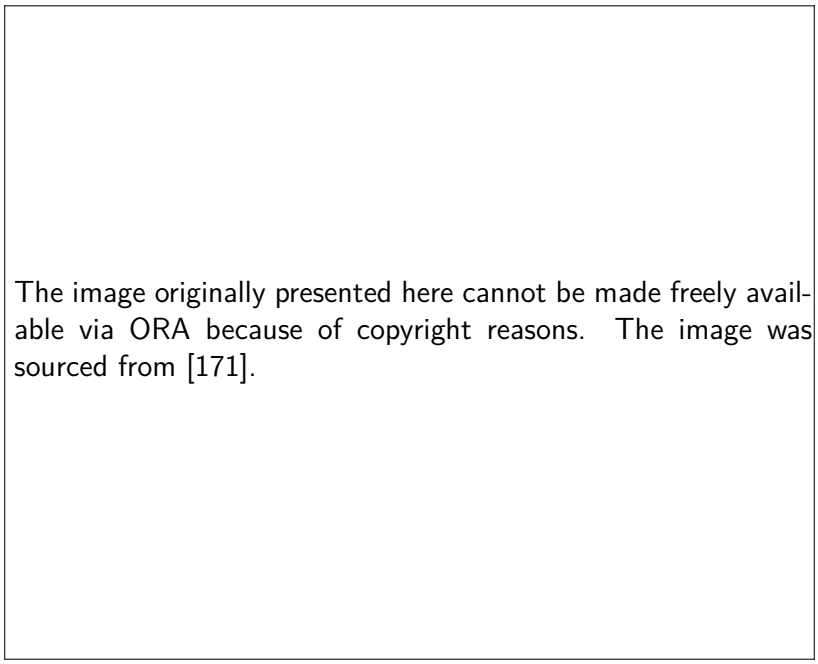


Figure 5.7: Measurements from [171] of the Hamamatsu R11410 PMT dark rate as a function of the photoelectron threshold. The rate is approximately 40 Hz at the 1 phe threshold.

5.4 Cable Model

The equivalent circuit for an ideal cable is modelled as a simple $RCLG$ circuit, with an inductor L and resistor R in series, in parallel with a capacitor C and conductance G, as shown in Fig. 5.8.

For the case at hand, the high-frequency regime of the cable is studied. The

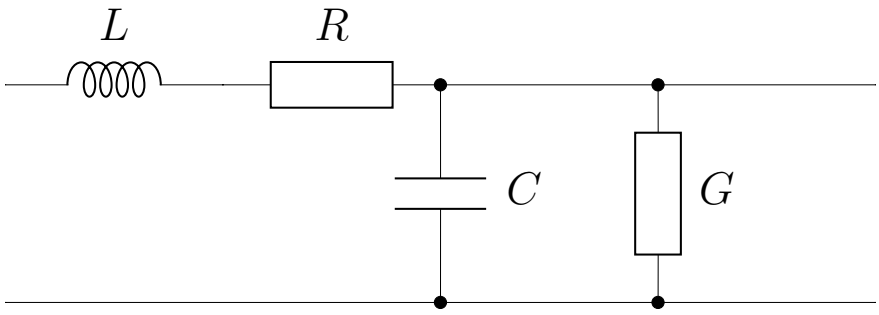


Figure 5.8: Equivalent circuit of a cable, showing an inductance L, a resistance R, a capacitance C, and a conductance G.

resistance R can be modelled by the cable's skin. The skin-effect of the cable gives rise to a characteristic skin depth δ

$$\delta = \sqrt{\frac{2}{\omega\mu\sigma}}, \tag{53}$$

from which the equivalent resistance is derived

$$R = \frac{1}{W\delta\sigma} = \frac{1}{W}\sqrt{\frac{\omega\mu}{2\sigma}}, \tag{54}$$

where W [m] is the width of the part of the cable that carries the signal, ω [rad s^{-1}] is the angular frequency, μ [H m^{-1}] is the magnetic permeability of free space, and σ [S m^{-1}] is the conductivity of the cable material.

The capacitance C can be modelled by the relative permittivity, since it is a ratio of capacitances (of a capacitor with a particular choice of dielectric, to the same one but replacing the dielectric material with a vacuum) such that

$C_1/C_2 \propto \varepsilon_1/\varepsilon_2 = \varepsilon_r$. From the definition of permittivity

$$\hat{\varepsilon} = \frac{D_0}{E_0} = |\varepsilon| \exp i\theta \tag{55}$$

it follows that

$$\varepsilon_{total}(\omega) = \varepsilon_a(\omega) + i\varepsilon_b(\omega) = \left|\frac{D_0}{E_0}\right| (\cos\theta + i\sin\theta)\,, \tag{56}$$

where D_0, E_0 are the displacement field and the electric field. The angle θ is the phase angle describing loss due to dissipation - the subscripts on ε are there to distinguish that $\varepsilon_a, \varepsilon_b$ are distinct numbers. The loss tangent is defined as

$$\tan\theta = \frac{\varepsilon_b}{\varepsilon_a}. \tag{57}$$

Re-arranging the above, one obtains [175–190]

$$\varepsilon_{total} = \varepsilon_a(\omega)\left(1 + i\frac{\varepsilon_b}{\varepsilon_a}\right) = \varepsilon_a\left(\omega\right)\left(1 + i\tan\theta\right). \tag{58}$$

The signal attenuation of a cable is then modelled in the frequency (ω) domain as a function of physical parameters: the cable core width W and its length l, its characteristic impedance Z_0, its conductance σ, the relative dielectric constant of the dielectric ε_r, the loss tangent of the cable $\tan\theta$, the magnetic permeability of free space μ, and the speed of light c. The result is an expression for the transfer function of the cable[56]

$$\frac{A_l}{A_0} = e^{-\alpha l}, \alpha = \alpha_1 + \alpha_2 = \frac{1}{2WZ_0}\sqrt{\frac{\omega\mu}{2\sigma}} + \frac{\omega\sqrt{\varepsilon_r}\tan\theta}{2c}. \tag{59}$$

A series of pole replacement elements in the time domain can be used to approximate the slope of the roll-off of the cable attenuation in the frequency domain as it represents the transfer function [175–190]. The slope of the cable attenuation is typically -1 (corresponding to the signal power), but for an

[56] Derivation in Appendix D.

implementation in the time-domain one needs the voltage (slope of $-1/2$). Using pole replacement elements to produce a fit to the cable attenuation over a region in the frequency domain gives an approximation to time constants that enable modelling the cable attenuation in the time-domain.

A pole-zero replacement term can be written as a sum of a low-pass and a high-pass filter (times a constant factor which is the ratio of the time constants τ_2/τ_1 of the filter) [176]

$$\frac{1+i\omega\tau_2}{1+i\omega\tau_1} = \frac{1}{1+i\omega\tau_1} + \frac{\tau_2}{\tau_1}\frac{i\omega\tau_1}{1+i\omega\tau_1} \tag{60}$$

which has the familiar form of a low-pass filter and a high-pass filter for the first and second term respectively. The high-pass filter itself can in turn be re-written as the difference between the unfiltered signal and a low-pass term as

$$lowpass\,(\tau_1) + \frac{\tau_2}{\tau_1} highpass(\tau_1) = lowpass(\tau_1) + \frac{\tau_2}{\tau_1}\left(1 - lowpass(\tau_1)\right). \tag{61}$$

Collecting terms

$$\frac{\tau_2}{\tau_1} + \left(1 - \frac{\tau_2}{\tau_1}\right) lowpass(\tau_1). \tag{62}$$

Fig. 5.9 shows the fit to the model using 6 terms to approximate the slope. The residual as a percentage deviation of the fit to the model is shown on the bottom plot. The pole-zero replacement elements achieve a good fit to the model, capturing the roll-off up to frequencies higher than the sampling rate of 100 MHz, and allow an accurate approximation in the time domain to be made [191].

Fig. 5.10 shows the model compared to the LZ TPC PMT signal cable[57] that is used for signal readout of the Hamamatsu R11410 TPC PMTs. The model prediction is a first order approximation that gives the expected straight-line response. The attenuation magnitude is linear in the length of the cable. The

[57] The manufacturer of the cable is Axon and the cable model is A21482C.

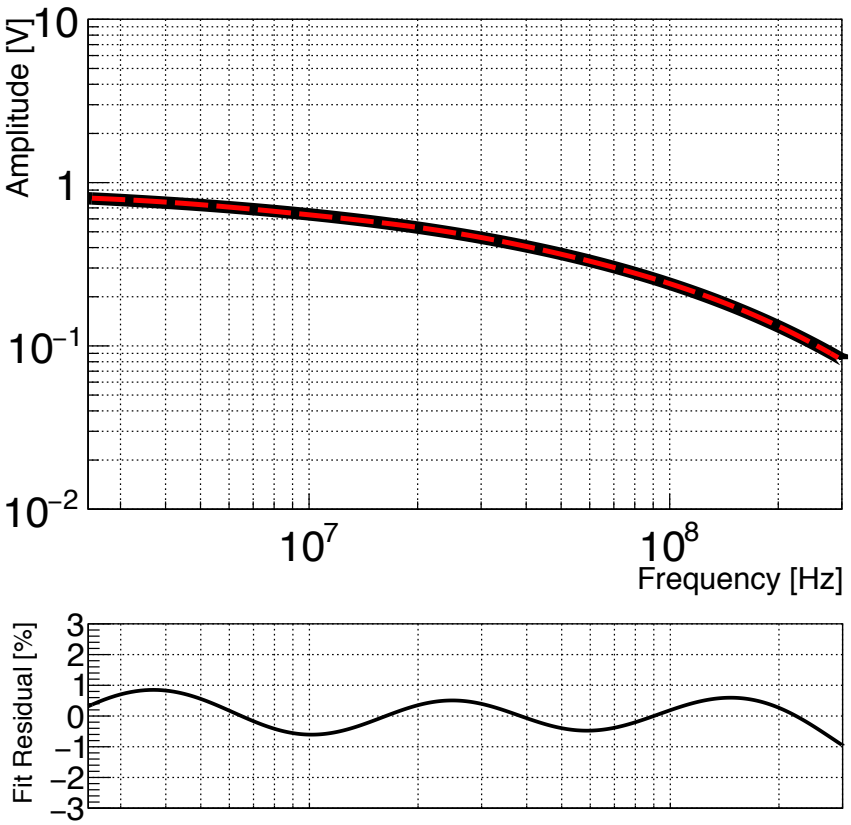


Figure 5.9: Model prediction of amplitude variation (black solid line) of the cable response versus frequency for 45 feet of Axon A21482C cable, and superimposed fit (red dashed line) using pole and zero elements. The model parameters are $c = 3 \times 10^8\,\mathrm{m\,s^{-1}}$, $\mu = 1.26\,\mu\mathrm{H\,m^{-1}}$, $\sigma = 5.96 \times 10^7\,\mathrm{S\,m^{-1}}$, $Z_0 = 50\,\Omega$, $\tan\theta = 7 \times 10^{-4}$, $W = 2.5\,\mathrm{mm}$, $l = 13.72\,\mathrm{m}$.

slope results from the cable parameters as described in Fig. 5.9. At approximately 0.5 GHz, the measured data reveal a slight departure from the model. The measured attenuation may be altered slightly by changes to ε_r, μ, and $\tan\theta$ at higher frequencies. Physical changes to the cable such as through handling, or the environment, can also alter the response when making a measurement. However, 0.5 GHz is well above the sampling rate of LZ of 100 MHz so this has a negligible impact on the signal.

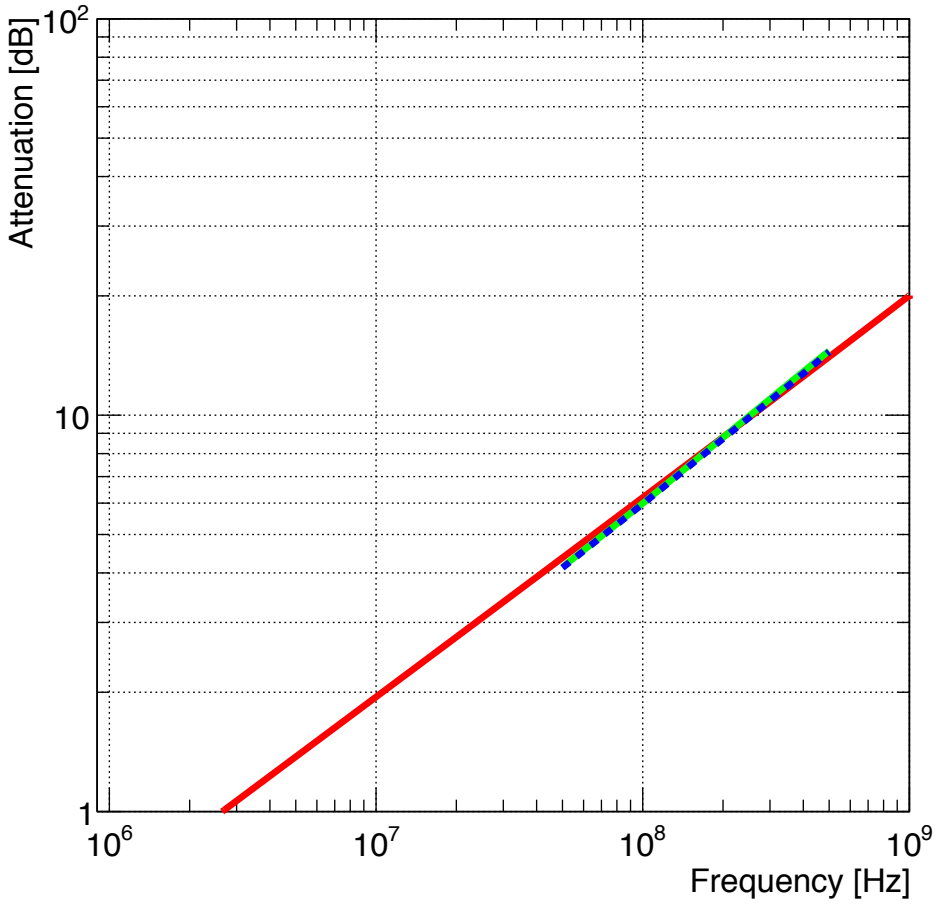


Figure 5.10: Comparison of simulated and measured attenuation in dB of 45 feet of Axon A21482C cable. The blue and green dashed lines are two sets of real data measured by the LZ collaboration, the red line represents the model prediction (not a fit).

5.4.1 Algorithmic Implementation

For an input signal In, an output signal Out, a timebase T, and time constants τ_1, τ_2, the implementation of a single filter block is

$$accu_i = \exp\left(-\frac{T}{\tau_1}\right) accu_{i-1} + \left(1 - \exp\left(-\frac{T}{\tau_1}\right)\right) In_i \tag{63}$$
$$Out_i = \left(1 - \frac{\tau_2}{\tau_1}\right) accu_i + \frac{\tau_2}{\tau_1} In_i,$$

where $i \in \mathbb{R}$ denotes the i-th value in the time series, and $accu$ is an accumulator. Fig. 5.11 shows the signal flow diagram for the implementation, where z^{-1} denotes a unit delay. Each pole-zero term has its own set of distinct τ_1, τ_2 values obtained from the fit in Fig. 5.9. Each set of Eq. (63) forms a block, and the output of each block is inputted into a subsequent block[58]. A temporary variable *temp* represents the output that is passed through all blocks. This results in the following procedure

1. Update *temp* with the latest value of In_i.
2. Apply the first line of Eq. (63) where In_i is replaced by *temp*.
3. Assign the second line of Eq. (63) to *temp* which replaces Out_i.
4. Input *temp* to the next block of Eq. (63): go to step 2.

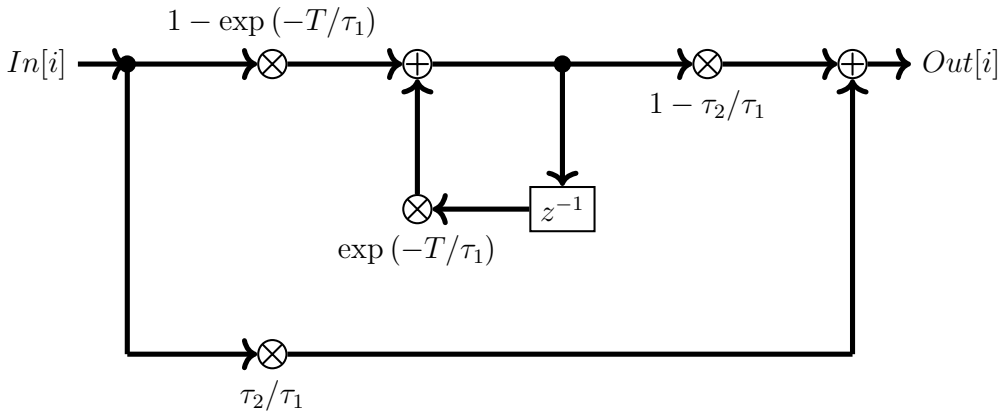


Figure 5.11: Signal flow diagram for the implementation of the cable.

[58] In the simulation, the accumulators are given time to settle before processing waveform data.

5.5 Amplifier Model

LZ will use a two gain amplifier system, whereby the same input signal from each PMT is amplified in a low-gain (LG) and a high-gain (HG) channel simultaneously during data-taking. The HG channel is sensitive to events with few incident photons, and the LG channel is less likely to clip for large S2 signals associated with higher energy recoil events. The combination of LG and HG increases the effective dynamic range of the LZ DAQ.

The charge signal from the PMTs is amplified (which increases the area of the signal), and shaped, thereby spreading the single photoelectron waveforms out in time by altering the time profile of the response. This facilitates detection of the fast single photoelectron response PMT pulses with a digitiser timebase of 10 ns. Fig. 5.12 shows a block diagram of the amplifier board.

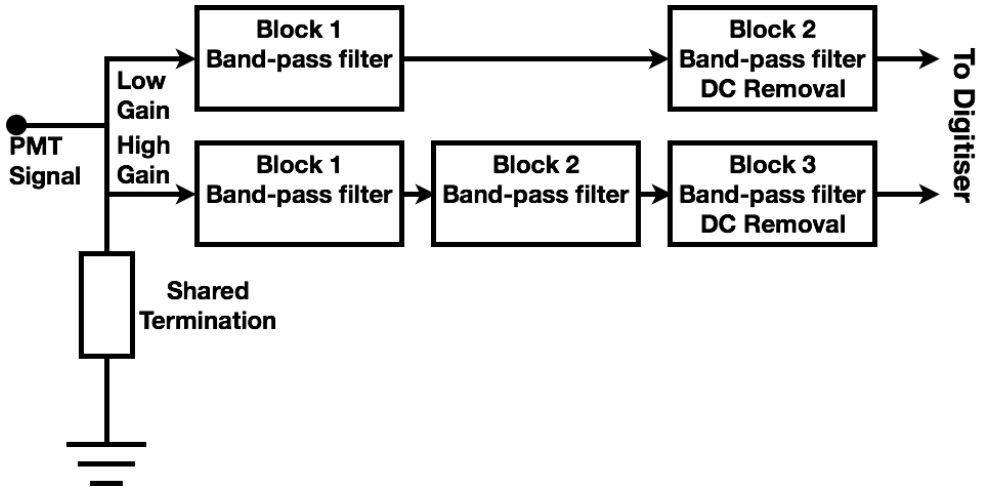


Figure 5.12: Block diagram of the amplifier. Each of the blocks provides a combination of amplification and shaping. Block 2 in the low-gain and block 3 in the high-gain provide Direct Current (DC) offset removal and baseline restoration, and have the same circuit layout.

The low-gain and the high-gain channel receive the same PMT input signal and share a common termination. The amplifier consists of various stages, or blocks, each of which performs amplification and shaping of the transient response of the signal.

The low-gain and high-gain channels both have the same design for the final stage (i.e. the second block in the low-gain channel, and the third block in the high-gain), differing only in the choice of component values. This last stage provides DC offset removal through a feedback circuit.

Towards achieving a model of the amplifier board, the transfer functions for the amplifier board are calculated analytically. The DER result is compared to the transfer function that is predicted by a SPICE simulation. Then, in order to achieve the implementation of the transient response, the transfer function is represented in terms of filter algorithms. Table 5.1 shows an overview of the filter types that will be identified from the transfer functions of the amplifier blocks.

Table 5.1: Overview of mathematical forms of various filter types. Time constants are, generically, $\tau = RC$.

Term	**Filter Type**
$\frac{1}{1+i\omega\tau}$	Low-pass filter
$\frac{i\omega\tau}{1+i\omega\tau}$	High-pass filter
$\frac{1+i\omega\tau'}{1+i\omega\tau}$	Pole-zero element
$\frac{1}{1+i\omega\left(\tau+\tau'\right)+(i\omega)^2\tau\tau'}$	Sallen-Key element

Finding the poles and zeros of the transfer function is part of the process of obtaining the time constants. The pole solutions are complex numbers of the form $s = a + ib$ where a, b are the pole solutions. If the pole is purely real ($b = 0$), then for a causal system the time constant τ is the inverse of the pole. If the pole is complex ($b \neq 0$) then the time constants are

$$\tau = \frac{a}{a^2 + b^2}, \tau' = \frac{b}{a^2 + b^2}. \tag{64}$$

The time-domain representation for each of the terms in Table 5.1 are needed in order to implement the transient response of the whole amplifier board. The time-domain representation for a low-pass filter was demonstrated in Eq. (37) on page 91. The time-domain representation for a high-pass filter is simply $1 - lowpass(\tau)$. The time-domain representation for a pole-zero element was shown in Eq. (60) on page 132, and Eq. (63) on page 135, and is composed of a low-pass, and a high-pass. The time-domain representation of the Sallen-Key element is derived in Appendix E.3, and involves finding the Laplace transform of the transfer function.

The following pages focus on the derivation of the transfer function of each block of the low-gain and the high-gain amplifier, towards the combined model for the transient response of the amplifier.

5.5.1 Low-Gain Channel Stage 1

In the low-gain channel, there are two blocks which form a band-pass filter. The circuit diagram for the first stage of the low-gain channel is shown in Fig. 5.13 and its transfer function is plotted in Fig. 5.14 (derivation in Appendix E.1.1).

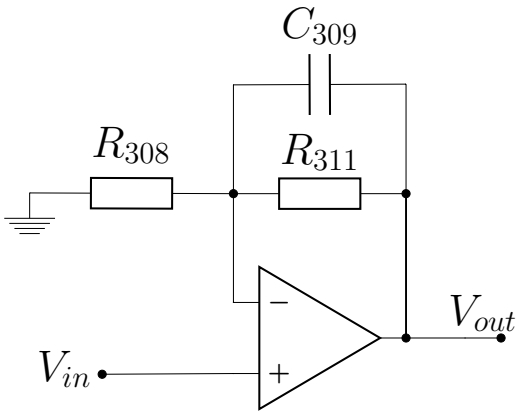


Figure 5.13: Circuit diagram for the first stage (Block 1) of the low-gain channel of the amplifier board.

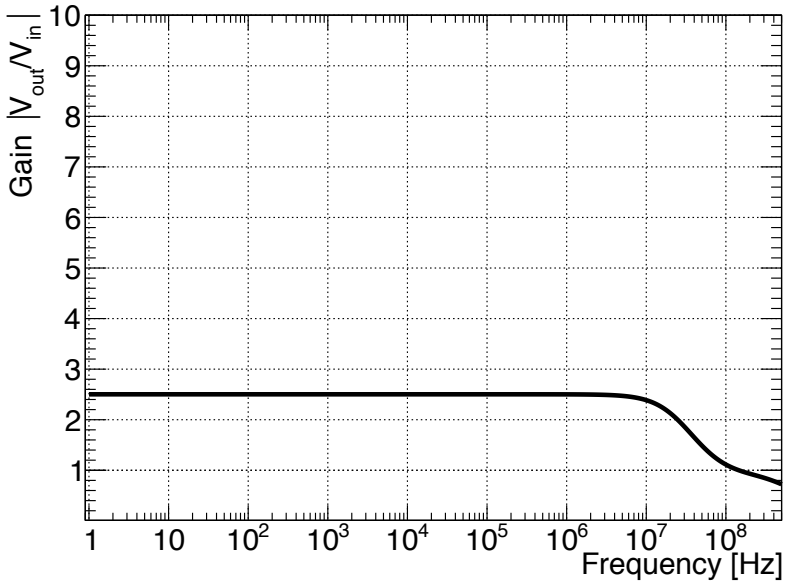


Figure 5.14: Transfer function of the first stage of the low-gain channel of the amplifier board showing the absolute magnitude of the amplitude gain as a function of frequency.

5.5.2 Low-Gain Channel Stage 2

The circuit diagram for the second stage of the low-gain channel is shown in Fig. 5.15 and its transfer function is shown in Fig. 5.16.

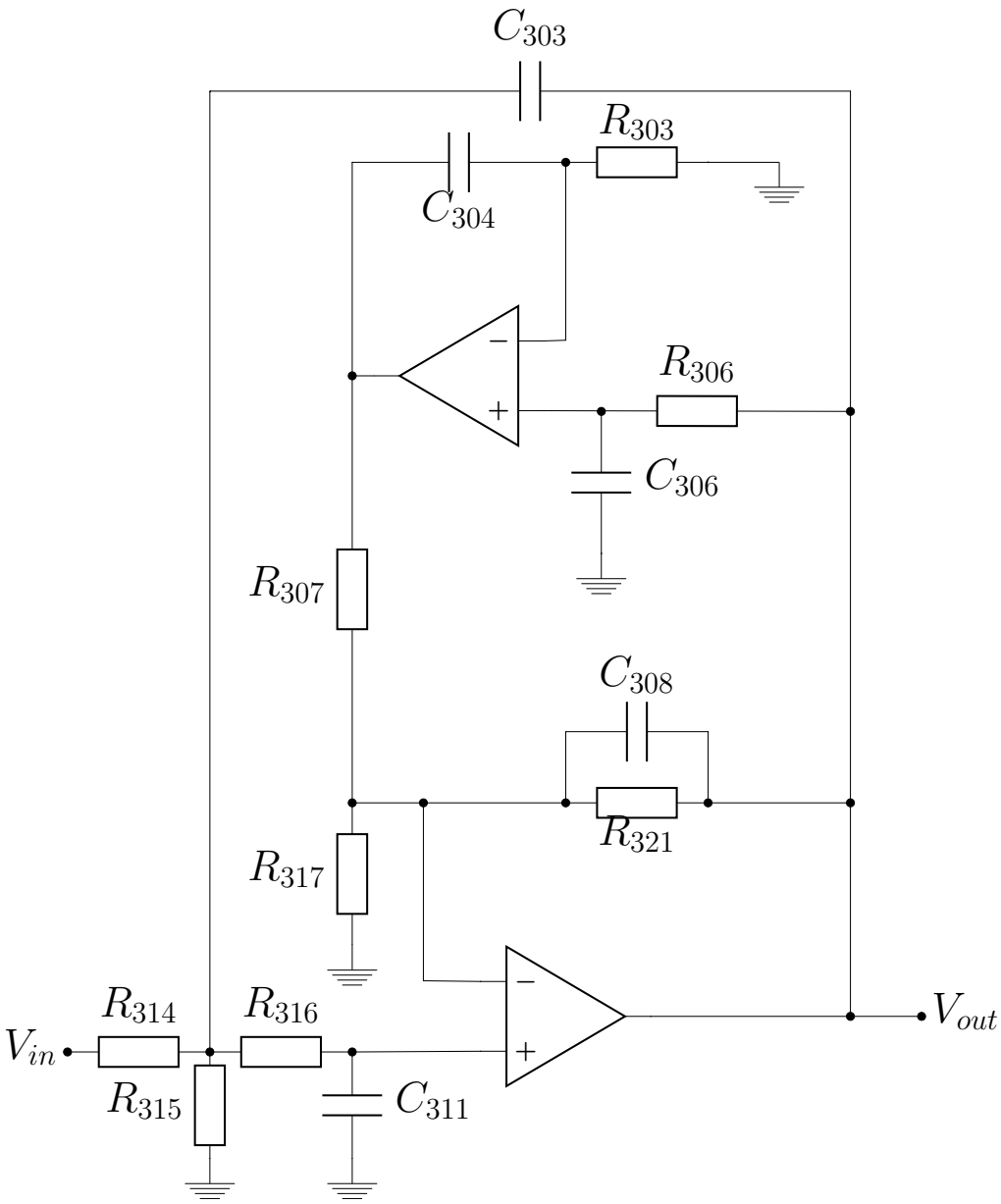


Figure 5.15: Circuit diagram for the second stage (Block 2) of the low-gain amplifier board.

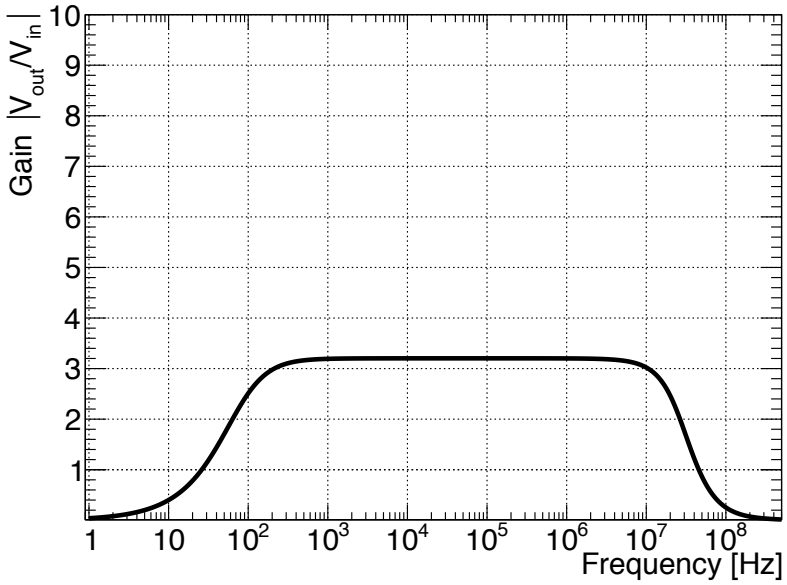


Figure 5.16: Transfer function of the second stage of the low-gain channel of the amplifier board showing the absolute magnitude of the amplitude gain as a function of frequency.

The complete transfer function for the low-gain amplifier channel is

$$V_{out} = \frac{R_{311}}{R_c}\frac{1+i\omega R_c C_{309}}{1+i\omega R_{311}C_{309}}\times \tag{65}$$
$$\frac{R_b R_{307}}{R_{314}R_a}\frac{i\omega R_{303}C_{304}\left(1+i\omega R_{306}C_{306}\right)\left(1+i\omega R_a C_{308}\right)}{\left(1+i\omega\left(R_{316}C_{311}+R_bC_{311}+R_bC_{303}\right)+(i\omega)^2 R_{316}C_{311}R_bC_{303}\right)}$$
$$\times\frac{1}{\left(1+i\omega R_{303}C_{304}\left(1+\left(1+i\omega R_{306}C_{306}\right)\left(\frac{R_{307}}{R_{321}}\left(1+i\omega R_{321}C_{308}\right)\right)\right)\right)}$$
$$\frac{}{-(i\omega)^2 R_bC_{303}R_{303}C_{304}\frac{R_{307}}{R_a}\left(1+i\omega R_{306}C_{306}\right)\left(1+i\omega R_aC_{308}\right)}V_{in}.$$

This gives a gain in the passband for the low-gain channel of

$$G = \frac{R_{311}R_bR_{307}}{R_cR_{314}R_a}\frac{R_{303}C_{304}}{\tau_4} \approx 8.02, \tag{66}$$

where $\tau_4 \approx 2.00\,\text{ms}$ is one of the poles of the circuit.

5.5.3 High-Gain Channel Stage 1

In the high-gain channel, there are three blocks which form a band-pass filter which provides additional shaping - shown in Fig. 5.17 (transfer function in Fig. 5.18), Fig. 5.19 (transfer function in Fig. 5.20), and Fig. 5.21 (transfer function in Fig. 5.22).

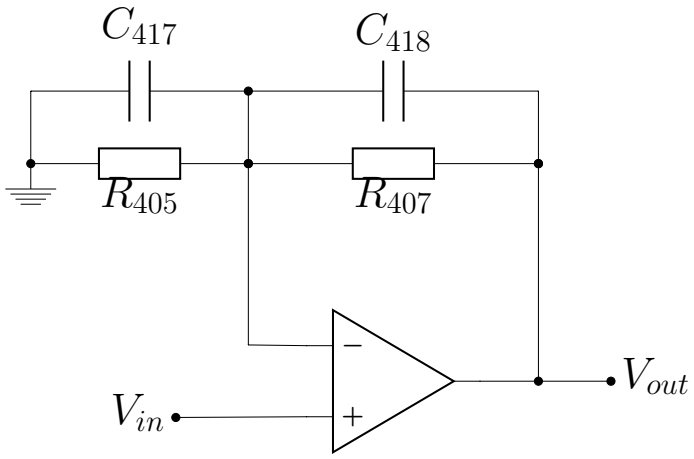


Figure 5.17: Circuit diagram for the first stage (Block 1) of the high-gain channel of the amplifier board.

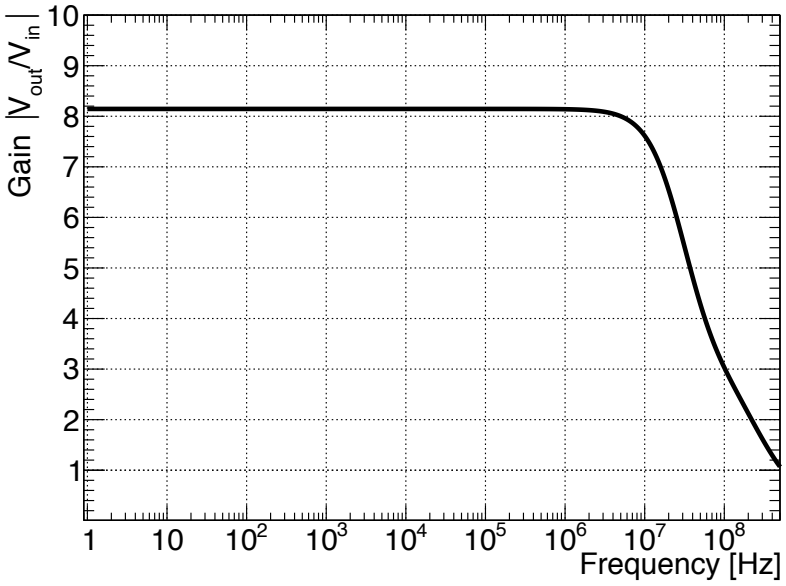


Figure 5.18: Transfer function of the first stage of the high-gain channel of the amplifier board showing the absolute magnitude of the amplitude gain as a function of frequency.

5.5.4 High-Gain Channel Stage 2

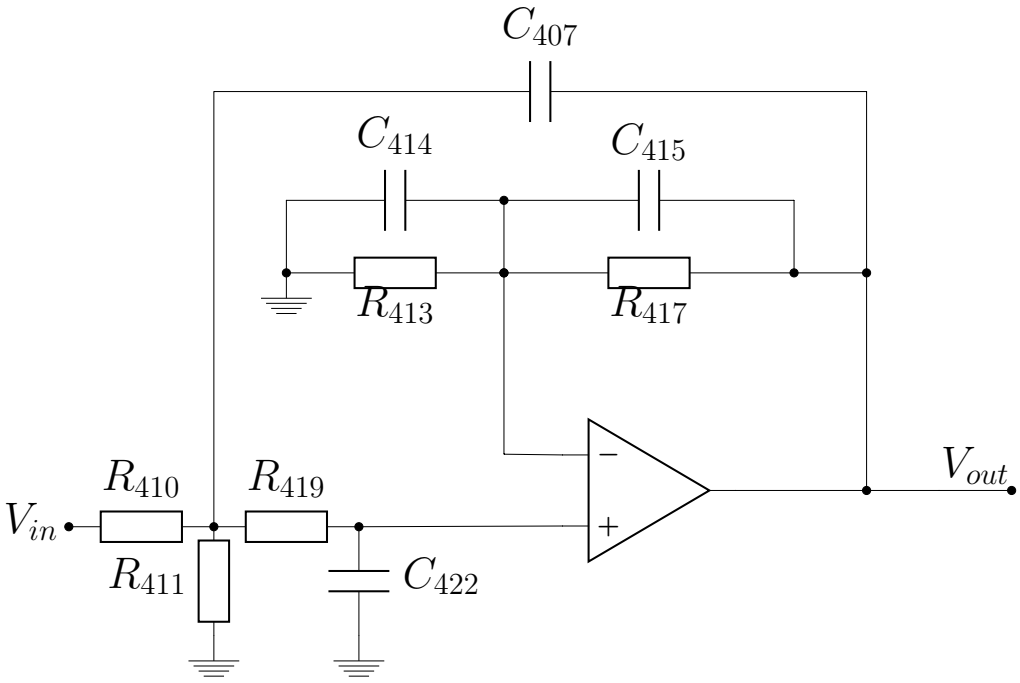


Figure 5.19: Circuit diagram for the second stage (Block 2) of the high-gain channel of the amplifier board.

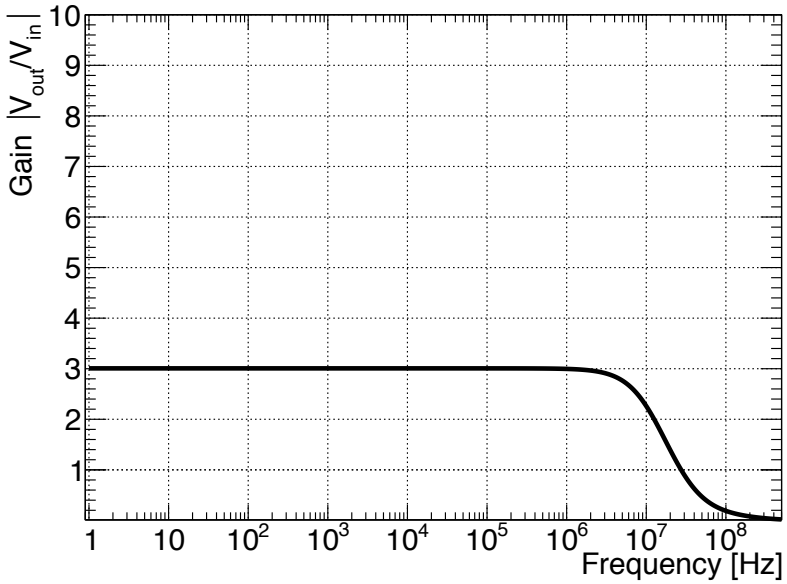


Figure 5.20: Transfer function of the second stage of the high-gain channel of the amplifier board showing the absolute magnitude of the amplitude gain as a function of frequency.

5.5.5 High-Gain Channel Stage 3

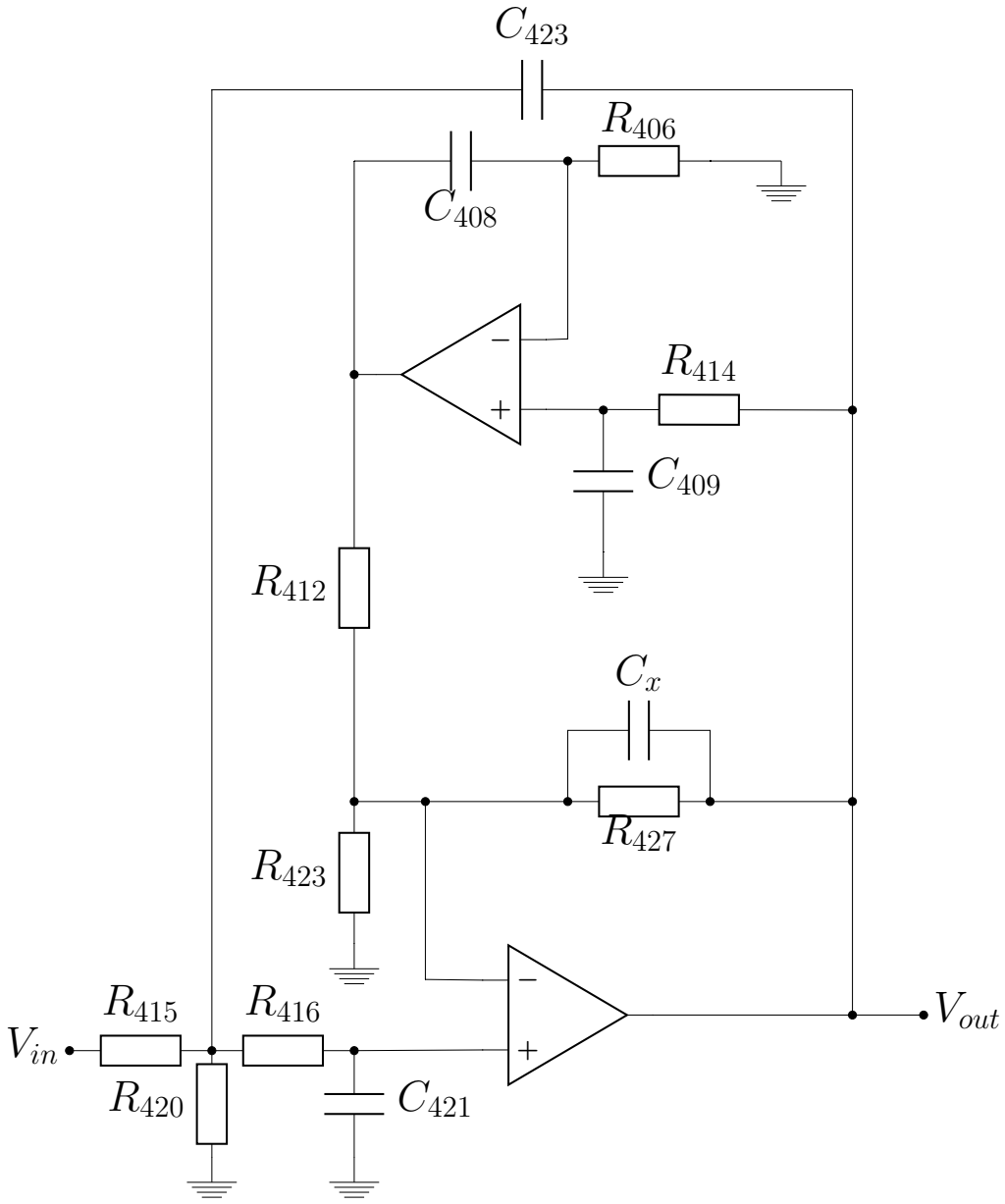


Figure 5.21: Circuit diagram for the third stage (Block 3) of the high-gain channel of the amplifier board.

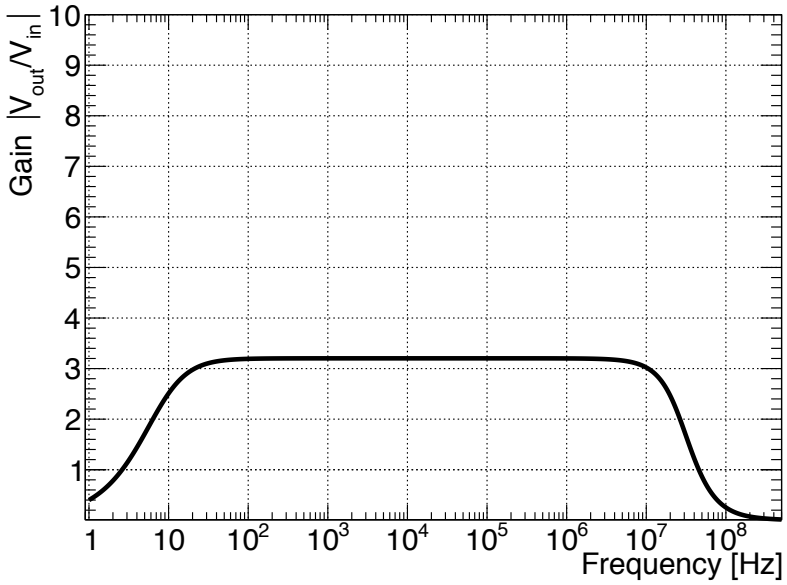


Figure 5.22: Transfer function of the third stage of the high-gain channel of the amplifier board showing the absolute magnitude of the amplitude gain as a function of frequency.

The transfer function for the entire high-gain channel is

$$V_{out} = \frac{R_{407}}{R_c}\frac{1+i\omega R_c\left(C_{417}+C_{418}\right)}{1+i\omega R_{407}C_{418}} \times \frac{R_{417}R_e}{R_dR_{410}}\frac{1+i\omega R_d\left(C_{414}+C_{415}\right)}{1+i\omega R_{417}C_{415}} \times Block3 \times V_{in}, \tag{67}$$

where $Block3$ is equivalent in form to that of the low-gain. The gain in the passband for the high-gain channel is

$$G = \frac{R_e}{R_{410}}\frac{R_{407}}{R_c}\frac{R_{417}}{R_d}\frac{R'_bR_{412}R_{406}C_{408}}{R_{415}R'_a\tau'_4} \approx 78.55, \tag{68}$$

where R'_a, R'_b, τ'_4 are analogous to the low-gain, differing only in the component labels and values. The calculations and several abbreviations are detailed in Appendix E.

Fig. 5.23 shows the respective poles for the portion of the transfer function responsible for offset removal (i.e. the final stage), yielding the time constants of the system.

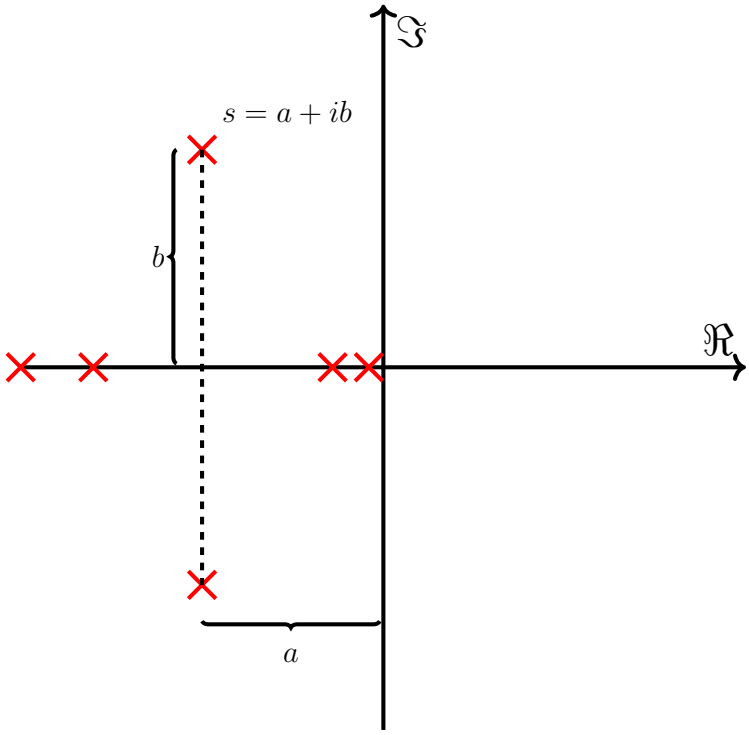


Figure 5.23: Pole plot of the final stage of the high-gain amplifier channel. Shown are the poles (crosses) of the high-gain amplifier board, including the dominating pole due to the finite gain-bandwidth product of the op-amp defining the open-loop gain of the op-amp.

Just as for the other stages in the amplifier (see Appendix E), the poles (and zeros) are all on the left-hand side of the imaginary axis and are all finite, extending towards the origin from the largest real pole part - showing the system is Bounded-Input, Bounded-Output (BIBO) stable and causal.

Shown in Fig. 5.24 is a portion of the derived DER transfer function compared to that simulated by SPICE, highlighting the improvement in the agreement achieved by including the effect of the open-loop gain in the calculation. A ratio of 1 indicates perfect agreement. The DER response is slightly reduced at higher frequencies, effectively shifting the curve to the left somewhat, thereby falling in line with the SPICE simulation. As can be seen in the bottom plots

showing the ratio of DER to SPICE on a linear scale, the overall agreement is greatly improved at high frequencies through the introduction of the open-loop gain of the op-amps. In particular, the position of the corner frequency is in much closer agreement, and there is a slight adjustment in the slope of the roll-off resulting in better agreement over several orders of magnitude at higher frequencies.

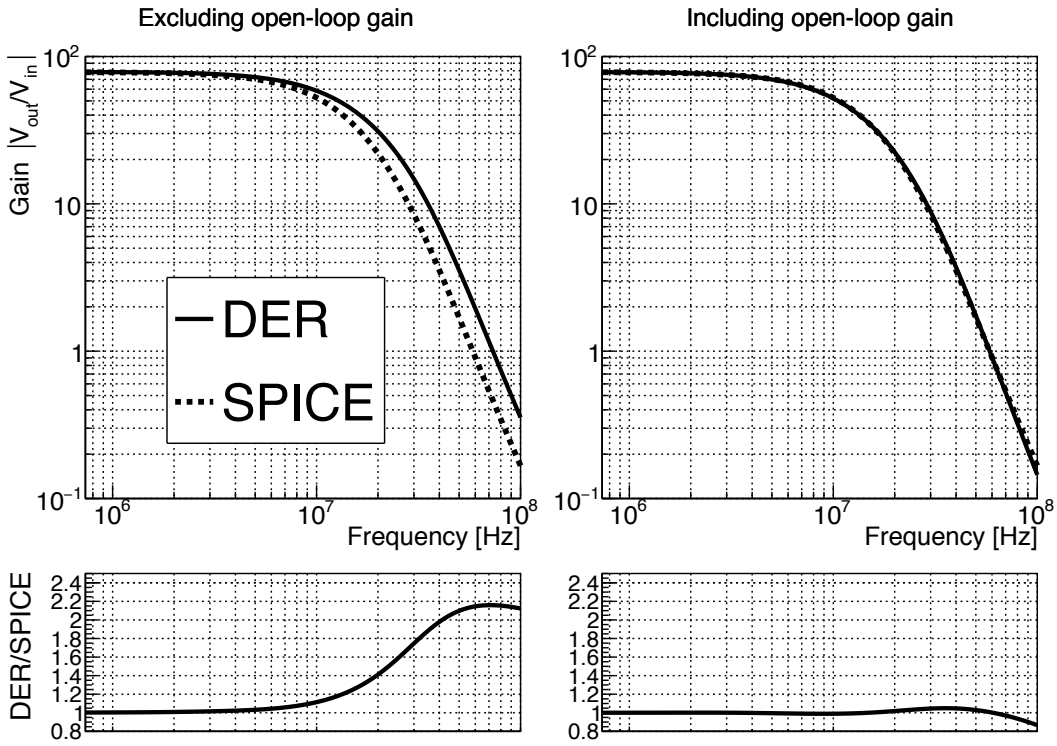


Figure 5.24: Comparison of the transfer function of the high-gain amplifier chain as calculated by DER and simulated by SPICE, excluding (left) and including (right) the effect of the open-loop gain.

Table 5.2 shows the time constants for the transfer functions of the low-gain and high-gain channels of the amplifier board at each stage. For the denominators of the transfer function, the expressions are solved numerically using the eigenvalues of the companion matrix of the polynomial.

Table 5.2: Time constants for each stage of the low-gain and high-gain channels of the amplifier (shown with more numerical precision in Appendix E).

Stage	**Time Constant**	**Value**	**Pole/Zero**
Low-Gain Stage 1	τ_1	0.26 ns	Pole
	τ_2	5.43 ns	Pole
	τ_3	$R_c C_{309}$	Zero
Low-Gain Stage 2	τ_1	0.16 ns	Pole
	τ_2	4.81 ns + 3.07i ns	Pole
	τ_3	4.81 ns − 3.07i ns	Pole
	τ_4	0.001 s	Pole
	τ_5	0.002 s	Pole
	τ_6	0.23 ns	Pole
	τ_7	$R_{306} C_{306}$	Zero
	τ_8	$R_a C_{308}$	Zero
High-Gain Stage 1	τ_1	0.80 ns	Pole
	τ_2	6.46 ns	Pole
	τ_3	$R_c\,(C_{417} + C_{418})$	Zero
High-Gain Stage 2	τ_1	0.17 ns	Pole
	τ_2	5.36 ns	Pole
	τ_3	12.58 ns	Pole
	τ_4	0.38 ns	Pole
	τ_5	$R_d\,(C_{414} + C_{415})$	Zero
High-Gain Stage 3	τ_1	0.16 ns	Pole
	τ_2	4.81 s + 3.07i ns	Pole
	τ_3	4.81 s − 3.07i ns	Pole
	τ_4	0.01 s	Pole
	τ_5	0.02 s	Pole
	τ_6	0.23 ns	Pole
	τ_7	$R_{414} C_{409}$	Zero
	τ_8	$R_a C_x$	Zero

The complete transfer functions for the entire low-gain and high-gain channel are shown in Fig. 5.25. A good agreement between DER and SPICE has been achieved with an analytical model of the LG and HG transfer functions of the amplifier board. The different corner frequencies of the high-pass of the low-gain versus the high-gain are due to the different choice of capacitors on the amplifier boards. For the low-gain $C_{304} = C_{306} = 0.01\,\mu\text{F}$, whereas for the high-gain $C_{408} = C_{409} = 0.1\,\mu\text{F}$.

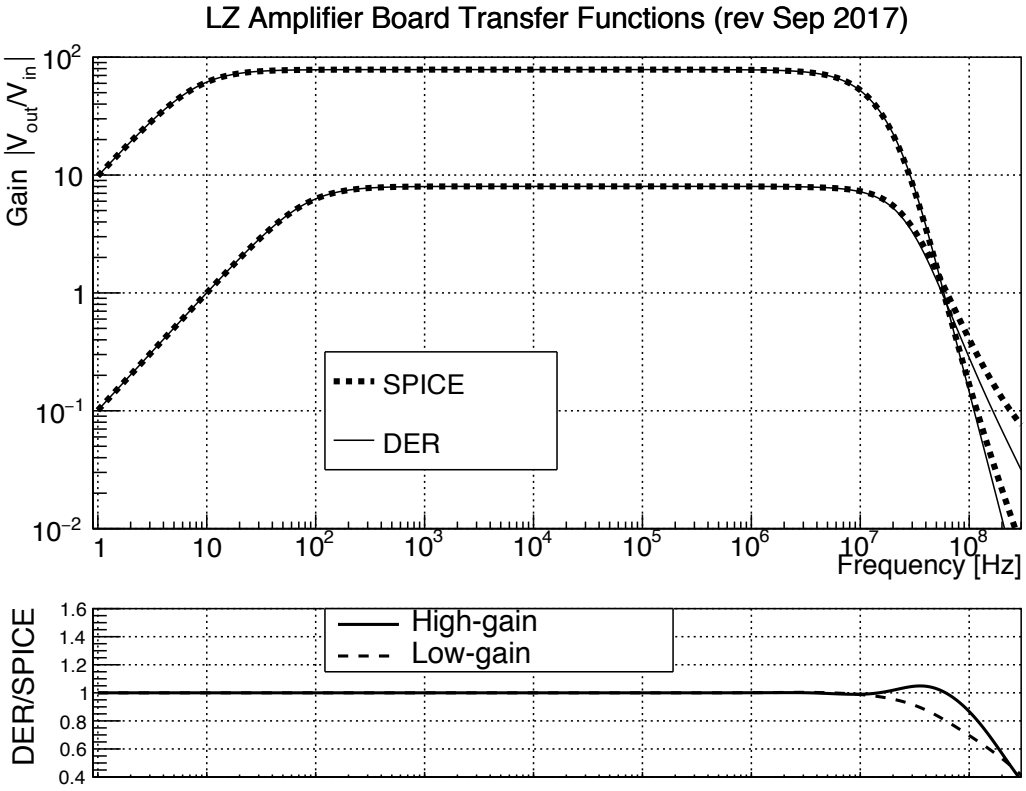


Figure 5.25: Transfer function of the low-gain and the high-gain amplifier channels showing the absolute magnitude of the amplitude gain as a function of frequency. The DER model as calculated from first principles is shown as a solid line in the top plot, the dashed line shows the SPICE simulation (not a fit). In the bottom plot, the ratio of the amplitude gain of the DER to the SPICE simulation is shown, with the solid line referring to the high-gain channel, and the dashed line to the low-gain channel.

By applying the time constants to the implementations of the filter types, the time-domain implementation of the transfer function for the transient response is obtained. The time constants from Table 5.2 are identified from the terms of Table 5.1 from Eq. (65) (see page 141) for the low-gain channel, and from Eq. (67) for the high-gain channel (see page 145).

Fig. 5.26 shows a comparison of the transient response of the amplifier between DER (solid lines) and SPICE (dashed lines) to a test input - a Gaussian waveform with a Full Width Half Maximum (FWHM) of 7.45 ns (green line with black dots). The shaping times produced by SPICE and DER agree to within 1 ns. The shaping times of 30 ns (low-gain) and 60 ns (high-gain) Full Width Tenth Maximum (FWTM) have been achieved.

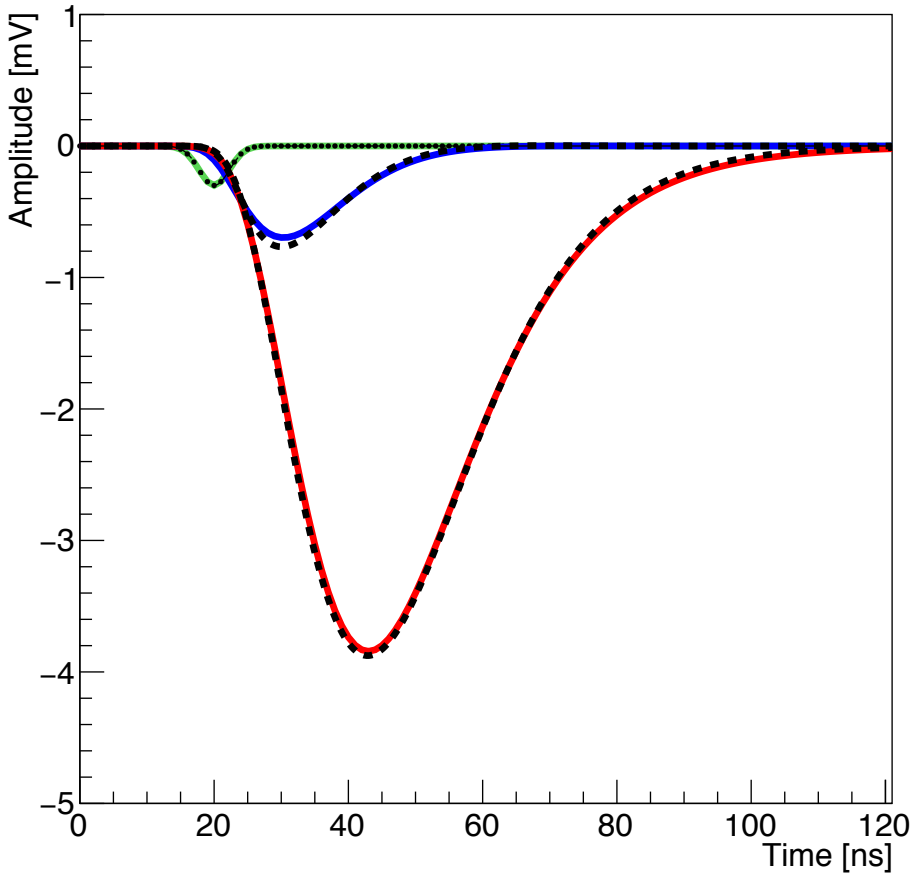


Figure 5.26: Comparison of the transient response of the low-gain and high-gain amplifier channels (not a fit), for SPICE (dashed lines) and DER (solid lines), to a test input signal (green solid line with black dots).

5.5.6 Digitiser Anti-Aliasing Filter

At the input of the digitiser board there is an anti-aliasing filter that is a second-order Bessel low-pass filter configured with a multiple feedback topology. The circuit diagram is shown in Fig. 5.27, and the transfer function is shown in Fig. 5.28.

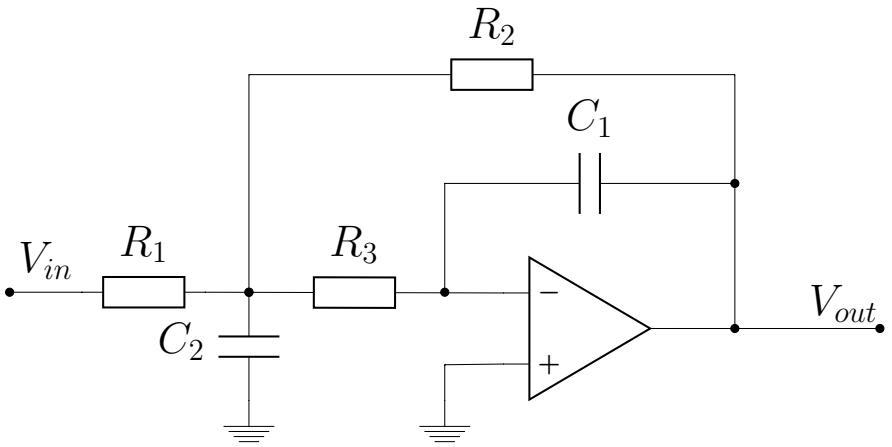


Figure 5.27: Circuit diagram of the digitiser anti-aliasing filter.

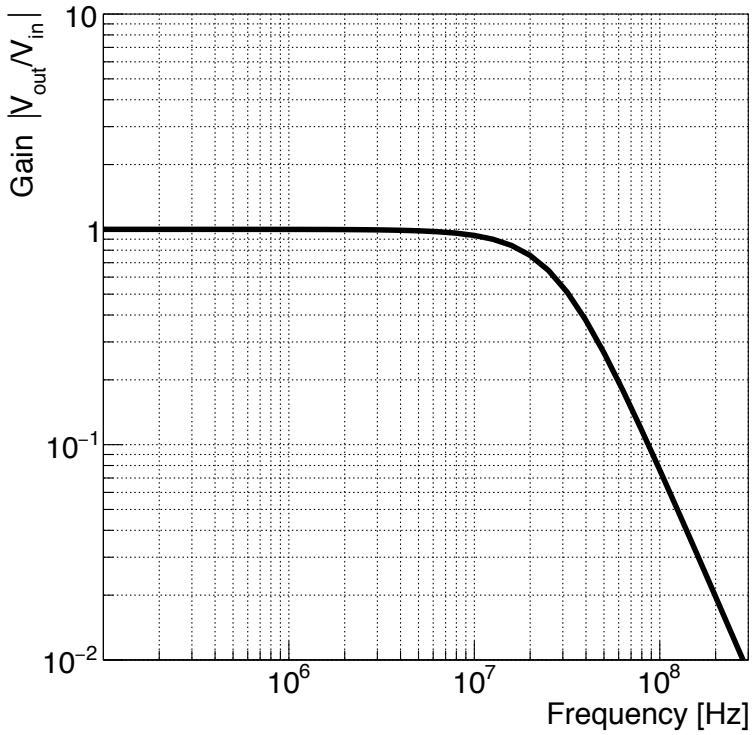


Figure 5.28: Transfer function of the digitiser anti-aliasing filter, showing the absolute magnitude of the amplitude gain as a function of frequency.

The transfer function of the filter is[59]

$$\frac{V_{\text{out}}}{V_{\text{in}}} = -\frac{R_2}{R_1}\frac{1}{1 + (i\omega)\left(R_3C_1 + R_2C_1 + \frac{R_2R_3C_1}{R_1}\right) + (i\omega)^2\left(R_3C_1R_2C_2\right)}, \quad (69)$$

and its corner frequency is 28 MHz. The 50 Ω series-parallel termination between the amplifier and the digitiser board, shown in Fig. 5.29, halves the signal amplitude.

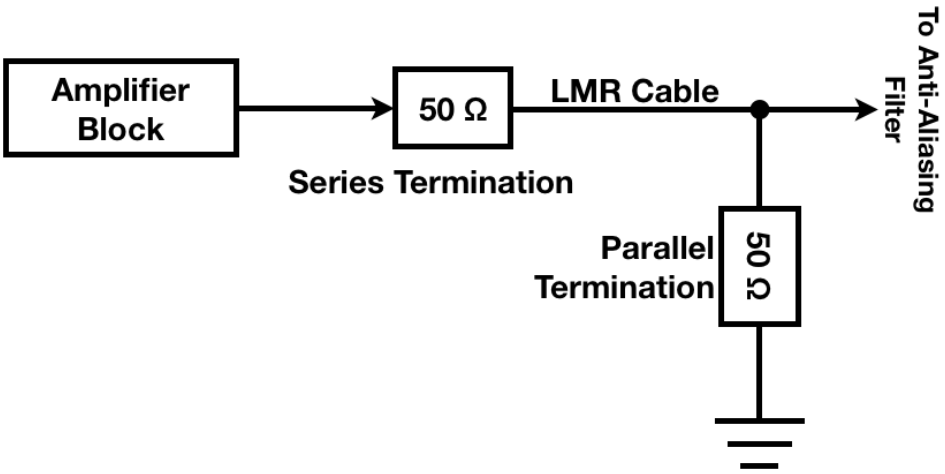


Figure 5.29: Series-parallel termination of the output of the amplifier and the input of the digitiser board, which are connected by an LMR cable, results in halving the signal.

Fig. 5.30 shows the PMT single photoelectron response and the transient response at each stage of the analogue signal chain. The dispersion due to the Axon PMT cabling, and the response of the amplifier, can be seen. The low-gain channel amplifier area gain[60] is 4.004 (design goal is 4) and the high-gain channel area gain is 39.177 (design goal is 40) (area integral from 0 ns to 1024 ns). The amplifier output signal possesses a small (fractional) overshoot of on the order of 4×10^{-6} and 3×10^{-5} (peak-to-peak) for high-gain and low-gain respectively. The long time constants on the order of 2 ms (low-gain) and 20 ms (high-gain) provide baseline restoration for PMT pulse overshoots and DC offset removal. Due to the dispersion of the signal through the cables,

[59] Derivation in Appendix F.

[60] The ratio of the integral of the signal after amplification to that before amplification.

the peak amplitude of the signal becomes smaller and the pulse is elongated. For instance, while the area gain loss due to the Axon cable is roughly 20 % (integrated from 0 ns to 128 ns), the overall effective area gain lost from 0 ns to 1024 ns is approximately 1 %.

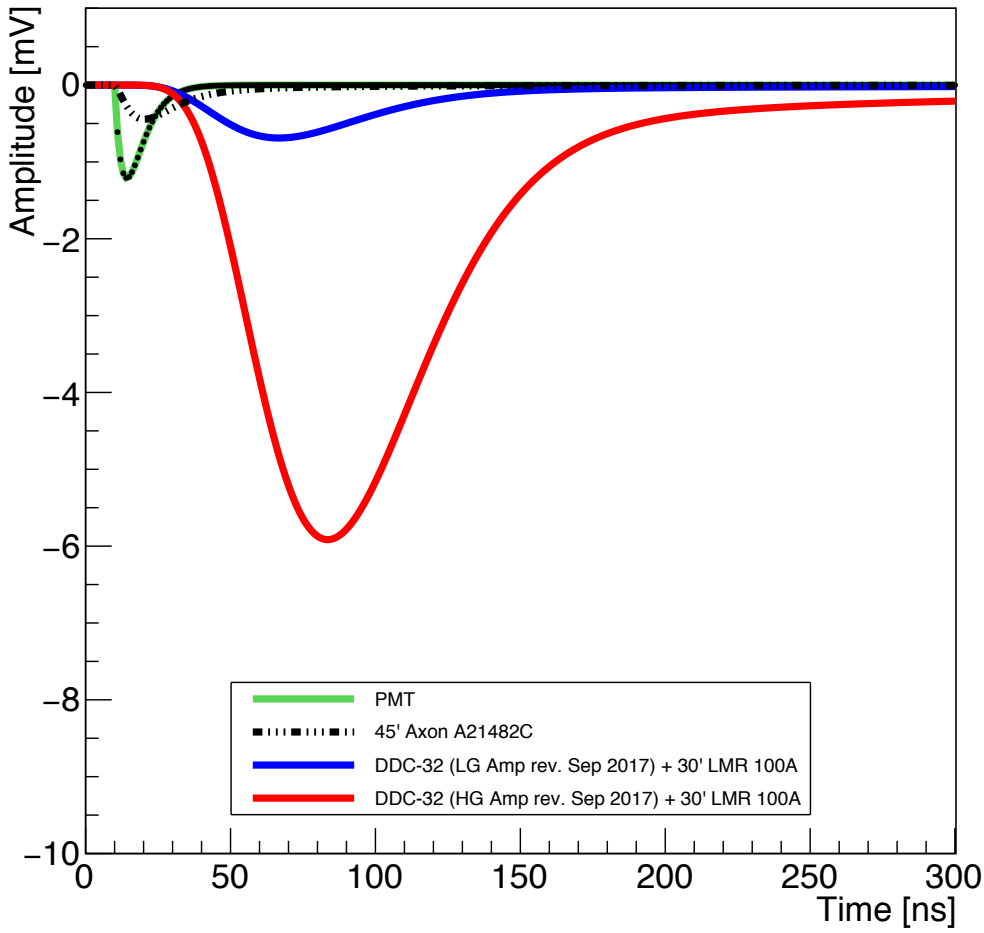


Figure 5.30: Transient response for the complete DER model, considering all stages of the analogue signal chain, showing the single photoelectron response for a nominal PMT gain of 3.5×10^6, a rise time of 2.46 ns FWTM, and a fall time of 14.44 ns FWTM.

5.6 Digitisation and Triggering

A 14 bit Analogue-to-Digital Converter (ADC) samples the analogue signal with a timebase of 10 ns. The ADC converts a voltage input into a number of ADC counts. The full-scale of the ADC is 2 V, from −1 V to 1 V (−8192 ADCC to 8191 ADCC). At the amplifier output, the signals have a baseline offset of 0 V DC. The dynamic range depends on the maximum photoelectron response that can be collected without loss of information. Therefore, the analogue signal is offset by +900 mV (7372 ADCC), so that the (negative polarity) PMT pulses have a larger usable portion of the full-scale dynamic range of the ADC. 100 mV of the range is kept free for pulse overshoots due to large signals. This helps reduce the likelihood of saturation occurring for larger S2-like signals.

Waveform data that contain pulses of interest need to be stored efficiently. Waveforms with too much uninteresting baseline require more disk storage. LZ uses zero-suppression and data sparsification to sample only the most relevant parts of the waveform. Zero-suppression means to reduce the number of baseline samples that are needed to be saved to disk. Data sparsification is a way to reduce the number of samples that are saved to disk by only triggering on the signals that are anticipated to include a waveform.

To achieve this, the so-called POD mode of acquisition is used by the LZ DAQ. The concept of a POD is that it consists principally of all signals that were sufficiently above the baseline. A POD is the outcome of a trigger that is applied by the LZ triggering system. A POD is a unit digitised waveform that exists on a single channel. A single channel can have multiple PODs (or none, if there were no waveforms on it). POD amplitudes are in units of ADCC over time in units of samples. A POD includes pre- and post-trigger samples. A POD can consist of multiple waveforms and additional samples if additional criteria are met. For example, if two adjacent waveforms occur close in time (defined by the start and end times of the trigger), then the two waveforms

and their associated pre- and post-trigger samples (and all the samples between each pulse (inter-pulse samples)) are considered as a single POD. The POD is the unit waveform in subsequent analysis.

An example to illustrate how PODs are identified from waveforms is shown in Fig. 5.31. A static trigger requires adjustment when there is a change in baseline or the relative signal size, whereas a rolling baseline does not. In this example, Waveform 1 and Waveform 2 have both triggered above the rolling baseline (dotted red line) for sufficiently long. Waveform 1 and Waveform 2 are sufficiently close to one another, and are therefore bundled with their respective pre-trigger samples and post-trigger samples to become POD 1. Waveform 3 is sufficiently far away from the end of Waveform 2, and becomes POD 2.

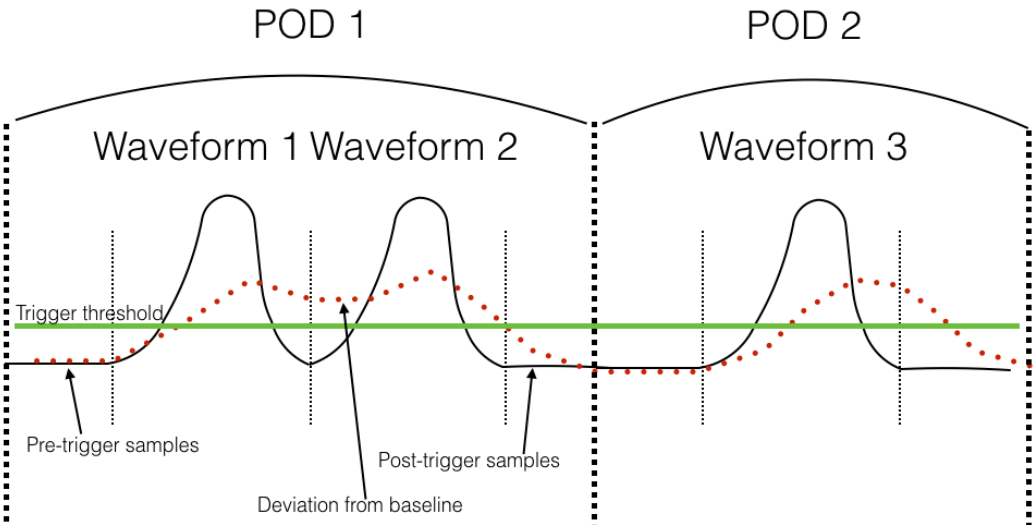


Figure 5.31: Identification of PODs from waveforms. The vertical black dotted lines show figurative boundaries within the collected waveform data. The red dotted line indicates the rolling baseline average and the green solid line indicates the trigger threshold in the case of a static trigger.

In the DER, a rolling baseline is calculated for each channel by processing samples continuously at the same time as they are checked against the trigger criteria, following the same procedure using low-pass filters (see Table 5.1 on page 137) as in Eq. (37) (from page 91).

As each sample is processed, it is evaluated by calculating the deviation from the baseline as $dev = |x_i - bsl_i|$ where x_i is the current sample and bsl_i is the current value of the baseline. The trigger condition is

$$dev > n \times rms_i, \tag{70}$$

where n is the number of standard deviations.

If the test condition returns true, a counter that tracks how many samples have met this criterion is incremented. If a subsequent sample is below threshold, the counter is decremented. The counter increments until it reaches 3, and decrements until it reaches 0. At 3 samples, a waveform is considered to have been identified. Once a waveform has been identified, the counter is reset and disregarded for the remainder of the waveform, and the baseline threshold value is held fixed. When the signal drops below the threshold again, it is considered the end of the waveform without requiring that the counter reaches 0 first.[61]

The start and end times of all of the waveforms are compared against one another. Waveforms are only grouped if the end time of a previous waveform is sufficiently close to the start time of the next waveform. This process continues until all waveforms are found, and grouped as needed. Pre- and post-triggers are added before and after the first and last waveform in every group of waveforms, and then the resulting POD is saved to disk.

The DER has configurable trigger thresholds for low-gain and high-gain channels, and for the number of samples for the inter-waveform trigger condition. The number of pre- and post-trigger samples in the POD can also be separately adjusted.

A sample containing digitised pulses collected from a simulated high-gain amplifier channel is shown in Fig. 5.32.

[61] The waveforms are first compared to adjacent waveforms (if there were any), and also padded with pre- and post-samples.

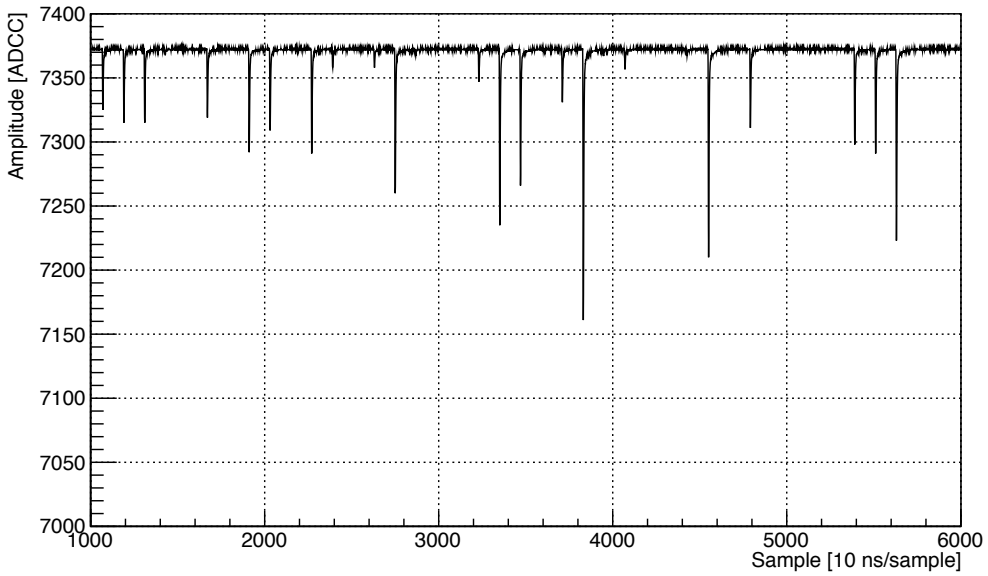


Figure 5.32: Simulated digitised sample waveforms on a single high-gain channel showing (single and double) photoelectron production, and the baseline ADCC (offset by +900 mV so that the baseline is at 7372 ADCC) with Gaussian white noise added into the DER model.

The dynamic range depends on the maximum number of single photoelectrons that can be collected without incurring a loss of information due to the effect of clipping on the digitised signal. Since the PMT signal is safely in the pass band of the analogue front-end, the gain implies a nominal S1 single photoelectron pulse height of about 6 mV for the high-gain channel. In light of the 22 % double photoelectron emission enhancement, this implies a dynamic range of 259 phd (316 phe), assuming each single photoelectron response is identical and that all responses occur at exactly the same point in time on a single PMT. As an example, using the LZ estimate in [122] of 470 scintillation photons which would be produced in a 10 keV electron recoil event, and then multiplying by the maximum possible optimistic scenario for the photon detection efficiency (around 15 %) gives 70 photons, representing only 27 % of the dynamic range when all of those photons are incident on a single PMT.

5.7 ^{83m}Kr Calibration Source Simulation

The DER must preserve the timing structure of the particle simulations from BACCARAT, not just for the single photoelectron response, but also for larger signals such as the S2. The detector response is checked by propagating events through BACCARAT and DER, and verifying the dispersion in the S2 signal that is seen in the entire top array. This forms an important part of reconstructing events and validating the detector response that is seen by the DAQ.

^{83m}Kr is a useful calibration source since, due to its short half-life, it does not pose a big risk to the detector, and it can be circulated easily. The initial energy deposit is 32.1 keV which is followed by a secondary recoil of 9.4 keV for a total of 41.5 keV. The decay scheme for ^{83m}Kr is shown in Fig. 5.33.

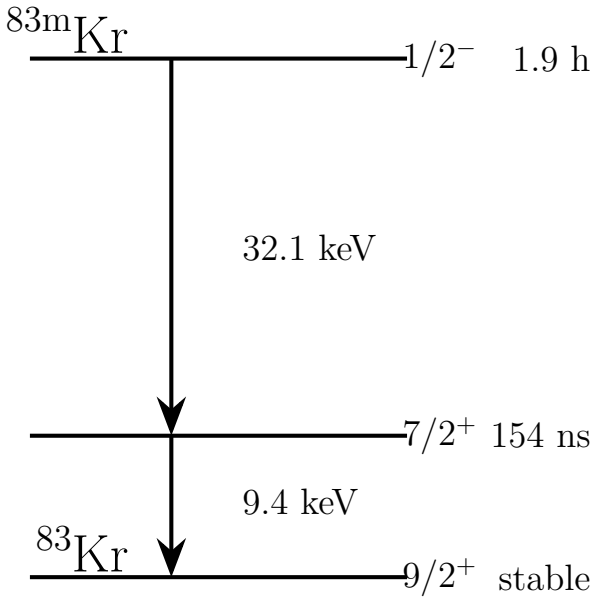


Figure 5.33: Decay scheme of ^{83m}Kr.

The S2 signal of a ^{83m}Kr decay event propagated through the DER model is shown in Fig. 5.34, with the accompanying total S1 signal in Fig. 5.35. The reconstructed energy of the event is 40.6 keV, and the actual total energy deposited was 41.5 keV, which is correct to within 2.2 %. The S2 width is 1.2 µs ± 0.08 %; it is expected to be 1.2 µs.

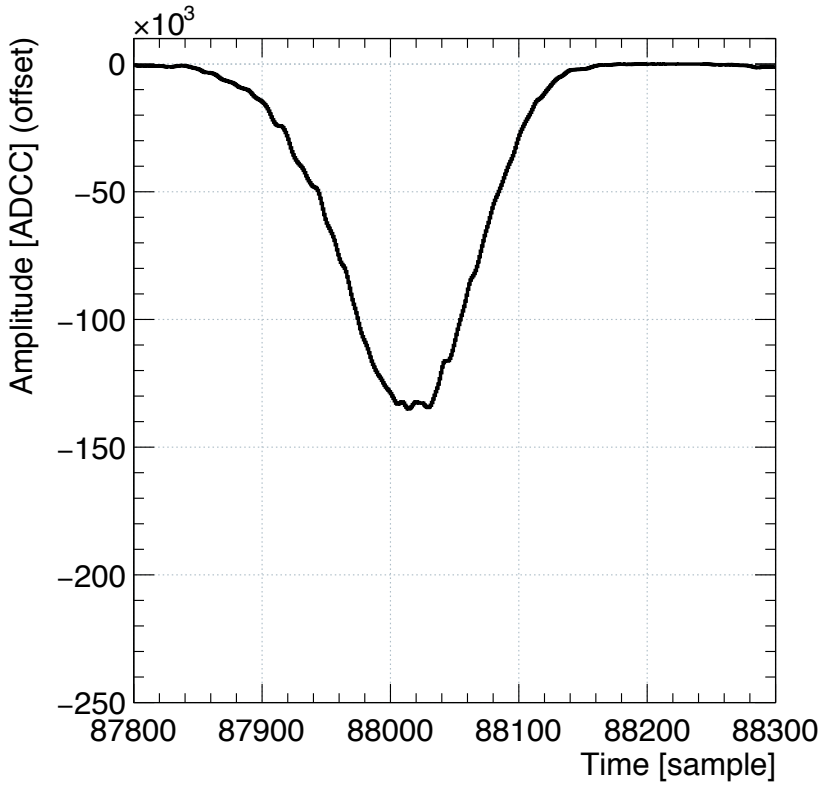


Figure 5.34: High-gain summed top PMT array S2 for a ^{83m}Kr decay event.

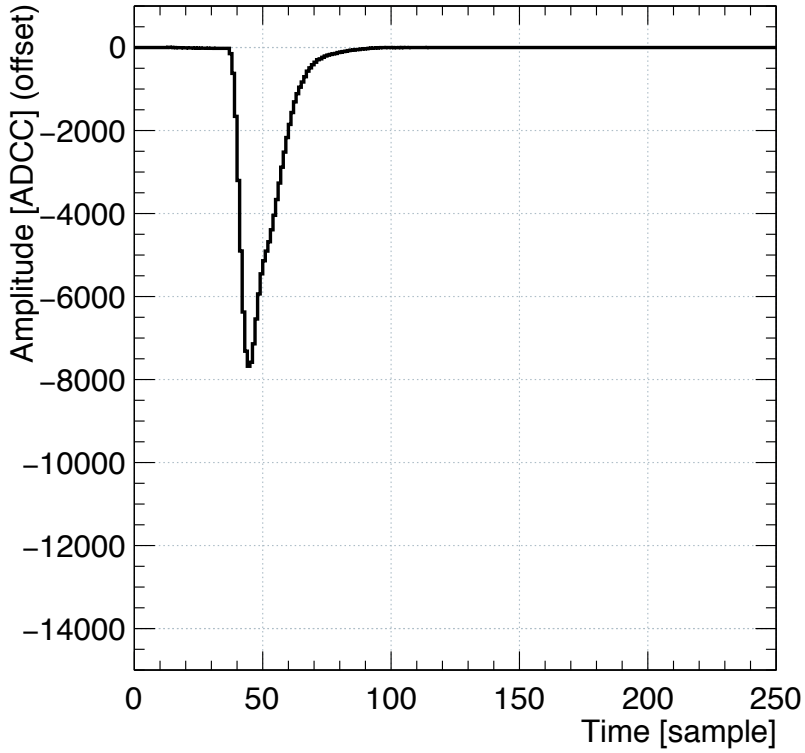


Figure 5.35: High-gain summed bottom and top PMT array S1 for a ^{83m}Kr decay event.

5.8 Energy Reconstruction

To test the complete DER with higher statistics, a simulation of 94 423 electron recoil events with energies in the range 0 keV to 10 keV are processed through the full simulation chain from BACCARAT to DER and LZap, with the goal of reconstructing the energy of the events. The events are simulated about the central position in the TPC liquid, which is at $x = y = 0\,\text{cm}, z = 75\,\text{cm}$ relative to the centre of the cathode. An accurate determination of the number of S1 and S2 photons detected depends on the single photoelectron response from the DER, and on analysis of the waveform data such as through photon counting, to account for the double photoelectron effect. The analysis uses a three-fold cut on S1 photons, which cuts events that are close to or below the 1 keVee level. A 350 phd minimum cut on the S2 signal is also applied. A total of 84 286 events pass all cuts.

The energy reconstruction process uses Eq. (25) (from page 53) to calculate the reconstructed electron recoil energy from the number of S1 and S2 quanta

$$E_{\text{ER}}^{rec} = \left(\frac{\text{S1}}{g_1} + \frac{\text{S2}}{g_2}\right) W. \tag{25}$$

where $g_1 = 0.085, g_2 = 70\,\text{phd/e}$, and $W = 13.8\,\text{eV}$, which are nominal values[62] [1].

Shown in Fig. 5.36 is the reconstructed recoil energy distribution produced by analysing the events in light of the known analogue signal chain single photoelectron response due to the DER, having used LZap to produce corrected reduced quantities. Shown also is the recoil energy based on the true number of S1 and S2 photons. Fig. 5.37 shows a scatter plot of the true and reconstructed energy of the recoil events, indicating on average the analysed events closely agree with the expectation based on the Monte Carlo truth data, while at the individual event level the resolution shows a larger variation near threshold than at intermediate and higher energies.

[62] See Table 2.1 on page 45, and page 71.

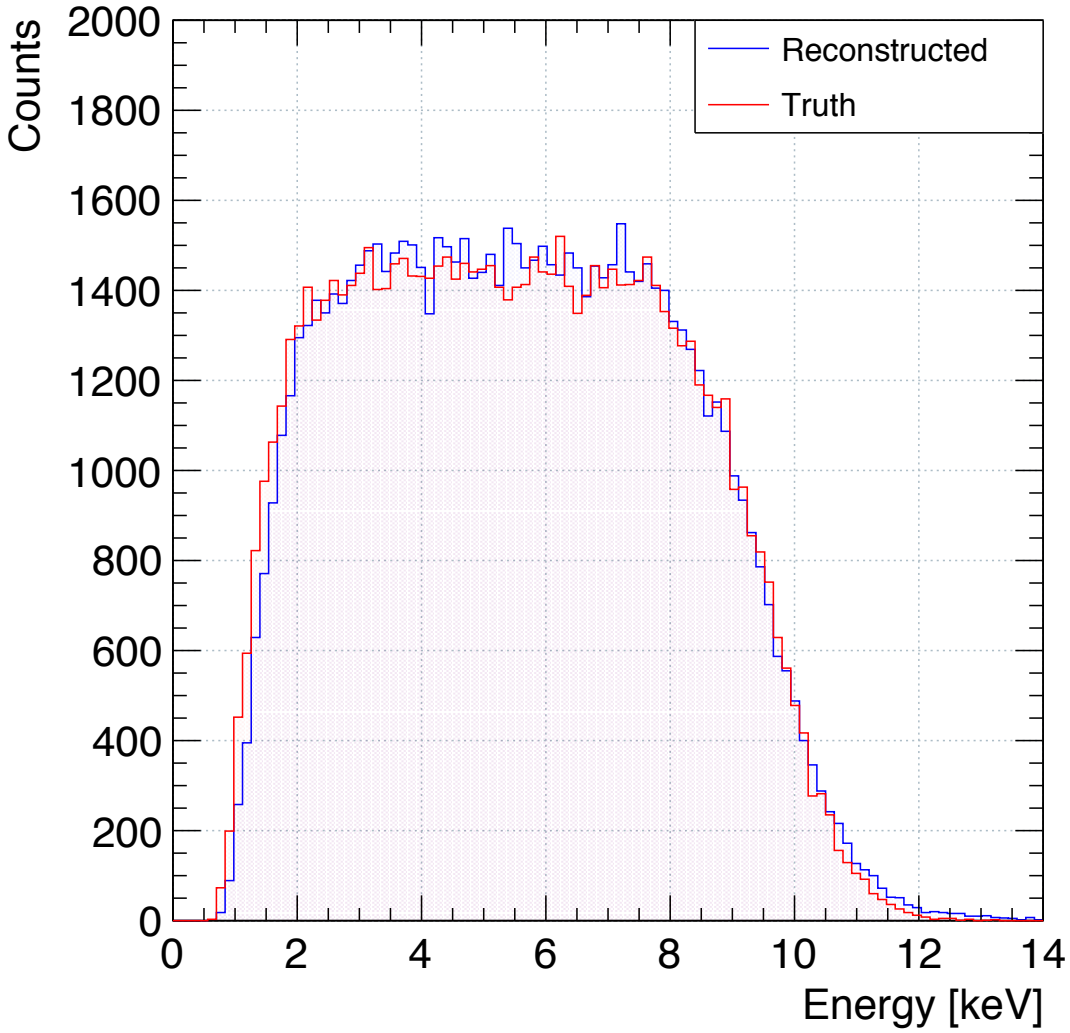


Figure 5.36: Reconstructed recoil energy distribution (blue) for simulated electron recoil events, superimposed with the energy spectrum based on the truth information (red).

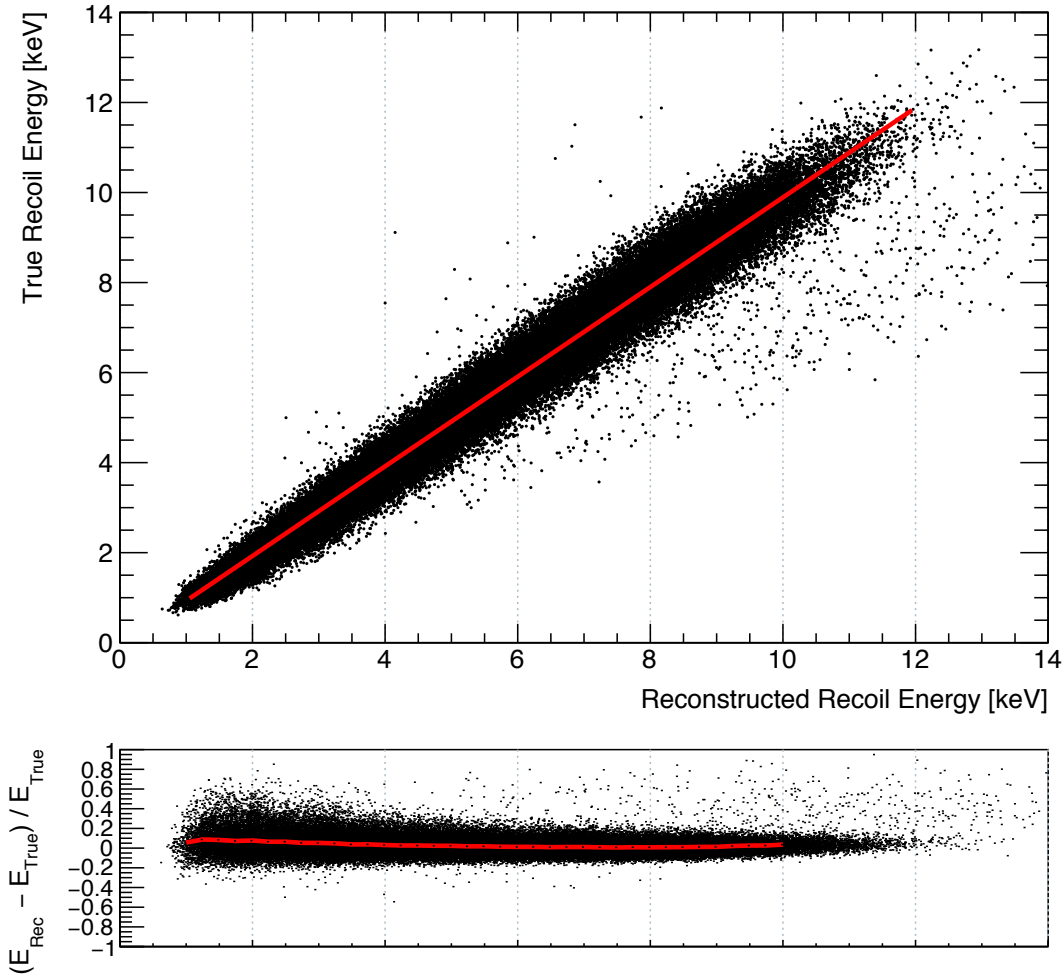


Figure 5.37: Scatter plot of the reconstructed recoil energy versus Monte Carlo truth. In the top plot, a perfect reconstruction corresponds to a straight-line through the origin $x = y$. The fit (slope value $0.99 \pm 0.06\,\%$) is shown as a solid red line. A small fraction of the events fall below the $x = y$ line, indicating an overestimation of the reconstructed quanta in LZap compared to the true number of quanta. In the bottom plot, the fractional differences between the reconstructed energy $\mathrm{E_{Rec}}$ and the Monte Carlo truth energy $\mathrm{E_{True}}$ are shown, along with a solid red line to indicate the mean; which was calculated by binning the data into 0.25 keV intervals from the 1 keV threshold to 10 keV.

5.9 Expected Event Data Processing

Assessing the anticipated resource requirements for processing simulated and real events is a key part of the readiness of the experiment. LZ has data centres in the US and in the UK which provide storage capacity for simulated and real data. The production of simulation data will require on the order of 100 TB of capacity until the year 2020. The USDC has 220 TB of disk space while the UKDC storage will increase from 220 TB ($\sim$ 2016) to 650 TB in 2019 in preparation for real data [1].

Furthermore, for real LZ, raw DAQ files must be quickly processed in realtime by the Event Builder (EB) system into event level files that are offloaded to storage - ready for analysis. The data rate of the EB is a function of the types of events being collected, and it determines the resource requirements on rack space and the number of computers that are required to operate in parallel to process events in a timely manner.

In order to simulate the event data rate and volume, the DER was used to produce simulated raw DAQ data so that the EB system could process it as if it were real data. The purpose of this is to stress test the performance of the EB computers and the processing toolchain. Shown in Table 5.3 are the data volume and processing rates reported by the EB computers[63]. The sources used in these benchmarks are representative of calibration sources that LZ can use, and they provide a range of event recoil energies to test the EB system under different data-taking scenarios.

Compared to the anticipated event rate of these sources, ^{83m}Kr (expect 140 Hz) and ^{131m}Xe fare well and agree with expectations for LZ based on LUX experience. The DD neutron events (2.45 MeV) are at the upper end of the energy spectrum of typical calibration sources and are processed more slowly - to that end an intermediate storage of binary files followed by later event building is being considered.

[63] Specifications of the computer in Appendix G.

Table 5.3: Data processing rates and compression ratio for events simulated by the DER in the binary output format that were processed by the LZ Event Builder [192]. For DD neutrons the energy is 2.45 MeV.

Source	**Rate** [Hz]	**Size** [MB/evt]	**Compression**
^{83m}Kr	192.98	0.42	1.83
^{131m}Xe	125.00	0.64	1.54
DD Neutrons	3.0	5.29	1.57

The DER is a Monte Carlo simulation package that contains an analytical model of the analogue front-end detector electronics of LZ. The response of the detector electronics has been quantified, and several example events including a calibration source have been analysed. The performance of the data acquisition system that will be used for real event data has been benchmarked with a number of simulated sources. The single photoelectron response underpins the data taking process of the LZ experiment, and the DER provides a simulated environment within which physics data can be analysed.

6 Summary and Outlook

The hardware contribution of this thesis has characterised the sensor performance, and, based on experience gained at the LZ System Test, gives confidence that acoustic sensors will increase the fidelity of the data in LZ. The sensors serve as a diagnostic veto for acoustic signals accompanying TPC events. The requirement is that bubbles are detected from an in-situ calibration via a resistor heating the LXe. An algorithm that identifies the presence of bubbles correctly 99 % of the time has been developed, and this gives confidence that bubbles can be identified during the calibration and data-taking. An analysis module that distinguishes between bubbles and other types of sound has been developed. All eight acoustic sensors for real LZ have been cleaned, assembled, characterised, and delivered to SURF ready for installation.

The contribution of this thesis to the analysis software is an analytical model of the front-end detector electronics response of the TPC, that includes the photomultiplier tubes, the amplifiers, the digitiser, and the interconnecting cabling. The work of the thesis has led to a more optimal design of the front-end electronics. The model predicts the single photoelectron response correctly to within 1 % and 2 % of the design goal (area gain 4 and 40 for low-gain and high-gain channels) and characterises the single photoelectron dynamic range at 259 phd. Furthermore, a software package was created for the analytical model that is fully integrated into the LZ simulation packages and the analysis framework. The performance of the simulation is $O(N)$, and is over 10^4 times faster than engineering tools such as SPICE. The simulation has benchmarked and validated the performance of the LZ event builder with the calibration sources ^{83m}Kr at 193 Hz, ^{131m}Xe at 125 Hz, and 2.45 MeV DD neutrons at 3.0 Hz. A demonstration of the application of the model was performed by reconstructing the energy of 0 keVer to 10 keVer recoil events and the calibration source ^{83m}Kr. The analysis of simulated physics events in LZ builds on the model and the simulation that were developed in this thesis.

7 References

[1] B. J. Mount *et al.*, "LUX-ZEPLIN (LZ) Technical Design Report," arXiv:1703.09144 [physics.ins-det].

[2] Malling, D. C. et al., "After LUX: The LZ Program," *ArXiv e-prints* (Oct., 2011) , arXiv:1110.0103 [astro-ph.IM].

[3] G. Bertone and J. Silk, *Particle Dark Matter Observations, Models and Searches*. Cambridge University Press, United States of America, 2010.

[4] M. Milgrom, "Dynamics with a non-standard inertia-acceleration relation: an alternative to dark matter," *Annals Phys.* **229** (1994) 384–415, arXiv:astro-ph/9303012 [astro-ph].

[5] J. D. Bekenstein, "Relativistic gravitation theory for the MOND paradigm," *Phys. Rev.* **D70** (2004) 083509, arXiv:astro-ph/0403694 [astro-ph]. [Erratum: Phys. Rev.D71,069901(2005)].

[6] R. Scarpa, "Modified newtonian dynamics, an introductory review," *AIP Conf. Proc.* **822** (2006) 253–265, arXiv:astro-ph/0601478 [astro-ph]. [,253(2006)].

[7] B. W. Carroll and D. A. Ostlie, *An Introduction to Modern Astrophysics*. Pearson Addison-Wesley, United States of America, 2 ed., 2007.

[8] B. A. Bassett and R. Hlozek, "Baryon Acoustic Oscillations," arXiv:0910.5224 [astro-ph.CO].

[9] D. Samtleben, S. Staggs, and B. Winstein, "The Cosmic microwave background for pedestrians: A Review for particle and nuclear physicists," *Ann. Rev. Nucl. Part. Sci.* **57** (2007) 245–283, arXiv:0803.0834 [astro-ph].

[10] **Planck** Collaboration, P. A. R. Ade *et al.*, "Planck 2013 results. XVI. Cosmological parameters," *Astron. Astrophys.* **571** (2014) A16,

arXiv:1303.5076 [astro-ph.CO].

[11] C. L. Bennett *et al.*, "Nine-year Wilkinson Microwave Anisotropy Probe (WMAP) Observations: Final Maps and Results," *The Astrophysical Journal Supplement* **208** (Oct., 2013) 20, arXiv:1212.5225.

[12] D. N. Spergel and P. J. Steinhardt, "Observational evidence for selfinteracting cold dark matter," *Phys. Rev. Lett.* **84** (2000) 3760–3763, arXiv:astro-ph/9909386 [astro-ph].

[13] R. Barkana, Z. Haiman, and J. P. Ostriker, "Constraints on warm dark matter from cosmological reionization," *Astrophys. J.* **558** (2001) 482, arXiv:astro-ph/0102304 [astro-ph].

[14] M. Viel, J. Lesgourgues, M. G. Haehnelt, S. Matarrese, and A. Riotto, "Constraining warm dark matter candidates including sterile neutrinos and light gravitinos with WMAP and the Lyman-alpha forest," *Phys. Rev.* **D71** (2005) 063534, arXiv:astro-ph/0501562 [astro-ph].

[15] M. Kuhlen, M. Vogelsberger, and R. Angulo, "Numerical Simulations of the Dark Universe: State of the Art and the Next Decade," *Phys. Dark Univ.* **1** (2012) 50–93, arXiv:1209.5745 [astro-ph.CO].

[16] V. Springel *et al.*, "Simulating the joint evolution of quasars, galaxies and their large-scale distribution," *Nature* **435** (2005) 629–636, arXiv:astro-ph/0504097 [astro-ph].

[17] J. Baur, N. Palanque-Delabrouille, C. Yèche, C. Magneville, and M. Viel, "Lyman-alpha Forests cool Warm Dark Matter," *JCAP* **1608** no. 08, (2016) 012, arXiv:1512.01981 [astro-ph.CO].

[18] H. Tananbaum, M. C. Weisskopf, W. Tucker, B. Wilkes, and P. Edmonds, "Highlights and Discoveries from the Chandra X-ray Observatory," *Rept. Prog. Phys.* **77** (2014) 066902, arXiv:1405.7847 [astro-ph.HE].

[19] **SDSS** Collaboration, P. McDonald *et al.*, "The Lyman-alpha forest

power spectrum from the Sloan Digital Sky Survey," *Astrophys. J. Suppl.* **163** (2006) 80–109, arXiv:astro-ph/0405013 [astro-ph].

[20] F. Zwicky, "Die Rotverschiebung von extragalaktischen Nebeln," *Helvetica Physica Acta* **6** (1933) 110–127.

[21] A. Einstein, "Kosmologische Betrachtungen zur allgemeinen Relativitätstheorie," *Sitzungsberichte der Königlich Preußischen Akademie der Wissenschaften (Berlin), Seite 142-152.* (1917) 1 ff.

[22] A. Einstein, "Zum kosmologischen problem der allgemeinen relativitätstheorie," *Sitzungsber. Preuss. Akad. Wiss.* **142** (1931) 235–237.

[23] G. Woan, *The Cambridge Handbook of Physics Formulas.* Cambridge University Press, United States of America, 2003 ed., 2009.

[24] F. Zwicky, "On the masses of nubulae and of clusters of nebulae," *The Astrophysical Journal* **86** no. 3, (1937) 1 ff.

[25] V. C. Rubin and W. K. Ford, Jr., "Rotation of the Andromeda Nebula from a Spectroscopic Survey of Emission Regions," *apj* **159** (Feb., 1970) 379.

[26] V. C. Rubin, N. Thonnard, and W. K. Ford, Jr., "Extended rotation curves of high-luminosity spiral galaxies. IV - Systematic dynamical properties, SA through SC," *apjl* **225** (Nov., 1978) L107–L111.

[27] D. Clowe, M. Bradac, A. H. Gonzalez, M. Markevitch, S. W. Randall, C. Jones, and D. Zaritsky, "A direct empirical proof of the existence of dark matter," *Astrophys. J.* **648** (2006) L109–L113, arXiv:astro-ph/0608407 [astro-ph].

[28] D.-C. Dai, R. Matsuo, and G. Starkman, "Gravitational Lenses in Generalized Einstein-Aether theory: The Bullet Cluster," *Phys. Rev.* **D78** (2008) 104004, arXiv:0806.4319 [gr-qc].

[29] M. L. Kutner, *Astronomy A Physical Perspective*. Cambridge University Press, Cambridge, United Kingdom, 2 ed., 2011.

[30] Y. Ali-Haïmoud and M. Kamionkowski, "Cosmic microwave background limits on accreting primordial black holes," *Phys. Rev.* **D95** no. 4, (2017) 043534, arXiv:1612.05644 [astro-ph.CO].

[31] **EROS-2** Collaboration, P. Tisserand *et al.*, "Limits on the Macho Content of the Galactic Halo from the EROS-2 Survey of the Magellanic Clouds," *Astron. Astrophys.* **469** (2007) 387–404, arXiv:astro-ph/0607207 [astro-ph].

[32] M. A. Monroy-Rodríguez and C. Allen, "The End of the MACHO Era, Revisited: New Limits on MACHO Masses from Halo Wide Binaries," *The Astrophysical Journal* **790** (Aug., 2014) 159, arXiv:1406.5169.

[33] B. J. Carr, K. Kohri, Y. Sendouda, and J. Yokoyama, "New cosmological constraints on primordial black holes," *Phys. Rev.* **D81** (2010) 104019, arXiv:0912.5297 [astro-ph.CO].

[34] S. Clesse and J. García-Bellido, "The clustering of massive Primordial Black Holes as Dark Matter: measuring their mass distribution with Advanced LIGO," *Phys. Dark Univ.* **10** (2016) 002, arXiv:1603.05234 [astro-ph.CO].

[35] S. Bird, I. Cholis, J. B. Muñoz, Y. Ali-Haïmoud, M. Kamionkowski, E. D. Kovetz, A. Raccanelli, and A. G. Riess, "Did LIGO detect dark matter?," *Phys. Rev. Lett.* **116** no. 20, (2016) 201301, arXiv:1603.00464 [astro-ph.CO].

[36] B. Carr, F. Kuhnel, and M. Sandstad, "Primordial Black Holes as Dark Matter," *Phys. Rev.* **D94** no. 8, (2016) 083504, arXiv:1607.06077 [astro-ph.CO].

[37] **MACHO, EROS** Collaboration, C. Alcock *et al.*, "EROS and MACHO combined limits on planetary mass dark matter in the

galactic halo," *Astrophys. J.* **499** (1998) L9, arXiv:astro-ph/9803082 [astro-ph].

[38] **Planck** Collaboration, P. Ade *et al.*, "Planck 2015 results. XIII. Cosmological parameters," arXiv:1502.01589 [astro-ph.CO].

[39] Y. Sofue and V. Rubin, "Rotation curves of spiral galaxies," *Ann.Rev.Astron.Astrophys.* **39** (2001) 137–174, arXiv:astro-ph/0010594 [astro-ph].

[40] R. J. Wilkinson, J. Lesgourgues, and C. Boehm, "Using the CMB angular power spectrum to study Dark Matter-photon interactions," *JCAP* **1404** (2014) 026, arXiv:1309.7588 [astro-ph.CO].

[41] J. Ellis, "Casting Light on Dark Matter," arXiv:1106.2923 [hep-ph].

[42] S. P. Martin, "A Supersymmetry primer," arXiv:hep-ph/9709356 [hep-ph].

[43] J. Ellis and K. A. Olive, "Supersymmetric Dark Matter Candidates," arXiv:1001.3651 [astro-ph.CO].

[44] A. Birkedal, A. Noble, M. Perelstein, and A. Spray, "Little Higgs dark matter," *Phys. Rev.* **D74** (2006) 035002, arXiv:hep-ph/0603077 [hep-ph].

[45] J. L. Feng, "Dark Matter Candidates from Particle Physics and Methods of Detection," *Ann. Rev. Astron. Astrophys.* **48** (2010) 495–545, arXiv:1003.0904 [astro-ph.CO].

[46] S. Liem, G. Bertone, F. Calore, R. Ruiz de Austri, T. M. P. Tait, R. Trotta, and C. Weniger, "Effective Field Theory of Dark Matter: a Global Analysis," *JHEP* **09** (2016) 077, arXiv:1603.05994 [hep-ph].

[47] **SuperCDMS** Collaboration, K. Schneck *et al.*, "Dark matter effective field theory scattering in direct detection experiments," *Phys. Rev.* **D91** no. 9, (2015) 092004, arXiv:1503.03379 [astro-ph.CO].

[48] M. Bauer *et al.*, "Towards the next generation of simplified Dark Matter models," arXiv:1607.06680 [hep-ex].

[49] M. Lisanti, "Lectures on Dark Matter Physics," in *Theoretical Advanced Study Institute in Elementary Particle Physics: New Frontiers in Fields and Strings (TASI 2015) Boulder, CO, USA, June 1-26, 2015.*

[50] R. Massey, T. Kitching, and J. Richard, "The dark matter of gravitational lensing," *Rept. Prog. Phys.* **73** (2010) 086901, arXiv:1001.1739 [astro-ph.CO].

[51] R. D. Peccei, "The Strong CP problem and axions," *Lect. Notes Phys.* **741** (2008) 3–17, arXiv:hep-ph/0607268 [hep-ph]. [,3(2006)].

[52] C. A. Baker *et al.*, "Improved experimental limit on the electric dipole moment of the neutron," *Phys. Rev. Lett.* **97** (Sep, 2006) 131801.

[53] R. D. Peccei and H. R. Quinn, "CP Conservation in the Presence of Pseudoparticles," *Phys. Rev. Lett.* **38** (Jun, 1977) 1440–1443.

[54] D. J. E. Marsh, "Axion Cosmology," *Phys. Rept.* **643** (2016) 1–79, arXiv:1510.07633 [astro-ph.CO].

[55] P. Sikivie, "Experimental Tests of the Invisible Axion," *Phys. Rev. Lett.* **51** (1983) 1415–1417. [Erratum: Phys. Rev. Lett.52,695(1984)].

[56] N. D. Barrie, A. Kobakhidze, M. Talia, and L. Wu, "750 GeV Composite Axion as the LHC Diphoton Resonance," *Phys. Lett.* **B755** (2016) 343–347, arXiv:1602.00475 [hep-ph].

[57] T. Higaki, K. S. Jeong, and F. Takahashi, "The 7 keV axion dark matter and the X-ray line signal," *Phys. Lett.* **B733** (2014) 25–31, arXiv:1402.6965 [hep-ph].

[58] M. Kawasaki and K. Nakayama, "Axions: Theory and Cosmological Role," *Ann. Rev. Nucl. Part. Sci.* **63** (2013) 69–95, arXiv:1301.1123 [hep-ph].

[59] **CAST** Collaboration, V. Anastassopoulos *et al.*, "New CAST Limit on the Axion-Photon Interaction," *Nature Phys.* **13** (2017) 584–590, arXiv:1705.02290 [hep-ex].

[60] **CAST** Collaboration, E. Arik *et al.*, "Probing eV-scale axions with CAST," *JCAP* **0902** (2009) 008, arXiv:0810.4482 [hep-ex].

[61] R. Ballou *et al.*, "Latest Results of the OSQAR Photon Regeneration Experiment for Axion-Like Particle Search," in *Proceedings, 10th Patras Workshop on Axions, WIMPs and WISPs (AXION-WIMP 2014): Geneva, Switzerland, June 29-July 4, 2014.*

[62] K. van Bibber and G. Carosi, "Status of the ADMX and ADMX-HF experiments," in *8th Patras Workshop on Axions, WIMPs and WISPs (AXION-WIMP 2012) Chicago, Illinois, July 18-22, 2012.*

[63] S. Chaudhuri, P. W. Graham, K. Irwin, J. Mardon, S. Rajendran, and Y. Zhao, "Radio for hidden-photon dark matter detection," *Phys. Rev.* **D92** no. 7, (2015) 075012, arXiv:1411.7382 [hep-ph].

[64] I. P. Stern, "Axion Dark Matter Searches," *AIP Conf. Proc.* **1604** (2014) 456–461, arXiv:1403.5332 [physics.ins-det].

[65] **Particle Data Group** Collaboration, C. Patrignani *et al.*, "Review of Particle Physics," *Chin. Phys.* **C40** no. 10, (2016 and 2017 update) 100001.

[66] X.-J. Bi, P.-F. Yin, and Q. Yuan, "Status of Dark Matter Detection," *Front.Phys.China* **8** (2013) 794–827, arXiv:1409.4590 [hep-ph].

[67] **CMS** Collaboration, V. Khachatryan *et al.*, "Search for dark matter, extra dimensions, and unparticles in monojet events in proton-proton collisions at $\sqrt{s} = 8$ TeV," *Eur. Phys. J.* **C75** no. 5, (2015) 235, arXiv:1408.3583 [hep-ex].

[68] **ATLAS** Collaboration, M. Aaboud *et al.*, "Search for dark matter at $\sqrt{s} = 13$ TeV in final states containing an energetic photon and large

missing transverse momentum with the ATLAS detector," *Eur. Phys. J.* **C77** no. 6, (2017) 393, arXiv:1704.03848 [hep-ex].

[69] **DES, Fermi-LAT** Collaboration, A. Albert *et al.*, "Searching for Dark Matter Annihilation in Recently Discovered Milky Way Satellites with Fermi-LAT," *Astrophys. J.* **834** no. 2, (2017) 110, arXiv:1611.03184 [astro-ph.HE].

[70] **Fermi-LAT** Collaboration, E. Charles *et al.*, "Sensitivity Projections for Dark Matter Searches with the Fermi Large Area Telescope," *Phys. Rept.* **636** (2016) 1–46, arXiv:1605.02016 [astro-ph.HE].

[71] **IceCube** Collaboration, M. G. Aartsen *et al.*, "Improved limits on dark matter annihilation in the Sun with the 79-string IceCube detector and implications for supersymmetry," *JCAP* **1604** no. 04, (2016) 022, arXiv:1601.00653 [hep-ph].

[72] A. E. Currie, *Direct searches for WIMP dark matter with ZEPLIN-III.* PhD thesis, Imperial College London, 2012.

[73] **CoGeNT** Collaboration, C. E. Aalseth *et al.*, "CoGeNT: A Search for Low-Mass Dark Matter using p-type Point Contact Germanium Detectors," *Phys. Rev.* **D88** (2013) 012002, arXiv:1208.5737 [astro-ph.CO].

[74] **EDELWEISS** Collaboration, E. Armengaud *et al.*, "A search for low-mass WIMPs with EDELWEISS-II heat-and-ionization detectors," *Phys. Rev.* **D86** (2012) 051701, arXiv:1207.1815 [astro-ph.CO].

[75] **CRESST-II** Collaboration, G. Angloher *et al.*, "Results on low mass WIMPs using an upgraded CRESST-II detector," *Eur. Phys. J.* **C74** no. 12, (2014) 3184, arXiv:1407.3146 [astro-ph.CO].

[76] "A prototype detector for the CRESST-III low-mass dark matter search," *Nuclear Instruments and Methods in Physics Research Section A: Accelerators, Spectrometers, Detectors and Associated Equipment*

845 no. Supplement C, (2017) 414 – 417. Proceedings of the Vienna Conference on Instrumentation 2016.

[77] G. Angloher *et al.*, "Results from 730 kg days of the CRESST-II Dark Matter search," *European Physical Journal C* **72** (Apr., 2012) 1971, arXiv:1109.0702.

[78] **CDMS-II** Collaboration, Z. Ahmed *et al.*, "Dark Matter Search Results from the CDMS II Experiment," *Science* **327** (2010) 1619–1621, arXiv:0912.3592 [astro-ph.CO].

[79] K. Freese, M. Lisanti, and C. Savage, "Colloquium: Annual modulation of dark matter," *Rev. Mod. Phys.* **85** (2013) 1561–1581, arXiv:1209.3339 [astro-ph.CO].

[80] R. Bernabei *et al.*, "Final model independent result of DAMA/LIBRA-phase1," *Eur. Phys. J.* **C73** (2013) 2648, arXiv:1308.5109 [astro-ph.GA].

[81] R. Barnabei, "First model-independent results by DAMA/LIBRA-phase2." Presentation from Scientific Committee Meeting March 2018, 3, 2018.

[82] "The DAMA/LIBRA apparatus," *Nuclear Instruments and Methods in Physics Research Section A: Accelerators, Spectrometers, Detectors and Associated Equipment* **592** no. 3, (2008) 297 – 315.

[83] E. Fernandez-Martinez and R. Mahbubani, "The Gran Sasso muon puzzle," *JCAP* **1207** (2012) 029, arXiv:1204.5180 [astro-ph.HE].

[84] **CRESST** Collaboration, G. Angloher *et al.*, "Results on light dark matter particles with a low-threshold CRESST-II detector," *Eur. Phys. J.* **C76** no. 1, (2016) 25, arXiv:1509.01515 [astro-ph.CO].

[85] **CDMS** Collaboration, R. Agnese *et al.*, "Silicon Detector Dark Matter Results from the Final Exposure of CDMS II," *Phys. Rev. Lett.* **111** no. 25, (2013) 251301, arXiv:1304.4279 [hep-ex].

[86] **SuperCDMS Collaboration** Collaboration, R. Agnese *et al.*, "Improved WIMP-search reach of the CDMS II germanium data," *Phys. Rev. D* **92** (Oct, 2015) 072003.

[87] **SuperCDMS Collaboration** Collaboration, R. Agnese *et al.*, "New results from the search for low-mass weakly interacting massive particles with the cdms low ionization threshold experiment," *Phys. Rev. Lett.* **116** (Feb, 2016) 071301.

[88] L. Hehn *et al.*, "Improved EDELWEISS-III sensitivity for low-mass WIMPs using a profile likelihood approach," *The European Physical Journal C* **76** no. 10, (Oct, 2016) 548.

[89] **XENON** Collaboration, E. Aprile *et al.*, "Low-mass dark matter search using ionization signals in XENON100," *Phys. Rev.* **D94** no. 9, (2016) 092001, `arXiv:1605.06262 [astro-ph.CO]`. [Erratum: Phys. Rev.D95,no.5,059901(2017)].

[90] **CRESST** Collaboration, F. Petricca *et al.*, "First results on low-mass dark matter from the CRESST-III experiment," in *15th International Conference on Topics in Astroparticle and Underground Physics (TAUP 2017) Sudbury, Ontario, Canada, July 24-28, 2017*.

[91] **CDEX** Collaboration, H. Jiang *et al.*, "Limits on light WIMPs from the first 102.8 kg-days data of the CDEX-10 experiment," `arXiv:1802.09016 [hep-ex]`.

[92] **LUX** Collaboration, D. S. Akerib *et al.*, "Improved Limits on Scattering of Weakly Interacting Massive Particles from Reanalysis of 2013 LUX Data," *Phys. Rev. Lett.* **116** no. 16, (2016) 161301, `arXiv:1512.03506 [astro-ph.CO]`.

[93] P. Beltrame, "LZ UK WIMP Challenge." Unpublished, 2016.

[94] G. J. Feldman and R. D. Cousins, "Unified approach to the classical statistical analysis of small signals," *Phys. Rev. D* **57** (Apr, 1998)

3873–3889.

[95] **LUX** Collaboration, D. S. Akerib *et al.*, "First results from the LUX dark matter experiment at the Sanford Underground Research Facility," *Phys. Rev. Lett.* **112** (2014) 091303, arXiv:1310.8214 [astro-ph.CO].

[96] Y.-Z. Chen, Y.-A. Luo, L. Li, H. Shen, and X.-Q. Li, "Determining the nuclear form factor for detection of dark matter in the relativistic mean field theory," *Commun. Theor. Phys.* **55** (2011) 1059–1064, arXiv:1101.3049 [hep-ph].

[97] V. Chepel and H. Araujo, "Liquid noble gas detectors for low energy particle physics," *JINST* **8** (2013) R04001, arXiv:1207.2292 [physics.ins-det].

[98] J. Bovy and S. Tremaine, "On the Local Dark Matter Density," *apj* **756** (Sept., 2012) 89, arXiv:1205.4033 [astro-ph.GA].

[99] D. G. Cerdeno and A. M. Green, "Direct detection of WIMPs," arXiv:1002.1912 [astro-ph.CO].

[100] F. Marinho, L. Paulucci, and D. Galante, "Propagation and energy deposition of cosmic rays' muons on terrestrial environments," *Astrobiology* **13** (2014) 319–323, arXiv:1410.7076 [astro-ph.EP].

[101] P. J. Fox and E. Poppitz, "Leptophilic Dark Matter," *Phys. Rev.* **D79** (2009) 083528, arXiv:0811.0399 [hep-ph].

[102] T. Doke, A. Hitachi, J. Kikuchi, K. Masuda, H. Okada, and E. Shibamura, "Absolute scintillation yields in liquid argon and xenon for various particles," *Japanese Journal of Applied Physics* **41** no. 3R, 1538.

[103] M. Schumann, "Dark Matter Search with liquid Noble Gases," arXiv:1206.2169 [astro-ph.IM].

[104] S. C. Soong, "Inner-Shell Contributions to Electron Degradation Spectra," *Radiation Research* **67** no. 2, (1976) 187–214. http://www.jstor.org/stable/3574409.

[105] E. Aprile, A. Bolotnikov, A. Bolozdynya, and T. Doke, *Noble Gas Detectors*. Wiley-VCH, Federal Republic of Germany, 2006.

[106] "WIMP dark matter direct-detection searches in noble gases," *Physics of the Dark Universe* **4** (2014) 50 – 59. DARK TAUP2013.

[107] H. Araujo, "LXe Physics For Particle Detection - PartI Primary Quanta and Part II Detection." LZ UK Collaboration Meeting Workshop, 2016.

[108] M. Szydagis, N. Barry, K. Kazkaz, J. Mock, D. Stolp, M. Sweany, M. Tripathi, S. Uvarov, N. Walsh, and M. Woods, "NEST: a comprehensive model for scintillation yield in liquid xenon," *Journal of Instrumentation* **6** no. 10, P10002.

[109] B. Lenardo, K. Kazkaz, A. Manalaysay, J. Mock, M. Szydagis, and M. Tripathi, "A Global Analysis of Light and Charge Yields in Liquid Xenon," *IEEE Trans. Nucl. Sci.* **62** no. 6, (2015) 3387–3396, arXiv:1412.4417 [astro-ph.IM].

[110] "Emission spectra from Ar-Xe, Ar-Kr, Ar-N2, Ar-CH4, Ar-CO2 and Xe-N2 gas scintillation proportional counters," *Nuclear Instruments and Methods in Physics Research* **205** no. 3, (1983) 591 – 596.

[111] J. B. Birks, "Scintillations from organic crystals: Specific fluorescence and relative response to different radiations," *Proceedings of the Physical Society. Section A* **64** no. 10, 874.

[112] L. Onsager, "Initial Recombination of Ions," *Phys. Rev.* **54** (Oct, 1938) 554–557.

[113] E. Aprile, W. H. Ku, and J. Park, "Delta electron production and the ultimate energy resolution of liquid argon ionization detectors," *IEEE Transactions on Nuclear Science* **35** no. 1, (Feb, 1988) 37–41.

[114] J. Thomas and D. A. Imel, "Recombination of electron-ion pairs in liquid argon and liquid xenon," *Phys. Rev. A* **36** (Jul, 1987) 614–616.

[115] "Performance and fundamental processes at low energy in a two-phase liquid xenon dark matter detector," *Nuclear Instruments and Methods in Physics Research Section A: Accelerators, Spectrometers, Detectors and Associated Equipment* **579** no. 1, (2007) 451 – 453. Proceedings of the 11th Symposium on Radiation Measurements and Applications.

[116] E. Aprile, K. L. Giboni, P. Majewski, K. Ni, and M. Yamashita, "Observation of Anti-correlation between Scintillation and Ionization for MeV Gamma-Rays in Liquid Xenon," *Phys. Rev.* **B76** (2007) 014115, arXiv:0704.1118 [astro-ph].

[117] C. E. Dahl, *The physics of background discrimination in liquid xenon, and first results from Xenon10 in the hunt for WIMP dark matter*. PhD thesis, Princeton U., 2009.

[118] **LUX** Collaboration, D. S. Akerib *et al.*, "Tritium calibration of the LUX dark matter experiment," *Phys. Rev.* **D93** no. 7, (2016) 072009, arXiv:1512.03133 [physics.ins-det].

[119] P. Sorensen and C. E. Dahl, "Nuclear recoil energy scale in liquid xenon with application to the direct detection of dark matter," *Phys. Rev.* **D83** (2011) 063501, arXiv:1101.6080 [astro-ph.IM].

[120] F. Neves, A. Lindote, A. Morozov, V. Solovov, C. Silva, P. Bras, J. P. Rodrigues, and M. I. Lopes, "Measurement of the absolute reflectance of polytetrafluoroethylene (PTFE) immersed in liquid xenon," *JINST* **12** no. 01, (2017) P01017, arXiv:1612.07965 [physics.ins-det].

[121] E. Aprile and T. Doke, "Liquid Xenon Detectors for Particle Physics and Astrophysics," *Rev. Mod. Phys.* **82** (2010) 2053–2097, arXiv:0910.4956 [physics.ins-det].

[122] **LZ** Collaboration, D. S. Akerib *et al.*, "LUX-ZEPLIN (LZ) Conceptual

Design Report," arXiv:1509.02910 [physics.ins-det].

[123] **XENON** Collaboration, E. Aprile *et al.*, "Physics reach of the XENON1T dark matter experiment," *JCAP* **1604** no. 04, (2016) 027, arXiv:1512.07501 [physics.ins-det].

[124] S. Andringa *et al.*, *Current Status and Future Prospects of the SNO+ Experiment*, vol. 2016. 08, 2015.

[125] D. C. Malling, S. Fiorucci, M. Pangilinan, J. J. Chapman, C. H. Faham, J. R. Verbus, and R. J. Gaitskell, "Dark Matter Search Backgrounds from Primordial Radionuclide Chain Disequilibrium," arXiv:1305.5183 [astro-ph.IM].

[126] D. Yu. Akimov *et al.*, "WIMP-nucleon cross-section results from the second science run of ZEPLIN-III," *Phys. Lett.* **B709** (2012) 14–20, arXiv:1110.4769 [astro-ph.CO].

[127] **ZEPLIN-III** Collaboration, D. Yu. Akimov *et al.*, "Limits on inelastic dark matter from ZEPLIN-III," *Phys. Lett.* **B692** (2010) 180–183, arXiv:1003.5626 [hep-ex].

[128] C. Ghag *et al.*, "Performance of the veto detector incorporated into the ZEPLIN-III experiment," *Astroparticle Physics* **35** (Sept., 2011) 76–86, arXiv:1103.0393 [astro-ph.CO].

[129] **LUX** Collaboration, D. S. Akerib *et al.*, "The Large Underground Xenon (LUX) Experiment," *Nucl. Instrum. Meth.* **A704** (2013) 111–126, arXiv:1211.3788 [physics.ins-det].

[130] **LUX** Collaboration, M. Szydagis *et al.*, "A Detailed Look at the First Results from the Large Underground Xenon (LUX) Dark Matter Experiment," in *Proceedings, 10th International Symposium on Cosmology and Particle Astrophysics (CosPA 2013): Honolulu, Hawaii, USA, November 12-15, 2013*.

[131] **LUX** Collaboration, D. S. Akerib *et al.*, "Results from a search for

dark matter in the complete LUX exposure," *Phys. Rev. Lett.* **118** no. 2, (2017) 021303, arXiv:1608.07648 [astro-ph.CO].

[132] D. S. Akerib *et al.*, "Radiogenic and Muon-Induced Backgrounds in the LUX Dark Matter Detector," *Astropart. Phys.* **62** (2015) 33–46, arXiv:1403.1299 [astro-ph.IM].

[133] **LUX Collaboration** Collaboration, D. S. Akerib *et al.*, "Calibration, event reconstruction, data analysis, and limit calculation for the LUX dark matter experiment," *Phys. Rev. D* **97** (May, 2018) 102008.

[134] **LUX** Collaboration, D. S. Akerib *et al.*, "Position Reconstruction in LUX," *JINST* **13** no. 02, (2018) P02001, arXiv:1710.02752 [physics.ins-det].

[135] **XENON** Collaboration, E. Aprile *et al.*, "The XENON1T Dark Matter Experiment," *Eur. Phys. J.* **C77** no. 12, (2017) 881, arXiv:1708.07051 [astro-ph.IM].

[136] K. Ni, "The XENONnT Dark Matter Experiment." Presentation from Division Particle Fields Conference 2017, 7, 2017.

[137] **XENON** Collaboration, E. Aprile *et al.*, "First Dark Matter Search Results from the XENON1T Experiment," *Phys. Rev. Lett.* **119** no. 18, (2017) 181301, arXiv:1705.06655 [astro-ph.CO].

[138] **XENON** Collaboration, E. Aprile *et al.*, "Dark Matter Search Results from a One Tonne×Year Exposure of XENON1T," arXiv:1805.12562 [astro-ph.CO].

[139] **PandaX** Collaboration, X. Cao *et al.*, "PandaX: A Liquid Xenon Dark Matter Experiment at CJPL," *Sci. China Phys. Mech. Astron.* **57** (2014) 1476–1494, arXiv:1405.2882 [physics.ins-det].

[140] **PandaX-II** Collaboration, X. Cui *et al.*, "Dark Matter Results From 54-Ton-Day Exposure of PandaX-II Experiment," *Phys. Rev. Lett.* **119** no. 18, (2017) 181302, arXiv:1708.06917 [astro-ph.CO].

[141] **DarkSide** Collaboration, P. Agnes *et al.*, "DarkSide-50 532-day Dark Matter Search with Low-Radioactivity Argon," arXiv:1802.07198 [astro-ph.CO].

[142] **DarkSide** Collaboration, P. Agnes *et al.*, "First Results from the DarkSide-50 Dark Matter Experiment at Laboratori Nazionali del Gran Sasso," *Phys. Lett.* **B743** (2015) 456–466, arXiv:1410.0653 [astro-ph.CO].

[143] **DEAP-3600** Collaboration, P. A. Amaudruz *et al.*, "Design and Construction of the DEAP-3600 Dark Matter Detector," *Submitted to: Astropart. Phys.* (2017) , arXiv:1712.01982 [astro-ph.IM].

[144] **DEAP-3600** Collaboration, P. A. Amaudruz *et al.*, "First results from the DEAP-3600 dark matter search with argon at SNOLAB," arXiv:1707.08042 [astro-ph.CO].

[145] Heindl, T. and Dandl, T. and Fedenev, A. and Hofmann, M. and Krücken, R. and Oberauer, L. and Potzel, W. and Wieser, J. and Ulrich, A., "Table-top setup for investigating the scintillation properties of liquid argon," *JINST* **6** (2011) P02011, arXiv:1511.07720 [physics.ins-det].

[146] C. S. Chiu, C. Ignarra, L. Bugel, H. Chen, J. M. Conrad, B. J. P. Jones, T. Katori, and I. Moult, "Environmental Effects on TPB Wavelength-Shifting Coatings," *JINST* **7** (2012) P07007, arXiv:1204.5762 [physics.ins-det].

[147] LZ, LBL, "The LZ Detector." http://lz.lbl.gov/wp-content/uploads/sites/6/2017/02/LZ2017.png. Online, accessed 24/09/2017.

[148] **LUX-ZEPLIN** Collaboration, D. S. Akerib *et al.*, "Projected WIMP sensitivity of the LUX-ZEPLIN (LZ) dark matter experiment," arXiv:1802.06039 [astro-ph.IM].

[149] "Identification of Radiopure Titanium for the LZ Dark Matter Experiment and Future Rare Event Searches," *Astroparticle Physics* (2017) .

[150] **LUX** Collaboration, D. S. Akerib *et al.*, "FPGA-based Trigger System for the LUX Dark Matter Experiment," *Nucl. Instrum. Meth.* **A818** (2016) 57–67, arXiv:1511.03541 [physics.ins-det].

[151] Hoff, M. and LZ Collaboration, "LZ Cryostat." LZ Internal.

[152] A. Trogé, R. O'Leary, G. Hayward, R. Pethrick, and A. J Mullholland, *Properties of photocured epoxy resin materials for application in piezoelectric ultrasonic transducer matching layers*, vol. 128. 11, 2010.

[153] *Manuals Combined: Nondestructive Testing (NDT) And Inspection (NDI).*

[154] P. Bloomfield, W.-J. Lo, and P. Lewin, *Experimental study of the acoustical properties of polymers utilized to construct PVDF ultrasonic transducers and the acousto-electric properties of PVDF and P(VDF/TrFE) films*, vol. 47. 12, 2000.

[155] Haller, M.I and Khuri-Yakub, B.T., "Tapered Acoustic Matching Layers." http://web.stanford.edu/group/khuri-yakub/publications/93_Haller_01.pdf.

[156] A. Jain, P. K. J., A. Kr. Sharma, A. Jain, and R. P.N, "Dielectric and piezoelectric properties of PVDF/PZT composites: A review,".

[157] M. Specialities, "Piezo Film Sensors Technical Manual." https://www.sparkfun.com/datasheets/Sensors/Flex/MSI-techman.pdf. Online, accessed 12/02/2018.

[158] P. Scovell, "Report on the Development of an Acoustic Sensor for LZ,".

[159] M. Specialities, "Piezo Film Elements." http://www.meas-spec.com/piezo-film-sensors/piezo-film-elements.aspx,

2015. Online, accessed 15/06/2015.

[160] Manfred Weber Metra Mess- und Frequenztechnik in Radebeul e.K., "Instrumentation 1. Transducers with Charge Output." HTTPS://WWW.MMF.DE/INSTRUMENTATION.HTM. Online: Accessed 19/02/2018.

[161] Karki, James, "Texas Instruments: Signal Conditioning Piezoelectric Sensors." HTTPS://WWW.TI.COM/LIT/AN/SLOA033A/SLOA033A.PDF. Online: Accessed 19/02/2018.

[162] S. Ahmed, *Physics and Engineering of Radiation Detection*. Elsevier Science, 2007.

[163] Födisch, P. and Berthel, M. and Lange, B. and Kirschke, T. and Enghardt, W. and Kaever, P., "Charge-sensitive front-end electronics with operational amplifiers for CdZnTe detectors," *JINST* **11** no. 09, (2016) T09001, arXiv:1603.05098 [physics.ins-det].

[164] N. Aupetit, "ST Microelectronics. AN4708 Application note, Signal conditioning for shock sensors,". http://www.st.com/content/ccc/resource/technical/document/application_note/03/c3/82/1e/a3/57/44/50/DM00188713.pdf/files/DM00188713.pdf/jcr:content/translations/en.DM00188713.pdf.

[165] Rankin, Ryan, "Bubble Resonance." HTTP://FFDEN-2.PHYS.UAF.EDU/311_FALL2004.WEB.DIR/RYAN_RANKIN/BUBBLE%20RESONANCE.HTM. Online: Accessed 03/03/2018.

[166] R. Maev, *Acoustic Microscopy: Fundamentals and Applications*.

[167] A. R. Klotz, "Bubble dynamics in N dimensions," *Physics of Fluids* **25** no. 8, (Aug., 2013) 082109, arXiv:1206.5753 [physics.flu-dyn].

[168] T. Leighton, *The Acoustic Bubble*. No. v. 10.

[169] ET Enterprises Electron Tubes, "Understanding Photomultipliers." https://my.et-enterprises.com/pdf/Understanding-pmts-2011.pdf. Online,

accessed 11/10/2016.

[170] T. Wright and A. Wright, *The Photomultiplier Handbook*. Oxford University Press, 2017.

[171] K. Lung *et al.*, "Characterization of the Hamamatsu R11410-10 3-Inch Photomultiplier Tube for Liquid Xenon Dark Matter Direct Detection Experiments," *Nucl. Instrum. Meth.* **A696** (2012) 32–39, arXiv:1202.2628 [physics.ins-det].

[172] Hamamatsu, "Photomultiplier Tube R11410-22 for LZ-7." Tentative Data Sheet produced for LZ, 7, 2014.

[173] C. H. Faham, V. M. Gehman, A. Currie, A. Dobi, P. Sorensen, and R. J. Gaitskell, "Measurements of wavelength-dependent double photoelectron emission from single photons in VUV-sensitive photomultiplier tubes," *JINST* **10** no. 09, (2015) P09010, arXiv:1506.08748 [physics.ins-det].

[174] H. P. K. E. Committee, *Photomultiplier Tubes Basics and Applications*. Hamamatsu Photonics K.K. Electron Tube Division, 3 ed., 2007.

[175] Sakshat Virtual Labs, "Attenuation & Dispersion Losses." http://iitd.vlab.co.in/?sub=65&brch=180&sim=302&cnt=1. Online, accessed 11/10/2016.

[176] Bernard Hyland, "An Improved and Simple Cable Simulation Model." https://www.maximintegrated.com/en/app-notes/index.mvp/id/5141. Online, accessed 11/10/2016.

[177] EE Times, "Microwave and RF Design: A Systems Approach." http://m.eet.com/media/1072731/C0466pt3.pdf. Online, accessed 11/10/2016.

[178] Donohoe, Patrick J., "Transmission Lines." http://my.ece.msstate.edu/faculty/donohoe/ece4333notes2.pdf. Online, accessed 11/10/2016.

[179] Mogami, "Phase velocity of electromagnetic waves and medium constants." http://www.mogami.com/e/puzzle/pzl-18.html. Online, accessed 11/10/2016.

[180] Capacitor Guide, "Parasitic Inductance." http://www.capacitorguide.com/tag/magnetic-permeability/. Online, accessed 11/10/2016.

[181] Department of Electrical and Computer Engineering, The University of Illinois at Urbana-Champaign, "Capacitance and conductance." http://jsa.ece.illinois.edu/ece329/notes/329lect10.pdf. Online, accessed 11/10/2016.

[182] S. Thierauf, *High-speed Circuit Board Signal Integrity*. Artech House microwave library.

[183] RFCafe, "Dielectric Constant, Strength, & Loss Tangent." http://www.rfcafe.com/references/electrical/dielectric-constants-strengths.htm. Online, accessed 11/10/2016.

[184] Swarthmore College, "Linear Physical Systems Analysis: The Unit Impulse Response." http://lpsa.swarthmore.edu/Transient/TransInputs/TransImpulse.html. Online, accessed 11/10/2016.

[185] LZ Collaboration, "Gore Cable Tests." http://teacher.pas.rochester.edu:8080/wiki/pub/Lz/CoaxialCables/Gore_cable_tests_6-6-16.pdf. LZ internal. Online, accessed 11/10/2016.

[186] Agilent. http://cp.literature.agilent.com/litweb/pdf/genesys200801/elements/substrate_tables/tablelosstan.htm. Online, accessed 11/10/2016.

[187] Pasternack, *Flexible RG178 Coax Cable Single Shielded with Tan FEP Jacket*. Online, accessed 11/10/2016.

[188] Farnell: pro-power, *Cable, Coax, RG178,100 M.* Online, accessed 11/10/2016.

[189] Hirose, Akira, Department of Physics & Engineering Physics, University of Saskatchewan, "Time Varying Fields, Simple Waves." `http://physics.usask.ca/~hirose/p812/notes/Ch4.pdf`. Online, accessed 11/10/2016.

[190] M. Sadiku, *Elements Of Electromagnetics 3E.* The Oxford Series in Electrical and Computer Engineering.

[191] Axon, *Axon A21482C, Coax type K3001 StK1 Cunu - 50 Ohms*, 5, 2016. Rev C.

[192] LZ Collaboration, "Results of the Event Builder from WBS 1.11 and WBS 1.8.".

[193] P. Starič and E. Margan, *Wideband Amplifiers.* Springer US, 2007.

[194] Karki, J., "Active Low-Pass Filter Design." `HTTP://WWW.TI.COM/LIT/AN/SLOA049B/SLOA049B.PDF`. Online: Accessed 12/04/2018.

[195] LZ Collaboration, "Quotation for Event Builder Computer by URTechStore." LZ internal document.

A Acoustic Sensors Quality Control, and Installation

The acoustic sensor works reliably when in thermal contact with −196 °C LN, and can still function even when submerged in LN, which shows that the sensors can operate in temperature conditions that exceed those anticipated in LZ. This was tested over a continuous period of days, during repeated cool-down tests and thermal cycling over a period of a few months.

A Quality Assurance protocol for the acoustic sensors has been developed that will ensure the quality of the sensors to the required standard from procurement to operation. Quality Control checks are also implemented that will verify that each sensor operates to the required standard and is safe to include in LZ. The protocols are driven by LZ cleanliness requirements and the need to ensure good functioning of the sensors.

Before being approved for installation, a basic test of functionality is performed on each sensor. The installation of the sensors has also been specified so as to ensure consistent performance. The quality assurance, quality control, and installation protocols have been successfully tested at Oxford and at the SLAC System Test.

The readout electronics interfaces to the LZ slow-control system through a Modbus interface, and data is available in software - enabling the storage and analysis of full waveform data. This level of integration with LZ subsystems is driven by LZ project requirements, and offers the flexibility to design the electronics and triggering in a way that is not trivially achievable with commercial alternatives.

B Minnaert Resonance Frequency

The radius of the sphere is described by $r(t) = r_0 - A\exp(i\omega_b t)$ where ω_b is the fundamental angular resonance frequency of the bubble. The kinetic energy of the oscillating sphere is [167, 168]

$$E_k = \frac{1}{2}\int_r^\infty 4\pi x^2 \rho \,\mathrm{d}x \left(\frac{\mathrm{d}x}{\mathrm{d}t}\right)^2. \tag{71}$$

Conservation of mass implies

$$\left(\frac{\mathrm{d}x}{\mathrm{d}t}\right) \times \frac{\mathrm{d}t}{\mathrm{d}r} = \frac{r^2}{x^2}, \tag{72}$$

where x is the radius of a sphere element used for the purposes of integration, and r is the bubble radius. The kinetic energy is maximised at $r = r_0$ for which $E_k = 2\pi r^3 \rho (A\omega_b)^2$. The potential energy of the bubble is the work done by an incompressible polytropic fluid on the bubble to change its radius (volume) to the minimum radius (volume), with p_b the pressure of the bubble and p_0 that of the liquid

$$E_p = -\int_{V_0}^{V_{\min}} (p_b - p_0)\, dV = -\int_{r_0}^{A} (p_b - p_0)\, 4\pi x^2 \,\mathrm{d}x, p_0 - p_b = \frac{3\gamma p x}{r}, \tag{73}$$

which gives a maximum of $E_p = 6\pi\gamma p r_0 A^2$ [167, 168]. Equating this result to the maximum kinetic energy

$$6\pi\gamma p r A^2 = 2\pi r^3 \rho (A\omega_b)^2 \tag{74}$$

yields the well-known Minnaert resonance frequency [167, 168]

$$f = \frac{1}{2\pi r}\sqrt{\frac{3\gamma p}{\rho}}, \tag{75}$$

where r is the radius of the bubble, $p = P_0$ is the pressure in the medium, ρ is the density of the medium, and γ is the polytropic coefficient [167, 168].

C Software Packages

This short summary and reference of software packages provides further information about the LZ software and analysis infrastructure.

C.1 DER

C.1.1 Version Control

The DER code is under version control in a dedicated LZ Git repository[64]. Documentation such as the Usage Guide, Release Notes, and Validation Tests track the changes to the software. Presently, everything DER-related is linked to from a single dedicated LZ DER TWiki Page[65].

C.1.2 Documentation

Extensive documentation has been developed discussing the software framework and its modules. There are in-code comments and explanations for every function, method, class, and section. There is also a doxygen[66] equivalent. There is a Usage Guide[67], with instructions on obtaining, running, and using the DER. There are Release Notes[68], which cover changes for each version, as well as an assessment of how software changes affects other groups, users, and interfaces as appropriate. All of these are updated during development to reflect the latest version. There are three major steps in the simulation effort. In order of operation they are: BACCARAT, DER, LZap. The interface between the DER and LZap is an LZap module that can read the output files from the LZ EB according to LZ-ICD-08-0007.

[64] `https://lz-git.ua.edu/sim/ElectronicsSimulation`.

[65] `http://teacher.pas.rochester.edu:8080/wiki/bin/view/Lz/DetectorElectronicsResponse`.

[66] Doxygen is a program that can make a browsable HTML version of code illustrating class structures and comments.

[67] `http://teacher.pas.rochester.edu:8080/wiki/pub/Lz/DetectorElectronicsResponse/UsageGuide.pdf`.

[68] `http://teacher.pas.rochester.edu:8080/wiki/pub/Lz/DetectorElectronicsResponse/ReleaseNotes.pdf`

C.1.3 Interfaces

DER-ready input files are by definition .root files which contain as a minimum the following quantities:

1. Photon Time (in nanoseconds)
2. Photon Wavelength (in nanometers)
3. PMT Index
4. Original Event ID.

The inputs are assumed to be of type double, double, int, and int respectively. All quantities are scalar and there is one entry for each photon hit (there can be multiple entries for each PMT and event). All photons are assumed to have hit the PMT photocathode. The channel mapping of PMTs follows LZ-ICD-08-0008. PMT indices are assumed to be positive discontinuous integers, starting from 0 or higher. PMTs that do not have any photon hits are not assumed not to feature in the input file.

D Cable Derivation

The measure of the change in amplitude of a propagating signal can be expressed as the complex propagation constant γ in terms of the series impedance Z and the shunt admittance $Y = G + i\omega C$

$$\gamma = i\omega\sqrt{LC}\sqrt{\left(1 + \frac{R}{i\omega L}\right)\left(1 + \frac{G}{i\omega C}\right)}, \tag{76}$$

where R, L are the resistance and reactance respectively, and G, C are the conductance and susceptance respectively. γ can be re-arranged into the more usable form

$$\gamma = i\omega\sqrt{LC}\sqrt{1 + \frac{R}{i\omega L} + \frac{G}{i\omega C} - \frac{RG}{\omega^2 LC}} \tag{77}$$

then one makes a low-loss approximation $R \ll \omega L, G \ll \omega C$ such that $\frac{G}{\omega^2 C} \to 0$ leading to

$$\gamma = i\omega\sqrt{LC}\sqrt{1 + \frac{R}{i\omega L} + \frac{G}{i\omega C}}. \tag{78}$$

A Taylor series expansion in R gives

$$\gamma \approx i\omega\sqrt{LC}\left(1 + \frac{1}{2}\left(\frac{R}{i\omega L} + \frac{G}{i\omega C}\right)\right) + \cdots \approx i\omega\sqrt{LC}\left(1 + \frac{R}{2i\omega L} + \frac{G}{2i\omega C}\right). \tag{79}$$

The characteristic impedance in the low-loss approximation is $Z_0 \approx \sqrt{\frac{L}{C}}$, and using Eq. (54), and $\sqrt{L/C} = \sqrt{\varepsilon_r/\mu_r}$ where ε_r, μ_r are the relative permittivity and relative permeability of the shunt admittance, respectively, and letting $\mu_r = 1$

$$\gamma = i\omega\sqrt{LC} + \frac{1}{2WZ_0}\sqrt{\frac{\omega\mu}{2\sigma}} + \frac{\omega\sqrt{\varepsilon_r}\tan\theta}{2c}. \tag{80}$$

The attenuation constant is the real part of the propagation constant such that $\Re(\gamma) = \alpha$ which gives the attenuation of the amplitude of the cable as the ratio of the amplitude at $l = 0$ (no attenuation) to the amplitude at a length l. The gain (transfer function) of the cable is therefore

$$\frac{A_l}{A_0} = e^{-\alpha l}. \tag{81}$$

The attenuation in dB is

$$\mathrm{dB} = 20 \times \log\left(\frac{1}{e^{-\alpha l}}\right) = 20 \times \log e^{\alpha l} = 20\alpha l \log(e) \approx 8.69\alpha l, \tag{82}$$

which indicates increasing attenuation for increasing frequency. The cable attenuation is

$$\exp(\alpha) = \exp(\alpha_1 + \alpha_2) = \exp\left(\frac{1}{2WZ_0}\sqrt{\frac{\omega\mu}{2\sigma}} + \frac{\omega\sqrt{\varepsilon_r}\tan\theta}{2c}\right), \tag{83}$$

where

$$\alpha_1 = \frac{1}{2WZ_0}\sqrt{\frac{\mu}{2\sigma}}l\sqrt{\omega}, \alpha_2 = \frac{\sqrt{\varepsilon_r}\tan\theta}{2c}l\omega. \tag{84}$$

Re-writing $\omega = 2\pi f$

$$\alpha_1 = \frac{\sqrt{\pi}}{2WZ_0}\sqrt{\frac{\mu}{\sigma}}l\sqrt{f}, \alpha_2 = \frac{\pi\sqrt{\varepsilon_r}\tan\theta}{c}lf. \tag{85}$$

The attenuation of the cable is expressed in terms of physical parameters: the cable core width W and its length l, its characteristic impedance Z_0, its conductance σ, the relative dielectric constant of the dielectric ε_r, the loss tangent of the cable $\tan\theta$, the magnetic permeability of free space μ, and the speed of light c [175–190].

E Amplifier Derivation

E.1 Low-Gain

E.1.1 Low Gain Stage 1

For the first-block of the low-gain channel

$$\frac{V_{out}}{V_{in}} = \frac{R_{311}/R_c}{1+\frac{1}{G_F}\frac{R_{311}}{R_c}} \frac{1+i\omega R_c C_{309}}{(1+i\omega R_{311}C_{309})(1+i\omega\tau_F)}, \tag{86}$$

where τ_F is that pole of the op-amp which is due to the finite gain-bandwidth product. For the system including the finite open-loop gain with $G = 17000, \tau_F = 211\,\text{kHz}$ the solutions to the denominator polynomial are

$$\begin{aligned} p_1 &= -3.904693725465079 \\ p_2 &= -0.184122895332729. \end{aligned} \tag{87}$$

The pole solutions are all negative, implying a stable system with all solutions on the left of the imaginary axis. The time constants of the poles can be deduced respectively as

$$\begin{aligned} p_1 &= 0.2561020327\ \text{ns} \\ p_2 &= 5.4311550891\ \text{ns}, \end{aligned} \tag{88}$$

for the system including the open-loop gain. The component values used are

- $R_{308} = 249\,\Omega$
- $R_{311} = 249\,\Omega$
- $C_{309} = 10\,\text{pF}$.

E.1.2 Low Gain Stage 2

The second block of the low-gain channel contains a feedback element, increasing the complexity of the calculation. With the variables R, C as labelled on the circuit diagram, starting from

$$V_0 = \frac{E}{B\left(\frac{E}{G_F} + D\right) - AE} V_I \tag{89}$$

$$A = i\omega R_{314} C_{303}$$

$$B = \left[1 + \frac{R_{314}}{R_{315}}\right] \left[(1 + i\omega R_{316} C_{311}) \left(1 + i\omega \frac{R_{314} R_{315}}{R_{314} + R_{315}} C_{303}\right) + i\omega \frac{R_{314} R_{315}}{R_{314} + R_{315}} C_{311}\right]$$

$$D = 1 + i\omega R_{321} C_{308} + T \frac{R_{321}}{R_{307}}$$

$$E = 1 + i\omega R_{321} C_{308} + \frac{R_{321}}{R_{317}} + \frac{R_{321}}{R_{307}}$$

$$T = \frac{1 + i\omega R_{303} C_{304}}{1 + i\omega R_{306} C_{306}} \times \frac{1}{i\omega R_{303} C_{304}}.$$

Furthermore, define the numerator and denominator of T

$$T_n = 1 + i\omega R_{303} C_{304} \tag{90}$$

$$T_d = (1 + i\omega R_{306} C_{306})\, i\omega R_{303} C_{304}.$$

The solution strategy is to multiply out all terms from Eq. (89), grouping by powers of $i\omega$. Some of the terms from BD will contain T within them. Since T has a denominator containing $i\omega$, the strategy is to multiply out T_d across all of the other terms. The terms to compute are $E, BE/G_F, BD, AE$. Then, each of these terms is multiplied by T_d. Once this step is complete, all terms must be grouped into powers of $i\omega$ once more. The result is a sixth order polynomial.

The solutions to the denominator polynomial are

$$p_1 = -6.186977992109761 \times 10^9 \tag{91}$$
$$p_2 = -0.147534938347134 \times 10^9 + 0.094222995484104i \times 10^9$$
$$p_3 = -0.147534938347134 \times 10^9 - 0.094222995484104i \times 10^9$$
$$p_4 = -0.000001000000000 \times 10^9$$
$$p_5 = -0.000000498762097 \times 10^9$$
$$p_6 = -4.377731174767447 \times 10^9.$$

The pole solutions are all negative, implying a stable system with all solutions on the left of the imaginary axis. The time constants of the poles can be deduced respectively as

$$p_1 = 0.161\,629\,797\,5\,\text{ns} \tag{92}$$
$$p_2 = 4.814\,397\,021\,614\,77\,\text{ns} + 3.074\,708\,363\,377\,33\text{i}\,\text{ns}$$
$$p_3 = 4.814\,397\,021\,614\,77\,\text{ns} - 3.074\,708\,363\,377\,33\text{i}\,\text{ns}$$
$$p_4 = 0.001\,000\,000\,000\,\text{s}$$
$$p_5 = 0.002\,004\,963\,902\,\text{s}$$
$$p_6 = 0.228\,428\,827\,6\,\text{ns},$$

for the system including the open-loop gain.

Definitions for the low-gain component terms are

$$R_a = \frac{1}{\frac{1}{R_{321}} + \frac{1}{R_{307}} + \frac{1}{R_{317}}} \tag{93}$$

$$R_b = \frac{R_{314}R_{315}}{R_{314} + R_{315}} \tag{94}$$

$$R_c = \frac{R_{308}R_{311}}{R_{308} + R_{311}} \tag{95}$$

$$R_d = \frac{R_{413}R_{417}}{R_{413} + R_{417}} \tag{96}$$

$$R_e = \frac{R_{410}R_{411}}{R_{410} + R_{411}}. \tag{97}$$

For the high-gain equivalent, these definitions are analogous differing only in the label identifier and the component value to which it corresponds.

The component values used are

- $R_{303} = 100\,\mathrm{k\Omega}$
- $R_{306} = 100\,\mathrm{k\Omega}$
- $R_{307} = 1\,\mathrm{k\Omega}$
- $R_{314} = 332\,\Omega$
- $R_{315} = 215\,\Omega$
- $R_{316} = 332\,\Omega$
- $R_{317} = 75\,\Omega$
- $R_{321} = 499\,\Omega$
- $C_{303} = 2\,\mathrm{pF}$
- $C_{304} = 0.01\,\mu\mathrm{F}$
- $C_{306} = 0.01\,\mu\mathrm{F}$
- $C_{308} = 10\,\mathrm{pF}$
- $C_{311} = 10\,\mathrm{pF}$.

E.2 High-Gain

The procedure to calculate the time constants is the same, the difference is in the circuit diagram. The circuit diagram has a slightly modified first stage consisting of an extra parallel resistor/capacitor set. There is an additional intermediate stage that does not exist in the low-gain version of the amplifier. It consists of the input stage repeated inside a Sallen-Key structure as encountered in the feedback block in the low-gain amplifier.

E.2.1 High Gain Stage 1

The first stage (first block, or stage 1) has the transfer function

$$V_o = \left(1 + \frac{Z_F}{Z_G}\right) V_i, \tag{98}$$

thus

$$V_o = \frac{R_{407}}{R_c} \frac{1 + i\omega R_c \left(C_{417} + C_{418}\right)}{1 + i\omega R_{407} C_{418} + \frac{1}{G}\frac{R_{407}}{R_c}\left(1 + i\omega R_c \left(C_{417} + C_{418}\right)\right)} V_i, \tag{99}$$

where

$$R_c = \frac{R_{405} R_{407}}{R_{405} + R_{407}}. \tag{100}$$

For the system without the open loop-gain, the time constants are a pole with $\tau_1 = R_{407} C_{418} = 0.000\,000\,004\,99\,\mathrm{s}$ and a zero with $\tau_2 = R_c \left(C_{417} + C_{418}\right)$, and the gain is R_{407}/R_c.

Adding the open-loop gain to the first stage: $\frac{1}{G} = \frac{1}{G_F}\left(1 + i\omega\tau_F\right)$. Recovering a leading 1 in the denominator to get the gain factor involves pulling out a factor of

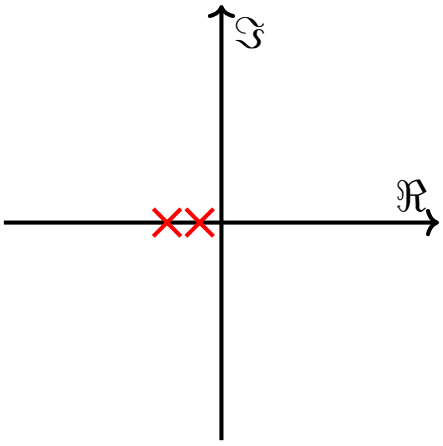
$$\frac{1}{1 + \frac{1}{G_F}\frac{R_{407}}{R_c}}, \tag{101}$$

thus the transfer function becomes

$$V_o = \frac{R_{407}}{R_c} \frac{1}{1 + \frac{1}{G_F}\frac{R_{407}}{R_c}} \frac{1 + i\omega R_c \left(C_{417} + C_{418}\right)}{1 + i\omega \frac{(G_F+1)R_{407}C_{418} + R_{407}C_{417} + \tau_F \frac{R_{407}}{R_c}}{G_F + \frac{R_{407}}{R_c}} + (i\omega)^2 \frac{\tau_F R_{407}(C_{417}+C_{418})}{G_F + \frac{R_{407}}{R_c}}} V_i. \tag{102}$$

The pole solutions are a pair of complex conjugate poles

$$\begin{aligned} p_1 &= -1.256323319917094 \times 10^9 \\ p_2 &= -0.154716209263360 \times 10^9. \end{aligned} \tag{103}$$



The pole solutions are all negative, implying a stable system with all solutions on the left of the imaginary axis. The time constants of the poles can be deduced respectively as

$$\begin{aligned} p_1 &= 0.7959734442 \text{ ns} \\ p_2 &= 6.4634468797 \text{ ns}. \end{aligned} \tag{104}$$

The component values used are

- $R_{405} = 69.8\,\Omega$
- $R_{407} = 499\,\Omega$
- $C_{417} = 27\,\text{pF}$
- $C_{418} = 10\,\text{pF}$.

E.2.2 High Gain Stage 2

The middle stage (middle block, or stage 2) of the high-gain is calculated here.

First note

$$Z_F = R_{417}\frac{1}{1+i\omega R_{417}C_{415}}, Z_G = R_{413}\frac{1}{1+i\omega R_{413}C_{414}}. \tag{105}$$

Therefore V_- is

$$V_- = V_o\left(1+\frac{Z_F}{Z_G}\right)^{-1}V_o, \tag{106}$$

so

$$V_- = \frac{(1+i\omega R_{417}C_{415})}{(1+i\omega R_{417}C_{415})+\frac{R_{417}}{R_{413}}(1+i\omega R_{413}C_{414})}. \tag{107}$$

V_+ is

$$V_+ = V_*\frac{1}{1+i\omega R_{419}C_{422}}, \tag{108}$$

and current conservation implies

$$(V_o - V_*)\, i\omega C_{407} = \frac{V_* - V_i}{R_{410}} + \frac{V_*}{R_{411}} + \frac{V_*}{R_{419}+\frac{1}{i\omega C_{422}}}. \tag{109}$$

This can be re-arranged and solved for V_*, and this expression is in turn substituted back into the expression for V_+ giving

$$V_+ = \frac{i\omega R_{410}C_{407}V_o + V_i}{\frac{R_{410}}{R_b}\left[(1+i\omega R_{419}C_{422})(1+i\omega R_bC_{407})+i\omega R_{410}C_{422}\right]}. \tag{110}$$

The transfer function is then

$$V_o = G_F\left(V_+ - V_-\right). \tag{111}$$

Substituting V_+, V_- into this expression the same form as was calculated for the low-gain last block is achieved. Starting from the same form as was done

for the last stage of the low-gain but now for the high-gain

$$V_0 = \frac{E}{B\left(\frac{E}{G_F} + D\right) - AE} V_I \tag{112}$$

$$A = i\omega R_{410} C_{407}$$

$$B = \frac{R_{410}}{R_b}\left[\left(1 + i\omega R_{419} C_{422}\right)\left(1 + i\omega R_b C_{407}\right) + i\omega R_b C_{422}\right]$$

$$D = 1 + i\omega R_{417} C_{415}$$

$$E = 1 + i\omega R_{417} C_{415} + \frac{R_{417}}{R_{413}}\left(1 + i\omega R_{413} C_{414}\right).$$

Note the definition

$$R_b = \frac{R_{410} R_{411}}{R_{410} + R_{411}}. \tag{113}$$

For the system including the finite open-loop gain with $G = 17000, \tau_F = 211\,\text{kHz}$, the transfer function is the same as calculated previously for the low-gain, differing only in component values.

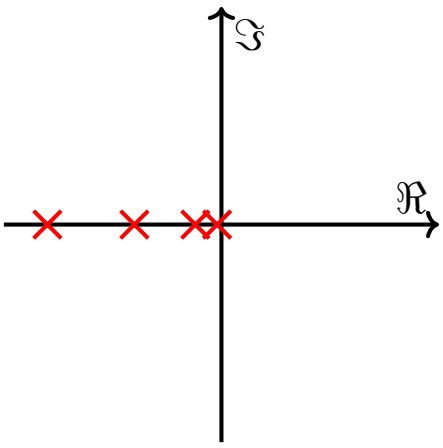
The solutions to the denominator polynomial are

$$p_1 = -5.798144551595068 \times 10^9 \tag{114}$$

$$p_2 = -0.186648805310668 \times 10^9$$

$$p_3 = -0.079514282468923 \times 10^9$$

$$p_4 = -2.606801047674741 \times 10^9.$$



The pole solutions are all negative, implying a stable system with all solutions

on the left of the imaginary axis. The time constants of the poles can be deduced respectively as

$$p_1 = 0.1724689668 \text{ ns} \tag{115}$$

$$p_2 = 5.3576555089 \text{ ns}$$

$$p_3 = 12.5763569632 \text{ ns}$$

$$p_4 = 0.3836119373 \text{ ns}.$$

The component values used are

- $R_{410} = 332\,\Omega$
- $R_{411} = 215\,\Omega$
- $R_{413} = 75\,\Omega$
- $R_{417} = 499\,\Omega$
- $R_{419} = 332\,\Omega$
- $C_{407} = 2\,\text{pF}$
- $C_{414} = 10\,\text{pF}$
- $C_{415} = 27\,\text{pF}$
- $C_{422} = 10\,\text{pF}.$

E.2.3 High Gain Stage 3

The final stage (stage 3, block 3) of the high-gain amplifier is equivalent to the final stage (stage 2) of the low-gain, differing only in component values.

Only the following substitutions are necessary:

- R303 → R406
- R306 → R414
- R307 → R412
- R314 → R415
- R315 → R420
- R316 → R416
- R317 → R423
- R321 → R427
- C303 → C423
- C304 → C408
- C306 → C409
- C308 → C? → Has a question mark on diagram, denote it Cx
- C311 → C421.

Furthermore this means

$$R_a = \left(\frac{1}{R_{427}} + \frac{1}{R_{412}} + \frac{1}{R_{423}}\right)^{-1}, R_b = \frac{R_{415}R_{420}}{R_{415} + R_{420}}. \tag{116}$$

$$p_1 = -6.186977988516630 \times 10^9 \tag{117}$$

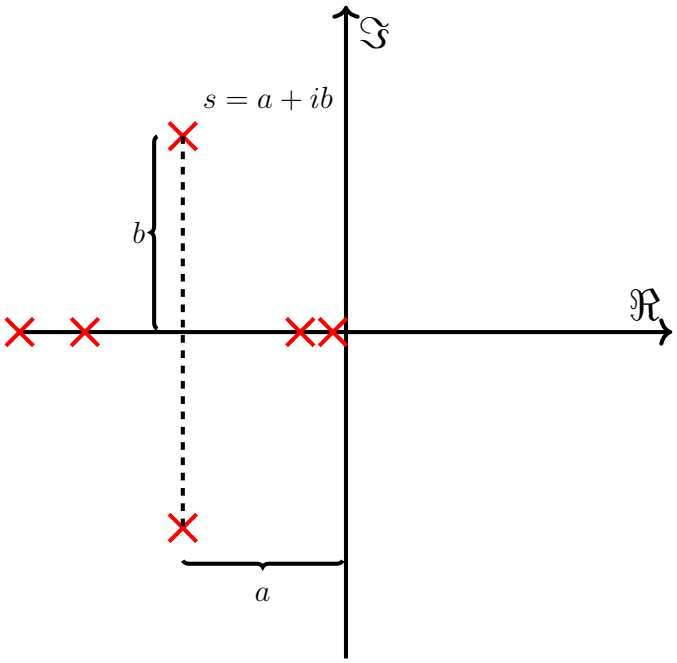
$$p_2 = -0.147535169557336 \times 10^9 - 0.094223008603138i \times 10^9$$

$$p_3 = -0.147535169557336 \times 10^9 + 0.094223008603138i \times 10^9$$

$$p_4 = -0.000000100000000 \times 10^9$$

$$p_5 = -0.000000049876095 \times 10^9$$

$$p_6 = -4.377731164826183 \times 10^9.$$



The pole solutions are all negative, implying a stable system with all solutions on the left of the imaginary axis. The time constants of the poles can be

deduced respectively as

$$p_1 = 0.1616297976 \text{ ns} \tag{118}$$

$$p_2 = 4.81439345995137 \text{ ns} - 3.07470169829301i \text{ ns}$$

$$p_3 = 4.81439345995137 \text{ ns} + 3.07470169829301i \text{ ns}$$

$$p_4 = 0.01 \text{ s}$$

$$p_5 = 0.02004968512 \text{ s}$$

$$p_6 = 0.2284288282 \text{ ns},$$

for the high-gain system including the open-loop gain.

The component values used are

- $R_{406} = 100\,\mathrm{k\Omega}$
- $R_{412} = 1\,\mathrm{k\Omega}$
- $R_{414} = 100\,\mathrm{k\Omega}$
- $R_{415} = 332\,\Omega$
- $R_{416} = 332\,\Omega$
- $R_{420} = 215\,\Omega$
- $R_{423} = 75\,\Omega$
- $R_{427} = 499\,\Omega$
- $C_{408} = 0.1\,\mu\mathrm{F}$
- $C_{409} = 0.1\,\mu\mathrm{F}$
- $C_{421} = 10\,\mathrm{pF}$
- $C_{423} = 2\,\mathrm{pF}$
- $C_{\mathrm{x}} = 10\,\mathrm{pF}$.

E.3 Laplace Transform for Sallen-Key Element

The Sallen-Key term must be mapped onto a time-domain representation. The frequency domain transfer function for the Sallen-Key element can be transformed into the time-domain by using the Laplace transform. For this demonstration, the expression $\exp(at)\sin(bt)$ will be converted from the time-domain into the frequency domain, and it will be shown that this form is consistent with the transfer function of the Sallen-Key.

First use the general result that

$$\mathcal{L}\{\exp(at)\sin(bt)\} = \frac{b}{b^2+(a-s)^2}, s > a. \tag{119}$$

Now setting

$$e^{-\gamma t}\sin\alpha t \tag{120}$$

one sets $a = -\gamma, b = \alpha$. Then

$$e^{-\gamma t}\sin(\alpha t) = \frac{\alpha}{\alpha^2+(-\gamma-s)^2}, \tag{121}$$

where $s > -\gamma$. This function has poles at $\alpha^2 = -(\gamma-s)^2$. Let $s = i\omega$ be the complex mapping from the s-domain into the ω-domain, so that

$$e^{-\gamma t}\sin(\alpha t) = \frac{\alpha}{\alpha^2+\gamma^2+(i\omega)^2+2\gamma i\omega}. \tag{122}$$

Pulling out a factor $\alpha/(\alpha^2+\gamma^2)$ one obtains

$$\frac{\alpha}{\alpha^2+\gamma^2}\left(\frac{1}{1+i\omega\frac{2\gamma}{\alpha^2+\gamma^2}+(i\omega)^2\frac{1}{\alpha^2+\gamma^2}}\right), \tag{123}$$

which has the same form as the Sallen-Key transfer function.

Note that the Sallen-Key Laplace transform in the time domain can be re-written as

$$\exp(at)\sin(bt) = \Im\left(\exp(at)\exp(bt)\right). \tag{124}$$

Now it is possible to evaluate the time domain incremental change in the response $g(t)$

$$g(t) = \exp(-\gamma t)\exp(i\alpha t) = \exp(i\alpha t - \gamma) \tag{125}$$

so that

$$\int_{t_1}^{t_2} g(t)\,\mathrm{d}t = \frac{1}{-\gamma + i\alpha}\left(\exp\left((i\alpha - \gamma)\,\Delta t\right) - 1\right), \tag{126}$$

where $\Delta t = t_2 - t_1$. Now it is clear that iterations of $g(t)$ for each Δt will introduce factors of $\exp(-\gamma + i\alpha)\,\mathrm{d}t$, in addition to multiplying the input by

$$\frac{1}{\gamma - i\alpha}\left(1 - \exp\left((\gamma + i\alpha)\,\mathrm{d}t\right)\right). \tag{127}$$

The coefficients γ, α are obtained by comparing coefficients for powers of ω

$$\frac{1}{\gamma^2 + \alpha^2} = \tau_0\tau_1,\ \frac{2\gamma}{\gamma^2 + \alpha^2} \implies \gamma = \frac{\tau_0 + \tau_1}{2\tau_0\tau_1} \implies \alpha = \sqrt{\frac{1}{\tau_0\tau_1} - \left(\frac{\tau_0 + \tau_1}{2\tau_0\tau_1}\right)^2}. \tag{128}$$

F Digitiser Anti-Aliasing Filter Derivation

Let V_{in} be the input voltage that is coming from the amplifier, V_2 the voltage at the node that has C_2 to ground, and V_1 the voltage at the node between R_3 and C_1. V_{out} is the voltage at the output of the op-amp. The inputs to the op-amp are V_+, V_- for the positive and negative terminal, respectively. There are two simultaneous equations for the nodal currents [193, 194]

$$\frac{V_{in} - V_2}{R_1} = \frac{V_2 - V_{out}}{R_2} + V_2 i\omega C_2 + \frac{V_2}{R_3} \tag{129}$$

$$\frac{V_2 - V_1}{R_3} = \frac{V_1 - V_{out}}{1/\left(i\omega C_1\right)}, \tag{130}$$

where $V_+ = 0, V_- = V_+$ so $V_1 = 0$. Furthermore

$$\frac{V_2}{R_3} = -V_{out} i\omega C_1, \tag{131}$$

so that

$$V_2 = -V_{out} i\omega R_3 C_1. \tag{132}$$

Re-arranging Eq. (129) for V_{in} and then substituting Eq. (132)

$$V_{in} = -V_{out} i\omega R_3 C_1 \left(\frac{R_1}{R_2} + i\omega R_1 C_2 + \frac{R_1}{R_3} + 1\right) - V_{out}\frac{R_1}{R_2}, \tag{133}$$

from which the transfer function follows

$$\frac{V_{\text{out}}}{V_{\text{in}}} = -\frac{R_2}{R_1}\frac{1}{1 + (i\omega)\left(R_3 C_1 + R_2 C_1 + \frac{R_2 R_3 C_1}{R_1}\right) + (i\omega)^2 \left(R_3 C_1 R_2 C_2\right)}. \tag{134}$$

The pole solutions are a complex conjugate pair $s = -1.527\,116\,418\,897\,901 \times 10^8 \pm 0.894\,685\,387\,963\,745 \times 10^8 i$. The component values used are $R_1 = 453\,\Omega$, $R_2 = 453\,\Omega$, $R_3 = 261\,\Omega$, $C_1 = 10\,\text{pF}$, $C_2 = 27\,\text{pF}$.

G Event Builder Specifications

The machine specifications of the event builder computer are [195]

- Processor: Intel® Xeon® processor. ES-2630 V3 2.4 GHz, 20 MB cache.[69]
- Memory: 16 GB 2400 MT/S RDIMMS 2400MT.
- Hard drive: 1 TB 7200 RPM SATA 6 GB s^{-1}.

[69] Intel and Xeon are trademarks of Intel Corporation or its subsidiaries in the U.S. and/or other countries.